Effects of Axial Turbine Tip Shroud Cavity Flow on Performance and Durability

by

Timothy R. Palmer

B.S., University of California, San Diego (2009)
S.M., Massachusetts Institute of Technology (2011)

Submitted to the Department of Mechanical Engineering
in partial fulfillment of the requirements for the degree of

Doctor of Philosophy

at the

MASSACHUSETTS INSTITUTE OF TECHNOLOGY

February 2015

Author .....
Department of Mechanical Engineering
September 19, 2014

Certified by .....
Choon S. Tan
Senior Research Engineer, Department of Aeronautics and Astronautics
Thesis Supervisor

Certified by .....
John G. Brisson
Professor of Mechanical Engineering
Chairman, Thesis Committee

Accepted by .....
David E. Hardt
Professor of Mechanical Engineering
Chair, Graduate Program Committee

Effects of Axial Turbine Tip Shroud Cavity Flow on Performance and Durability

by

Timothy R. Palmer

Submitted to the Department of Mechanical Engineering
on September 19, 2014, in partial fulfillment of the
requirements for the degree of
Doctor of Philosophy

Abstract

Flow through tip shroud cavity in a representative axial turbine vane-rotor stage environment is assessed for its role in loss generation and turbine durability. Steady and unsteady three-dimensional flow computations, complemented by control volume analyses, for varying shroud configurations provided results for establishing quantitative links between loss and flow processes as well as loss level scalings. Specifically tip shroud cavity flow is dominated by two counter-rotating vortices upstream, and a free expansion leakage jet downstream, of the tip seal, followed by a mixing shear layer at cavity exit. One of the vortices, the cavity inlet toroidal vortex, sets the loss level within the cavity inlet and the mass flow recirculated out of the cavity into the main flow path. It is found that tip shroud cavity flow incurs a 0.85% debit in stage efficiency per 1% of main flow fluid through the cavity with approximately 50% generated in the free expansion of the tip seal leakage jet and 50% from cavity exit mixing. The proportion of total loss attributable to cavity exit mixing increases with tip seal gap. In addition, vane-rotor unsteady interaction induces an additional 0.25% debit in efficiency per 1% of main flow fluid through the cavity. The additional efficiency penalty induced by vane-rotor unsteady interaction results from an enhancement of the cavity inlet toroidal vortex and associated recirculated mass flow. Overall cavity loss is set by cavity mass flow fraction, stagnation pressure ratio across tip seal, velocity disparity between cavity exit flow and rotor exit flow, and cavity inlet vortex strength. These findings were used to formulate a modified tip shroud configuration that nearly eliminates cavity exit mixing loss, but it incurs a penalty associated with cavity flow low Reynolds number effects and induced mismatching between vane and modified tip shroud. In the process of designing this modified tip shroud, it was found that the turbine main flow perceives the cavity as a line sink-source pair, permitting estimation of flow redistribution in the main flow path. Finally, any operational transients which eliminate tip seal clearance would lead to enhanced impingement heat transfer at blade tip due to recirculating flow from cavity inlet; this can increase the likelihood of blade failure.

Thesis Supervisor: Choon S. Tan
Title: Senior Research Engineer, Department of Aeronautics and Astronautics

Acknowledgments

I owe a great debt of gratitude to many for all the love and support lent to me during completion of this thesis. The following is my attempt to convey my thanks and appreciation.

Above all, I want to acknowledge God the Father. His Providence and blessing saw me through the periods of trial and uncertainty, of mind-wracking frustration when attempting to solve a problem, as well as the periods of rejoicing. His Hand also guided my path so that it crossed those of many of the others to follow in these acknowledgments. The relationships which have been so crucial during this time in my life are all of His blessing. Without God, and my faith in Him, none of this would have been possible.

Of the many individuals who aided me in the completion of this thesis, I would like to first thank my advisor, Dr. Choon Tan. Over these past years, his guidance has been invaluable, and the dedication to his students unmatched. He has pushed me to improve and solve problems I did not think I could. He has also given me the opportunities to grow professionally by inviting me to participate more fully in the professional community and mentor my fellow students. For these traits, among others, I am ever grateful to have had him as my advisor.

I would also like to thank the rest of my committee for all of their contributions during the project. Despite being exceptionally busy with other commitments in their own labs or duties for the Institute (or in Professor Cumpsty's case, being a visiting international professor), each member has done everything possible to be available to provide guidance and advice and to be flexible in scheduling of committee meetings. Their differing perspectives and unique backgrounds have provided several unique perspectives on the project which has been quite beneficial in interpreting the results.

Throughout this work, I collaborated regularly with engineers from Siemens Energy. In particular, I would like to thank Dr. Matthew Montgomery, Dr. Tony Malandra, Mr. Dave Little, and Dr. Kunyuan Zhou for their valuable insights and discussions. Drs. Matthew Montgomery and Tony Malandra were also very helpful in interfacing with Siemens Corporate when attempting to publish this research in papers and presentations. I would also like to especially thank Dr. Humberto Zuniga and Mr. Martin Bowers for their assistance in creating meshes for computations and teaching me the intricacies of CFX.

I also would like to acknowledge my fellow labmates and everything they did to support me throughout this work. In particular, I would like to thank Dr. Andreas Peters (now with GE Aviation), Mr. David Hall, Mr. Arthur Huang, Mr. Anjaney Kottapalli (now with Lockheed Martin), Mr. Max Brand (now with Pratt and Whitney), Dr. Claudio Lettieri, Dr. Danial Cuppoletti, and Mr. Andras Kiss. From tech support to attending practice presentations to late-night discussion of research and aerodynamics, all of these individuals enriched my time during the PhD. All of their time and patience was greatly appreciated; I could not have asked for better colleagues.

Finally, to all my family and friends, thank you for your support and encouragement these past few years. I especially want to thank my parents, Brian and Bonnie, and my sister, Becky, for tolerating me when overwhelmed and be willing to tell me to suck it up when necessary. To my adopted family at Hope Fellowship Church, it has been a blessing to worship and serve with you these past years. I cannot thank you enough for the prayers and encouragement. I especially want to thank my best friend and (former) fellow MIT graduate student, Dr. Jon Gilbert, for your invaluable friendship. You suffered through several practice presentations and joined me for more than a few de-stress workouts that most others would balk at. As the show Scrubs says, no one can survive medical school (or in this case, graduate school) without a strong core group of friends. Similarly, your support, Jon, and that of all those at Hope, has played a large role in this success.

Contents

1 Introduction **25**

1.1 Motivation 26

1.2 Technical Objectives and Hypotheses 27

1.3 Literature Review 29

1.4 Research Framework 32

1.5 Major Findings and Contributions 46

1.6 Thesis Organization 48

2 Isolation of Major Loss Mechanisms in Steady Cavity Flow **49**

2.1 Quantifying Losses Associated with the Cavity 50

2.2 Primary Loss Mechanisms 52

2.2.1 Free Expansion Losses of the Tip Leakage Jet 52

2.2.2 Losses due to Mixing 61

2.2.2.1 Quantification of Loss with Varying Injected Sealing Flow 61

2.2.2.2 Trends in Loss Mechanism Contributions 63

2.2.2.3 Control Volume Analysis of Mixing Losses 65

2.2.2.4 Importance of Relative Flow Angle and Swirl Disparity 67

2.2.3 Mixing Loss Enhancement with Asymmetric Shroud 72

2.2.4 Dependence of Mixing Loss on Machine Size 74

2.2.5 Limitations on Controlling Mixing Losses 75

2.3 Summary of Major Loss Sources in Tip Shroud Cavity Flow 78

3 Effects of Nozzle Guide Vane-Rotor Interaction on Tip Shroud Cavity Flow **81**

3.1 Influence of Interaction Effects on Datum Loss Levels 82

3.2 Enhancement of the Cavity Inlet Toroidal Vortex 85

3.2.1 Increased Scrubbing Losses on Cavity Inlet Casing 85

3.2.2 Cavity Inlet Mass Recirculation 93

3.2.3 Mass Recirculation Effects on Component Durability 102

3.2.4 Generalization of Cavity Inlet Vortex Behavior 106

3.2.4.1 Mechanism of Cavity Inlet Vortex Configuration Change 106

3.2.4.2 Qualitative Design Guidelines for an Efficient Cavity Inlet Vortex 110

3.2.4.3 Operational Limits of the Cavity Inlet Toroidal Vortex 112

3.2.4.4 Importance of Radial versus Axial Elongation 125

3.3 Summary of NGV-Rotor Interaction Effects in Generic Cavity 126

4 The Hybrid Blade Design for Mitigating Cavity Mixing Losses **129**

4.1 The Hybrid Blade Underlying Concept and Configuration Details . . 130

4.1.1 Physical Reasoning Motivating the Hybrid Blade Design . . . 130

4.2 Cavity Coupling with the Main Flow Path 135

4.2.1 Cavity as a Potential Flow Sink-Source Pair with Finite Separation 136

4.2.2 Assessment of Cavity Coupling Model with Computations . . 138

4.2.3 Extrapolation of Hybrid Blade Performance 141

4.3 Computational Results for the Hybrid Blade Design 144

4.3.1 Overview of Hybrid Blade Loss Levels 144

4.3.2 Reduction in Mixing Losses using the Hybrid Blade 149

4.3.3 Comparison of Tip Seal Jet Free Expansion and Bladelet Loss Mechanisms 152

4.3.4 Loss Increases in Hybrid Blade Main Flow Path: Stator Domain 156

4.3.4.1 Origin of Increased Loss in Hybrid Blade Stator . . 158
4.3.4.2 Quantification of Cavity Upstream Influence 160
4.3.5 Loss Increases in Hybrid Blade Main Flow Path: Diffuser . . 164
4.3.6 Synthesis of Loss Mechanisms and Definition of Performance Limits 170
4.4 Summary of Hybrid Blade Effectiveness at Mitigation of Cavity Loss Mechanisms 174

5 Summary and Conclusions 177
5.1 Main Conclusions 180
5.2 Future Work 181
5.2.1 Optimization of the Hybrid Blade Configuration 182
5.2.2 Free Expansion of the Tip Seal Leakage Jet 182
5.2.3 Further Generalization of Findings 184
5.2.4 Cavity Inlet Toroidal Vortex 185
5.2.4.1 Quantification of Inlet Vortex Limits, ... 186
5.2.4.2 Quantification of Elliptical Vortex Cores 187

A Sensitivity of Results to Changes in Operational Back Pressure 189
A.1 Variation of Generic Shroud Losses with Off-Design Operation 190
A.1.1 Steady Off-Design Operation 190
A.1.2 Sensitivity of Vane-Rotor Interaction Effects to Off-Design Operation 193
A.1.3 Off-Design Operation and Shroud Asymmetry 194
A.2 Summary of Off-Design Operation Results 195

B Estimation of Uncertainty in Loss 197

C Control Volume Estimation of Free Expansion Losses 201

D Mass Flow Rate Variation with Pressure Ratio through Sharp-Edged Orifice 207

E Mixing Loss between Two Streams **213**

F Influence of Area Ratio on Choking Condition in Swirling Flow **219**

List of Figures

1-1 Generic tip shroud cavity geometry and computed flow field for representative axial gas turbine. 29

1-2 Computational domain and nomenclature for generic cavity domain regions and features 33

1-3 Computational domain for the idealized baseline stage with no rotor tip cavity 34

1-4 Computational geometry of the scalloped shroud configuration. 36

1-5 Ideal expansion of two streams. 40

1-6 Schematic of division of subdomains to localize change in loss between major cases. The stator domain includes the interface between stator and rotor (i.e. it contains the mixing plane for those calculations using the Stage frame change model, or the sliding interface for transient calculations) 43

1-7 Isometric view of the Hybrid Blade design and computational geometry. 47

2-1 Difference in loss accumulation between the generic cavity and baseline configurations at axial locations from inlet to exit of flow domain. . . 51

2-2 Contour plot of normalized $\dot{S}'''_{visc}$ highlighting regions of high loss generation in the cavity. 51

2-3 Total stage loss versus fraction of the main flow which passes through the cavity. 53

2-4 Breakdown of loss contribution for primary mechanisms when varying tip gap. 54

2-5 Simple axisymmetric model of tip seal orifice. 55
2-6 Comparison of free expansion jet loss model with loss levels from CFD, as a function of tip gap. 57
2-7 Comparison of free expansion jet loss model with mixing length correlative factor with loss levels from CFD, as a function of tip gap. . . 58
2-8 Comparison of total, and individual contributions to, cavity loss for several injected sealing flow rates. 62
2-9 Simple axisymmetric model of mixing between an injected flow and main flow [1]. 64
2-10 Importance of relative flow angle in Cavity Mixing. 66
2-11 Variation of relative flow angle between cavity exit flow and rotor exit flow versus injected sealing mass flow rate. 67
2-12 Cavity (black) and main flow streamlines (magenta) at interaction interface at cavity exit. 67
2-13 Variation of loss coefficient in the Cavity Mixing process with swirl parameter. 69
2-14 Variation of loss coefficient in the Exit Mixing process with swirl parameter, Sw. 69
2-15 Contour plots of swirl parameter (based on axial velocity) at the interface between cavity exit flow and rotor exit flow. 71
2-16 Comparison of axial accumulation of loss in the rotor and cavity domains only of the scalloped and generic shroud configurations. 73
2-17 Axial profile of the difference in loss accumulation of 4 times nominal injected sealing mass flow rate, with swirl minus no swirl. 76
2-18 Contour plots of volumetric viscous entropy generation for injected sealing flow case with and without injected swirl. 77

3-1 Axial profile of the difference in loss accumulation between the steady baseline case and the other steady and unsteady major cases. 83

3-2 Breakdown of loss by subdomain for steady and unsteady major cases compared to the steady baseline case. 83
3-3 Comparison of axial accumulation of loss within the cavity for steady and time-averaged unsteady generic shrouds. 86
3-4 Contours comparing volumetric viscous entropy generation using two different calculation methods. 87
3-5 Contour of difference in circumferential vorticity between the steady and time-averaged unsteady generic shroud (steady minus time-averaged unsteady). 88
3-6 Contour of difference in volumetric viscous entropy generation rate between the steady and time-averaged unsteady generic shroud (steady minus time-averaged unsteady). 89
3-7 Time-averaged unsteady profiles of loss accumulation in the tip shroud cavity for nominal and 1.8x nominal tip gaps. 91
3-8 Contour of difference in circumferential vorticity between the 1.8x and nominal tip gap time-averaged unsteady cases (1.8x gap minus nominal gap). 91
3-9 Contour of difference in volumetric viscous entropy generation rate between the 1.8x and nominal tip gap time-averaged unsteady cases (1.8x gap minus nominal gap). 92
3-10 Contour plot of normalized mass flux at cavity inlet demonstrating definite regions of mass ingress and egress. 94
3-11 Fraction of mass flow which enters the cavity, circulates around the inlet toroidal vortex, and re-enters the main gas path at the rotor leading edge as a function of tip gap. 94
3-12 Variation of recirculating mass fraction in the cavity inlet as a function of the average vorticity of the inlet toroidal vortex. 96
3-13 Contour of difference in volumetric viscous entropy generation between steady and time-averaged unsteady nominal tip gap cases (steady minus time-averaged unsteady) in both the cavity and main flow path. . 97

3-14 Contours at several axial planes spanning the cavity inlet which demonstrate the process of rotor tip passage vortex formation due to cavity inlet mass recirculation. 101

3-15 Contour of blade surface temperature (normalized to the temperature area-averaged over the blade surface) with cavity inlet toroidal vorticity and inlet toroidal vortex system. 103

3-16 Contour of difference in blade surface temperature (no tip gap minus nominal tip gap) as percentage of the temperature area-averaged over the blade in the nominal tip gap case. 104

3-17 Contours of time-averaged static pressure normalized to stage inlet time-averaged dynamic head for the nominal and 1.8x tip gap cases. . 107

3-18 Difference in volumetric viscous entropy generation rate highlighting the difference between off-design back pressure cases in toroidal vortex dividing streamline trajectories. 109

3-19 Difference in normalized circumferential vorticity within the cavity inlet for the off-design back pressure cases. 110

3-20 Schematic of coexisting main flow and orthogonal cavity inlet toroidal vortex. 112

3-21 Contours of normalized circumferential vorticity, $\omega_\theta/(v/c_x)$, in the tip shroud cavity inlet. 117

3-22 Instantaneous circumferential variation of cavity inlet vortex core cross-section and stator wake momentum deficit (99% span) for unsteady scalloped shroud configuration. 119

3-23 Comparison of hypothesized cavity inlet vortex radial jet limit with computational results. 120

3-24 Contours of volumetric viscous entropy generation rate with overlaid velocity vectors in the cavity inlet region for several tip gaps. 123

3-25 Schematic of high, mid, and low loss cavities, according to [2]. 126

4-1 Schematic of tip seal flow area incorporating turning channels for reducing circumferential momentum disparity between cavity flow and main flow. 131
4-2 Schematic of tip seal flow area incorporating turning channels highlighting flow area regions. 132
4-3 Variation of critical flow properties in cavity inlet versus tip seal flow area. 132
4-4 Contours of meridional Mach number for generic shroud case with a tip gap of 7.5 times the nominal gap height. 133
4-5 Computational geometry for the Hybrid Blade configuration. 135
4-6 Schematic of sink-source pair with finite separation representing cavity inlet and exit. 137
4-7 Assessing cavity coupling model estimated reduction of main flow mass flux against CFD results for steady nominal tip gap case. 139
4-8 Assessing cavity coupling model estimated reduction of main flow mass flux against CFD results for steady 1.8x tip gap case. 139
4-9 Comparison of coupling model estimated reduction in main flow mass flux with computational results for the time-averaged unsteady nominal tip gap case. 140
4-10 Sample schematic of arrangement of sinks (black) and sources (white) to refine cavity model to account for cavity inlet mass recirculation. . 142
4-11 Difference in axial accumulation of loss, Hybrid Blade configuration minus scalloped shroud with simple tip seal configuration. 145
4-12 Sample control volumes used to isolate viscous loss generation in cavity flow and main flow for the scalloped shroud-based configurations. . . 147
4-13 Difference in integrated viscous loss generation for cavity flow only, Hybrid Blade minus simple seal. 147
4-14 Difference in integrated viscous loss generation for main flow only, Hybrid Blade minus simple seal. 148

4-15 Local volumetric viscous entropy generation rate is significant in cavity control volumes and in rotor control volumes immediately at the interface between cavity flow and main flow. 148
4-16 Contours of volumetric viscous entropy generation rate at bladelet 5% span to compare mixing losses between cavity flow and main flow. . . 150
4-17 Comparison of loss accumulation through simple seal/bladelets only. . 152
4-18 Comparison of loss accumulation *per unit mass* through simple seal/bladelets only. 153
4-19 Loss accumulation through Hybrid Blade bladelets, normalized to the ideal bladelet work output. 155
4-20 Contour of volumetric viscous entropy generation rate at bladelet midchord. 155
4-21 Contour on axial plane of normalized axial velocity at bladelet row inlet with overlaid tangential flow vectors. 157
4-22 Circumferential variation at bladelet inlet, midspan, of relative swirl and radial velocity. 157
4-23 Spanwise variation of difference in local loss generation through stator (Hybrid Blade minus simple seal with scalloped shroud). 159
4-24 Contour of difference in volumetric viscous entropy generation rate in the stator at 95% span (Hybrid Blade minus simple seal with scalloped shroud). 159
4-25 Contour of difference in flow Mach number in the stator at 95% span (Hybrid Blade minus simple seal with scalloped shroud). 161
4-26 Distribution of coefficient of pressure, C_p, for main configurations overlaid with important cavity characteristic length scales. 163
4-27 Contour of difference in volumetric viscous entropy generation rate near downstream diffuser endwall (Hybrid Blade minus simple seal with scalloped shroud). 164
4-28 Viscous entropy generation rate near diffuser shroud endwall for large tip gap cases demonstrating existence of discrete loss regions. 165

4-29 Contour of circumferential vorticity near downstream diffuser shroud endwall with isosurface bounding blade trailing vortex core, Hybrid Blade case. 166

4-30 Contours of circumferential vorticity near downstream diffuser shroud endwall with isosurface bounding blade trailing vortex core, large tip gap cases. 167

4-31 Operational example of leading edge extension (i.e. strake) on a F-18 Super Hornet used to generate a vortex along wing upper surface to delay separation. 169

4-32 Classification of Hybrid Blade cavity flow components for extrapolation of performance with extension of intershroud bridge. 170

4-33 Extrapolation of overall cavity loss in the Hybrid Blade configuration versus proportion of cavity occupied by intershroud bridge. 172

4-34 Extrapolation of overall cavity loss in the Hybrid Blade configuration versus proportion of cavity occupied by intershroud brdige with linearly varying bladelet Mach number. 173

5-1 Schematic of gradual area change seal to limit mass flow rate while limiting free expansion losses. 184

A-1 Variation of axial accumulation of loss at different operating conditions. 191

A-2 Spanwise profiles of swirl at the rotor exit. 191

A-3 Variation of free expansion losses at different operating conditions. . . 192

A-4 Axial profiles of difference in loss accumulation between time-averaged unsteady and steady cases at different back pressures. 193

A-5 Difference in accumulated loss as a function of axial coordinate, scalloped case minus generic case, at various operating back pressures. . . 195

B-1 Varition of sample flow property at two example monitor points for a well-converged steady, generic shroud configuration computation. . . . 198

C-1 Schematic of simple contraction at the tip seal with an incoming swirling flow. 201

D-1 Computational geometry to model results from Cunningham [3]. . . . 208
D-2 Computational geometry to approximate the tip seal geometry of the turbine blade. 208
D-3 Experimental measurements of pressure ratio as a function of axial location from Cunningham's work [3]. 209
D-4 Computed pressure ratio as a function of axial location for the model of Cunningham's experimental apparatus. 210
D-5 Variation of mass flow rate through the sealing orifice as a function of orifice pressure ratio for the basic 2D orifice and the generic shroud computations. 211
D-6 Contours of meridional Mach number above the tip seal for different injected sealing mass flow rates. 212

E-1 Arbitrary control volume for the mixing of two uniform streams. . . . 213
E-2 Simple axisymmetric model of mixing between an injected flow and main flow [1]. 216

F-1 Schematic of simple contraction at the tip seal with an incoming swirling flow. 220
F-2 Variation of the critical pressure ratio for choked flow as a function of local swirl angle. 222

List of Tables

1.1 Key parameters characterizing representative turbine stage 34

1.2 Defining geometric and aerodynamic characteristics of generic and Scalloped shroud configurations. 37

2.1 Key mixing loss flow properties in scalloped shroud case, normalized to generic shroud values. 73

2.2 Key changes in mixing loss terms for swirl injection case. 77

3.1 Key ratios and results of Equation 3.10a for the steady generic and scalloped shroud configurations. 116

3.2 Variation of sensitivity in F and $F/(L_{cav}/R)$ for cavity inlet vortex at several circumferential cuts. 119

4.1 Comparison of computed key quantities with previously extrapolated values using cavity coupling model and scaling rules. 143

4.2 Key mixing loss flow properties in the Hybrid Blade case, normalized to values for the simple seal with scalloped shroud. 151

4.3 Characteristic length scales of cavity inlet regions for each shroud configuration. 162

Nomenclature

α = flow angle in stationary frame

A = area

b = span

c_p = specific heat capacity at constant pressure

c_x = axial chord

δ = tip gap (dimensional unless otherwise noted)

F' = total net effect of external forces on a control volume

G = mass flux

L = length

m = volumetric strength

$\dot{m}$ = mass flow rate

Ω = angular velocity

p = pressure

ρ = density

r = radius (from machine axis)

R = ideal gas constant

Sw = swirl parameter (ratio of circumferential to axial velocity)

$\dot{S}'''$ = entropy generation rater per unit volume

τ_{ij} = shear stress tensor

θ = relative angle between vectors

θ_0 = passage pitch angle

T = temperature

v = velocity

w = specific work

$\dot{W}$ = total rate of work transfer

Subscripts and Supercripts

A = area-averaged

cav = cavity

ext = spanwise extent (of cavity influence)

$f1, f2$ = fraction for enumerated stream

in = inlet

m = meridional

ma = mass-averaged

Rin = rotor inlet

RLE = rotor leading edge

$seal$ = at the radial sealing fin (or its equivalent axial coordinate)

$t1, t2$ = stagnation property at enumerated station

$visc$ = due to viscous effects

wa = work-averaged

Non-Dimensional Quantities

AR = Aspect ratio

C_p = pressure coefficient, $\frac{P-P_{in}^A}{P_{t,in}^{ma}-P_{in}^A}$

γ = ratio of specific heat capacities, c_p/c_v

λ_R = Degree of reaction

M = Mach number

$\pi_{t,stage}$ = Stage total pressure ratio

Φ = Flow coefficient (defined at midspan)

Θ = temperature ratio

ζ = loss coefficient (equivalent to debit in efficiency)

ξ = normalized spanwise coordinate

Chapter 1

Introduction

The basic concept underlying the operation of axial flow turbines has existed for nearly 80 years. During that time, researchers have expended large amounts of effort in improving overall pressure ratios, maximum turbine inlet temperatures, and reducing viscous losses of the main flow path in an effort to increase the overall efficiencies of these devices. However, after decades of research, further investigations of these features are showing diminishing returns. Secondary flow passages and clearance cavities, including the tip shroud cavity region investigated in this thesis, are comparatively less well-studied and perhaps hold further opportunities to improve turbine efficiency. In addition, these regions often determine the component lifetime and engine maintenance cycles, begetting the possibility of improving component durability by in-depth understanding of the flow field in and around such regions. As practical limitations of turbine development require these features for effective operation, any efficiency or durability improvements would have nearly ubiquitous application in turbine design. The objective of this thesis is to examine turbine tip shroud cavity flow fields in detail to: i) identify the primary loss mechanisms, ii) determine how the loss levels scale with key turbine design parameters, and iii) synthesize these findings to suggest design modifications or practices for improving aerodynamic efficiency and component durability.

1.1 Motivation

The axial turbine is one of modern society's primary enabling technologies, playing critical roles in global transportation and power generation. The general populace is familiar with the gas turbine's application in air travel, powering the majority of commercial and military aircraft, but axial turbines also power many commercial and military maritime vessels. In the energy sector, axial turbines, via the Rankine steam cycle and/or the Brayton gas cycle, produce the vast majority of the world's electricity by converting thermal energy from fuels or other heat sources. Yet, regardless of the application, one of the primary figures of merit for turbine performance (as in any heat engine) has always been efficiency as this metric relates directly to performance in the end application. To that end, much research has been devoted in past decades to optimizing properties of the main gas path. However, as demand for increased energy production and lower emissions continues to rise amidst global development and concerns regarding climate change, further improvement of axial turbine performance becomes evermore critical.

One comparatively less well-studied avenue for increasing turbine efficiency is improving the understanding of the complex aerodynamics within, and resulting from, clearance cavities throughout the device. In particular, some turbine designs link neighboring blades with a metallic ring known as a shroud, requiring a large gap between the rotating blade-shroud system and the stationary casing. This gap exists to allow growth of the blade due to centrifugal and thermal strains during steady state operation, as well as to accommodate transients and prevent rubbing of components. The engineering trade-off is that these cavities ingest main flow fluid, generating loss, changing flow distribution entering blade rows, and providing an alternate flowpath for the fluid. While some aerospace engines use shrouded blades to improve the aerodynamics of the main flow path [4], the majority of shrouded blades are employed in steam turbines or later stages of industrial gas turbines used for power generation. Consequently, any improvement in efficiency translates directly into reduced fuel consumption and reduced emissions of greenhouse gases and pollutants per unit

of electricity generated.

In addition to aerodynamic efficiency, another important aspect of these tip shroud cavity flows is their impact on component durability. Specifically, they are characterized by regions of slowly circulating, high temperature fluid not unlike the hot gas ingestion of labyrinth seals, so actively avoided to protect against damage to rotor disks [5,6]. Thus, a better understanding of the flow structures within the tip shroud cavity will not only provide insight into methods of improving aerodynamic efficiency, but potentially also areas of greatest concern for material life and methods to reduce the material requirements.

A review of the literature (summarized in Section 1.3) reveals that much of the research on tip shroud cavity flows has focused on low-aspect ratio blading characteristic of steam turbines or first stages of gas turbines. On the other hand, relatively less focus has been given to later gas turbine stages. The findings of each study are generally specific to the flow structure or the geometric configuration of the device. Relatively sparse effort is applied in synthesizing all of the aerodynamic mechanisms to provide a holistic, quantitative, and generalizable summary of the important characteristics of these flows. In addition, those researchers who have suggested methods of mitigating losses [7–9] have had mixed success with often conflicting or vague explanations as to why a proposed design did or did not perform as expected. As a result, there remains opportunity to advance the general state of knowledge regarding this topic.

1.2 Technical Objectives and Hypotheses

Given the envisioned impacts of this research, several technical objectives guide the effort to advance the state of the art of tip shroud cavity flows:

1. Identify the critical physical mechanisms which set the loss level in turbine tip shroud flow paths.

2. Determine the sensitivity of the associated loss levels of these physical mecha-

nisms to parameters that characterize turbine design and operation

3. Suggest design strategies or geometric alterations to help mitigate these losses and potentially improve component durability

Taken together, these technical objectives constitute a systematic examination of the cavity flow field, each successive objective building upon the understanding of those that precede it. As a result, it is difficult to formulate a hypothesis to the third objective as its fulfillment requires a synthesis of the findings of objectives 1 and 2.

Nevertheless, basic fluid mechanics can provide some qualitative insight into the anticipated findings in pursuit of objectives 1 and 2. Although the main flow path of modern gas turbines is meticulously contoured and its components streamlined, typical tip shroud cavity flow paths are characterized by simple geometries. In this case, the simplicity is functional, often featuring rapid area changes and sharp edges designed to hinder and limit flow. Figure 1-1 depicts a sample cavity geometry (shown in more detail in Figure 1-2) which utilizes such rapid area expansions and contractions, sharp turns in flow direction, a radial sealing fin, and resulting recirculation regions (shown by the overlaid velocity vectors with circulation direction indicated by the white arrows). Accordingly, two of the anticipated major loss mechanisms are separation and recirculation zones, and free expansion of flow through rapid area expansions. Loss associated with the latter process is well-known to be proportional to the dynamic head of the flow for incompressible fluids. For compressible flows like those found in gas turbines, it is reasonable to expect losses to follow a qualitatively similar trend. In fact, Figure 1-1, which includes a contour of volumetric viscous entropy generation rate, shows the significant increase in entropy through the sample cavity as fluid expands left to right through the tip seal. Upstream of the tip seal, the recirculating zones are accompanied by additional entropy generation as expected, albeit at more modest levels than downstream.

Another expected critical loss mechanism is mixing between the cavity flow and the main flow at the interfaces both upstream and downstream of the blade (especially downstream, as demonstrated in Figure 1-1). To illustrate this reasoning, take the

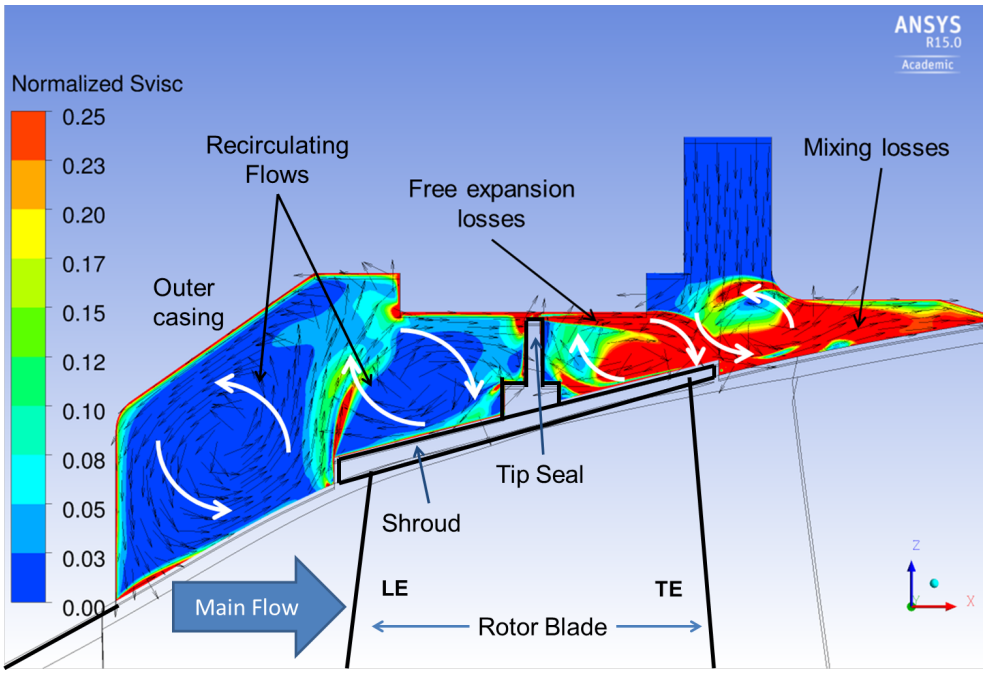

Figure 1-1: Generic tip shroud cavity geometry and computed flow field for representative axial gas turbine.

interaction of the separate flows at the cavity exit downstream of the main blade. The cavity flow and main flow will be at two different states due to the different processes each undergoes in the separate flowpaths between cavity inlet/rotor leading edge and cavity exit/rotor trailing edge. Basic fluid mechanics dictates the loss will scale approximately with Δv^2, or the difference between fluid velocities at which two streams mix.

Thus, the aggregate task of this research program is to assess these hypotheses while identifying more subtle loss mechanisms and their important characterizing parameters. Then, this knowledge is synthesized to create innovative solutions for mitigating loss and improving efficiency.

1.3 Literature Review

While the body of work on secondary flows is small in comparison to previous research on the main flow path, it is still extensive in its own right. The majority of work on secondary flows has been in low- and medium-aspect ratio blading, such as the

shrouded blades of steam turbines or unshrouded high pressure gas turbine stages. In this context, secondary flow effects significantly impact overall loss mechanisms. In fact, Denton's canonical review paper [10] claims that nearly 1/3 of the total loss in axial turbines arises in secondary flows (including cavity and vortical flows). Hunter and Manwaring [11] performed computational and empirical studies on cavity leakage flows in turbines. Their primary finding focused on the interaction of the cavity flow when reentering the main flow at the cavity exit. They determined that a disparity in circumferential momentum of the cavity and main flows led to increased loss and strong streamwise vortices downstream as the non-uniformity mixes out. Gier et al. [12] performed a similar study, expanding Hunter and Manwaring's analysis to include both hub and shroud cavities and breaking down the individual contributions of the various loss mechanisms. They determined that the mixing during cavity leakage reentry highlighted by Hunter and Manwaring et al. accounted for up to 50% of the losses linked to cavity flow. Several groups have investigated the use of turning elements in the cavity to reduce the circumferential disparity at the cavity exit with mixed results [7–9]. Wallis et al. [7] incorporated turning devices onto the shroud surface so that the cavity flow is turned to the same angle as the main flow at the blade row exit. While this increased work output of the rotor, the improvement was offset by increased loss from main flow ingress and egress at the cavity exit, leading to a reduction in efficiency of 3.5%. Rosic and Denton [8] took a different approach after Wallis et al., using stationary vanes at the cavity exit instead to redirect the cavity exit flow. In their experimental rig, they measured an improvement of 0.4% in overall aerodynamic efficiency due to reduction in mixing losses between the cavity and main flows and mitigation of secondary flows in the downstream stator row. Gao et al. [9] also used stationary vanes fixed to the casing, but between radial sealing fins, in order to turn the cavity leakage flow before mixing with the main flow. Their results demonstrate that while turning elements can reduce mixing losses, maximum increase in efficiency is achieved only when considering all three components of velocity of the mixing streams instead of just the circumferential component. Rosic et al. [13] and Abhari et al. [14] examined the effect of cavity volumes and length scales

on turbine efficiency. Both research groups found that minimizing cavity volume was critical for reducing cavity flow induced losses. Although, some methods of reducing the volume actually increased loss by changing the structure of the vortices in the cavity. Pau et al. [15] also found an inextricable link between viscous entropy generation and the vortices in the cavity flow field. However, none of these studies derive direct quantitative relationships between viscous entropy generation and vorticity to demonstrate why loss distributions in cavity flow so closely corresponds to vorticity distribution. Nor do they attempt to offer quantitative design guidelines for minimizing these losses, instead offering geometry-specific trends or qualitative suggestions.

The aforementioned work focused on steady calculations or time-averaged measurements, neglecting the unsteady effects inherent in turbomachinery. It is reasonable to expect that the time-varying pressure field induced by the passing stator wakes and rotating pressure fields of the rotors would influence flow through the cavity and its interaction with the main flow. In turn, these unsteady pressure fields could potentially alter the routes to loss generation. Pfau et al. [16] and Barmpalias et al. [17] sought to examine this question in their experimental studies, both indicating strong time dependence in the cavity inlet vortex. In an earlier study, Pfau et al. [18] studied labyrinth seal flow interactions with the main gas path, including a suggested development of design guidelines for non-axisymmetric shroud and cavity geometries to reduce unsteady effects in the cavity. This, in turn, is suggested to reduce mixing losses when the cavity flow reenters the main flow path, and also reduce downstream effects such as negative incidence on subsequent blade rows. They have suggested a stage efficiency gain of 0.2-0.5% for low-aspect ratio stages is possible with appropriate management of flow unsteadiness.

While several sources of loss mechanisms have been identified and suggested in the literature, a rigorous quantitative causal link between loss generation (manifestation) and specific flow processes and drivers (causes) is lacking. In particular, unsteady flow situations inherent in the turbine flow environment are significantly less characterized compared to quasi-steady flow features. Furthermore the effects of flow coupling in the

tip shroud cavity flow and main flow have not been assessed for its role on blade inlet profiles. In summary, there is a lack of a quantitative traceability of any attendant performance change to the responsible specific flow process/driver at the component as well as system level.

1.4 Research Framework

The research presented herein represents a systematic study of a generic vane-rotor-cavity system representative of the final stage in a large, shrouded industrial gas turbine such as a Siemens F/H-class machine. The generic vane-rotor stage and the tip shroud system are shown in Figure 1-2. For the purpose of delineating loss mechanisms in the tip shroud cavity flow, this geometry (and its variations) are compared to a baseline case consisting of the same stator and rotor domains as in Figure 1-2, but without the cavity domain (see Figure 1-3). Comparison of the geometry of interest with an idealized baseline case with no cavity allows isolation of flow structures modified or created by the presence of the cavity. Variations of the geometry in Figure 1-2 serve to perturb these flow features, thus permitting identification and quantification of loss mechanisms and their relative importance in contributing to the overall loss associated with the cavity. Each variation adds additional complexity to the generic cavity system, thus isolating the effects of geometric features or operational characteristics by comparison. The characteristics of this representative stage are summarized in Table 1.1. In Table 1.1, Ω is the rotational speed of the rotor; $\pi_{t,stage}$ is stagnation pressure ratio across the stage, $P_{t,out}/P_{t,in}$; $AR_{rotor} \equiv \frac{b^2}{A} \approx \frac{b}{c_x}$ is the aspect ratio of the rotor blade, where A is the planform area of the blade, b is the span, and c_x is the axial chord; $\Phi \equiv \frac{V_x}{U}$ is the flow coefficient evaluated at midspan, where V_x is the axial velocity and U is the rotor speed; M_{Rin} is the rotor inlet Mach number; $\lambda_R \equiv \frac{\Delta h_{rotor}}{\Delta h_{stage}}$ is the degree of reaction.

There exists a perceived challenge (but not insurmountable) in quantifying effects of tip shroud cavity flow on turbine performance on computational as well as experimental basis. This is so because only a small fraction of the main flow (ranging from

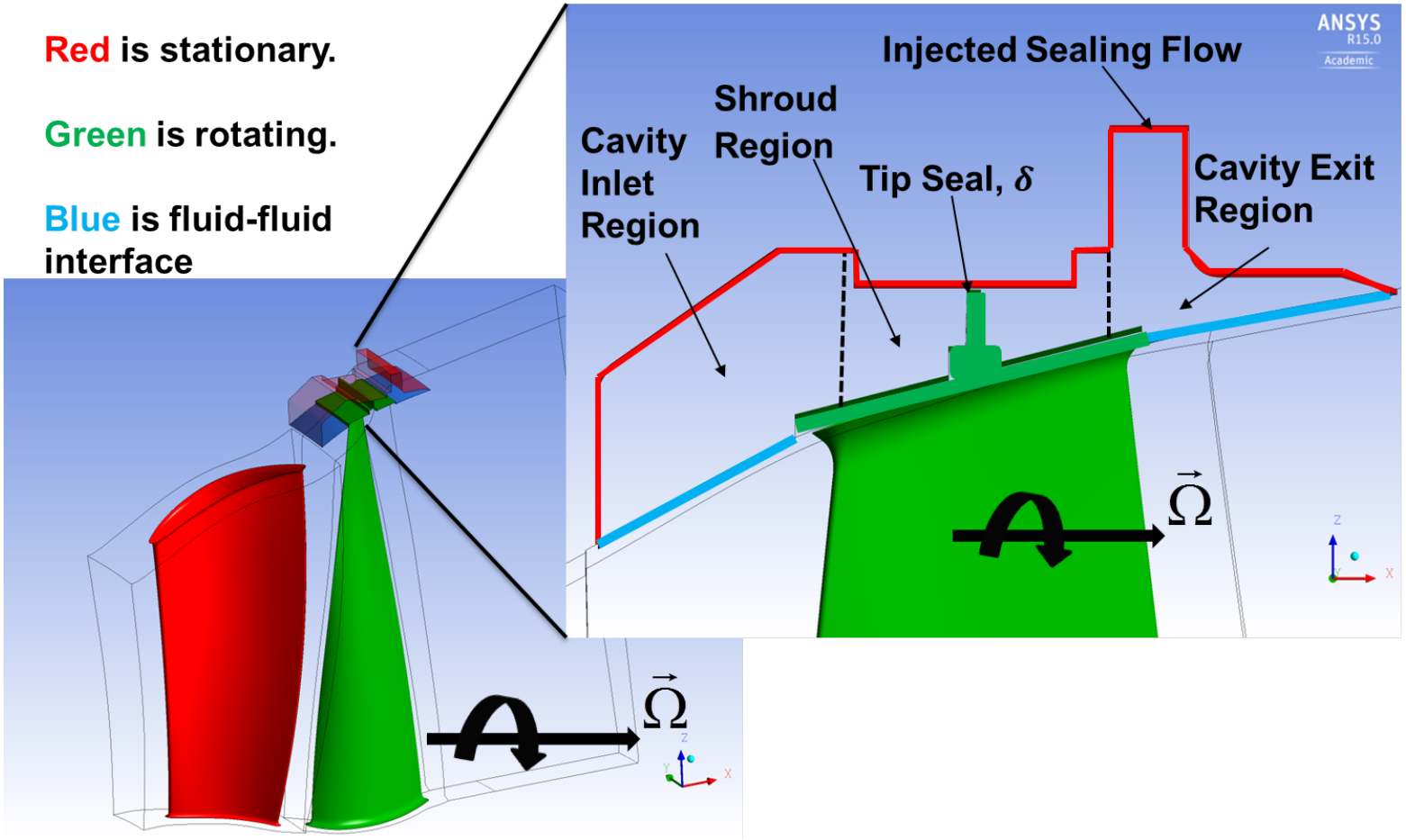

Figure 1-2: Computational domain and nomenclature for generic cavity domain regions and features

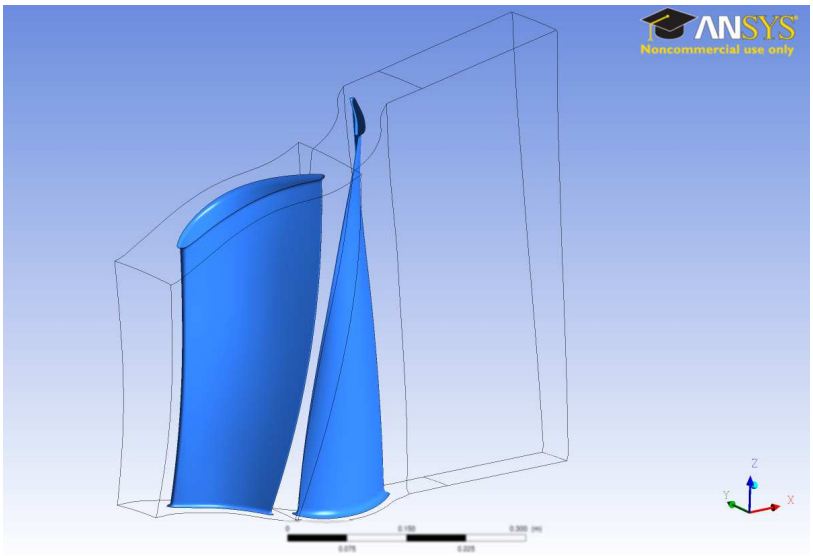

Figure 1-3: Computational domain for the idealized baseline stage with no rotor tip cavity

Parameter	Value	Parameter	Value
Ω (rad/s)	400	$\pi_{t,stage}$	0.472
AR_{rotor}	~ 5	Φ	0.721
M_{Rin}	0.542	λ_R	0.633

Table 1.1: Key parameters characterizing representative turbine stage

0.4% to 1%) passes through the cavity with relatively small anticipated induced flow changes. As such, prudent steps must be taken to calculate or to measure the changes in a manner that reflects the underlying responsible flow processes. Here, the steps taken include the following:

1. Assess and interrogate computed flow fields of a turbine stage with and without a tip shroud cavity to identify changes in the flow field upon incorporating a tip shroud cavity system on a back-to-back basis (so as to eliminate systematic errors);

2. Assess the sensitivity of the flow changes in response to a range of key controlling parameters that include tip seal gap and injected sealing flow for a given turbine stage and tip shroud cavity system;

3. Determine and assess the consistency of the results from (1) and (2) against basic physical principles;

4. Complement the assessments and analyses of the results in (1) to (3) with simple flow models based on control volume approach;

5. Implement an error analysis of the computational efforts in order to establish the error bound on the computed results.

In addition the inferred changes in turbine stage performance were corroborated with data and observation on rigs and installations by Siemens (during monthly teleconferences with Siemens collaborators). This collaborative evaluation of the results served as a plausibility check of the physical validity of the inferred changes.

The variations which perturb the flow field include the injection of sealing flow in the cavity, the size of the tip gap, stage back pressure (off-design operation), shroud asymmetry, and the effects of unsteadiness. Investigating the effects of unsteadiness involves assessing unsteady flow against steady flow with and without a cavity. Figure 1-4 depicts a single flow passage and a closer view of the asymmetric shroud. The shroud closely conforms to the airfoil cross-section at the blade tip (a.k.a. "conformal shroud"), but with slightly greater area so that it extends beyond the blade cross-section like a winglet. The stator domain remains unchanged as compared to the generic shroud configuration, but the rotor and cavity domains have both been modified. The interface between the two domains is now defined at approximately 95% of rotor blade span rather than having separate inlet and exit regions in the generic shroud case. The cavity inlet region has been enlarged and some of the rapid area changes made less severe, and the cavity-diffuser interface has a much smoother transition compared to the reflex angle in the generic shroud configuration. Table 1.2 quantitatively compares several of the defining geometric and aerodynamic characteristics of each configuration. In general, the aerodynamic characteristics remain unchanged between cases since the cases operate with the same inlet and outlet conditions. However, the geometric characteristics of the cavity inlet are significantly different.

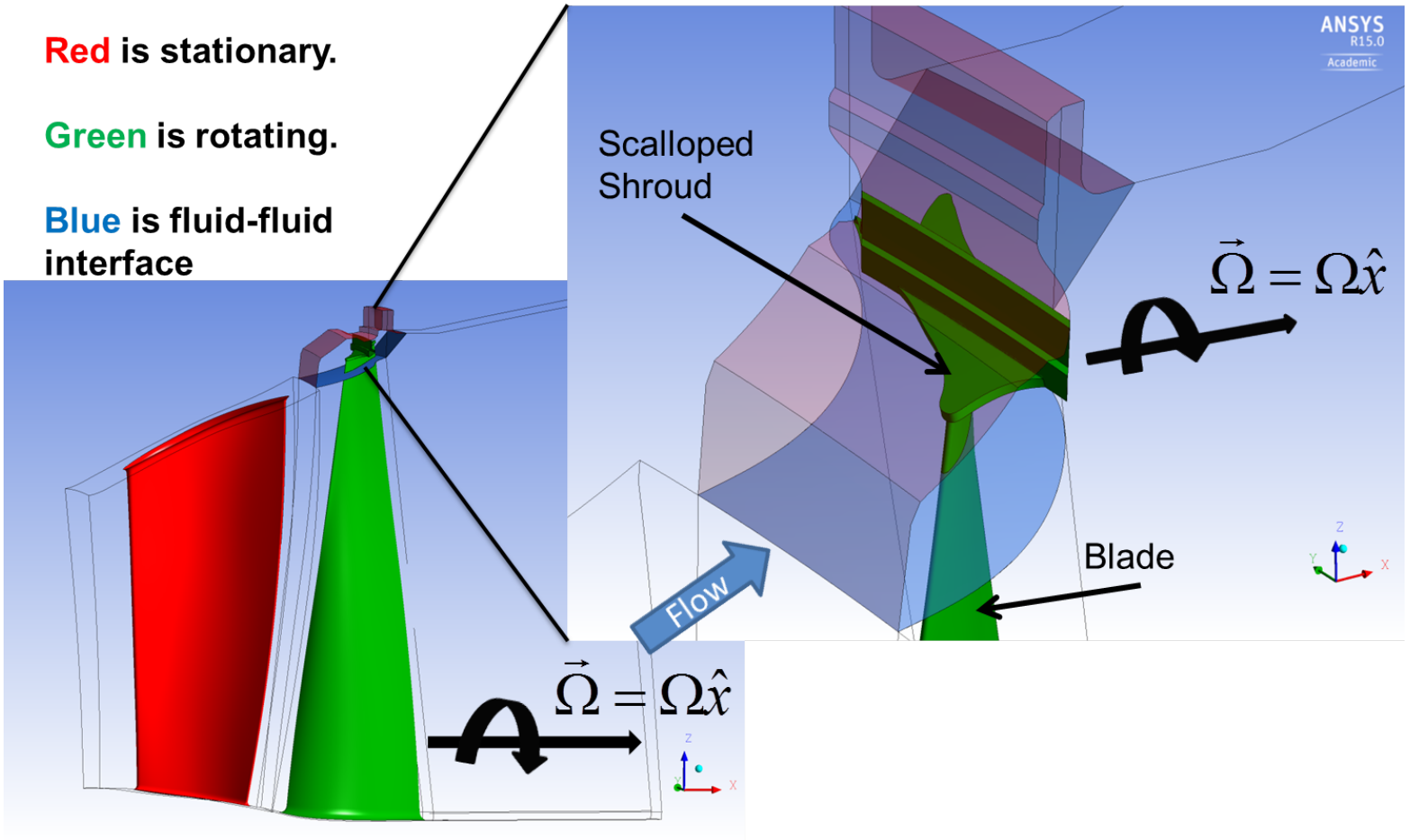

Figure 1-4: Computational geometry of the scalloped shroud configuration.

Case	Cavity Inlet Axial Length, L_x (%span)	Cavity Inlet Radial Length, L_r (%blade spacing)	Tip Gap, δ (%span)	Rotor Inlet Swirl Angle, α	$\left(\frac{P_{t_{in}}}{P_{out}}\right)_{rotor}$	$\pi_{t_{rotor}}$	$\frac{\dot{m}_{cav}}{AP_t}\sqrt{\frac{RT_t}{\gamma}}$	$\frac{\dot{m}_{cav}}{\dot{m}_{stage}}$	Φ
Generic Shroud	7	67	0.2	56.3°	2.61	0.493	0.453	0.4%	0.721
Scalloped Shroud	10.4	152	0.2	56.3°	2.58	0.488	0.451	0.4%	0.722

Table 1.2: Defining geometric and aerodynamic characteristics of generic and Scalloped shroud configurations.

For all other parameters which perturb the flow field, calculations were implemented for a range of the given variable. The range of each was normalized to the design value of that parameter for the representative stage. The sealing mass flow rate, $\dot{m}_{injected}$, was specified using a mass flow inlet boundary condition with normal (i.e. purely radial) velocity components and specified static temperature. The mass flow rate ranged from 0 to 16 times the nominal value, and the tip gap, δ, varied from 0.8 to 1.8. The stage back pressure was varied from 86% to 110% of the nominal stage pressure ratio in order to investigate the effects of off-design operation on the cavity loss mechanisms. Where applicable to the flow physics being discussed, the results of the off-design computations are included. However, the majority of the results are presented in Appendix A as off-design operation does not significantly alter the findings and conclusions based on the nominal back pressure computations.

Computations were performed using the ANSYS CFX solver on structured and structured/unstructured hybrid grids and were augmented by simplified analytical models where applicable. Steady computations applied the mixing plane model within CFX at the interface between stator and rotor domains and used the single passage geometries shown in Figures 1-2 through 1-4. The mixing plane model permits steady calculations by mixing out the circumferential non-uniformities in the flow field induced by the stator. The model divides the interface into many bands defined by discrete radial ranges and computes a replacement, circumferentially uniform flow which obeys all conservation equations in each band. In so doing, it incurs an in-

stantaneous loss and removes any potential interaction between stator wakes and the rotor potential field (though the cavity and rotor can still have an upstream influence by affecting the pressure level of the mixed out state). Unsteady computations required using a full sector ($1/28^{th}$ of a full wheel) due to CFX requiring a 1:1 pitch across interfaces when employing a time-accurate change of frame between stationary and rotating components. Thus, computational domains for unsteady calculations included 2 stator domains and 3 rotor domains (and for all but the baseline, 3 cavity domains).

The single flow passage domain for the generic shroud configuration consists of a structured grid containing a total of 3.4 million nodes. These 3.4 million nodes are distributed with 1.3 million in the rotor domain, 0.6 million in the stator domain, and 1.5 million in the cavity domain. While the generic case is a fully structured mesh in all domains, the geometric complexity (especially the smooth angles and curves) of the scalloped shroud configuration required the use of an unstructured mesh in the cavity domain[1]. All three domains contain a total of 3.8 million nodes with 0.6 million in the stator domain, 1.5 million in the rotor domain, and 1.7 million in the cavity domain. This equates to an increase of 0.4 million nodes overall compared to the generic shroud, half in the rotor domain and half in the cavity domain. Naturally, nodes were concentrated in the cavity and rotor to resolve the flow features of interest in this investigation (i.e. the tip shroud cavity flow field). These grid resolutions were chosen by the Siemens collaborating engineers according to industry experience and CFD best practices for grid independence and fidelity with test rigs. Furthermore, this grid density is higher than others in the reported literature for similar geometries [12] and which show strong agreement with experimental data. All cases applied the $k-\omega$ shear stress transport model with wall functions ($y+ < 10$ and typical turbulence intensity of 10%). Calculations were considered converged when all RMS residuals reached 10^{-5}, or when both residuals and monitor points[2] displayed periodic signals

[1]Using a structured mesh with the same geometry would require a much denser mesh than using unstructured elements due to the curvature of the shroud. The mesh density would unnecessarily increase the computational cost compared to the hybrid mesh employed in this thesis.

[2]There were 18 monitor points spaced at key points throughout the computational domain (e.g. both midspan and tip of stator trailing edge and rotor leading and trailing edges, as well as the rotor-

for at least three passage or sector passings for steady and unsteady calculations, respectively. In those cases where the latter convergence criterion was used, the RMS residual for mass conservation was at the desired 10^{-5} level while the momentum residuals were all between 10^{-4} and 10^{-5}.

Entropy in the form of lost opportunity to do work is used to analyze the results of the various calculations according to the procedure described by Zlatinov [1] and using averaging methods consistent with those suggested by Cumpsty and Horlock [19]. The entropy generation rate is further divided into thermal and viscous dissipation. The primary reasoning behind this delineation of loss sources holds that entropy generated through viscous dissipation sets the technological level of turbine design while entropy generated through thermal dissipation should be reflected in the cycle efficiency. Thus when looking at the component level, viscous dissipation is more readily mitigated by improved component design. The relevant equations and methodology are reproduced below.

Zlatinov first considered a simple case featuring two streams at different stagnation properties expanding through an ideal turbine. To further simplify the analysis, the streams were assumed thermally isolated during expansion, and that both streams were expanded to the same stagnation pressure, P_{t_2}, as shown in Figure 1-5.
After the expansion step, the streams would be in mechanical equilibrium but not thermal equilibrium; therefore potential still exists for further work extraction using an ideal heat engine. Zlatinov referred to these two processes with the subscripts, *expand* and *heat engine*, respectively, and gave expressions for their ideal work output. However, since there is no opportunity in real gas turbines to extract work from two streams in mechanical but not thermal equilibrium, the heat engine contribution was ignored. This logic forms the physical basis in the preceding paragraph which justifies focusing on viscous dissipation and ignoring thermal dissipation when comparing turbine component performance. The ideal expansion work for these two streams is given by:

cavity interfacial plane and cavity inlet plenum), each monitoring several important flow variables.

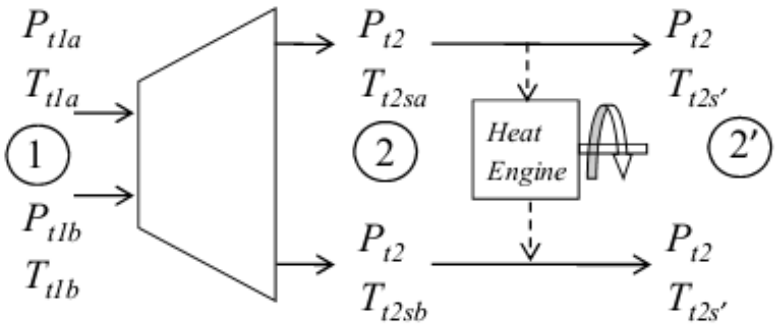

(a) Engine schematic from [1].

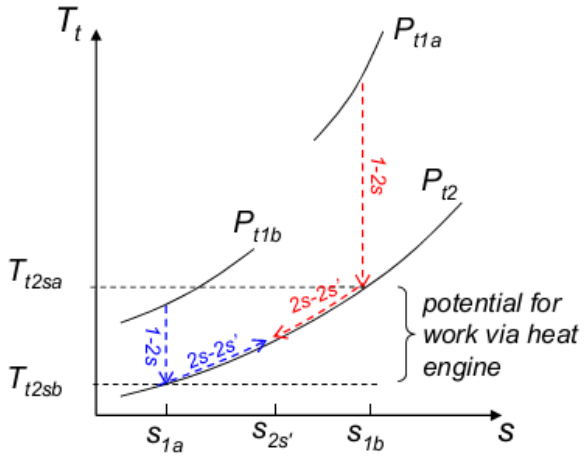

(b) T-s diagram from [1].

Figure 1-5: Ideal expansion of two streams.

$$w_{expand} = \sum_i \frac{\dot{m}_i}{\dot{m}_{total}} c_p \left(T_{t_{1,i}} - T_{t_{2s,i}} \right), \tag{1.1}$$

where i represents the stream and $T_{t_{2s}}$ the ideal stagnation temperature if the stream is isentropically expanded to pressure, P_{t_2}. The non-uniform flows in the configurations examined in this thesis are essentially an infinite number of independent streams undergoing expansion through the turbine.

Given the spatial non-uniformities in the flow inherent in the prescribed boundary conditions, the non-uniform flow must be replaced with a representative uniform flow in order to apply Zlatinov's thermodynamic analysis. This is accomplished according to the averaging techniques described by Cumpsty [19]. Namely, stagnation enthalpy and temperature are mass-averaged while pressures are work-averaged, thus ensuring the substituted uniform flow obeys conservation of momentum and energy. These averaging techniques are mathematically described in Equations 1.2 and 1.3:

$$T_t^{ma} = \frac{\int T_t \, d\dot{m}}{\int d\dot{m}}, \tag{1.2}$$

$$P_t^{wa} = \left[\frac{\int T_t d\dot{m}}{\int \left(\frac{T_t}{P_t^{\frac{\gamma-1}{\gamma}}} \right) d\dot{m}} \right]^{\frac{\gamma}{\gamma-1}}, \tag{1.3}$$

In order to compare data using the mixing plane approximation with time-accurate simulations, Equations 1.2 and 1.3 must be adjusted to allow for proper time-averaging, thus replacing a spatially non-uniform, unsteady flow with an equivalent uniform, steady flow [1]. As both equations are integrals over infinitesimal amounts of the mass flow, the integrand represents a product of fluid properties. It is this integrand which must be time-averaged prior to the spatial integration:

$$T_t^{ma,ta} = \frac{\int \left(T_t \rho v_x\right)^{ta} dA}{\int \left(\rho v_x\right)^{ta} dA}, \tag{1.4}$$

$$P_t^{wa,ta} = \left[\frac{\int \left(T_t \rho v_x\right)^{ta} dA}{\int \left(\frac{\rho v_x T_t}{P_t^{\frac{\gamma-1}{\gamma}}} \right)^{ta} dA} \right]^{\frac{\gamma}{\gamma-1}}, \tag{1.5}$$

Using this uniform flow with appropriately averaged flow properties, the viscous lost work per unit mass can be calculated according to Equation 1.6:

$$\Delta w_{visc,loss} = c_p \left(T_{t,2}^{ma} - T_{t,1}^{ma} \left(\frac{P_{t,2}^{wa}}{P_{t,1}^{wa}} \right)^{\frac{\gamma-1}{\gamma}} \right), \tag{1.6}$$

Since stations 1 and 2 can be defined anywhere in the flow domain, Equation 1.6 enables the construction of axial loss profiles which quantitatively traces changes in loss generation to responsible regions in the flow domain. Typically, station 1 is assigned to the inlet of the stator while station 2 is a variable location throughout the rest of the computational domain.

This approach allows loss to be quantified as a debit in efficiency directly attributable to viscous losses. A loss coefficient, ζ, is defined as the ratio of viscous lost work to the ideal work output of the stage:

$$\zeta = \frac{\dot{W}_{visc,loss}}{\sum \dot{m}_i c_p (T_{t,i}^{ma})(1 - (\frac{P_{t,out}^{wa}}{P_{t,i}^{wa}})^{\frac{\gamma-1}{\gamma}})}, \tag{1.7}$$

where the summation is over the input streams to the domain and the subscript, i, denotes the stream. For the flow configurations assessed in this research, the input

streams are the main flow entering the nozzle guide vane (NGV) and the injected sealing flow. An estimate of the uncertainty in Equation 1.7 (i.e. the minimum loss level that can be resolved) is given in Appendix B. This minimum is estimated at 0.02% debit in efficiency for steady calculations. However, to account for increased uncertainty in unsteady calculations and to be conservative in affirming significance of loss sources, the minimum significant loss level is defined as three times this resolution, or 0.06%, analogous to a 95% confidence interval. Further, all reported losses are rounded to the nearest 0.1% according to traditional practice of reporting results in the literature.

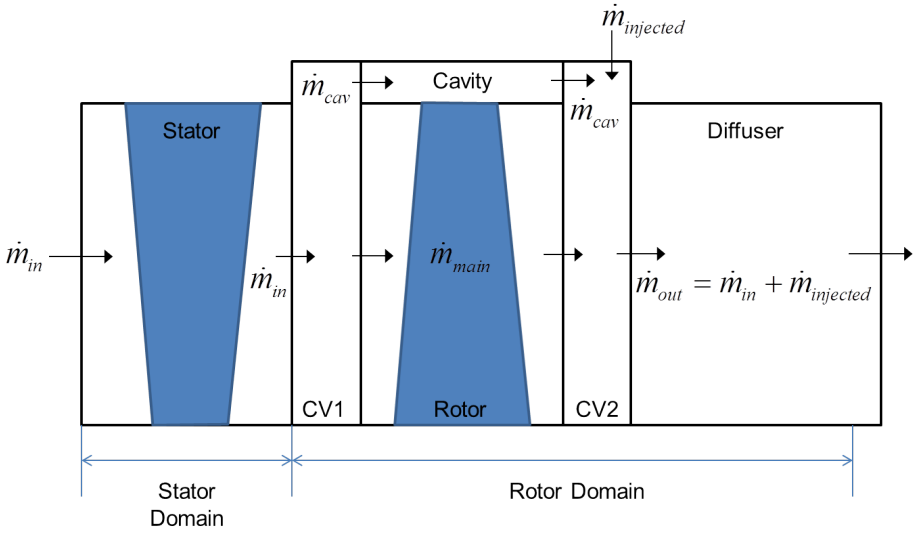

Figure 1-6: Schematic of division of subdomains to localize change in loss between major cases. The stator domain includes the interface between stator and rotor (i.e. it contains the mixing plane for those calculations using the Stage frame change model, or the sliding interface for transient calculations)

Equation 1.7 is used to generate axial profiles of cumulative debits in efficiency due to viscous losses, thus localizing areas of altered loss to specific streamwise regions. The subregions are labeled in the schematic in Figure 1-6 for the generic shroud design. Regions CV1 and CV2 represent mixing regions where flow is either entering or exiting the cavity with flow structures on the order of the region's axial length. Qualitatively the subdomains for the asymmetric shroud geometries are similarly defined. The

exception is that due to the shroud asymmetry, the mixing regions are not as clearly defined as in the generic case, nor are the cavity and main flow segregated for the same axial distance as implied by the Cavity subdomain in Figure 1-6. While this does not prohibit the use of loss profiles to isolate axial locations of increased loss generation, some ability to localize loss generation to specific subdomains is lost in practice[3].

Region CV2 is of particular importance as it contains one of the primary cavity loss mechanisms and directly follows another primary loss mechanism. Its upstream boundary within the cavity is defined as the furthest downstream plane before the injected sealing flow enters the computational domain and before the trailing edge of the tip shroud. In the main flow path, the upstream boundary is defined by a surface aligned with the rotor blade trailing edge. Its downstream face is defined as the inlet of the diffuser, downstream of the interface between the cavity and rotor computational domains. The portion of CV2 within the cavity computational domain is taken to contain the loss attributable to mixing between the cavity flow and injected sealing flow. Similarly, the portion of CV2 within the rotor computational domain contains the loss attributable to the mixing of the flow exiting the cavity with the main flow. The latter mixing process may extend into the diffuser subdomain, and will thus be complete by the exit of the computational domain. The mixing within the cavity, on the other hand, is only mostly complete due to the relatively short length available for mixing before interaction with the main flow. As a result, the choice of turbulence model will not affect the overall loss since all mixing is complete. However, when attempting to divide the loss contributions between mixing processes, the choice of turbulence model may affect the loss level attributable to each mechanism as the details of mixing become important. Complementary control volume analysis suggests that the chosen SST model is adequate for the present flow

[3]A control volume may always be defined in order to isolate entropy generation to specific volumes. However, pre-defined interfaces such as those at the cavity inlet and exit in the generic shroud case provide more precise surfaces over which to apply conservation integrals than surfaces defined by geometric planes or variable-based isocontours. This is because, by definition, mesh interfaces contained well-ordered nodal points while geometric planes and isocontours rely on interpolation between mesh points, introducing additional errors.

environment and conditions as set by the configuration. In addition, ANSYS CFX documentation suggests SST as the best model within the set of two-equation models as it is better suited for separated flows (which constitute the entire cavity flow field). Alternate models suitable for highly separated flows include additional models within the set of Reynolds stress turbulence models (utilizing six equations). However these models would require altered meshes or more computationally expensive unsteady calculations. Therefore, assessment of the reported results against other turbulence models constitutes potential future work.

Regardless, since the loss coefficient is based on averaged quantities, it cannot isolate specific loss generating mechanisms/flow structures. Identification of these loss mechanisms is enabled by assessing the local dissipation rate per unit volume, $\dot{S}'''$, given in [1, 20]:

$$\dot{S}''' = \frac{1}{T}\tau_{ij}\frac{\partial u_i}{\partial x_j} + \frac{k}{T^2}\left(\frac{\partial T}{\partial x_i}\right)^2, \tag{1.8}$$

The first term in Equation 1.8 represents viscous dissipation while the second term is associated with thermal entropy generation. As previously argued, this research focuses on viscous entropy generation rather than thermal as the former is directly tied to component design while the latter is charged to the thermodynamic cycle. For the remainder of this thesis, the first term in Equation 1.8 referring to viscous entropy generation rate per unit volume is labeled as $\dot{S}'''_{visc}$. For grids with the same (or nearly the same) densities, the differences in volumetric entropy generation rate can be used to qualitatively identify and highlight the spatial distribution of loss and dominant loss mechanisms [1]. Under the conditions, assumptions, and approaches that the computations, modeling, and analyses have been implemented, the results have been postprocessed and interrogated to arrive at the findings outlined in the next section.

1.5 Major Findings and Contributions

The key findings of this work are as follows:

1. The tip shroud cavity flow incurs approximately 1% debit in efficiency per 1% main flow through the cavity. The primary loss mechanisms with their corresponding loss level scalings have been synthesized for these and previously studied configurations in the literature, and they are:

   (a) Free expansion of the tip seal jet. The loss is proportional to fraction of main flow mass which passes through the cavity and scales with the stagnation pressure ratio across the tip seal.

   (b) Mixing at the cavity exit between cavity flow and main flow. The generated loss is a function of the mass flow rate through the cavity, the square of the velocity difference between streams, the product of the velocities at mixing, and the relative angle between the streams.

   (c) Frictional losses and shear layer mixing in the cavity inlet associated with vane-rotor interaction. The loss increases with increasing cavity inlet toroidal vortex average local swirl velocity (characterized by average vorticity and related to contained circulation and core size) and the fraction of ingested fluid which is recirculated into the main flow path.

   (d) The tip seal jet, mixing at cavity exit, and the vane-rotor induced flow unsteadiness each account for approximately one-third of the total loss (0.38%, 0.38%, and 0.25% debits in efficiency per 1% main flow through the cavity, respectively). The proportion of total cavity loss attributable to the exit mixing process increases with increasing tip gap.

2. The main flow perceives the cavity as a sink-source pair. This provides a simple, direct way to estimate the main flow redistribution due to the tip shroud cavity.

3. The attributes of an effective tip shroud cavity include:

(a) Minimal tip shroud cavity mass flow fraction and blade tip pressure ratio.

(b) Zero difference in swirl parameter and velocity magnitude between the cavity flow and main flow.

(c) Minimal cavity inlet volume with maximum allowable cavity inlet radial to axial length ratio while retaining a cavity inlet toroidal vortex.

The Hybrid Blade design concept (shown in Figure 1-7) satisfies the second attribute while replacing the loss mechanisms which motivate the first and third attributes with different loss mechanisms. The Hybrid Blade as designed herein successfully recovers 1/2 of the loss associated with mixing in the Scalloped Shroud with knife-edge seal configuration, with a best achievable recovery of greater than 2/3 of the mixing loss. However, this gain in efficiency is offset by the efficiency limits of the bladelets themselves. Examination of results in literature [21, 22] suggest that these losses can be minimized, and the improvement in overall stage efficiency recovered, by proper optimization of the bladelets for low Reynolds number flows and asymmetric inlet conditions.

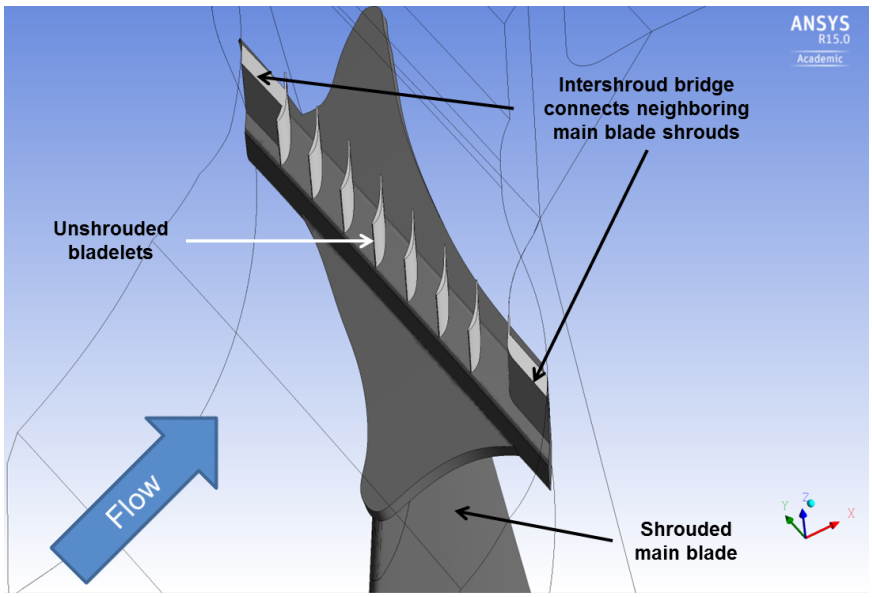

Figure 1-7: Isometric view of the Hybrid Blade design and computational geometry.

1.6 Thesis Organization

The remainder of this thesis will present research carried out to generate the results contributing to the main findings presented in Section 1.5. Chapter 2 will focus on identifying the major loss sources and their scalings found in the steady flow approximation of the turbine stage with both the generic and scalloped tip shroud cavity. Chapter 3 then expands the analysis of the tip shroud cavity to include unsteady effects associated with vane-rotor interactions. The analysis includes discussion of effects on both aerodynamic loss mechanisms as well as potential adverse effects of tip shroud cavity aerodynamics on component durability.

Combining the findings and results of Chapters 2 and 3, Chapter 4 presents a novel turbine tip shroud configuration. Referred to as the Hybrid Blade, particular attention is paid to this design's effects on cavity-main flow mixing and the trade-off involved with replacing the free expansion losses with the profile and tip vortex losses of the bladelets. Since the bladelets were mated to the more realistic scalloped shroud, circumferential asymmetry also plays a vital role in the Hybrid Blade performance. In an effort to realize the improvement in overall stage efficiency from reducing cavity exit mixing losses, design recommendations for the next iteration of the Hybrid Blade are also articulated. Finally, Chapter 5 summarizes the major findings and design recommendations for turbine tip shroud cavity flows, as well as suggestions for future work.

Chapter 2

Isolation of Major Loss Mechanisms in Steady Cavity Flow

In accord with the established research framework of gradual increase in complexity (see Section 1.4), this chapter describes the primary loss mechanisms associated with steady tip shroud cavity flow. All results presented herein utilize a mixing plane approximation at the interface between the stationary stator domain and the rotating rotor and cavity domains. This model consists of mixing out the circumferential non-uniformities of the upstream flow at many spanwise locations, incurring a local, instantaneous loss at the interface. This approximation also significantly reduces or eliminates any potential interaction effects between rotor and stator. The identified loss mechanisms and their attendant loss level scalings form the basis upon which the analysis of unsteady flows are performed. First, to quantify the level of loss associated with the tip shroud cavity flow and demonstrate the framework of analysis, a direct comparison is made between the baseline case in Figure 1-3 and the generic shroud case in Figure 1-2. Having gained some insight into the important flow features, a series of virtual "experiments" are performed, varying the the tip seal gap size, the mass flow rate of the injected sealing flow, and incorporating shroud asymmetry to perturb

the primary loss mechanisms. The results of these perturbations suggest a strategy to mitigate one of the loss mechanisms, specifically losses associated with mixing between streams. However, it is shown instead that there are inherent limitations on methods for controlling cavity mixing losses.

2.1 Quantifying Losses Associated with the Cavity

To determine the flow field differences which arise from the presence of the cavity, a comparison is performed between the idealized baseline case and the generic shroud case with no injected sealing flows. Thus, any changes in loss or flow features must be a result of the cavity itself. Quantifying loss generation as outlined in Section 1.4 yields an axial profile of loss accumulation as shown in Figure 2-1, thus permitting tracing of loss increases to specific flow regions. For the datum comparison (i.e. generic cavity with no injected sealing flow versus the idealized baseline case), Figure 2-1 shows that the cavity introduces an additional 0.4% debit in efficiency. Since the fraction of the total flow passing through the cavity is 0.4%, this loss level translates to approximately 1% debit in efficiency per 1% of the total mass flow through the cavity. This trend is consistent with previous findings in both experiments and computations in the literature for loss attributable to tip shroud cavity flow [8, 13].

As evident in the loss profile, the majority of this loss generation occurs in the axial region spanned by the rotor and cavity domains. Further dividing this difference in loss generation by subdomain (see Figure 1-6), it is found that approximately 50% of the loss is generated in the cavity itself (i.e. 0.2% debit in efficiency) with the remaining 50% attributed to loss generating processes between the rotor exit and diffuser inlet. Determining where exactly in these regions the loss is generated, and which flow structures are responsible, requires assessing local entropy generation rates using Equation 1.8. Figure 2-2 plots contours of $\dot{S}'''_{visc}$ (normalized by multiplying by inlet stagnation temperature and dividing by flow kinetic energy over rotor passage

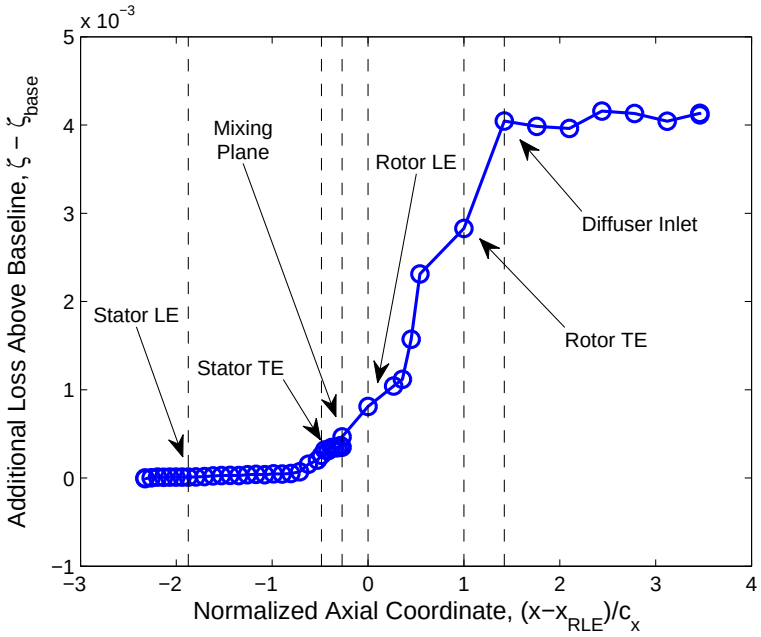

Figure 2-1: Difference in loss accumulation between the generic cavity and baseline configurations at axial locations from inlet to exit of flow domain.

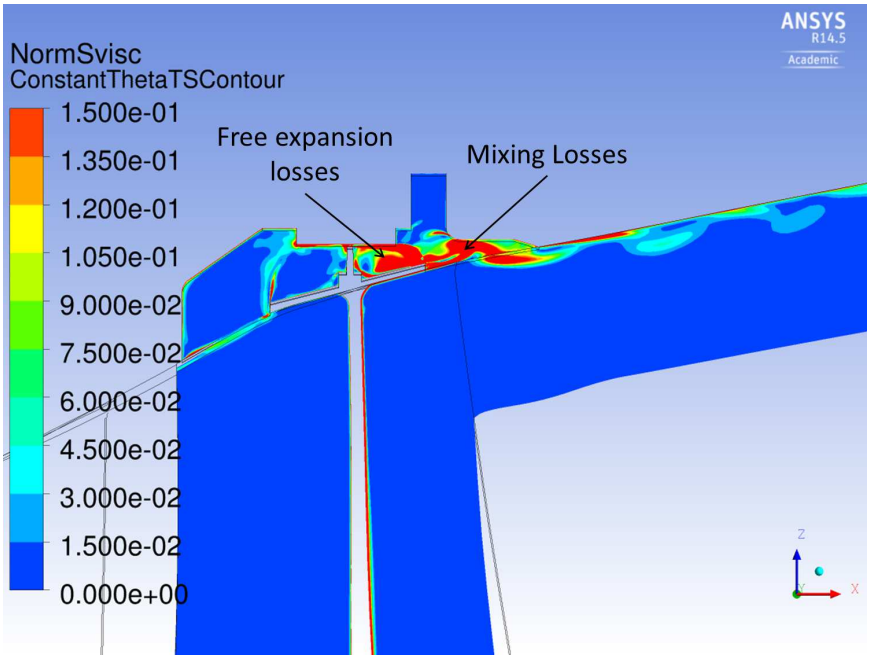

Figure 2-2: Contour plot of normalized $\dot{S}'''_{visc}$ highlighting regions of high loss generation in the cavity.

residence time). As indicated, there are two major loss sources: the free expansion of the flow passing over the tip seal, and the mixing losses occurring downstream at the interface between the cavity flow and main flow.

2.2 Primary Loss Mechanisms

This section focuses on the quantitative aspects of loss mechanisms for this particular tip shroud cavity configuration and how they change when the flow field is perturbed by changes in operation (i.e. injected sealing flow mass flow rates) or geometry (i.e. tip gap height).

2.2.1 Free Expansion Losses of the Tip Leakage Jet

Basic fluid mechanics dictates that losses are inevitable in rapid area changes due to regions of separation and recirculation. The tip seal in the cavity requires these sharp area changes to perform its function of limiting mass ingestion into the cavity. The resulting free expansion of the leakage jet into the much larger flow area downstream contributes 50% of the total loss in this and other cavity configurations [12]. As these tip seals are in essence sharp-edge orifice flowmeters, it is expected that their performance (and therefore, loss) will depend on throat area, area contraction ratio, and pressure drop across the throat [23]. The latter of these factors is set by the pressure ratio across the rotor, while the first two are functions of geometry, with a strong dependence on the tip gap size. A cursory investigation of the variation due to pressure drop is presented with the results from off-design operation in Section A.1. First, however, the effect of geometric variation is described in detail.

The effect of tip gap size on the free expansion loss was investigated by varying the spacing between the outer casing and seal tip from 0.8 to 1.8 times its nominal value. Due to manufacturing tolerance constraints prohibiting tip gaps less than the current design value, it was determined that larger gaps were of greater interest with only slightly smaller gaps required for completeness. Figure 2-3 shows that overall loss of the stage increases approximately linearly with the fraction of main flow that passes

through the cavity. In other words, the tip shroud cavity incurs a $\sim 1\%$ debit in efficiency per 1% of the main flow which passes through the cavity which is the same loss level relationship reported by Rosic et al. in References [8, 13]. A significantly larger and unrealistic tip gap (7.5x the design value) was also tested to significantly increase the leakage fraction. However, the computed loss level extrapolates to only approximately 0.67% debit in efficiency per 1% main flow passing through the cavity, likely due to the transonic (rather than sonic) flow over the tip seal generating less entropy per unit mass flow rate. For tip gaps between 0.8 and 1.8 times the design value, the total mass flow rate through the device is essentially constant (varying by only 0.4% over the range of tip gaps investigated)[1], implying that the loss is also proportional to the tip gap size.

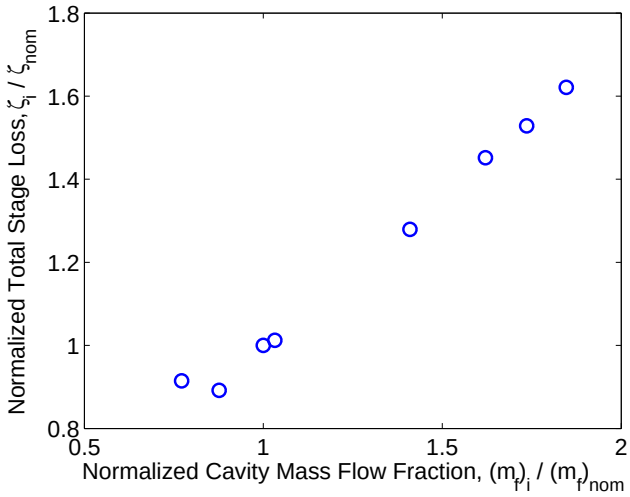

Figure 2-3: Total stage loss versus fraction of the main flow which passes through the cavity.

It is possible to further separate the loss contributions of the freely expanding tip jet and the exit mixing process, as shown in Figure 2-4. Figure 2-4a indicates that, with the exception of the 0.8x tip gap, both processes are nearly linearly pro-

[1]Over the range of gaps investigated, the pressure ratio across the blade is sufficiently high to choke the seal, thus maintaining a nearly constant corrected mass flow rate per unit area. As the upstream stagnation properties are roughly constant, the mass flow rate is then proportional to area for choked flow. The area, in turn, is proportional to tip gap since the gap height is much less than the radius of the tip seal. Any variation from this proportionality is due to the slight influence of the contraction coefficient, C_c, which generally varies from 0.6 to 0.8 depending on area contraction ratio [20]

portional (albeit with different slopes) to the mass flow fraction through the cavity while the *share* for each mechanism of the total loss linearly diverges (see Figure 2-4b). Specifically, the mixing process generates ~ 1 additional unit[2] of loss for every 1 unit of additional cavity mass flow fraction, normalized to the design case. On the other hand, the free expansion of the tip jet generates ~ 0.5 additional units of loss for every additional 1 unit of cavity mass flow fraction. This suggests that the exit mixing process is the most important to control of these two loss mechanisms as the penalty associated with an increase in cavity mass flow fraction is higher for that process. This logic is a major impetus behind the novel tip seal geometry proposed and analyzed in Chapter 4. Section 2.2.2 discusses the physical justification of this trend with mass fraction for the exit mixing process in more detail. The remainder of this section will focus exclusively on the tip jet and the relevant flow physics.

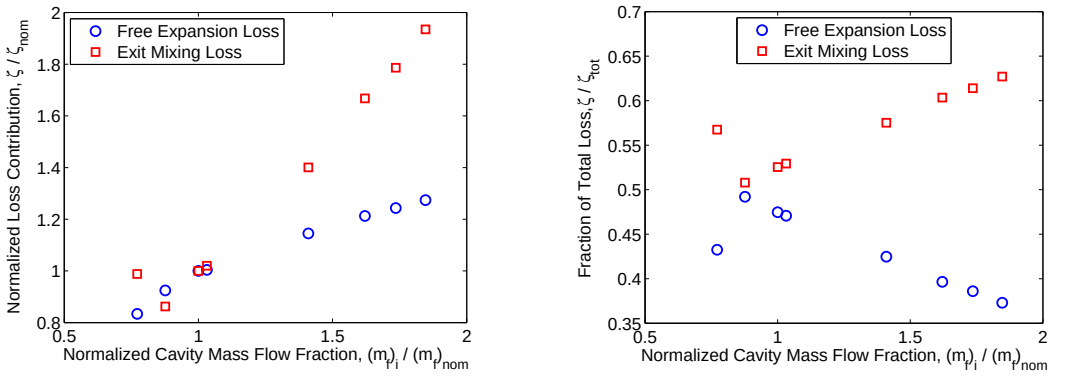

(a) Debit in efficiency versus mass fraction for each loss mechanism when varying tip gap.

(b) Portion of total debit in efficiency of each loss mechanism versus mass fraction when varying tip gap.

Figure 2-4: Breakdown of loss contribution for primary mechanisms when varying tip gap.

The free expansion jet can be reasonably modeled by a simple control volume analysis using an approximate orifice geometry shown in Figure 2-5. Since the flow is choked at the throat of the orifice, the control volume analysis requires compressible flow equations rather than an incompressible approximation. This requirement also means that the flow swirl must be taken into account as it will affect the Mach number

[2]Here, a "unit" represents a multiple of the value at design conditions (i.e. 0.2% for debit in efficiency and 0.4% of the main flow passing through the cavity, representing mass flow fraction).

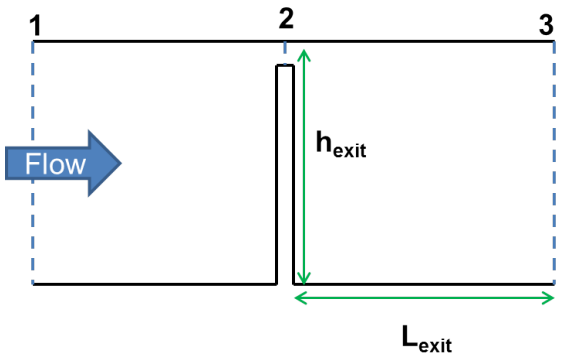

Figure 2-5: Simple axisymmetric model of tip seal orifice.

used in the isentropic flow equations. In swirling flow, it is the meridional Mach number, M_m, which determines whether a throat will be choked since it only includes the flow aligned in the axial direction. On the other hand, the total Mach number, M, relates static and stagnation properties through the isentropic flow relations. Since the height of the tip seal is much less than the average radius of the orifice, and since the relative motion between shroud and casing exerts negligible torque, angular momentum is approximately constant. Thus, by applying continuity, conservation of linear momentum, conservation of energy, and the ideal gas equation of state, respectively, the system of equations for determining the final mixed-out state is given by:

$$\text{Continuity: } \frac{A_3}{A_2}\frac{P_3}{RT_3}u_{x_3} = C_c P_{t_2}\sqrt{\frac{\gamma}{RT_{t_2}}}\frac{\rho_2}{\rho_{t_2}}\sqrt{\frac{T_2}{T_{t_2}}}, \tag{2.1a}$$

$$\text{Momentum: } P_3 + \rho_3 u_{x_3}^2 = P_2\left(1 + \gamma\frac{A_2}{A_3}\right), \tag{2.1b}$$

$$\text{Energy: } T_3 + \frac{u_{x_3}^2}{2c_p} = T_{t_2} - \frac{u_\theta^2}{2c_p}, \tag{2.1c}$$

$$\text{Equation of State: } P_3 = \rho_3 R T_3, \tag{2.1d}$$

where C_c is the contraction coefficient to account for the blockage effect of separation at the orifice leading edge. A typical range of C_c is 0.6 to 0.8, but in general, it depends on the orifice area and pressure ratios [2, 20, 24, 25].

The set of equations presented in Equation 2.1 represent a system of four coupled equations which must be solved iteratively. After finding the final state, defined by $q = [u_{x_3}, \rho_3, P_3, T_3]$, the generated loss may be estimated using the following equation:

$$\zeta_{max} = \frac{T\Delta s}{\dot{W}_{ideal}} = -\frac{\dot{m}RT_3}{\dot{W}_{ideal}} \ln \frac{P_{t_3}}{P_{t_2}}, \tag{2.2}$$

It is important to note that this analysis assumes a fully mixed out, uniform flow at station 3, and therefore Equation 2.2 is an estimate of the maximum loss associated with the free expansion of the tip seal leakage jet. Appendix C contains the full derivation and list of assumptions which yield Equations 2.1 and 2.2.

Assuming spanwise profiles of the key fluid properties in Equations 2.1 are known at the rotor inlet, estimates can be made of the flow properties at station 2 by assuming isentropic flow from the values at the blade tip. Once the properties at station 2 are known, an estimate for total loss is possible. Such an analysis was performed to evaluate the model against the CFD calculations for the set of variable tip gap cases, the results of which are shown in Figure 2-6. While the analysis replicates the linear trend with increasing tip gap observed in the CFD, the magnitude of the loss is nearly double the loss calculated in the CFD. In addition, the slope of the linear increase is larger using the control volume analysis. The discrepancy may be attributable to the flow not being fully mixed out and uniform in the final state 3 (taken as the shroud trailing edge for comparison with the CFD). Figure 2-2 supports this explanation, implying only a partial mixing and therefore only a fraction of the maximum total loss. For a better estimation of the free expansion losses, established

best practices regarding orifice flow meters provide an approximate minimum mixing length to reach a nearly uniform, mixed out state. Specifically, national standards BS 1042 and ISO 5167 for orifice flowmeters recommend a minimum of 5 pipe diameters downstream of an orifice before coupling to other components. For the generic shroud, the gap between shroud and outer casing downstream of the tip seal is analogous to the pipe diameter for standard flowmeters. In this configuration, the axial distance between tip seal and shroud trailing edge (where free expansion transitions to mixing) totals only 2.8 "pipe diameters". This distance is consistent with the CFD only accumulating between 50% and 60% of the maximum realizable loss. Therefore, a correlative factor given by $\frac{L_{exit}}{5h_{exit}} \leq 1$ modifies Equation 2.2 to account for partial mixing[3]. When incorporating this correlative factor, the model estimates loss levels in much better agreement with those observed in the CFD (see Figure 2-7).

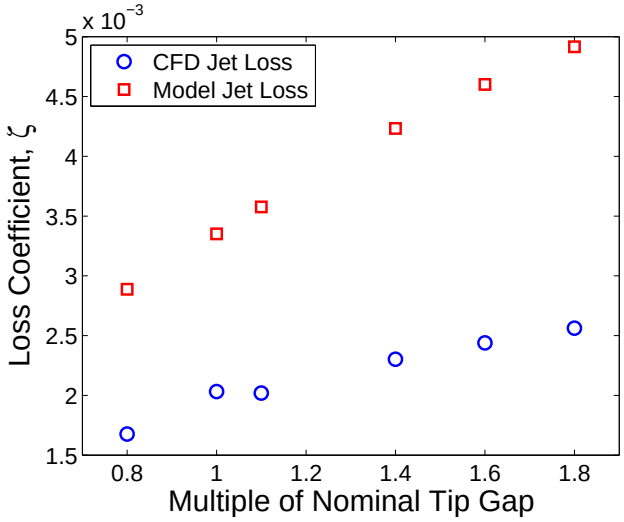

Figure 2-6: Comparison of free expansion jet loss model with loss levels from CFD, as a function of tip gap.

Another plausible contributing factor (and which may contribute to the larger slope with increasing tip gap when applying the control volume model) is the dependence of Equation 2.2 on the mixed out static temperature, T_3. Rigorously, the total viscous lost work for the free expansion should be calculated as:

[3]If the pre-factor is greater than 1, it should be omitted and the original Equation 2.2 used.

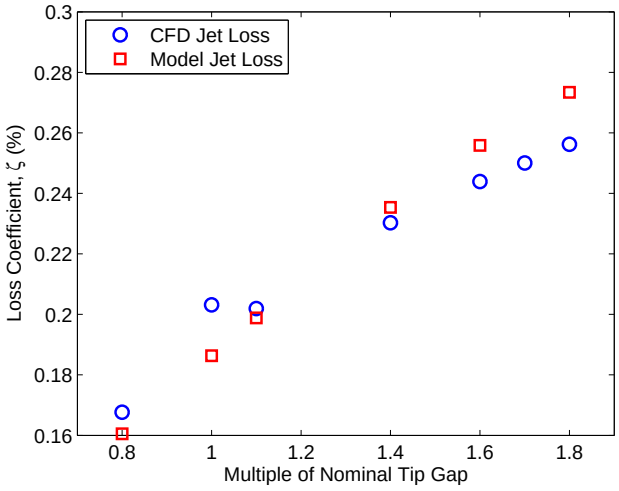

Figure 2-7: Comparison of free expansion jet loss model with mixing length correlative factor with loss levels from CFD, as a function of tip gap.

$$\dot{W}_{loss} = \int T\Delta s d\dot{m} \tag{2.3}$$

where T is dependent on the local Mach number. As a result, the static temperature at station 3 in the control volume analysis will be at the maximum for the mixing process (corresponding to the minimum Mach number). Thus, by assuming that all the mixing occurs at the station 3 temperature, Equation 2.2 provides an upper bound on loss generation. In addition, since the final temperature is dependent on the inlet properties and solution of the system of equations in Equation 2.1, the static temperature becomes another coefficient for total loss, along with cavity mass flow fraction. It is conceivable that this could result in the slope discrepancy observed in Figure 2-6.

Even with the simplifying assumptions, this analytical model, when appropriately correlated with the labyrinth seal area ratio, reasonably approximates the loss trend determined from computations. Equation 2.2 can further be rewritten to reflect the dependence on turbine design parameters (derivation in Appendix C):

$$\zeta_{jet} \approx -\left(\frac{L_{exit}}{5h_{exit}}\right)\left(\frac{\dot{m}_{f_{cav}}}{\gamma\psi_{tip}M_{tip}^2}\right)\left(1+\phi_{tip}^2\right)\ln\pi_t, \tag{2.4}$$

where L_{exit} is the axial distance between the tip seal and shroud trailing edge; h_{exit} is the radial gap between shroud and outer casing downstream of the tip seal; M_{tip} is the local design Mach number at the tip of the rotor trailing edge; ψ_{tip} is the total stage loading based on rotor tip speed; ϕ_{tip} is the local flow coefficient at the tip of the rotor trailing edge; and π_t is the stagnation pressure ratio across the blade. The factor of 5 multiplying h_{exit} is based on the aforementioned standards BS 1042 and ISO 5167, included to account for incomplete mixing. If $\frac{L_{exit}}{5h_{exit}} \geq 1$, the first factor in parenthesis may be omitted. Whether the exact analytical model in Equations 2.1 and 2.2 is used, or the design-based approximation in Equation 2.4, depends entirely on the information available to the designer and the desired level of sensitivity or accuracy. Section A.1 evaluates Equation 2.4 against computations of the turbine stage with varying stage pressure ratio to demonstrate its usefulness in a design context.

Equations 2.2 and 2.4 do not explicitly depend on the size of the machine, and therefore would not imply larger losses for smaller machines. However, as previously noted, the free expansion loss is directly proportional to the mass flow fraction through the cavity which in turn depends on the size of the gap between the radial sealing fin and outer casing. Since that gap is typically choked by the pressure ratio across the rotor, the mass flow rate may be estimated with corrected mass flow for swirling flow [20]:

$$\frac{\dot{m}}{AP_t}\sqrt{\frac{RT_t}{\gamma}} = M_m f(M) = M_m \frac{\rho}{\rho_t}\sqrt{\frac{T}{T_t}}, \tag{2.5}$$

where $f(M)$ depends on the flow total Mach number only, and M_m is the meridional Mach number (i.e. Mach number of the flow normal to the cross-sectional area). If comparing two designs of different size but constant Mach numbers, total mass flow

rates, and stagnation properties, the expected mass flow fraction through the cavity of the smaller device will be less than the larger device with proportionality factor equal to the ratio of tip radii, r_{small}/r_{large}[4]. Thus for smaller machines with otherwise similar operating conditions, the free expansion losses are expected to be less due to the lower fraction of the main flow passing through the cavity. An alternate approach to this conclusion recognizes that if the tip seal is choked, it is passing the maximum mass flow per unit area for the given stagnation conditions. Utilizing a smaller device with the same stagnation properties would then yield a smaller mass flow rate through the cavity due to its smaller flow area over the tip gap. It should be noted, however, that this analysis assumed the same total mass flow rate when moving to a smaller machine. Such an assumption is likely invalid if machine size changes significantly as main flow design characteristics may preclude operation altogether (e.g. choking of the main flow path).

On the other hand, if the stagnation properties vary (when analyzing an earlier stage, for example), the mass flow fraction, and thus, losses, may instead increase. Large turbines such as the one under investigation here often employ shrouds on both the third and fourth stages due to the lengths of the blades in these stages. Comparing the third stage to the fourth stage, the ratio of cavity mass flow rates through a choked tip seal is approximated by:

$$\frac{\dot{m}_3}{\dot{m}_4} \approx \frac{r_3}{r_4}\left(\frac{P_{t_3}}{P_{t_4}}\right)^{1-\frac{1}{2}\left(\frac{\gamma-1}{\gamma}\right)}, \tag{2.6}$$

where the subscripts, 3 and 4, denote properties of the third and fourth stages, respectively. As this is a turbine, the stagnation pressure of the third stage will be higher than that of the fourth. Using an assumed size ratio of 0.8 and the pressure ratio of the representative turbine given in Table 1.1, the ratio of mass flow rates is approximately 1.5. Since the two stages will have the same total mass flow rate by

[4]The tip gap does not appear in this ratio as it depends on manufacturing tolerances (which are absolute length scales and do not scale with other characteristics of machine size) and stage operational characteristics (which were stated as assumed constant).

continuity, the third stage is expected to have 50% greater cavity mass flow fraction, and consequently 50% greater free expansion losses from the tip jet. In either case, it is not the size of the machine which directly matters with respect to the loss generation, but rather how the size and operational characteristics combine to affect cavity mass flow fraction and pressure ratio across the cavity. Based on Equation 2.2, these parameters determine to the greatest extend the loss level attributable to the free expansion of the tip seal jet.

2.2.2 Losses due to Mixing

Having investigated the variation of loss levels associated with the free expansion over the tip seal, it remains to determine the loss sensitivities in the other primary loss mechanism in tip shroud cavity flow: mixing at the cavity exit. This configuration in fact has two separate, serial mixing processes. The first is between the tip leakage flow and the injected sealing flow labeled in Figure 1-2. The resulting flow from that mixing process then rejoins and mixes with the main flow at the cavity exit. The injected sealing flow provides a useful means of interrogating the response of these two loss mechanisms, not only because it provides direct control over one mixing process, but also modifies the flow field at the cavity exit to perturb the mixing process between the cavity exit flow and the rotor exit flow.

2.2.2.1 Quantification of Loss with Varying Injected Sealing Flow

The parameter varied in the investigation of the mixing losses was the mass flow rate of the injected sealing flow. The mass flow rate was varied from 1 to 16 times the nominal design value of 0.1% of the mass flow rate through the stage (in factors of 2). A similar analysis procedure as that in Section 2.1 was then performed to determine the effect on the various loss contributors. Even at the greatest injected mass flow rate, the injected flow still amounted to only 1.6% of the main flow. As a result, the majority of the main flow path does not feel any influence; only the tip region of the rotor exit and the mixing processes of interest are significantly affected.

Figure 2-8 summarizes the loss breakdown for several of the injected sealing flow cases. The total change in loss for the cases versus the baseline geometry with no cavity is shown by the red bars and normalized to the cavity loss of the datum case (generic shroud, no injected sealing flow). The blue, cyan, and yellow bars split this total loss into the contributions of the primary mechanisms, normalized to the total cavity loss of that particular case. Specifically the different categories are: the free expansion of the tip seal leakage jet, the mixing between the tip seal leakage flow and injected sealing flow ("Cavity Mixing"), and the mixing between the total cavity flow and the rotor exit flow ("Exit Mixing").

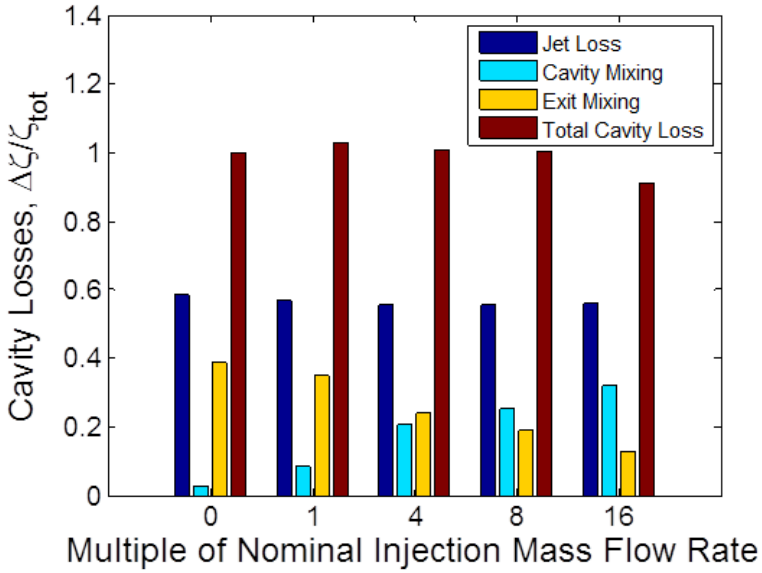

Figure 2-8: Comparison of total, and individual contributions to, cavity loss for several injected sealing flow rates. "Jet Loss" refers to the loss associated with the free expansion of the tip jet. "Cavity Mixing" refers to the mixing loss between the cavity flow and the injected sealing flow. "Exit Mixing" refers to the mixing loss between the flow exiting the cavity and flow exiting the rotor.

The first trend to notice in Figure 2-8 is that above the nominal injected sealing mass flow rate, the total additional loss over the baseline geometry decreases monotonically (albeit only slightly). Given the level of loss associated with the cavity in the datum case (i.e. 0.4% debit in efficiency), this slight decrease in overall loss is deemed negligible, amounting to $\sim 0.04\%$ in recovered efficiency. As mentioned above, the

maximum injected mass flow rate is only 1.6% of the total flow. Therefore it is not surprising the overall effect is small, though the monotonically decreasing trend does suggest potential, physically interesting aerodynamic effects. It is within this context of virtually constant loss that the contributions of the individual mechanisms are now examined in detail.

2.2.2.2 Trends in Loss Mechanism Contributions

Before focusing on the detailed physics of the mixing processes, the variation of the free expansion loss with injected mass flow rate merits further elaboration, especially in light of the trends and conclusions from the preceding section. Overall, the loss contribution of the tip jet to total loss is more or less constant at between 50% and 60% of the total. Given that the tip seal is choked at the operating pressure ratio of the stage, this fact makes sense as the flow process should be insensitive to changes downstream of the choke point so long as the pressure ratio is sufficiently aggressive (i.e. above the critical value). However, it is worth noting there is a slight but definite decrease in loss associated with the free expansion of the leakage jet as the injected mass flow rate is increased. The physical explanation for this somewhat unexpected trend is that the tip seal is more of a sharp-edged orifice than a traditional converging-diverging nozzle, meaning there will be some amount of separation above the knife-edge seal. In addition, the throat area for the flow over the seal is not set explicitly by the tip gap size but rather the throat area of the vena contracta formed between the outer casing and the separation bubble. As the injected mass flow rate is increased, the mixing losses downstream increase the perceived downstream static pressure which may propagate upstream through the separated boundary layer on the tip seal, reducing the vena contracta area, and thus reducing the mass flow over the tip seal slightly. As shown in Section 2.2.1, the loss associated with the free expansion of the tip seal leakage jet is proportional to the tip seal mass flow. Therefore, the slight decrease in mass flow yields the observed slight decrease in tip jet losses with increasing injected sealing mass flow rate. This effect of continued variation of orifice mass flow rate with changing pressure ratio is not unprecedented,

having been observed by Cunningham in orifice flow meters [3], and employed to a limited extent by Curtis et al. [26] where an injected air curtain was used to limit the mass flow over a turbine tip shroud. For further assessment of this reasoning, a simple computational model based on Cunningham's experiments is presented in Appendix D and compared to his findings.

Although the losses from the tip seal leakage jet do decrease over the range of injected mass flow rates, the decrease is insufficient to explain the decrease in overall loss. In addition, intuition leads one to expect an increase in loss simply because of the anticipated increase in mixing losses between the tip seal leakage flow and injected flow. This leads to the most interesting trend in Figure 2-8, namely the competing trends in loss levels between the two coupled mixing processes in the cavity exit region. Specifically, the cyan bars show that the mixing loss between the tip seal leakage jet flow and the injected mass flow increases significantly with increasing injected sealing mass flow rate. This mixing loss increases to the point that, for the maximum injected mass flow rate, $\sim 67\%$ of the losses associated with mixing in control volume CV2 are generated in the Cavity Mixing process. The decrease in overall loss, however, implies that the reduction in loss due to the Exit Mixing process dominates the Cavity Mixing process.

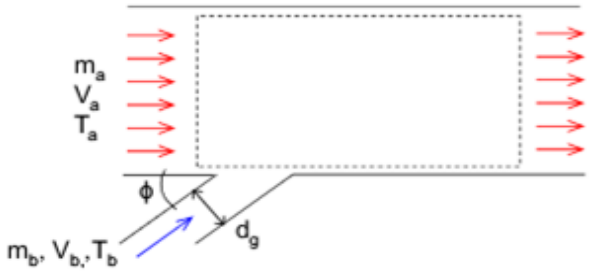

Figure 2-9: Simple axisymmetric model of mixing between an injected flow and main flow [1].

2.2.2.3 Control Volume Analysis of Mixing Losses

The exchange between mixing processes begs the question of what important parameters are changing to drive this trade-off. Denton [10] and Young-Wilcock [27] both suggest simple mixing models based on an axisymmetric geometry similar to the one in Figure 2-9. Zlatinov expanded the Young-Wilcock model to incorporate swirling flow [1], and this analysis serves as a simple approximation of both mixing processes (i.e. the Cavity and Exit mixing processes) in the present cavity. The estimation for viscous entropy generation is given by:

$$\frac{T_a \Delta \dot{S}_{visc}}{\frac{1}{2}\dot{m}_a(v_a - v_b)^2} = \frac{\dot{m}_b}{\dot{m}_a(v_a - v_b)^2}\left((v_{a_1} - v_{b_1})^2 + (v_{a_2} - v_{b_2})^2 + (v_{a_3} - v_{b_3})^2\right) \tag{2.7}$$

While Equation 2.7 has certain uses, the individual velocity components are not necessarily known *a priori* nor necessarily among the key design parameters. Therefore it may be beneficial to re-write Equation 2.7 in terms of differences in velocity magnitudes and an angle term which accounts for the misalignment of mixing streams:

$$\frac{\dot{W}_{loss}}{\frac{1}{2}\dot{m}_a(v_a - v_b)^2} = \frac{\dot{m}_b}{\dot{m}_a}\left(1 + 4\frac{v_a v_b}{(v_a - v_b)^2}\sin^2\frac{\phi}{2}\right) \tag{2.8}$$

where ϕ is the relative flow angle between mixing streams, consistent with Figure 2-9. Equation 2.8 is the Zlatinov limit of a more general expression derived in full in Appendix E.

As written, the two equations provide different insights into the physical basis for mixing losses. Both equations maintain the dependence on the mass flow involved in the mixing and the difference in velocity magnitudes. The Zlatinov approach allows one to trace the loss generation to velocity non-uniformities in specific flow directions, which implicitly includes relative alignment of the streams. On the other hand, Equation 2.8 explicitly depends on angle, but, importantly, also explicitly shows how the angle term depends on the speed at which the mixing occurs. For the cases

presented in Figure 2-8, the primary driver of loss level is the relative flow angle. Even with the large increases in injected diffuser leakage mass flow rate, the difference in velocity magnitudes did not vary as significantly. For example, in the cavity/rotor exit mixing process, the velocity magnitude of the main flow at the rotor exit decreases by only 16%, and the cavity exit velocity magnitude decreases by 40%, despite a 1500% increase in injected sealing mass flow rate (nominal to 16x case). While this certainly lowers the difference in velocity term of Equation 2.8, as well as the product of velocity magnitudes, the effect of the latter reduction is amplified by a factor of 5 due to the angle dependence (see Figure 2-11). Figures 2-10a and 2-11 plot the variation in relative flow angles between the respective mixing streams versus the injected sealing mass flow rate. In Figure 2-10a, the relative flow angle is slightly increasing with increasing injected sealing flow rate, consistent with the observed increase in mixing losses between the cavity flow and the injected sealing flow. In fact, when comparing Figure 2-10a with Figure 2-10b, the relative differences in loss in Figure 2-10b appear to correspond with the relative differences in flow angles in Figure 2-10a. On the other hand, Figure 2-11 depicts a much more drastic decrease in relative flow angle between the cavity exit flow and the rotor exit flow, consistent with the more dominant reduction in mixing losses at the cavity exit described above.

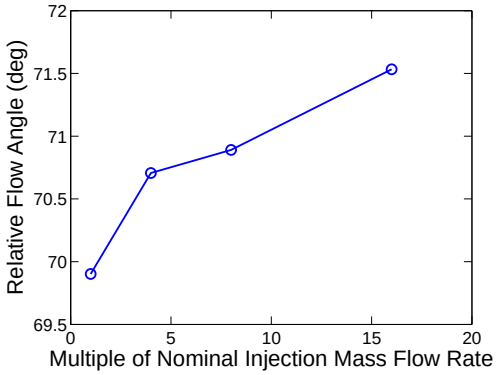

(a) Relative flow angle between tip seal leakage flow and injected sealing flow as a function of injected sealing mass flow rate.

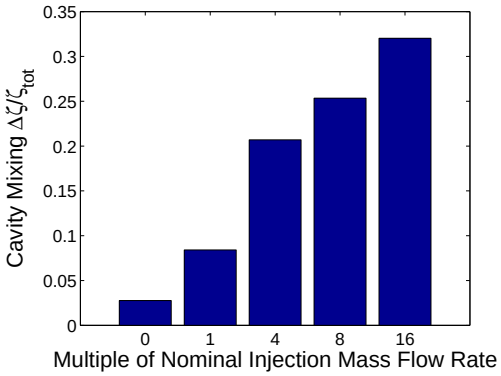

(b) Fraction of total cavity loss generated in mixing between tip seal leakage flow and injected sealing flow as a function of injected sealing mass flow rate.

Figure 2-10: Importance of relative flow angle in Cavity Mixing.

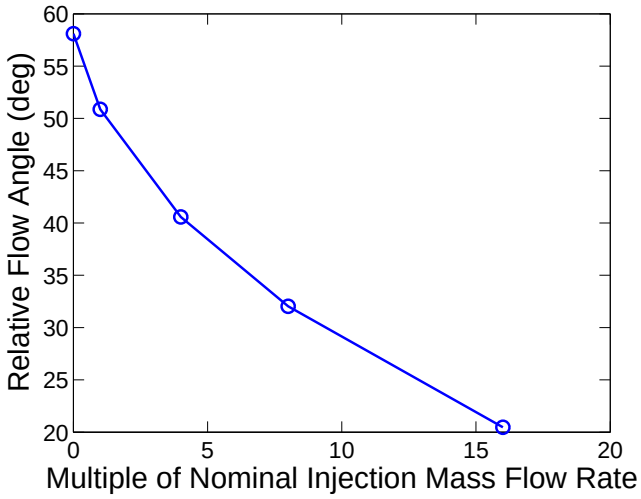

Figure 2-11: Variation of relative flow angle between cavity exit flow and rotor exit flow versus injected sealing mass flow rate.

2.2.2.4 Importance of Relative Flow Angle and Swirl Disparity

The reduction in relative angle with increased injected sealing mass flow rate is evident in the computed flow field. Figure 2-12 compares the streamlines of the cavity flow (black) and main flow (magenta) when they interact at the cavity exit for the nominal and maximum injected sealing flow cases. Vectors are added to highlight the directions of the streams at the point of interaction. It is visibly evident that the angles between flow vectors in the nominal injection case are significantly higher than those in the maximum injection case, consistent with the line plot in Figure 2-11.

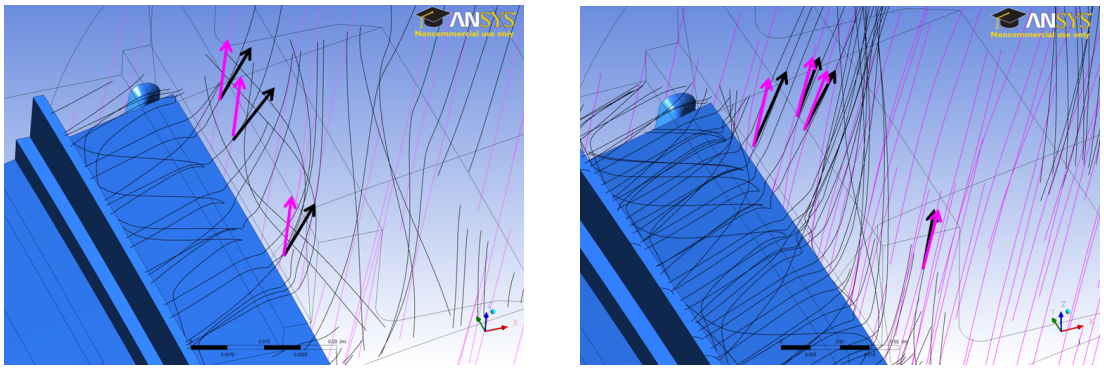

(a) Nominal injected sealing mass flow rate.

(b) Maximum injected sealing mass flow rate (16x nominal).

Figure 2-12: Cavity (black) and main flow streamlines (magenta) at interaction interface at cavity exit.

The implication of Equation 2.8 is that for the mixing of any two streams (such as a cavity flow and a main flow), minimum loss is achieved when the magnitude of the velocity difference and the relative flow angle between streams are both minimized. However, it is of engineering utility to develop scaling rules which would aid the designer in preliminary cavity design by casting trends in terms of design parameters. The logical design parameter for capturing relative flow angle in Equation 2.8 is the difference in swirl parameters of the two streams, as the tangent of swirl parameter is equivalent to the two-dimensional flow angle (projected on the circumferential-axial plane) of a particular stream. Several previous studies [7–9, 11, 12] support the approximation of the relative flow angle by its two-dimensional projection using swirl parameter as they indicate the dominance of circumferential momentum disparity in mixing losses associated with the cavity. Thus swirl parameter serves as an effective surrogate, provided the designer judiciously chooses which velocities to use to define the most relevant swirl parameter. For instance, in the current configuration, the logical choice for the Exit Mixing process is the traditional definition of swirl, or v_θ/v_x. However, an appropriate choice for the Cavity Mixing process would be v_θ/v_r as the injected sealing flow has purely radial velocity at injection.

Regardless of how precisely swirl parameter is defined, according to Equation 2.8, the viscous lost work due to the mixing processes should be approximately proportional to the square of the sine of the difference in swirl parameter between streams. A first-order Taylor expansion (or, equivalently application of the small angle approximation) simplifies this trend further such that loss is proportional to the square of the difference in swirl angle. Figures 2-13 and 2-14 show the losses for each mixing process as quantified in terms of both functional forms. For both processes, quantifying in terms of both functional dependencies agrees well with the computed loss from CFD.

The fitted trendlines in Figures 2-13 and 2-14, computed using regression analysis, are included mostly to emphasize the consistency between the CFD and the general flow physics contained in Equation 2.8. However the quadratic trendlines in Figures 2-13b and 2-14b exhibit an interesting reversal in concavity which is not expected

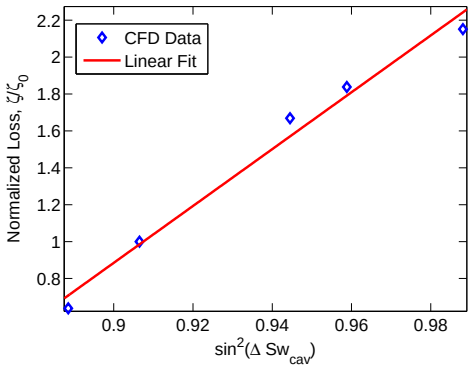

(a) Loss coefficient for the Cavity Mixing process, normalized to the nominal injection case, versus the square of the sine of the difference in swirl parameter.

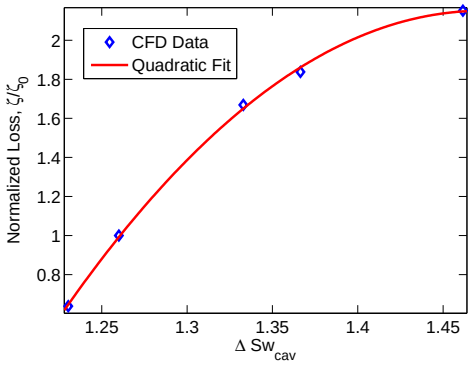

(b) Loss coefficient for the Cavity Mixing process, normalized to the nominal injection case, versus difference in swirl parameter.

Figure 2-13: Variation of loss coefficient in the Cavity Mixing process with swirl parameter.

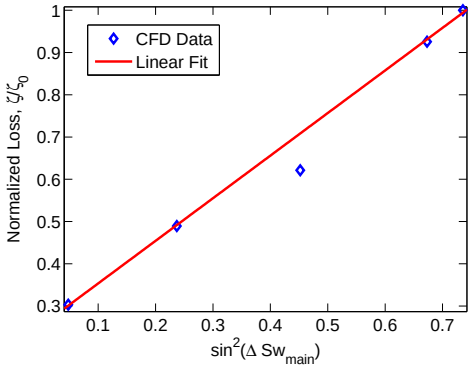

(a) Loss coefficient for the Exit Mixing process, normalized to the nominal injection case, versus the square of the sine of the difference in swirl parameter.

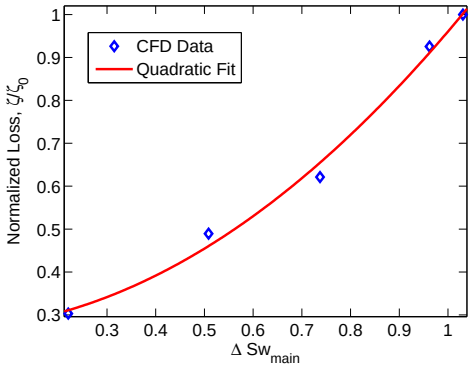

(b) Loss coefficient for the Exit Mixing process, normalized to the nominal injection case, versus difference in swirl parameter.

Figure 2-14: Variation of loss coefficient in the Exit Mixing process with swirl parameter, Sw.

from Equation 2.8. While the Exit Mixing process displays positive concavity as expected, the Cavity Mixing process has negative concavity. It is conceivable that this is a result of one of the primary underlying assumptions of Zlatinov's expansion of the Young-Wilcock model and upon which Equation 2.8 is based. Namely, the assumption that the injected mass flow rate is significantly less than the "main" mass flow rate. The ratio of cavity flow to injected flow in the Cavity Mixing process never exceeds 4; in fact, at maximum injected mass flow rate, the ratio reverses with the injected mass flow rate reaching 4 times the cavity mass flow rate. Therefore it is possible that velocities or changes in flow properties (such as pressure) could alter the expected trends. This is an example of when the more general expression derived in Appendix E might be more suitable. Nevertheless, the simpler Equation 2.8 captures the general functional dependence as evident by the linear dependence on the square of the sine of swirl parameter difference and quadratic dependence on the swirl parameter difference. For the purposes of simple estimation, and for the remainder of this thesis in which cavity geometries and operation conditions are compared without the added complexity of injected sealing flow, Equation 2.8 is appropriate as all mixing processes will involve one stream with significantly less mass flow rate than the other. Thus, Zlatinov's assumptions are expected to reasonably apply.

As with the streamlines in Figure 2-12, contour plots from CFD allow visualization of the reduction of the swirl parameter difference between flows. Figure 2-15 shows the contours of swirl parameter in the Exit Mixing process for both the nominal injection case and the maximum injection case. It is evident by visual comparison that the majority of the cavity exit flow has swirl near that of the main flow path in the maximum injection case, while the cavity exit flow in the nominal injection case shows significantly higher swirl over the majority of the interface. In fact, the only region of low swirl in Figure 2-15a corresponds to ingestion of main flow into the cavity exit. These observations are consistent with the data trend shown in Figure 2-14.

While the total loss attributable to mixing depends only on the end states, and

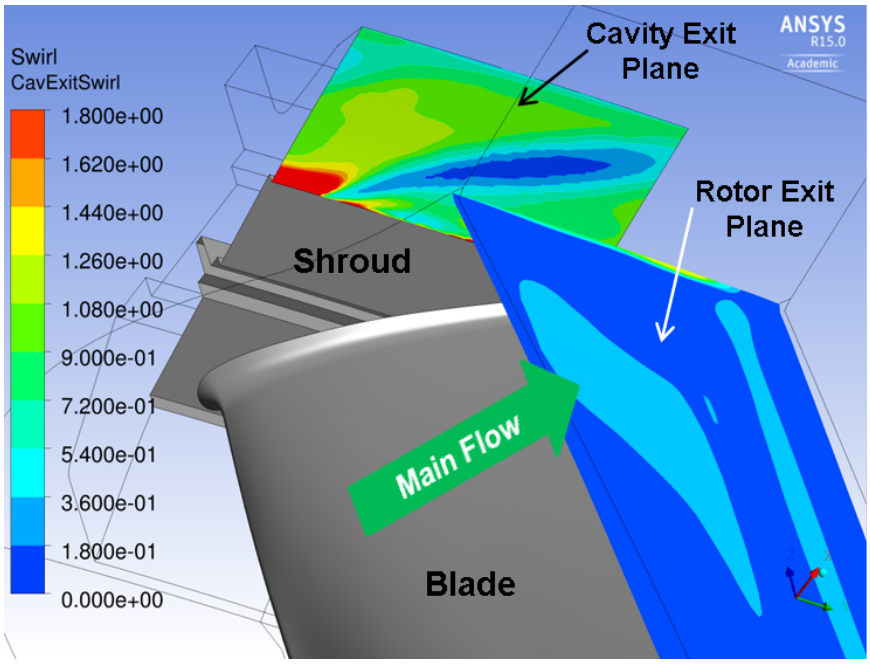

(a) Nominal injected sealing mass flow rate.

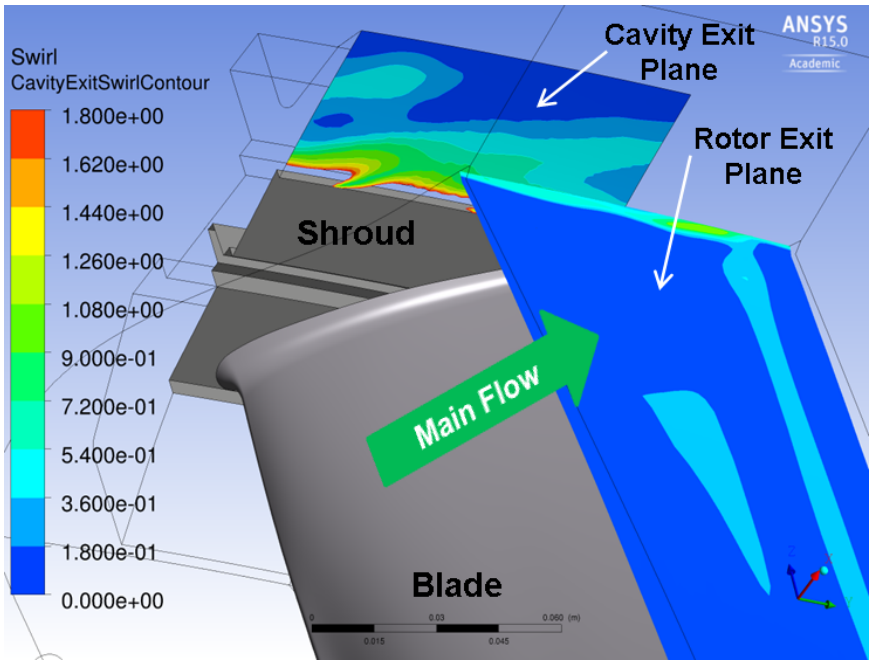

(b) Maximum injected sealing mass flow rate (16x nominal).

Figure 2-15: Contour plots of swirl parameter (based on axial velocity) at the interface between cavity exit flow and rotor exit flow.

therefore is independent of turbulence model, partial loss due to mixing will depend on the process and thus degree of mixing. Since the Cavity Mixing process is nearly (but not fully) complete prior to mixing with the main flow, the division of loss level due to mixing between Cavity Mixing and Exit Mixing processes may depend on the choice of turbulence model. However, the trends based on control volume analysis are in accord with the observed trends in the viscous entropy generation computed by the CFD. Thus, despite the uncertainty associated with the specific choice of turbulence model, the computed results appear physically consistent. It can therefore be inferred that the SST model is adequate for the configuration and environment encountered here. Nevertheless there exists a need to assess the sensitivity of the mixing process to the use of different turbulence models.

2.2.3 Mixing Loss Enhancement with Asymmetric Shroud

While shroud asymmetry does not affect tip jet free expansion loss levels and trends, it does increase losses due to mixing by 0.1% debit in efficiency. This is observed in Figure 2-16 which plots the loss accumulation through just the rotor and cavity for the generic shroud and asymmetric shroud configurations. Note that the divergence point between the two loss profiles corresponds to an axial location just downstream of the tip seal. Due to the shroud asymmetry, this divergence point also corresponds to the axial location where the cavity flow and main flow begins interacting again. The location where cavity flow and main flow begin to interact determines the flow properties upon which the main flow-cavity flow mixing process depends (Equation 2.8). Onset of interaction nearer the choked tip seal is expected to increase mixing losses between cavity flow and main flow by causing the mixing to occur at higher flow velocities (recall the importance of Δv and the scaling of the term depending on relative flow angle by the product of velocities, $v_1 v_2$, in Equation 2.8).

A detailed analysis of the flow field at the point of cavity-main flow interaction and application of Equation 2.8 confirms that mixing losses increase due to mixing at higher velocities. Table 2.1 presents the key flow variables for Equation 2.8 for the scalloped shroud case, normalized to those of the generic shroud case. Even though

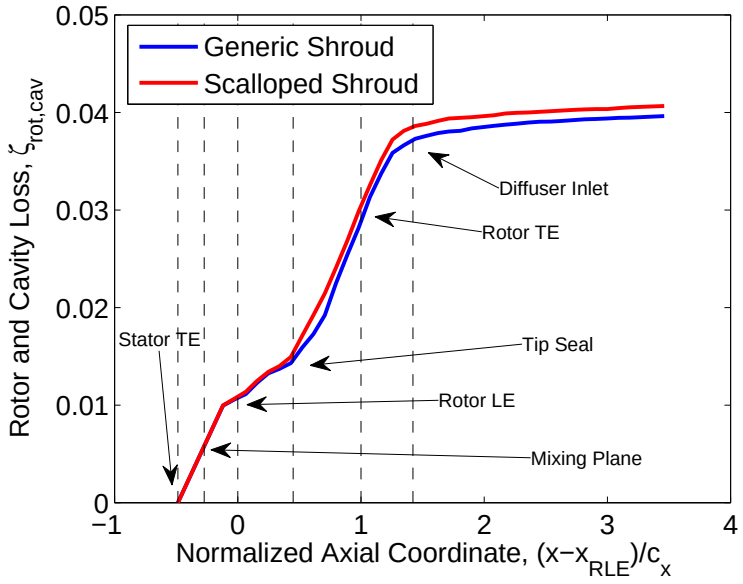

Figure 2-16: Comparison of axial accumulation of loss in the rotor and cavity domains only of the scalloped and generic shroud configurations.

the relative angle between streams at the onset of interaction is less in the scalloped shroud case, the significant increases in difference of velocities and product of velocities more than offset the efficiency gain expected from better stream alignment. These two simultaneous effects are a direct result of moving the point of interaction closer to the choke point of the tip jet. The angular momentum of flow leaking over the tip seal remains unchanged from case to case (same mass flow fractions and inlet swirl angle). However, the higher axial velocity near the tip seal means the flow angle decreases while simultaneously raising the magnitude of velocity of the cavity flow at mixing. Taking a ratio of the expected losses due to mixing for each stream using Equation 2.8, it is found that the scalloped case is expected to generate 40% more loss due to mixing than the generic case, or a debit in efficiency of $\sim 0.3\%$ compared to 0.2% in the generic case.

Δv	$v_1 v_2$	θ
3.6	2.4	0.4

Table 2.1: Key mixing loss flow properties in scalloped shroud case, normalized to generic shroud values.

2.2.4 Dependence of Mixing Loss on Machine Size

To complement the generalization of the free expansion losses to machines of different size, this section briefly discusses the dependence of mixing loss between the cavity flow and main flow on machine size. Zlatinov's expression for mixing loss, Equation 2.7, will be used to facilitate the discussion due to the traceability of momentum disparity to a specific direction. As before, the two hypothetical machines vary only in size but not operational characteristics. For a given operating point, the flow coefficient is constant; therefore if the rotor speed is the same, so must be the axial velocity. As a result, the designer expects the difference in axial velocities to remain unchanged. Similarly, the radial velocities are assumed unchanged as they are determined by the endwall rate of opening and the details of the cavity exit region geometry. However, if the stage work output remains the same, the difference in circumferential velocity will increase by a factor, r_{large}/r_{small}, according to Euler's turbine equation. The mass flow fraction through the cavity was previously shown to decrease for a choked tip gap with constant stagnation properties and operating point (see Section 2.2.1). Thus, while the decreasing mass flow fraction would tend to decrease mixing loss between the cavity flow and main flow for smaller devices, the quadratic dependence on the circumferential momentum disparity would tend to increase loss. Quantifying the amount of loss increase will depend on the details of the velocity differences as the comparison of loss is not a simple ratio. As an illustration, the difference in velocities in all three directions for the original, large machine is taken to be unity. For a size ratio, r_{large}/r_{small} of 1.2, the mixing loss in the smaller device is expected to be 96% that of the larger device. However, if the size ratio is increased above 2, the smaller device would have greater loss.

As in the free expansion of the tip seal jet analysis, this simple examination of the mixing loss dependence on machine size will likely breakdown for size ratios significantly different than 1 due to practical operational limits of the turbine. The important takeaway is that mixing loss also does not directly depend on machine size but rather the flow properties of the two interacting streams. Consequently, the

designer should seek to minimize the cavity mass flow fraction and the difference in velocities of the two streams, regardless of machine size.

2.2.5 Limitations on Controlling Mixing Losses

Given the strong dependence of the cavity-related mixing processes on the difference in swirl between streams, and the apparent dominance of the Exit Mixing process over the Cavity Mixing process, one may consider utilizing the serial nature of the mixing processes to decrease overall loss. For instance, if enough swirl is injected with the injected sealing flow such that the Cavity Mixing process results in a zero swirl flow at the cavity exit, will the stage loss decrease? A representative case was investigated to answer this question.

The basic principle requires that the net angular momentum at the cavity exit should be zero in order to minimize the Exit Mixing losses. Since the radial separation of the tip seal leakage flow and the injected sealing flow is negligible, this requirement determines the amount of circumferential velocity which must be injected:

$$v_{\theta_{injected}} = -\frac{\dot{m}_{cav}}{\dot{m}_{injected}} v^{ma}_{\theta_{cav}}, \tag{2.9}$$

The circumferential velocity of the tip seal leakage flow is high enough that, due to the factor of 4 introduced by the mass flow ratio, the injected circumferential velocity would need to be well above the speed of sound for the design injected sealing mass flow rate. Equation 2.8 is also proportional to mass flow rate, so the next lowest multiple case (i.e. 4 times the design injected sealing mass flow rate) was chosen for the sample case. For this injection rate, Equation 2.9 simply states that the required injected circumferential velocity is of equal magnitude but opposite sign to the circumferential velocity of the tip seal leakage flow.

Rather than decreasing overall losses as desired, however, this injection of swirl in the sealing flow increases the overall loss by $\sim$ 0.1%, as seen in Figure 2-17. Comparing contours of $\dot{S}'''_{visc}$, it is evident this additional loss is due to enhancement

of mixing in the Cavity Mixing process (see Figure 2-18). The green arrow highlights the region in which Exit Mixing losses are reduced, and the red arrow highlights the region where Cavity Mixing is enhanced. While the loss due to mixing between the cavity exit flow and rotor exit flow does appear to decrease, the increase in mixing between the tip seal leakage flow and injected sealing flow outweighs this gain in efficiency.

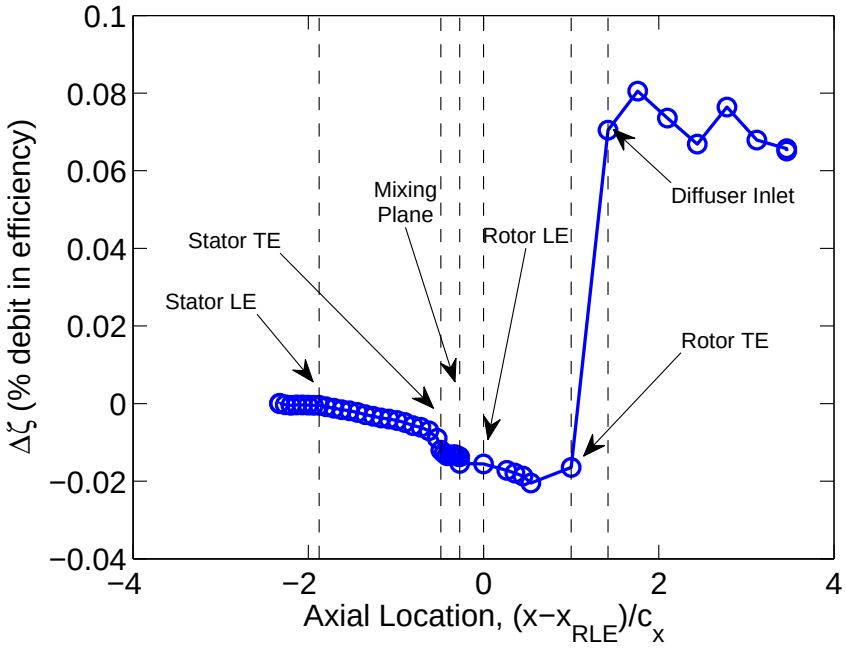

Figure 2-17: Axial profile of the difference in loss accumulation of 4 times nominal injected sealing mass flow rate, with swirl minus no swirl.

The increase in overall loss incurred by injecting reverse swirl is actually not surprising. Recalling Equation 2.8, adding swirl will decrease the Δv^2 term, but doing so also drastically increases the term dependent on relative flow angle. Another effect of adding swirl is an increase in the product of velocities which scale the loss increase due to misalignment between streams. In addition, the requirement of the injected swirl to be equal and opposite that of the tip seal leakage flow means the relative flow angle between streams drastically increases to above 110 degrees. Alternatively, the model in Equation 2.7 may readily be applied in this situation as the individual velocity components are known. While the differences in the radial and axial veloc-

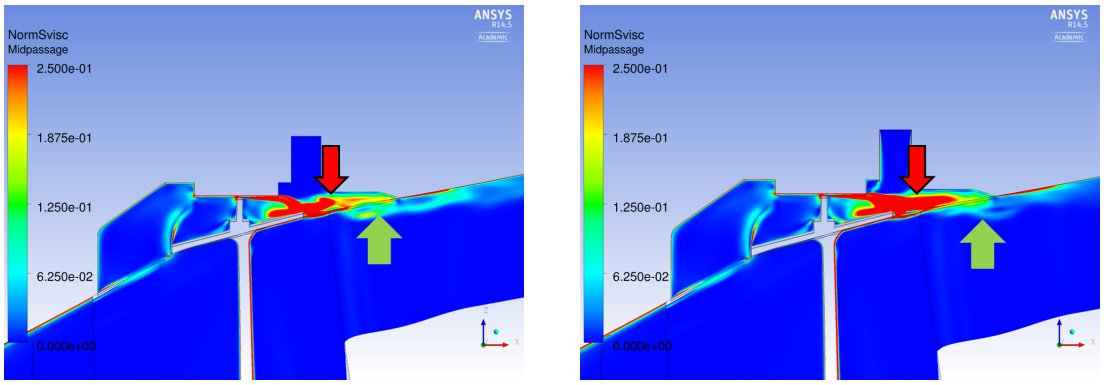

(a) No swirl.

(b) With swirl.

Figure 2-18: Contour plots of volumetric viscous entropy generation for injected sealing flow case with and without injected swirl.

ity components remain relatively unchanged, the circumferential velocity difference essentially doubles, which translates to a four-fold increase in mixing loss associated with circumferential mixing. Table 2.2 summarizes the changes in the relevant stream properties for important terms in both Equation 2.7 and Equation 2.8. The given ratios are defined as the value for the case with injected swirl divided by the original case with no injected swirl.

Parameter	Ratio
ϕ_{cav}	1.61
ϕ_{exit}	0.59
Δu_x[5]	1.0
$\Delta u_{\theta_{cav}}$	1.78
$\Delta u_{\theta_{exit}}$	0.37
$\Delta u_{r_{cav}}$	0.98
$\Delta u_{r_{exit}}$	0.85

Table 2.2: Key changes in mixing loss terms for swirl injection case.

The above analysis indicates that aerodynamic control of mixing losses at the cavity exit is impractical and likely to only lead to increased loss. The difference in circumferential velocity in Table 2.2 can be decreased by increasing the injected sealing mass flow rate (according to Equation 2.9), but it must always be greater than 1 as the injected swirl velocity must have the opposite sign of the swirling tip

[5]Ratio is the same for both Cavity Mixing and Exit Mixing.

seal leakage flow. In addition, increasing the mass flow rate incurs cycle penalties by increasing the amount of bleed air required from the compressor. Therefore, consideration should be given instead to potential hardware/configuration changes for mitigating loss generation, such as the one proposed and analyzed in Chapter 4.

2.3 Summary of Major Loss Sources in Tip Shroud Cavity Flow

Chapter 2 has focused on the primary loss mechanisms, their loss levels, and their important scaling parameters for a basic tip shroud cavity geometry. Namely,

1. The generic tip shroud cavity is responsible for 0.4% debit in efficiency over an idealized baseline case with no tip shroud cavity. The asymmetric shroud introduces an additional 0.1% due to an increase in mixing losses at the cavity exit.

2. The primary loss mechanisms in the tip shroud cavity are the free expansion of the tip seal leakage flow and the mixing processes between injected sealing flows and/or the cavity exit flow and rotor exit flow.

3. Of the 0.4% debit in efficiency in the generic shroud configuration, roughly 50% is generated in tip jet free expansion and the remainder generated in the mixing processes at the cavity exit. As the tip gap and cavity mass flow fraction increase, the fraction of total loss generated in the free expansion loss decreases while the fraction associated with the exit mixing loss correspondingly increases. For the 1.8x tip gap case, the mixing loss constitutes $\sim 62\%$ of the total loss with the free expansion comprising the remaining 38%.

4. The free expansion losses roughly scale according to Equation 2.4, depending on cavity mass flow fraction, rotor exit Mach at the tip, stage loading based on rotor tip velocity, tip flow coefficient, and stage stagnation pressure ratio.

A more rigorous control volume model results in Equation 2.2 but requires *a priori* knowledge of cavity inlet stagnation properties and swirl.

5. The mixing losses may be approximated by Zlatinov's expansion of the Young-Wilcock model or Equation 2.8. The former depends on the sum of the squares in the differences of velocity components, the static temperature at mixing, and the mass flow rates involved. The latter expression depends on the mass flow rates, the square of the difference in velocity magnitudes, the product of velocities at which mixing occurs, and the relative angle between the mixing streams. Difference in swirl parameter, Sw, between mixing streams is generally a good choice in design parameter to serve as a surrogate for the relative flow angle.

6. There are two competing processes setting the loss level in the generic tip shroud configuration, namely the mixing between the tip seal leakage flow and injected sealing flow, and the subsequent mixing between the cavity exit flow and main flow. As the injecting sealing mass flow rate increases, the first mixing process generates more loss. However, the average circumferential momentum exiting the cavity decreases, thus decreasing the loss generated when mixing with the main flow. The competition between these mixing processes is highlighted in a representative case in which enough circumferential momentum was injected with the sealing flow to reduce the disparity at the cavity exit to 0. The hypothesis held that the reduction in mixing loss at the exit would dominate over the increased mixing loss in the cavity for a net gain in efficiency. Instead, the mixing loss between the tip seal leakage flow and injected sealing flow exceeded the reduction at the exit, leading to an overall loss in efficiency.

Chapter 3

Effects of Nozzle Guide Vane-Rotor Interaction on Tip Shroud Cavity Flow

Building on the insights into the primary loss mechanisms in the tip shroud cavity flow field gained in the previous chapter, this chapter expands the analysis to include the effects of the interaction between the nozzle guide vane and rotor potential field. For the cases presented in this chapter, the mixing plane has been removed so that the flow field entering the rotor is now spatially non-uniform in the circumferential direction and is rotating relative to the rotor blade. This chapter compares the loss levels of the steady and unsteady baseline and datum[1] cases to identify the influence of any interaction effects on the cavity loss levels. A slight increase in loss in the first mixing control volume, CV1, motivates a detailed analysis of the cavity inlet toroidal vortex and its associated flow field.

[1] "Datum" case refers to the generic shroud cavity with no injected sealing flow.

3.1 Influence of Interaction Effects on Datum Loss Levels

In order to determine if and how the interaction effects change the loss levels observed in Chapter 2, the research framework described in Section 1.4 is once again employed. This requires the comparison of 4 major cases:

1. Baseline, steady (mixing plane approximation)
2. Baseline, unsteady, time-averaged (no mixing plane approximation)
3. Generic Cavity, steady (mixing plane approximation)
4. Generic Cavity, unsteady, time-averaged (no mixing plane approximation)

For the discussions presented in this section, differences in loss generation are calculated between cases 2-4 and the steady baseline case, and then normalized to the difference in loss between cases 1 and 3 (i.e. the datum loss). For the two unsteady flow situations, the quoted loss is time-averaged according to Equations 1.4 and 1.5. The profiles of difference in loss for cases 2-4 are presented in Figure 3-1, and the contributions of loss for the individual subdomains in each case are summarized in Figure 3-2. The blue arrows in Figure 3-2 indicate those regions with significant differences in loss generation. The losses generated in the Cavity and CV2 regions (which contain significant losses under the steady mixing plane approximation) were examined in detail in Chapter 2. This chapter instead focuses on the additional 0.1% which appears in the region CV1 when accounting for the effects of unsteadiness.

Figure 3-1 indicates that the total loss through the stage for the baseline unsteady case is the same as that for the steady case. The loss that is generated instantaneously at the mixing plane under the steady flow approximation is instead distributed throughout the various subdomains so that the overall difference is zero. The time-averaged unsteady cavity case shows an increase in loss of 9.4% of the steady cavity case, which equates to an increase in lost efficiency of $\sim 0.04\%$. As per

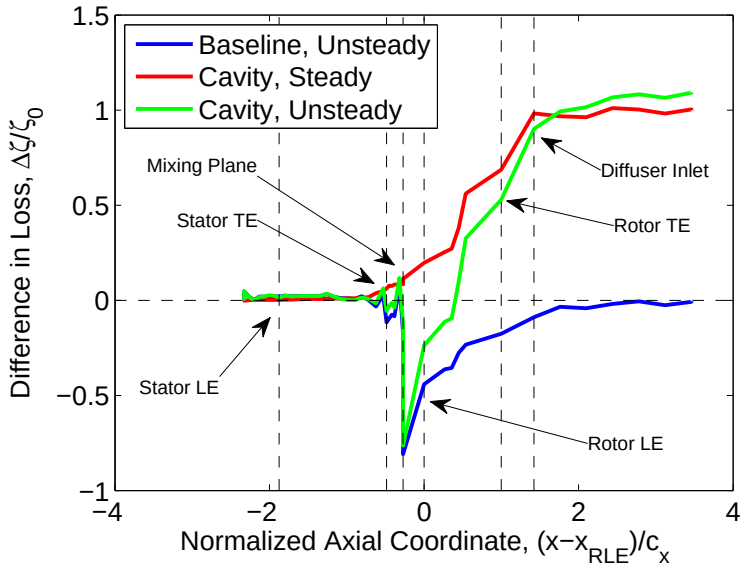

Figure 3-1: Axial profile of the difference in loss accumulation between the steady baseline case and the other steady and unsteady major cases.

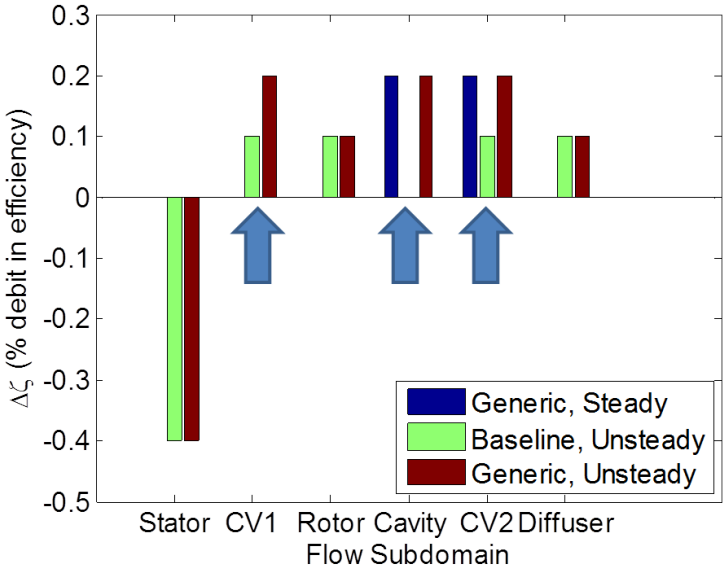

Figure 3-2: Breakdown of loss by subdomain for steady and unsteady major cases compared to the steady baseline case.

the discussion in Section 1.4, this difference is considered negligible, and the total debit in efficiency is rounded down to a value of 0.4% for the time-averaged unsteady cavity case. As a result, the presence of the cavity generates approximately the same amount of loss when using a mixing plane approximation as when time-averaging the time-accurate solution.

However, this rounding is somewhat misleading. Comparison of the profiles in Figure 3-1 shows definite differences between the steady and time-averaged unsteady cavity cases through the axial range spanned by the CV1, Rotor, Cavity, and CV2 subdomains. Due to the level of contribution to the overall loss in each of those subdomains, some losses are dampened by the rounding threshold defined in Section 1.4 (e.g. the mixing losses in CV2) while others are slightly exaggerated (e.g. the increase in losses over the time-averaged unsteady baseline in CV1). If the higher precision is preserved, then the effects of NGV-rotor interaction would generate an additional 0.08% debit in efficiency in the subdomain CV1 which is partially offset by a reduction in losses in CV2 of 0.04%. As the additional losses in CV1 are 4 times the estimated resolution described in Section 1.4 and much closer to the established reporting threshold of 0.1% change in loss, its origins will be the focus of the analysis in this chapter. While small in this case, linearly extrapolating the cavity inlet loss increase corresponds to an additional loss due to unsteadiness of 0.25% per every 1% of main flow ingested by the cavity. For low aspect ratio blading in which cavities are significant proportions of the span, cavity mass flow fractions of $1 - 2\%$ could reasonably be expected [8, 12, 13]. In addition, the same mechanism responsible for the increased cavity inlet loss also enhances a secondary flow feature in the main flow path. Thus this loss source could be significant in low aspect ratio stages and/or stages which are upstream of any following blade rows, and the aerodynamic mechanisms underlying this change deserve in-depth discussion.

3.2 Enhancement of the Cavity Inlet Toroidal Vortex

There are few flow features of interest within the control volume, CV1, which could explain this increase in loss due to the presence of the cavity. There are losses due to the boundary layers at the endwalls (essentially only the hub endwall as the shroud endwall is less than 10% of the axial length of CV1), but these are negligible due to the relatively short length of the control volume. In the absence of a mixing plane, some of the stator wake will mix out in this region. However, that mixing (i.e. mixing out of stator wakes) should occur in both the baseline and generic cavity cases. Thus, the only remaining flow feature is the cavity inlet toroidal vortex which occupies the entire cavity inlet region. Figure 3-3 compares the losses in the cavity upstream of the tip seal for the steady and time-averaged unsteady cases, demonstrating that a large part of the increase in loss when accounting for NGV-rotor interaction is localized in the cavity inlet region. This section will examine how the enhancement of the strength of this vortex leads to this increased loss, as well as how it affects secondary flows in the main flow path.

3.2.1 Increased Scrubbing Losses on Cavity Inlet Casing

Typically, increased circulation of a vortex will not necessarily result in increased rates of viscous entropy generation. Despite indications in the literature [13–15] and in this work (see Figure 2-2), loss is not directly related to the presence of vorticity but rather gradients in vorticity. This can be shown beginning with the equation for total viscous entropy generation rate given in [10]:

$$\dot{S} = m\dot{s} = -\int_V \frac{1}{T}\vec{v} \cdot \vec{F}_{visc} dV \tag{3.1}$$

Taking the integrand and substituting the expression for $\vec{F}_{visc}$ from the Navier-Stokes

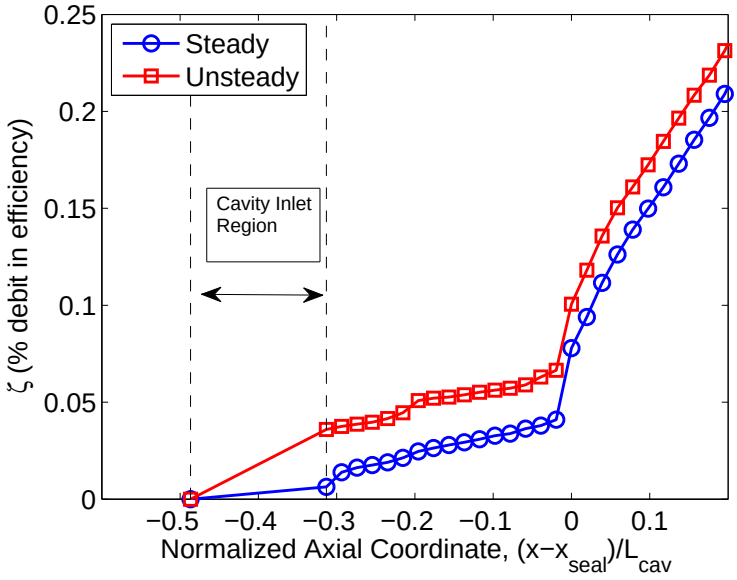

Figure 3-3: Comparison of axial accumulation of loss within the cavity for steady and time-averaged unsteady generic shrouds.

equation, it can be shown that the volumetric viscous entropy generation rate, $\dot{S}'''_{visc}$, can be written as:

$$\dot{S}'''_{visc} = \frac{\mu}{T}\vec{v} \cdot \left(\nabla \times \vec{\omega} - \frac{4}{3}\nabla \left(\nabla \cdot \vec{u} \right) \right), \tag{3.2}$$

The second term represents a compressibility correction which is typically only significant when shocks are present. Therefore, to leading order, the volumetric entropy generation is related to vorticity by:

$$\dot{S}'''_{visc} = \frac{\mu}{T}\vec{v} \cdot \left(\nabla \times \vec{\omega} \right) \tag{3.3}$$

Figure 3-4 compares contours of viscous entropy generation as calculated by Equations 1.8 and 3.2. The two contours qualitatively agree on regions of high viscous entropy generation, with Equation 3.2 over-estimating the magnitude of losses. At the same time, this equation highlights the flow features which are responsible for the viscous entropy generation, namely those regions where the sign of vorticity changes (e.g.

boundary layers along the outer casing, dividing streamlines between pairs of counter-rotating toroidal vortices, etc). Guided by this analysis, the search to identify the underlying cause of the increased loss in the cavity inlet region will focus on changes in these features.

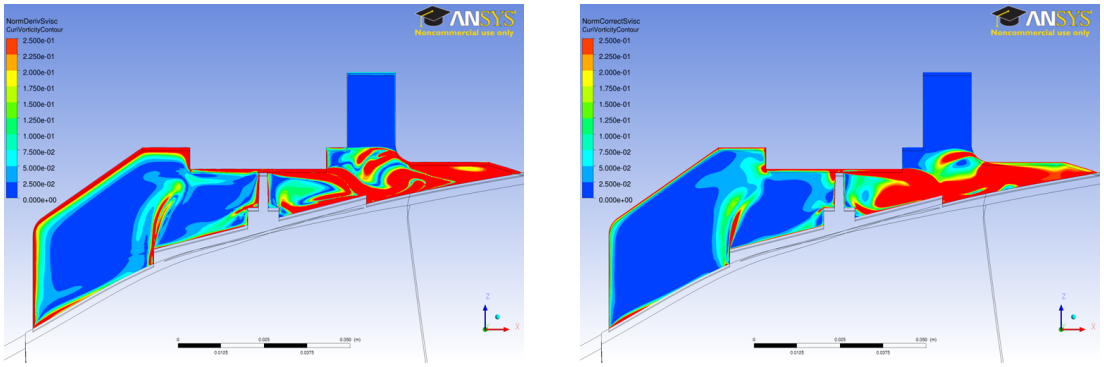

(a) Contour of volumetric viscous entropy generation as calculated by Equation 3.2.

(b) Contour of volumetric viscous entropy generation as calculated by Equation 1.8.

Figure 3-4: Contours comparing volumetric viscous entropy generation using two different calculation methods.

Since the changes are expected to be small, the best method for visualizing the differences in the flow fields of the steady and time-averaged unsteady cases is to plot the difference in the variable of interest rather than side-by-side visual comparison. Figure 3-5 uses this technique to plot the difference in circumferential vorticity in the tip shroud cavity. The difference is taken as *steady minus time-averaged unsteady* to highlight the change in the cavity inlet torodial vortex. Specifically, the inlet toroidal vortex should have negative circumferential vorticity (i.e. counter-clockwise swirl) as intuitively expected for a flow from left to right. However, Figure 3-5 shows the difference in the inlet toroidal vorticity is positive with clockwise swirl, implying that the time-average unsteady vortex has greater vorticity (and correspondingly greater circulation for vortices of similar size) compared to that under assumed steady flow. Quantitatively, the time-averaged unsteady inlet toroidal vortex has 11% more circulation than its steady counterpart. A similar enhancement of cavity inlet vortex strength was experimentally measured in Reference [16]. Pfau et al. attributed the enhancement to the unsteady pumping of the cavity inlet by the rotor pressure field

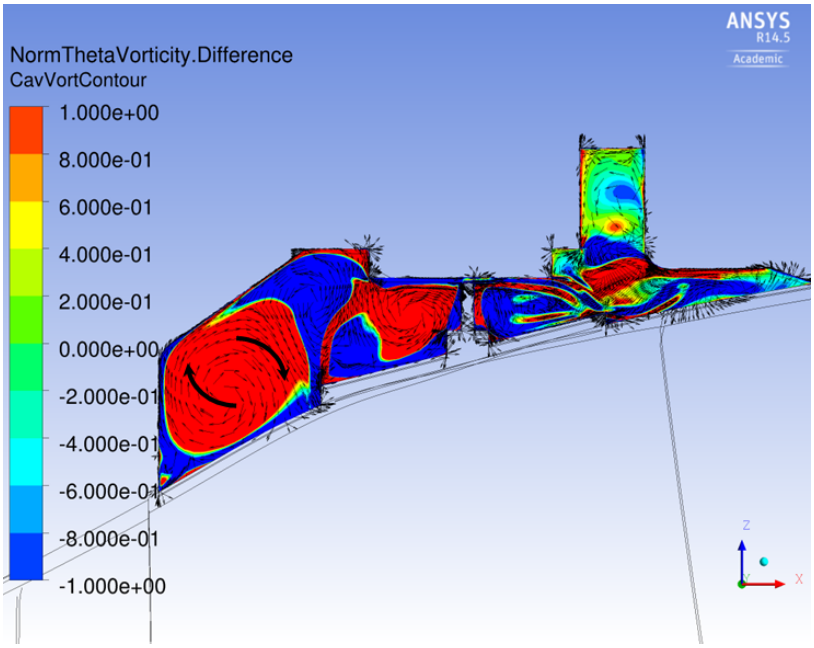

Figure 3-5: Contour of difference in circumferential vorticity between the steady and time-averaged unsteady generic shroud (steady minus time-averaged unsteady).

and tangential shear from the rotating tip shroud.

Circulation contained in a vortex is defined by the size of the vortex and either vorticity (when using core area) or local swirl velocity (when using core perimeter). This is expressed by:

$$\Gamma = \oint \vec{u} \cdot d\vec{l} = \int_A \vec{\omega} \cdot d\vec{A}, \tag{3.4}$$

Thus for two vortices of the same size but with different circulation, as in the comparison of the steady and time-averaged unsteady cavity inlet toroidal vortices, a larger average vorticity corresponds to a larger local swirl velocity. Near the stationary outer casing, an increased local swirl velocity begets increased shear stress and viscous dissipation along the wall; thus, based on the comparison in Figure 3-5, one would expect greater viscous dissipation in the casing boundary layer in the time-averaged unsteady case. Figure 3-5 supports this conclusion in that the regions of negative vorticity difference surrounding the core of the inlet toroidal vortex represent

differences in the rate of diffusion of vorticity from the stationary outer casing due to viscous shear forces. Typically, this vorticity would be of the positive sense; the fact the difference is negative implies that the time-averaged unsteady case has greater diffusion of vorticity from the stationary outer casing than the steady case, and thus higher viscous dissipation in the boundary layer. Plotting differences in volumetric viscous entropy generation rate, Figure 3-6 also demonstrates greater viscous dissipation in the time-averaged unsteady case. Once again, the difference is taken as steady minus time-averaged unsteady, so regions of higher loss in the unsteady case will register as a negative difference (blue) while positive differences (red) indicate regions in which the steady case has higher loss. Of particular note are the regions of negative difference along the stationary outer casing in the cavity inlet region, consistent with the argument of increased boundary layer dissipation outlined above.

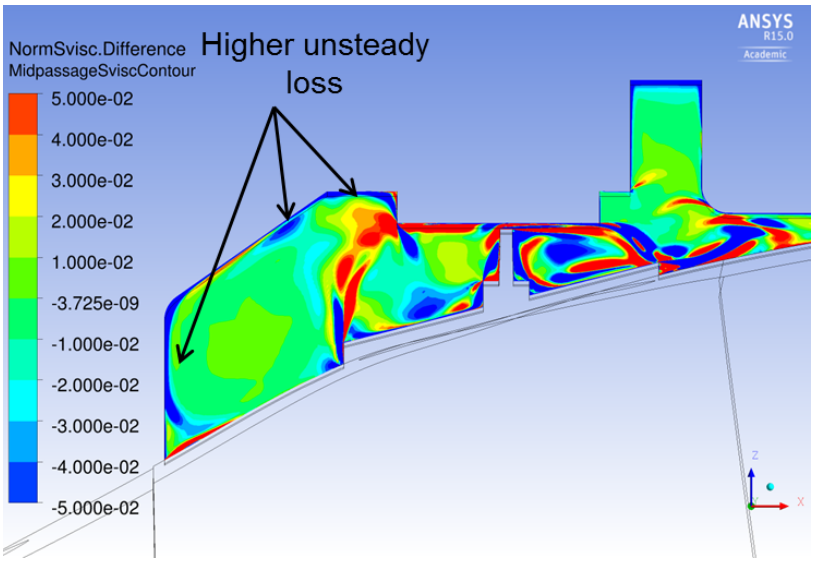

Figure 3-6: Contour of difference in volumetric viscous entropy generation rate between the steady and time-averaged unsteady generic shroud (steady minus time-averaged unsteady).

Equation 3.4 states that a vortex is characterized by its circulation, size, and either vorticity or local swirl velocity. The circulation associated with the inlet toroidal vortex originates from the boundary layer on the shroud casing upstream of the cavity inlet, and thus may be estimated as $\Gamma = u_E L_{shroud}$, where u_E is the freestream velocity just outside the boundary layer [20]. The magnitude of circulation is essentially

constant within each set of steady and unsteady cases, though the circulation in the steady cases is different from that in the unsteady cases. However, the difference in loss generation in the cavity inlet observed in the steady and time-averaged unsteady nominal tip gap cases is also observed when comparing some time-averaged unsteady tip gap cases (despite the constant circulation). This suggests that one of the other characteristics of the inlet toroidal vortex must vary between some cases. Further analysis reveals that this key quantity is the size of the cavity inlet toroidal vortex, which also affects the vorticity and local swirl velocity according to Equation 3.4.

Consider, for example, the set of cases in which the tip gap was varied, specifically the 1.8x nominal tip gap case (chosen to accentuate the flow field changes). As with the comparison between the steady and time-averaged unsteady cases of the nominal tip gap above, the difference in inlet toroidal vortex circulation between the 1.8x gap steady and time-averaged unsteady cases is approximately 10% of the steady circulation. Between the nominal and 1.8x time-averaged unsteady cases, the circulation of the inlet toroidal vortex varies by less than 2%. Yet, the loss in the cavity inlet region in the time-averaged unsteady 1.8x gap case shows a similar decrease compared to the time-averaged unsteady nominal gap as between the steady and time-averaged unsteady nominal gap cases (see Figure 3-7).

Applying the same analysis as used to compare the steady and time-averaged unsteady nominal tip gap cases, Figure 3-8 plots the difference in circumferential vorticity for the inlet toroidal vortex of the time-averaged unsteady nominal and 1.8x gap cases (taken as 1.8x gap minus the nominal gap). Again, the sense of vorticity and swirl velocity vectors in Figure 3-8 imply that the inlet toroidal vortex in the nominal gap case is stronger than the one in the 1.8x gap case. Consequently, the difference contour of $\dot{S}'''_{visc}$ in Figure 3-9 shows a similar reduction in boundary layer losses along the outer casing for the 1.8x gap case due to the lower swirling velocity of its inlet toroidal vortex near the wall.

It was previously stated that the circulation is essentially constant for the time-averaged unsteady nominal and 1.8x tip gap cases as it is determined by the vorticity diffusing from the casing upstream of the cavity inlet. It is the length of the contour

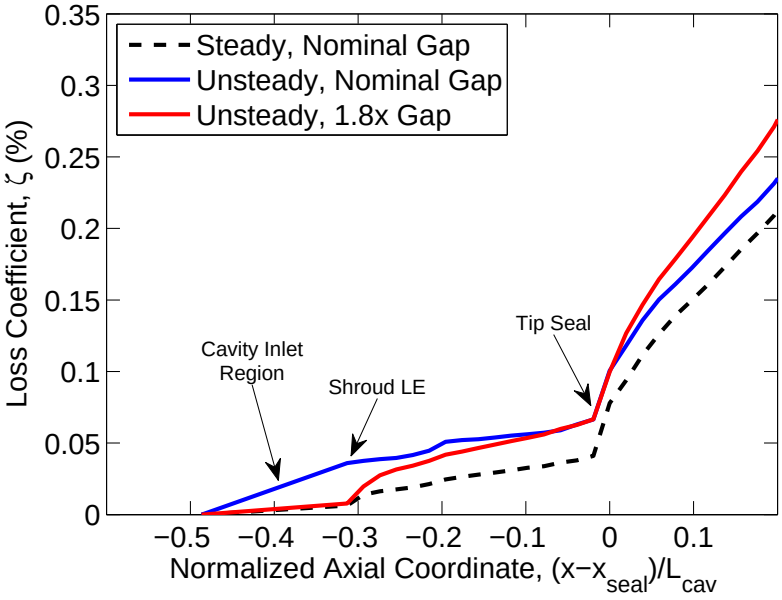

Figure 3-7: Time-averaged unsteady profiles of loss accumulation in the tip shroud cavity for nominal and 1.8x nominal tip gaps.

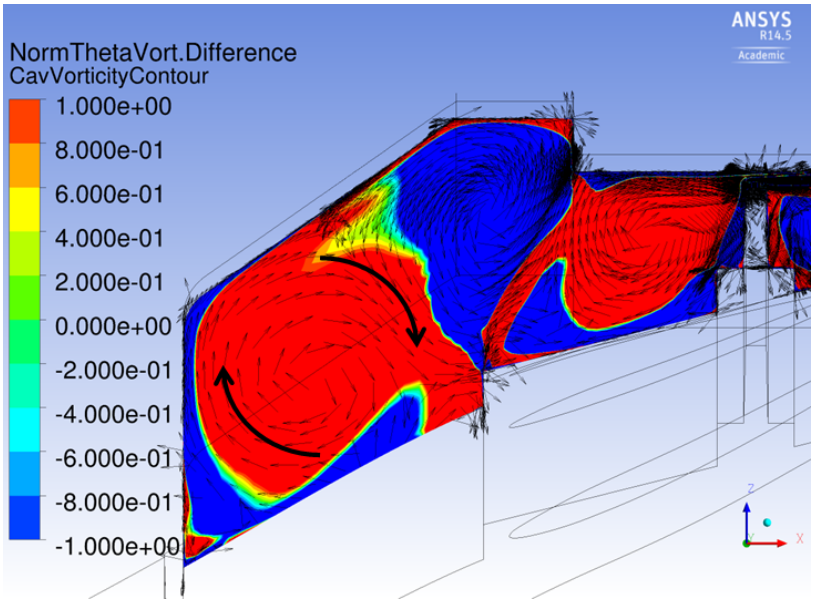

Figure 3-8: Contour of difference in circumferential vorticity between the 1.8x and nominal tip gap time-averaged unsteady cases (1.8x gap minus nominal gap).

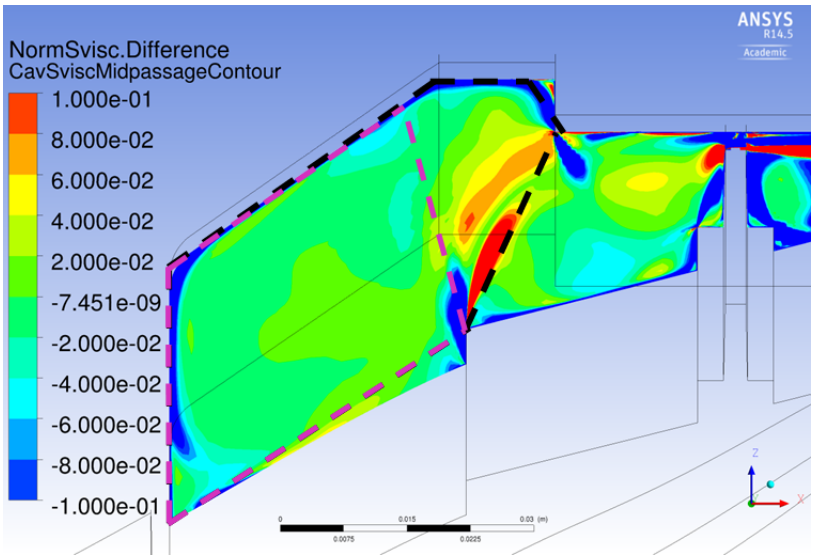

Figure 3-9: Contour of difference in volumetric viscous entropy generation rate between the 1.8x and nominal tip gap time-averaged unsteady cases (1.8x gap minus nominal gap).

bounding the inlet toroidal vortex (i.e. the size of the inlet toroidal vortex), rather than the vortex circulation, that changes significantly with tip gap variations. This is supported by the contour of the difference in volumetric entropy generation shown in Figure 3-9. The region of negative difference in loss emanating from the shroud leading edge marks the original trajectory of the dividing streamline between the inlet toroidal vortex and the opposing vortex immediately downstream in the nominal tip gap case. This trajectory is approximated by the magenta dashed line connecting the shroud leading edge with the casing. Similarly, the region of positive difference indicates the new trajectory of the dividing streamline in the 1.8x tip gap case (marked by the black dashed line emanating from the shroud leading edge). Based on the differences in trajectories of the dividing streamlines, the nominal tip gap case has a smaller contour than the 1.8x case.

For a fixed circulation, it follows from Equation 3.4 that a larger contour is accompanied by a smaller contour-aligned velocity, and thus decreased viscous losses along the stationary outer casing. This result also indicates that while circulation is important, variations in the cavity pressure field, induced by either geometric alterations as seen here or passing blades as in [17], may change the size of the vortex core.

Such a change will in turn alter the average vorticity and swirl velocity of the vortex. Therefore, a better correlation for viscous losses would be based on both contained circulation and size of the vortex core[2] as these determine the primary variable of interest: vortex local swirl velocity.

3.2.2 Cavity Inlet Mass Recirculation

Not only does the cavity inlet toroidal vortex set the loss generation in the cavity upstream of the tip seal, but it also controls a significant interaction between the cavity and main flow path. Specifically, not all of the fluid drawn into the cavity inlet region is passed over the tip seal. Some fraction will transit to neighboring blade passages by circulating around with the cavity inlet toroidal vortex, re-exit the cavity inlet region, and pass through the main flow path. This phenomenon, referred to in this thesis as cavity inlet mass recirculation or recirculating mass, contributes to shear layer losses at the interface between the cavity inlet and main flow path as well as potentially generating secondary flows in the rotor tip region. Since it occupies only $\sim 1-2\%$ of the blade span and involves only 0.1% of the main flow, any resultant secondary flows are not significant sources of loss in this configuration. However, these flow phenomena could have significant impacts on upstream turbine stages with greater cavity mass flow fractions and the following blade rows [13, 14, 16, 17].

Figure 3-10 depicts a representative case of recirculation for two flow passages of the steady nominal gap case. The contour marks levels of mass flux normalized by the average mass flux at the cavity inlet, along with velocity vectors projected normal to the cavity inlet interface. Red regions indicate positive mass flux (fluid flow into the cavity as indicated by the ingress arrow) while the blue regions mark regions of fluid egress. The spatial variation is correlated with the rotor potential field with maximum ingress/minimum egress aligned with the peak pressure of the pressure side and maximum egress/minimum ingress corresponding to the point of leading edge suction.

[2]The quotient of these two variables gives the average vorticity (if size is quantified by area) or average local swirl velocity (if size is based on perimeter) of the vortex core.

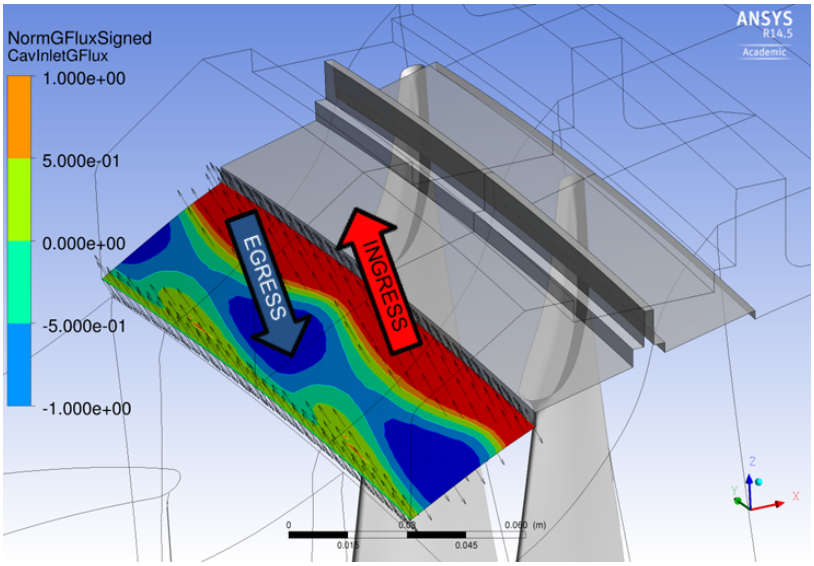

Figure 3-10: Contour plot of normalized mass flux at cavity inlet demonstrating definite regions of mass ingress and egress.

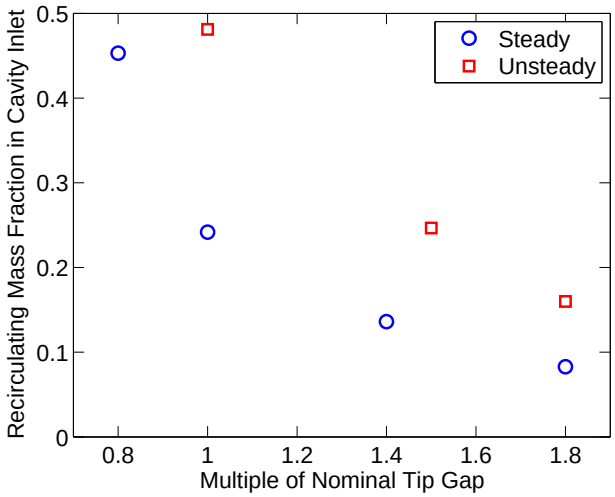

Figure 3-11: Fraction of mass flow which enters the cavity, circulates around the inlet toroidal vortex, and re-enters the main gas path at the rotor leading edge as a function of tip gap.

If changes in density of fluid entering the cavity are small from case to case, a change in circulation-induced velocity of the vortex would result in a qualitatively similar change in the recirculating mass flow rate. Figure 3-11 plots the recirculation fraction, defined as the fraction of the total mass entering the cavity which swirls around the cavity inlet region and exits back into the main gas path, as a function of tip gap for both the steady and unsteady cases. This recirculating mass fraction is calculated as one-half of the difference between the area integral of the absolute value of mass flux through the inlet surface and the net mass flow through the inlet, divided by the mass flow which enters the cavity. The recirculating mass fraction can thus be computed from:

$$\dot{m}_{f_{circ}} = \frac{\frac{1}{2}\int \rho \left(|\vec{v}\cdot\vec{n}| - \vec{v}\cdot\vec{n}\right) dA}{\dot{m}_{cav_{in}}} = \frac{\int \rho \left(|\vec{v}\cdot\vec{n}| - \vec{v}\cdot\vec{n}\right) dA}{\int \rho \left(|\vec{v}\cdot\vec{n}| + \vec{v}\cdot\vec{n}\right) dA}, \tag{3.5}$$

where $\dot{m}_{f_{circ}}$ is the recirculating mass fraction. The primary trend is that the recirculating fraction asymptotically decreases as the tip gap is increased (i.e. rate of change of recirculating mass fraction with tip gap size decreases for increasing tip gap). The second important implication is that unsteadiness exacerbates this recirculation effect on a time-averaged basis. For example, under the steady mixing plane approximation, the estimated recirculation fraction is 25% of the fluid entering the cavity (or $\sim 0.1\%$ of the main flow), while the more realistic unsteady calculation yields twice as much recirculating mass. Measurements in Reference [16] estimate an even higher time-averaged recirculating mass fraction of 75% of the fluid entering the cavity for the low aspect ratio test rig. Thus the computed recirculating mass flow fractions are reasonable based on observations in the literature.

Supporting the statement that cavity inlet vortex enhancement also enhances cavity inlet recirculating mass, the general correlation between vorticity of the cavity inlet toroidal vortex (analogous to circulation-induced velocity by Equation 3.4) and the recirculating mass flow rate is apparent in Figure 3-12. Specifically, increasing the average vorticity of the cavity inlet toroidal vortex results in an increase in the

recirculating mass fraction. The vorticity is normalized to an average estimate of the vorticity in the boundary layer on the casing upstream of the cavity inlet. It should also be noted that this plot quantitatively shows the increased average vorticity of the inlet toroidal vortex when accounting for NGV-rotor interaction.

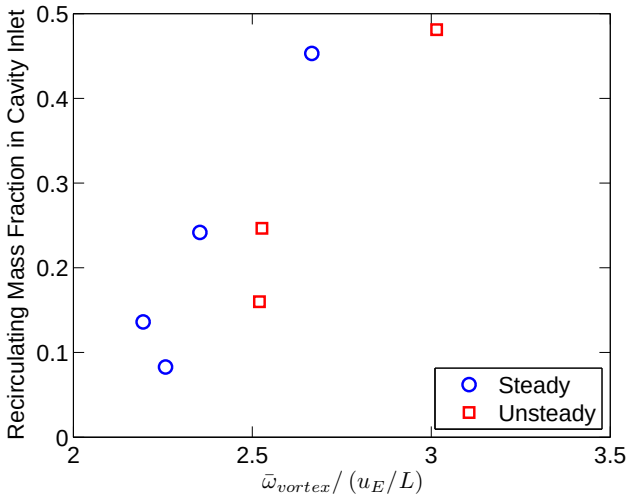

Figure 3-12: Variation of recirculating mass fraction in the cavity inlet as a function of the average vorticity of the inlet toroidal vortex.

While the recirculating mass fraction is an interesting phenomenon, this thesis is primarily concerned with its contributions to the primary figure of merit: loss generation. There are two potential avenues through which recirculation may affect stage loss: i) creation of a shear layer at the interface between inlet toroidal vortex and the main flow, and ii) generation of secondary flows such as a passage vortex in the rotor blade tip region. The first loss source is observed in Figure 2-2, which features a region of loss extending axially downstream at the interface between the cavity inlet and main flow path marking the shear layer between the inlet toroidal vortex and the main flow. Since this shear layer is essentially a mixing process, Equation 2.8 suggests that the strength of that shear layer should increase as the vortex circulation and the resulting mass recirculation also increase. Figure 3-13 demonstrates that this is indeed the case by again plotting the difference in normalized viscous entropy generation rate between the steady and time-averaged unsteady nominal tip gap cases. However, the region of interest has been expanded as compared to Figure 3-6 to include the main flow path and the limits of the scale broadened to emphasize the increase in shear

layer loss over the steady case. This increased shear layer loss, combined with the increasing boundary losses along the stationary outer casing in the cavity inlet region discussed in Section 3.2.1, account for the total difference in loss observed in the mixing region CV1 between the time-averaged unsteady baseline and generic shroud cases described in Section 3.1.

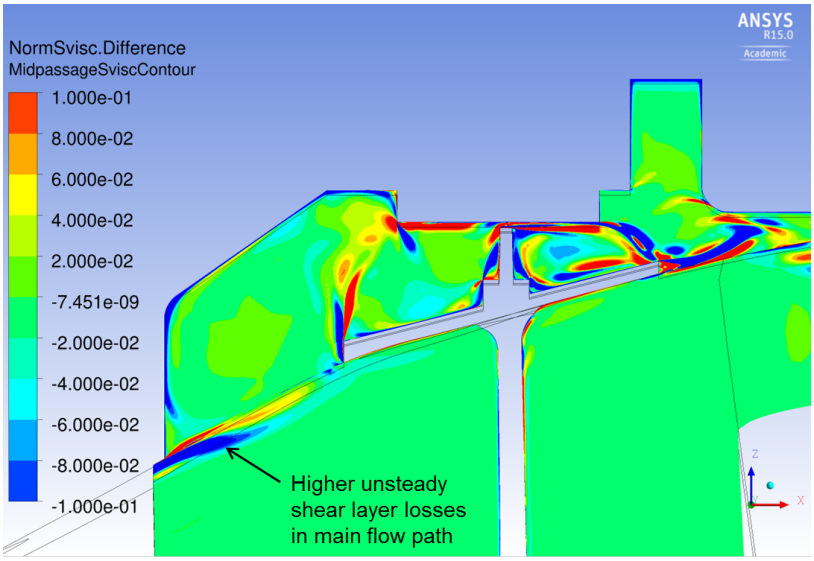

Figure 3-13: Contour of difference in volumetric viscous entropy generation between steady and time-averaged unsteady nominal tip gap cases (steady minus time-averaged unsteady) in both the cavity and main flow path.

The second potential loss source which arises due to cavity inlet mass recirculation (i.e. the generation of secondary flows within the rotor passage) is not a significant loss source in this configuration, as seen by the absence of significant loss difference through the rotor passage in Figure 3-13. However, this does not indicate these secondary flows are absent, only that their region of influence and involved mass flow fraction are so small as to not cause significant loss for this high aspect ratio stage. The mechanism of generation and transport should be assessed so as to generalize the findings to lower aspect ratio shrouded stages or those stages with downstream blade rows where these secondary flows may generate additional losses (e.g. [13, 14, 16, 17]). For example, the third turbine stage of large industrial gas turbines like the one upon which this generic fourth stage is based also typically employs a tip shroud

and is of lower aspect ratio. The secondary flows generated by this phenomenon in that configuration would convect downstream into this fourth stage, potentially with adverse interaction effects generating more loss.

Figure 3-14 compares the process of formation of the rotor tip passage vortex in the steady nominal and 1.8x gap cases. Viewed from upstream looking downstream towards the rotor, these contours plot mass flux on the cavity inlet (to mark recirculation) and contours of axial vorticity in the upper $\sim$ 20% of the main passage (a surrogate for streamwise vorticity which characterizes a passage vortex). Figures 3-14a and 3-14b show that the shear layer coincides with the regions of cavity inlet egress, where the mixing between the main flow and the recirculated cavity inlet flow generates axial vorticity. As the flow progresses downstream toward the rotor leading edge, the shear layer is convected towards the point of leading edge suction. Thus the streamlines begin to converge into a concentrated core (blue region in axial cut plane immediately upstream of rotor leading edge). However, due to the significant reduction in recirculating mass fraction in the 1.8x gap case which causes the majority of the shear layer to be re-ingested by the cavity, the 1.8x gap core is much smaller than its nominal gap counterpart (see Figures 3-14c and 3-14d). By the time this vortex core reaches the inlet of the rotor passage, a negligible fraction remains for the larger tip gap case (the vast majority having been re-ingested into the cavity) while a small but finite core still exists in the nominal tip gap case (evident by comparison of Figures 3-14e and 3-14f).

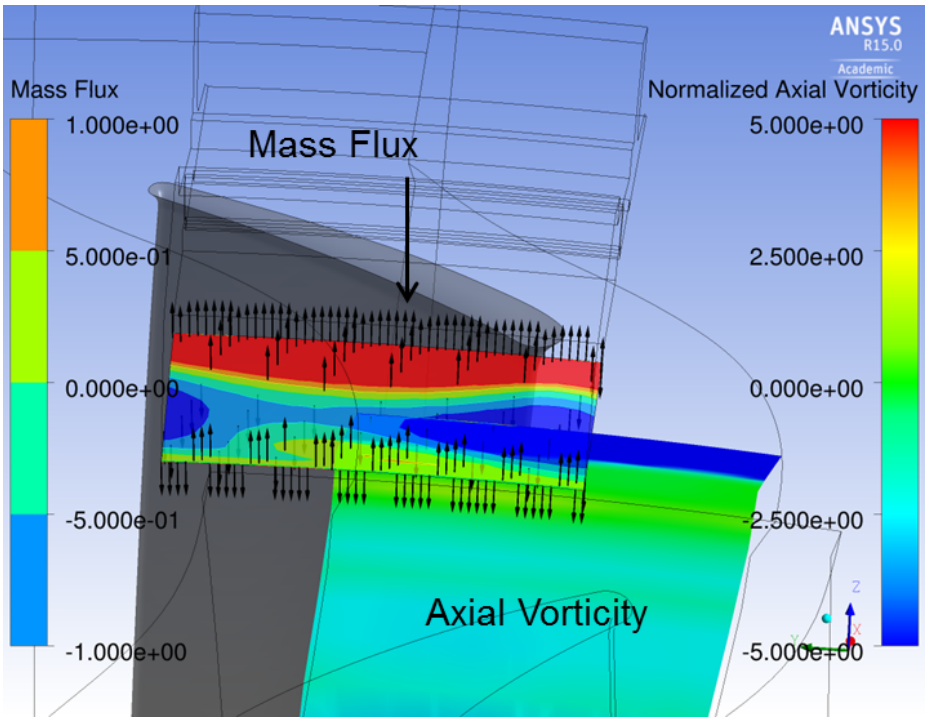

(a) Nominal gap

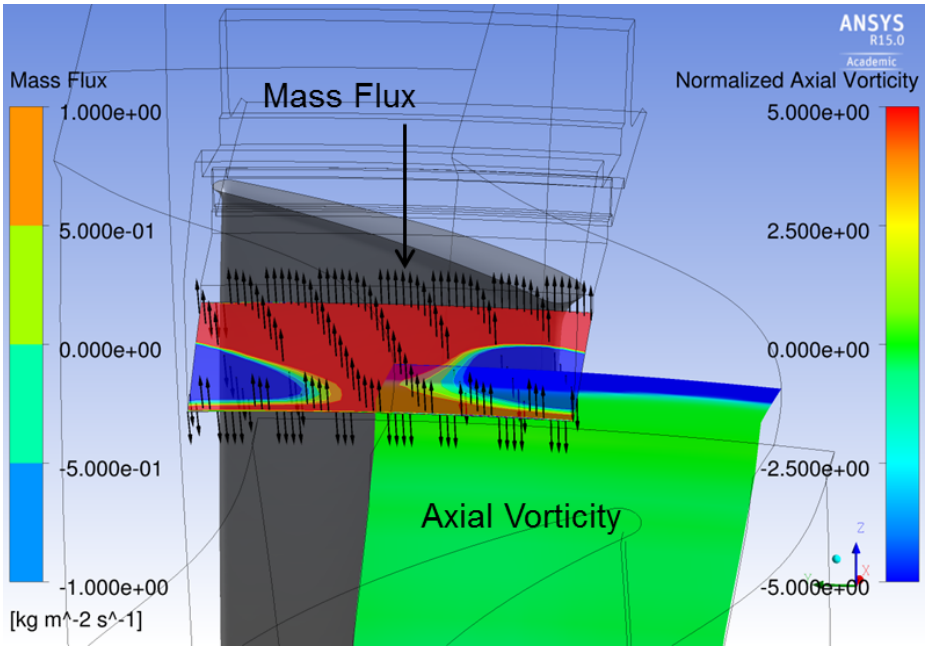

(b) 1.8x gap

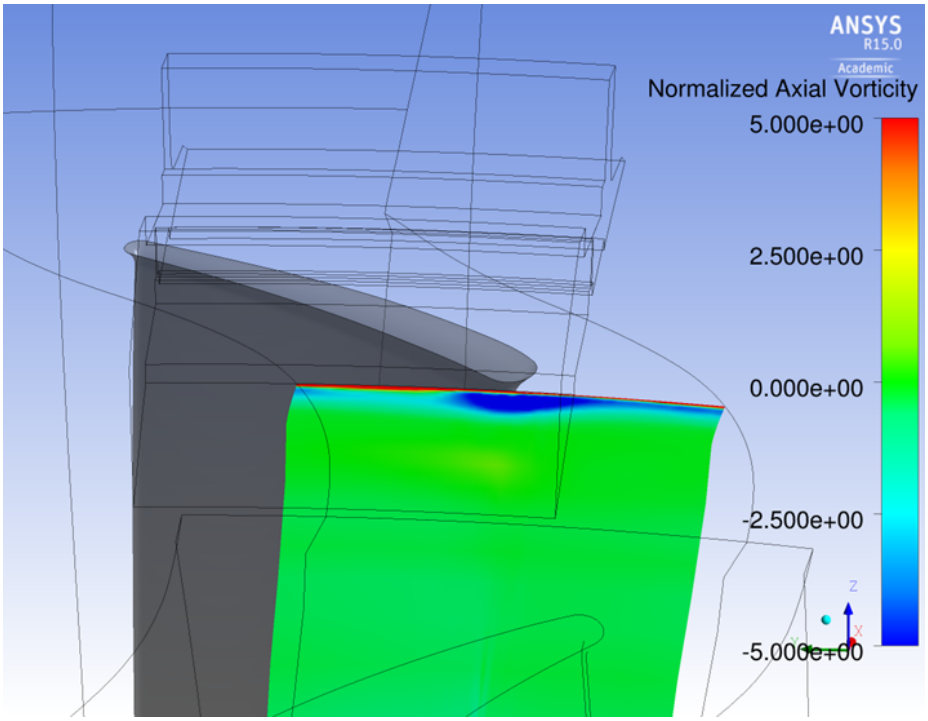

(c) Nominal gap

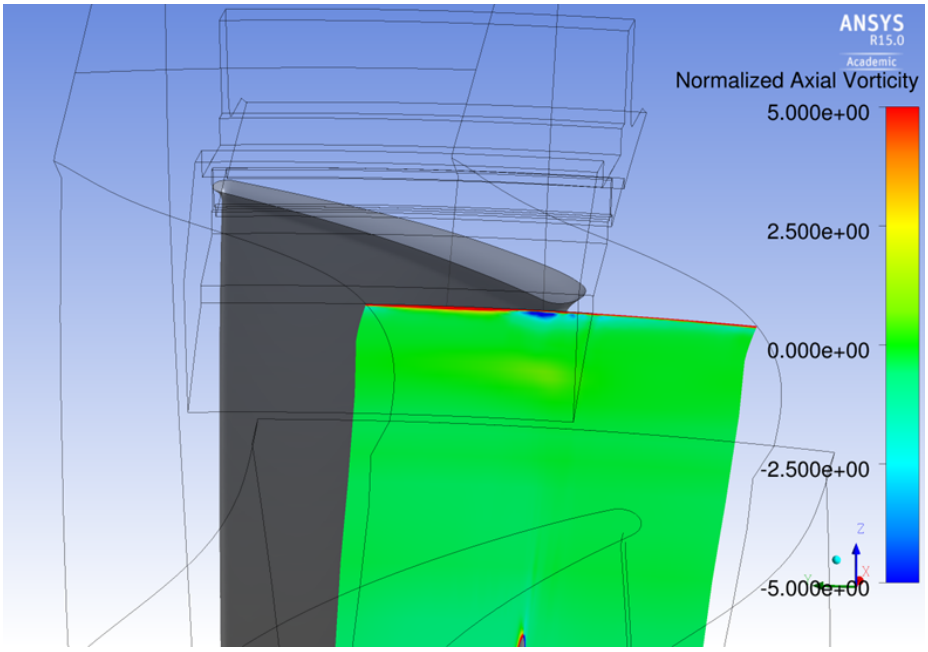

(d) 1.8x gap

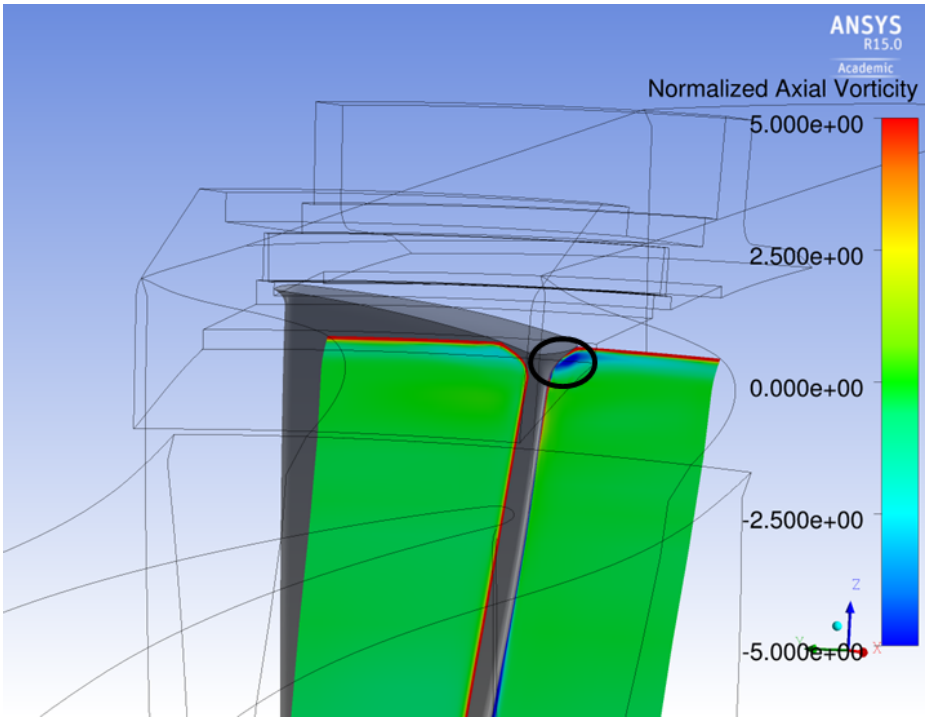

(e) Nominal gap

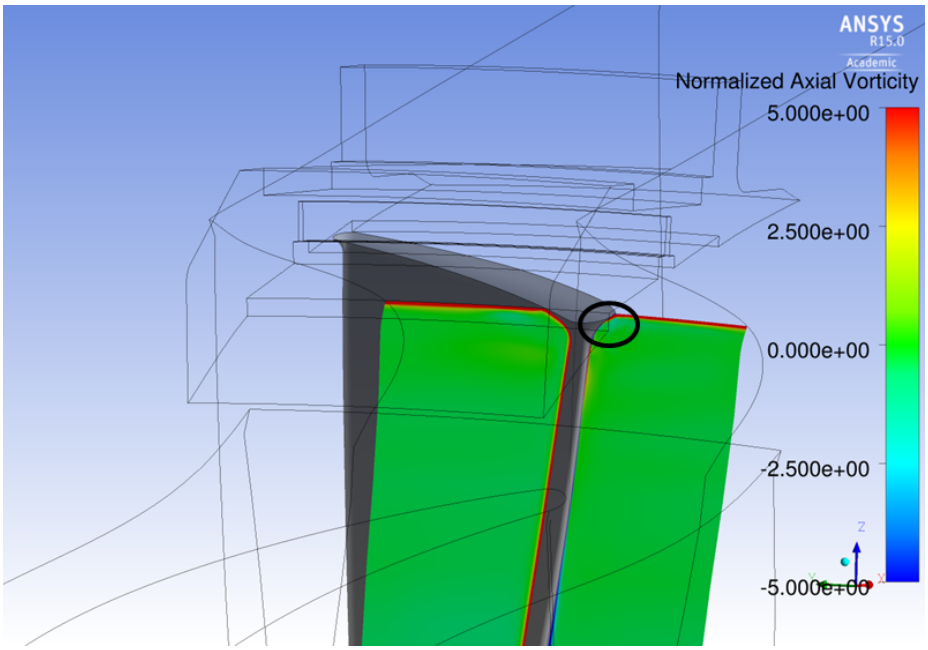

(f) 1.8x gap

Figure 3-14: Contours at several axial planes spanning the cavity inlet which demonstrate the process of rotor tip passage vortex formation due to cavity inlet mass recirculation.

3.2.3 Mass Recirculation Effects on Component Durability

Mass recirculation not only has aerodynamic implications for the turbine tip shroud cavity flow path, but also implications for component durability as the recirculated mass tends to increase impingement heat transfer on the blade tip. The most severe limiting case of this effect occurs during operational transients which cause contact between outer casing and the tip seal, thus preventing leakage flow through the cavity. There are known blade failures that have been observed just below the shroud due to such operational excursions (personal communication with Siemens Energy, Jan. 30, 2014). The underlying mechanism leading to this class of failure is the topic of this section.

To determine a plausible failure mechanism in such an operational excursion, computations were performed on a variation of the generic shroud configuration in which the tip seal gap was eliminated completely. As a result, the cavity inlet and exit regions became separate cavities open only to the main flow path at a single interface. Since peak blade temperatures occur at stagnation points, the cavity inlet is of primary interest as it is upstream with respect to the blade leading edge stagnation point. Figure 3-15 plots the normalized static temperature distribution on the blade surface for the case with no tip gap. The blade leading edge at the tip, just beneath the shroud, features a hot streak which also follows the tip passage vortex shown in Figure 3-14, known to originate from mass recirculation at the cavity inlet. Such a correlation between increased heat load and the impingement of induced flow from vortices containing high temperature fluid on a blade surface is consistent with previous findings in literature for other geometries [28].

Also shown in Figure 3-15 are the inlet toroidal vortex system (marked by vectors) and the vorticity of the cavity inlet toroidal vortex. Recall from Section 3.2.2 that higher recirculating mass flow rates are associated with changes in the main flow field in the tip region. In the case with eliminated tip gap, all of the fluid ingested by the cavity inlet must be returned to the main flow path. However, while it is extracted from a range of spanwise locations, findings to be presented in Section 4.2.2 (namely,

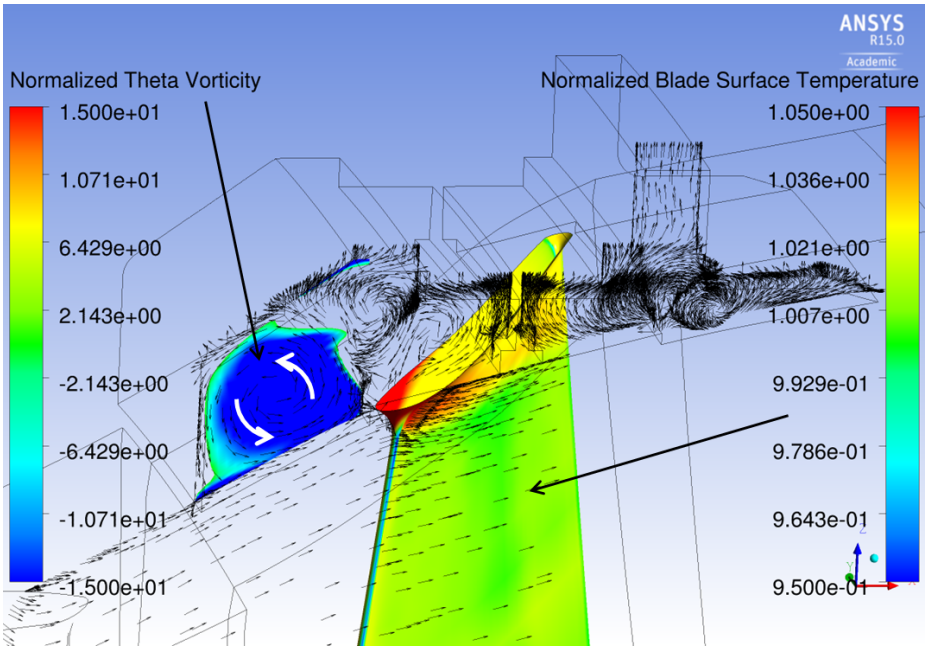

Figure 3-15: Contour of blade surface temperature (normalized to the temperature area-averaged over the blade surface) with cavity inlet toroidal vorticity and inlet toroidal vortex system.

Figure 4-9) suggest the recirculated mass is focused at a specific spanwise location just below the blade tip. This focused impingement on the blade leading edge creates a hot streak with peak temperature increase of 3.75% compared to the area-averaged blade wall temperature in the nominal tip gap case, as demonstrated in the difference contour in Figure 3-16. As evident in Figure 3-16, the only significant temperature increase on the blade is within this hot streak.

The location of the computed temperature increase in Figure 3-16 coincides precisely with the location of component failure observed in operational engines. However, the magnitude of the temperature rise appears insufficient to cause immediate failure of the blade. A 3.75% increase relative to a temperature well below the melting point would only lead to such immediate catastrophic failure if components were already designed for continuous operation at the very edge of material tolerances. This, instead, suggests a delayed failure mode such as fatigue (where cyclic forcing is provided by the time-dependent pressure field due to stator passing relative to the rotor) or growth of shear and bending stresses exerted by the rubbing of the tip seal

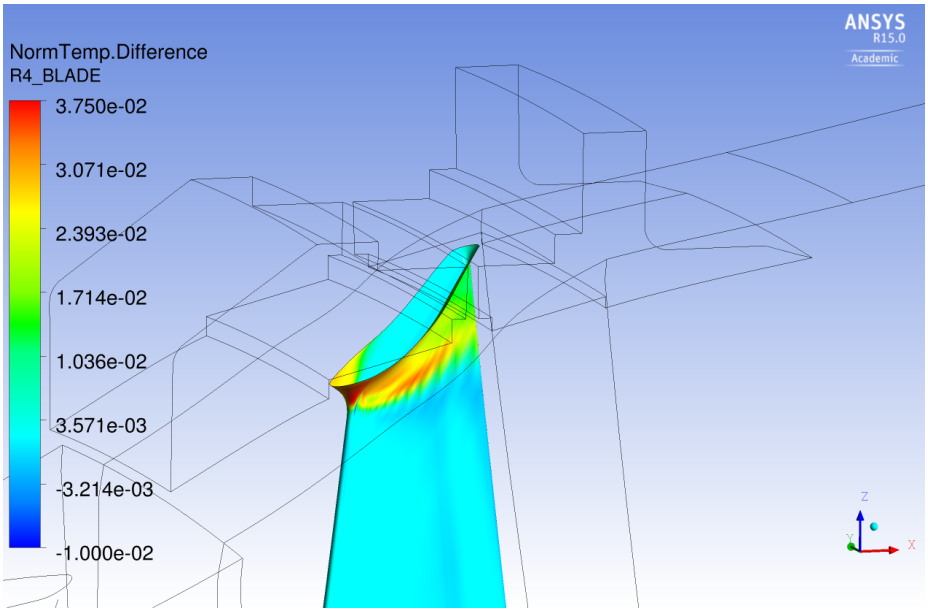

Figure 3-16: Contour of difference in blade surface temperature (no tip gap minus nominal tip gap) as percentage of the temperature area-averaged over the blade in the nominal tip gap case.

against the outer casing[3]. In either case, the expected time delay between onset of the responsible transient (i.e. sealing of the tip seal gap) and component failure affords an opportunity to mitigate the failure and improve blade resilience to such an operational excursion.

Based on the results of the computational model of a case with no tip gap, there are two possible solutions to prevent such operational excursions from damaging the rotor blades. The first and most obvious is to prevent the tip seal from sealing due to radial growth. For simple seals, cleverly designed abradable inserts, similar to those already in use but designed to abrade in such a way as to create small flow passages over the tip seal, could maintain even a slight clearance between seal and casing in the event of contact. Alternatively, a seal geometry which cannot completely isolate

[3]The time-delay inherent in fatigue failures is well-known. However, the growth of shear and bending stresses is more subtle. The temperature increase generated by the impingement on the blade tip will also increase internal stresses associated with thermal strain. The blade temperature will require time to equilibrate with the increased thermal load of the impingement heating, meaning these increased internal stresses must build over a period of time. Since the outer radius of the tip seal is fixed by the outer casing, the increased thermal stresses must be opposed by an equal and opposite normal force exerted by the outer casing in the radial direction. The shear force exerted by the outer casing on the tip seal (which also provides the bending moment around the point just below the shroud) depends on the magnitude of the normal force, so it also must increase over the same finite time interval.

cavity inlet and exit would also mitigate the strong recirculation responsible for the flow impingement and the attendant thermal issue at the leading edge. The Hybrid Blade design proposed in Chapter 4 is one such design. In the event of an excursion creating contact between the bladelet tips and outer casing, the bladelet passages would still remain open, allowing leakage flow to pass over the shroud. In addition, in the event of a failure, the anticipated stress concentrations lead to the expectation of a bladelet failure rather than a failure of the main blade. Even then, a bladelet failure can be avoided by making the bladelets slightly shorter than the tip seal of the intershroud bride, thus ensuring the first component to rub the casing is the more robust seal. While a bladelet failure may still require replacement of the entire blade, it would not be as potentially disruptive as the observed failure below the tip shroud. For those blades that do fail below the tip shroud, they may continue operating but at the risk of exciting aeromechanical modes which had been previously damped by the circumferential shroud (should an operational transient trigger an excursion into such a mode). In the Hybrid Blade case, however, the failure of a bladelet would not disrupt this critical function of the shroud.

The second option for addressing thermal loading increases due to closure of the tip gap relies on instrumentation of the outer casing to detect the onset of the offending transient. Presumably the rubbing of the tip seal against the outer casing during one of these events would lead to a measurable change in the casing. For example, the sealing of the tip gap should force a redistribution of the inlet toroidal vortex system to account for the blockage of the seal. Another possibility would be a modification to the frequency content and amplitudes of the outer casing vibrations as the tip seal rubs along its interior face. Due to the aforementioned anticipated time delay between the onset of the transient and the critical failure, there may be enough time to throttle the engine and allow the blade to return to a nominal separation. Of these solutions, the Hybrid Blade design is perhaps the most promising as the immunity to these impingement temperature loads advantageously accompanies the main purpose of increasing aerodynamic efficiency.

3.2.4 Generalization of Cavity Inlet Vortex Behavior

3.2.4.1 Mechanism of Cavity Inlet Vortex Configuration Change

The preceding sections have focused on the effects of variations in the cavity inlet toroidal vortex in terms of loss and impacts on the main flow. What remains is to explain what physical mechanism(s) act upon the inlet toroidal vortex to induce these changes. Currently the exact mechanism leading to greater circulation for unsteady cases compared to steady cases has not been quantified[4]. However, this section will present a hypothesis of how the vortex boundary contour (and thus vorticity for a given circulation) changes which is supported by the present computations as well as the results presented in [14, 17][5].

Since fluid flows directly follow from the pressure field, the most likely mechanism is a modification of the pressure distribution in the cavity. More specifically, streamline curvature, which sets the bounding contours shown in Figure 3-9, is directly related to local pressure gradients. Therefore, based on the variable seal gap calculations, alterations to the cavity geometry are expected to redistribute the pressure field within the cavity. In [14, 17], this alteration was achieved by changing the volume of the cavity inlet with the leading edge insert, thus changing the permitted size and shape of the cavity inlet toroidal vortex. In the results presented in this thesis, a similar effect was achieved through the geometric alteration of the tip seal gap. Figures 3-17a and 3-17b compare the pressure fields within the cavity upstream of the tip seal for the nominal and 1.8x tip gaps, respectively. The dividing streamline between the cavity inlet vortex and downstream toroidal vortices is highlighted in each figure by the white arrow overlaying the velocity vector field of the cavity flow field. The gradients in pressure level implied by the contours in Figures 3-17a and 3-17b clearly demonstrate how the attendant change in pressure field yields a

[4]Computations show a slightly larger freestream velocity, u_E, at the blade tip in the time-averaged unsteady case. This is likely due to a pumping effect of the rotor pressure field on the cavity, but the relationship is yet to be mathematically described.

[5]Both papers are from the same group. The first focuses on the effects of the cavity geometry changes while the second goes into greater detail about the unsteady flow features of the geometric modifications

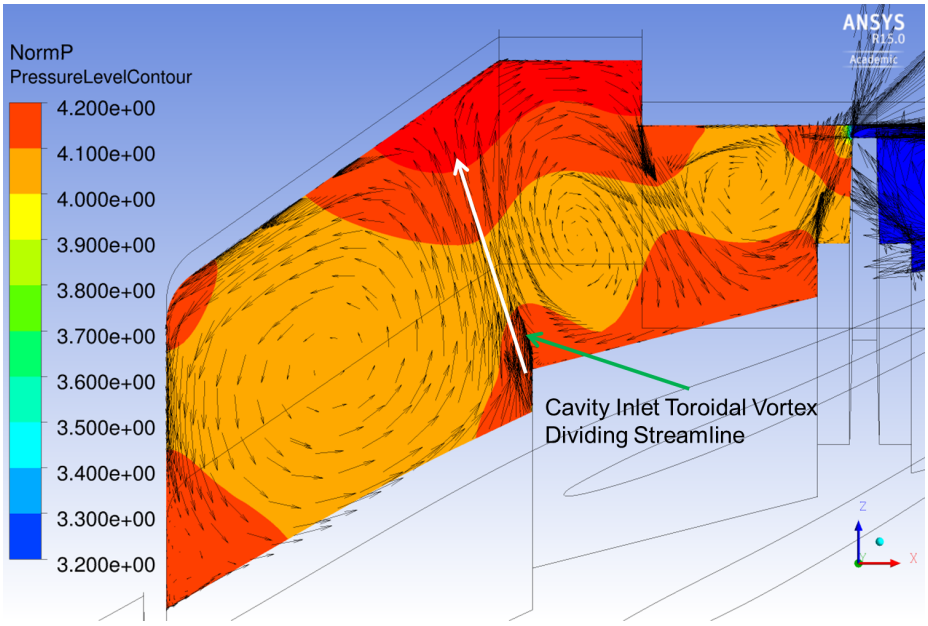

(a) Nominal tip gap.

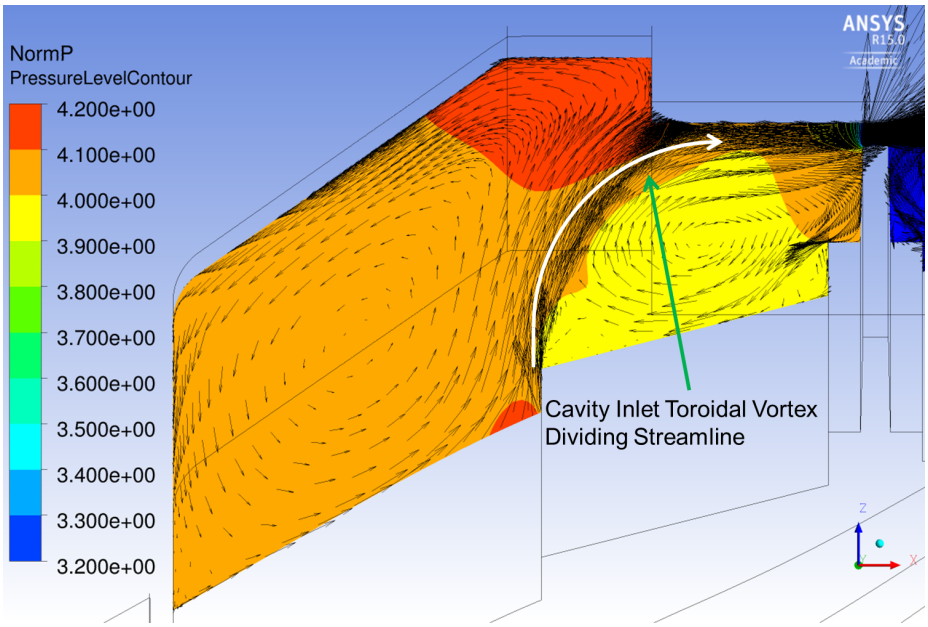

(b) 1.8x tip gap.

Figure 3-17: Contours of time-averaged static pressure normalized to stage inlet time-averaged dynamic head for the nominal and 1.8x tip gap cases.

downstream shift in the streamline for the 1.8x case.

This change in pressure field from the nominal to 1.8x tip gap case results from the increased effect of the larger low pressure region over the tip seal with the 1.8x tip gap. On an average basis, there is an unfavorable pressure gradient radially distributed from the shroud to end of the tip seal, tending to shift the dividing streamline upstream. On the other hand, since the tip seal is choked, the static pressure level is at its minimum level for the cavity domain; this level is also essentially constant from case to case. This creates a favorable pressure gradient in the same radial region as the tip gap tending to shift the streamline downstream. The larger the tip gap, the greater the range of radial values over which the favorable pressure gradient may act, and the further downstream the dividing streamline may shift.

The hypothesis on pressure field variation for control of inlet vortex bounding contour size was built on the results of the set of variable seal gap cases, but the off-design cases prove a useful test for the hypothesis as they also will affect the favorable pressure gradient, if only slightly. Based on the hypothesis, it is expected that the separating streamline of the over-expanded, lower back pressure case would have a more downstream trajectory than the design case because of the larger pressure ratio across the tip seal. The more downstream trajectory defines a larger inlet toroidal vortex size, which is in turn expected to yield weaker average inlet toroidal vorticity for a given circulation[6]. Similarly, the higher back pressure of the under-expanded case would create a less favorable pressure gradient at the tip gap, resulting in a more upstream streamline trajectory compared to the nominal case (i.e. smaller inlet toroidal vortex). This would in turn yield stronger average inlet toroidal vorticity for the same circulation. Figure 3-18 demonstrates the shift in dividing streamline trajectory by plotting a contour of the difference in volumetric viscous entropy generation rate between the lower and higher back pressure cases (lower back pressure case minus higher back pressure case). As in Figure 3-9, the difference in trajectory can be determined from the regions of positive or negative entropy generation rate

[6]As between the time-averaged unsteady variable tip gap cases, comparison of circulation of the inlet toroidal vortex between the two off-design back pressure cases reveals a variation of only 1.6%.

emanating from the shroud leading edge. The negative region indicates where the dividing streamline is for the higher back pressure case while positive indicates where it is for the lower back pressure case. The color-coordinated arrows approximate the tangent to the streamline at the tip of these loss regions. In the higher back pressure case, the dividing streamline is further upstream, while it is further downstream in the lower back pressure case. Thus, the contour is consistent with the expectations under the proposed hypothesis.

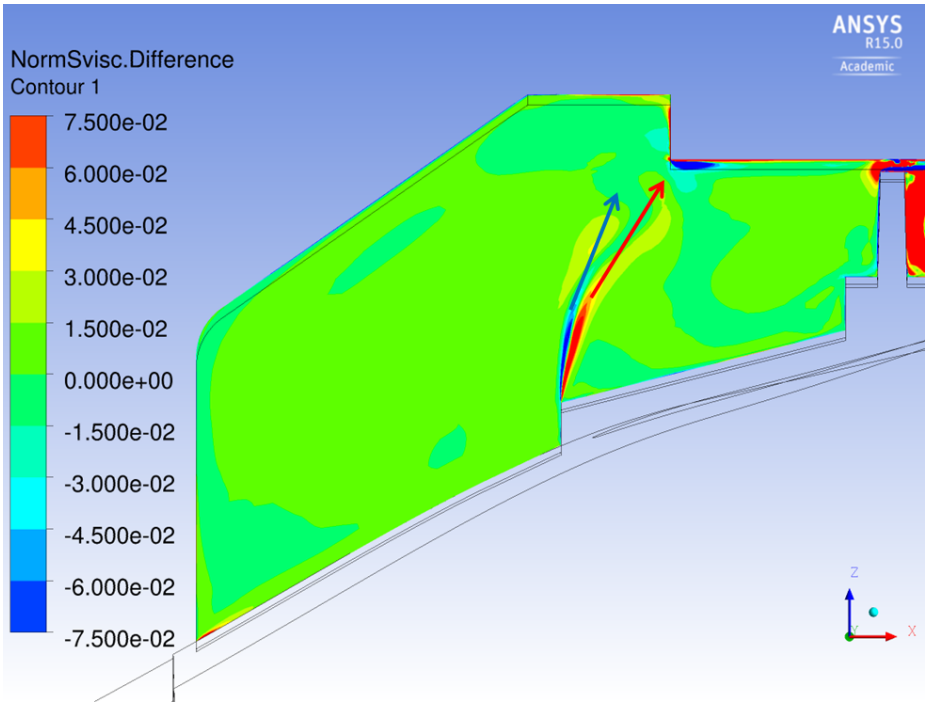

Figure 3-18: Difference in volumetric viscous entropy generation rate highlighting the difference between off-design back pressure cases in toroidal vortex dividing streamline trajectories. Difference is taken as lower back pressure case minus higher back pressure case.

The hypothesized attendant change in the cavity inlet vortex vorticity is expected to yield a weaker inlet toroidal vortex for the lower back pressure case. Figure 3-19, which plots the normalized circumferential vorticity of the lower back pressure case minus that of the higher back pressure case, demonstrates that the cavity inlet vortex core for the lower back pressure is indeed weaker. As was the case in Figures 3-5 and 3-8, the cavity inlet vortex should be of a negative sense with counter-clockwise swirl. Yet, Figure 3-19 shows a positive difference with clockwise swirl, indicating the

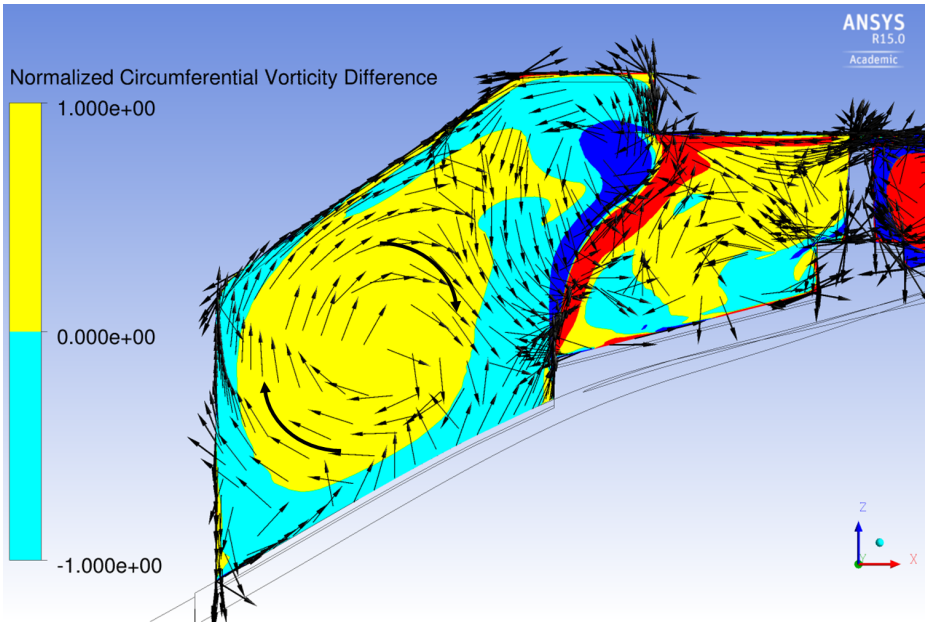

Figure 3-19: Difference in normalized circumferential vorticity within the cavity inlet for the off-design back pressure cases.Difference is taken as lower back pressure case minus higher back pressure case.

higher back pressure case has a cavity inlet vortex of greater strength. Again, this finding is consistent with the hypothesis regarding the influence of pressure gradients within the cavity inlet on cavity inlet vortex size and vorticity for a given circulation. Thus, understanding the kinematics of the cavity inlet toroidal vortex must take into account both its contained circulation (shed from the upstream casing boundary layer) and its size as determined by cavity geometry and tip seal back pressure.

3.2.4.2 Qualitative Design Guidelines for an Efficient Cavity Inlet Vortex

The results presented in this thesis along with those of [13, 14, 17] also suggest a qualitative guideline for the design of cavity inlets to minimize the impact of the inlet toroidal vortex on loss and mass recirculation. Whether by the axial restriction of cavity inlet dimensions in [13, 14, 17] or managing the dividing streamline trajectory, observations indicate changing the vortex core from a circular cross-section to an elliptical cross-section (with greater area) for a given circulation reduces the average local swirl velocity of the core. This, in turn, reduces both observed loss and mass

recirculation associated with the cavity inlet toroidal vortex by reducing its local swirl velocity.

References [14, 17] investigated three cavity sizes to determine their effects on machine performance. All three configurations featured radially elongated cavity inlet vortices (see Figure 10 of Reference [17]), so the investigation essentially represents an assessment of the effect of cavity inlet vortex elongation on performance. The configuration of peak efficiency investigated in References [14,17] featured an elliptical inlet toroidal vortex with major axis oriented in the radial direction and elongation, $\epsilon = \frac{b}{a}$, of approximately 2.7 (see Figures 10b and 10e of [17]). It was also on the verge of instability, demonstrating a bifurcation phenomenon due to the unsteady pressure associated with the interaction between stator wakes and rotor potential field. The datum configuration in [14, 17] featured a stable inlet toroidal vortex of elliptical cross-section also oriented in the radial direction, but with elongation of 2.25 (see Figures 10a and 10d in [17]). The third configuration tested and presented in [14, 17] would have had an elongation of 3.41 (see Figures 10c and 10f in [17]), but the cavity aspect ratio was too high to sustain an inlet toroidal vortex, resulting instead in a high loss jet. This would suggest that elongation should be pushed to the limit of stability, but only so long as toroidal vortices may still be sustained with ingress-egress jets avoided.

The present research supports this qualitative design guideline based on the variable tip gap results. Specifically, the cavity inlet vortex of the 1.8x tip gap configuration accumulated lower loss than its counterpart for the nominal tip gap as a result of core elongation. Unlike Referencens [14, 17], though, the major axis in the present configuration is oriented in both radial and axial directions. In addition, the cavity casing geometry (namely, the necessary clearances to allow for rotor movement) imposes additional restrictions on possible elongation compared to [14,17]. For example, the axial drift of the rotor in the present geometry requires a certain cavity inlet axial length to avoid rubbing between shroud and casing. Thus, simply decreasing the cavity inlet axial length to radially elongate the inlet toroidal vortex cross-section may not be a viable option and other solutions should be sought.

3.2.4.3 Operational Limits of the Cavity Inlet Toroidal Vortex

There are two foreseeable caveats to this guideline of elongation of the cavity inlet torodial vortex cross-section, however, to avoid inadvertently increasing the loss. First, a single, toroidal vortex core should be sustained based on the results presented in [14, 17] (though some degree of bifurcation may be permissible based on [14, 17]). The recommended elongation will depend on operating conditions of the turbine as flow velocities and pressure gradients both play a role in determining vortex core local radial equilibrium. However, an estimation of the limits of operation while maintaining a single toroidal vortex core is possible. Consider, for example, a swirling main flow with coexisting cavity inlet toroidal vortex as shown in Figure 3-20.

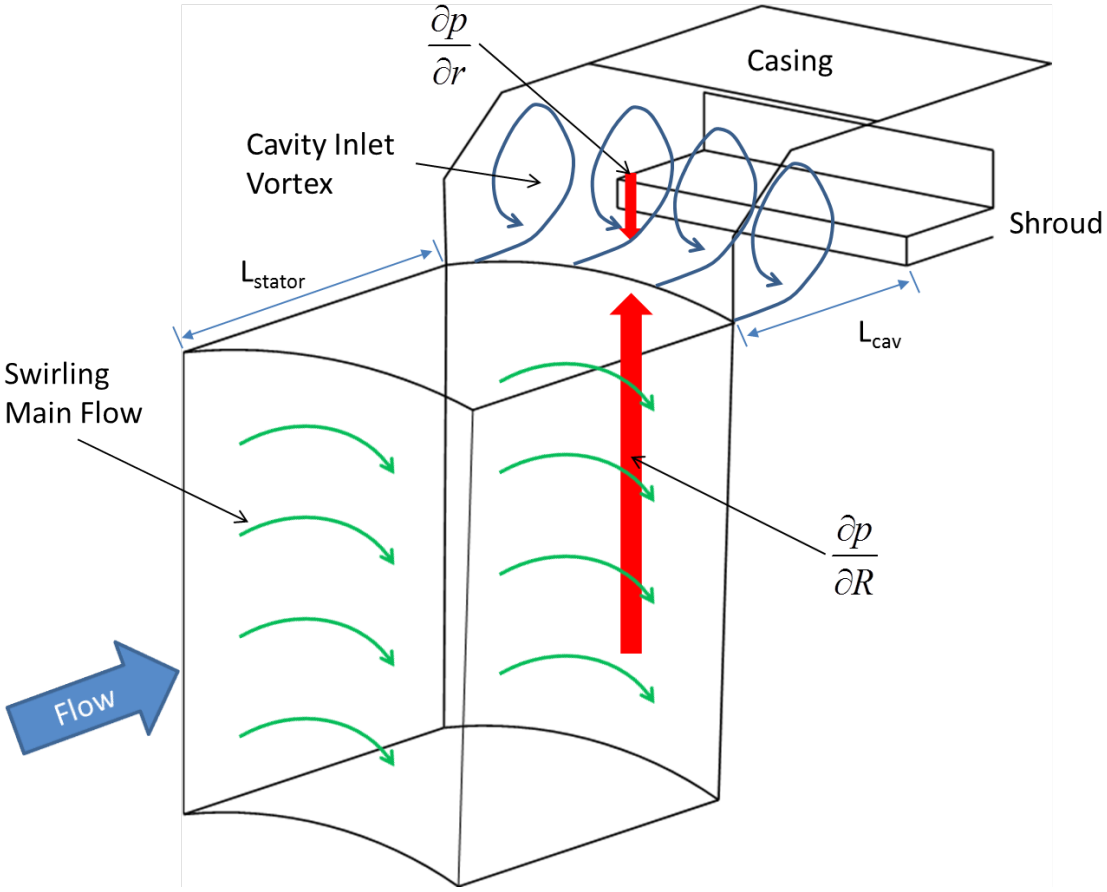

Figure 3-20: Schematic of coexisting main flow and cavity inlet toroidal vortex.

Both the main flow and the cavity inlet toroidal vortex have a swirling component which requires a local radial pressure gradient to provide the centripetal force

to maintain swirling flow. These pressure gradients are denoted by the red arrows in Figure 3-20 where $\frac{\partial p}{\partial r}$ is the local radial pressure gradient of the cavity inlet vortex and $\frac{\partial p}{\partial R}$ is the pressure gradient for the main swirling flow. Focusing on the interface between these two swirling flows, these radial pressure gradients exert forces opposite to each other. Therefore in order for the two flow structures to coexist, the two pressure gradients must be of similar order; if one dominates the other, its corresponding flow structure will also dominate the other. In other words, in order for the cavity inlet toroidal vortex to exist with a swirling main flow, its required local pressure gradient for its contained circulation must be comparable to the radial pressure gradient of the main flow.

In fact, the limits of the cavity inlet vortex existence may be further specified by considering the reaction of the dividing streamline to imbalances in these two radial pressure gradients. Consider first the case in which the local pressure gradient of the cavity inlet vortex, $\frac{\partial p}{\partial r}$, is greater than that of the main flow, $\frac{\partial p}{\partial R}$. The dividing streamsurface would tend to deflect upward to larger machine radii, but since this is desired for the formation of a cavity inlet toroidal vortex, it is not necessarily a limit. In the limit where the local pressure gradient is much greater than the main flow radial pressure gradient, however, the dividing streamsurface would tend to deflect upward with a much smaller radius of curvature. In essence, this would promote conditions conducive to the formation of a radial jet that then impinges on the stationary outer casing, leading to high loss, similar to the case observed in Figure 10c in [17]. On the other hand, if the local pressure gradient of the cavity inlet toroidal vortex is less than that of the swirling main flow, the cavity inlet vortex core would tend to redistribute its vorticity to ensure compatibility with the main flow pressure gradient. While the exact distribution is impossible to know *a priori*, the dividing streamsurface, near the upstream edge of the cavity inlet, should follow the same meridional angle as the outer casing. Simple force balance therefore implies the formation of a concentrated core near the upstream casing of the cavity inlet with local "radial" pressure gradient comparable to the main flow pressure gradient and a distribution of weaker vorticity throughout the rest of the cavity inlet region. This limit would be similar to the cases

of low edge pressure gradient resulting in core rapid area expansion and breakdown observed in References [29–31]. Thus the desired coexistence of the cavity inlet vortex and swirling main flow is favored when the local "radial" pressure gradient of the inlet toroidal vortex is greater than or equal to the radial pressure gradient of the main flow, but not exceedingly so (i.e. less than an order of magnitude greater). These limits are delineated below:

$$\text{Vortex exists: } \frac{\partial p}{\partial r} \geq \frac{\partial p}{\partial R}, \tag{3.6a}$$

$$\text{Large Expansion/Voriticty Redistribution: } \frac{\partial p}{\partial r} < \frac{\partial p}{\partial R}, \tag{3.6b}$$

$$\text{Radial Jet: } \frac{\partial p}{\partial r} \gg \frac{\partial p}{\partial R}, \tag{3.6c}$$

Equations 3.6 may be rewritten in terms of the swirl velocities and size of each swirling flow structure using radial equilibrium:

$$\frac{\partial p}{\partial r_c} = \frac{\rho u_\theta^2}{r_c}, \tag{3.7}$$

where u_θ is the swirl velocity of the vortex and r_c is the swirling flow radius of curvature. For a vortex of circular cross-section, the circulation of the vortex is related to the edge swirl velocity by the size of the vortex core according to Equation 3.8.

$$u_\theta = \frac{\Gamma}{2\pi r_c}, \tag{3.8}$$

where Γ is the contained circulation. The contained circulation originates in the boundary layer of the upstream vane casing as the cavity inlet toroidal vortex forms from the "rollup" of this boundary layer. The dependence of the local pressure gradient of the cavity inlet toroidal vortex on contained circulation supports the previously described vorticity distribution expected of the regime represented by Equation 3.6b. For a given shed circulation, the cavity inlet vortex core size, r_c, adjusts such that the local "radial" pressure gradient of the inlet toroidal vortex is comparable to that of the radial pressure gradient required in the main flow path. In the case characterized by Equation 3.6b which assumes a vortex size on the order of the cavity inlet axial length, a distribution which reduces r_c to increase $\frac{\partial p}{\partial r}$ is favored. This leads to a smaller, concentrated cavity inlet toroidal vortex near the cavity upstream casing.

The contained circulation may be estimated by $\Gamma = u_X L_{stator}$ according to [20], where u_X is the freestream axial velocity just outside the vane casing boundary layer, and L_{stator} is the axial length of the stator. Combining Equations 3.7, 3.8, and the estimation of Γ yields an alternative expression for the comparison of radial pressure gradients based on length scales and main flow swirl:

$$\frac{r_c}{R} \leq \frac{1}{4\pi^2} \frac{u_X^2}{u_\Theta^2} \left(\frac{L_{stator}}{r_c} \right)^2, \tag{3.9}$$

Since the cavity inlet axial length strongly determines the cavity inlet toroidal vortex size (as it fixes the cavity inlet vortex bounds), $r_c \approx L_{cav}$, where L_{cav} is the cavity inlet axial length scale. Equation 3.6 may then be rewritten in terms of characteristics of machine size and main flow swirl parameter, $Sw = \frac{u_\Theta}{u_X}$:

$$\text{Vortex exists: } \frac{L_{cav}}{R} \leq \frac{1}{4\pi^2} \frac{1}{Sw^2} \left(\frac{L_{stator}}{L_{cav}} \right)^2, \tag{3.10a}$$

$$\text{Large Expansion/Voriticty Redistribution: } \frac{L_{cav}}{R} > \frac{1}{4\pi^2} \frac{1}{Sw^2} \left(\frac{L_{stator}}{L_{cav}} \right)^2, \tag{3.10b}$$

$$\text{Radial Jet: } \frac{L_{cav}}{R} \ll \frac{1}{4\pi^2}\frac{1}{Sw^2}\left(\frac{L_{stator}}{L_{cav}}\right)^2, \tag{3.10c}$$

Value	Generic Shroud	Scalloped Shroud
L_{stator}/L_{cav}	7.14	4.35
Sw	2.34	2.35
L_{cav}/R	0.029	0.045
F	0.23	0.10

Table 3.1: Key ratios and results of Equation 3.10a for the steady generic and scalloped shroud configurations.

For simplicity and brevity in future comparisons, the right hand sides of Equation 3.10 will be denoted by F for the remainder of this section. Table 3.1 lists the relevant geometric and flow ratios for the steady generic shroud and scalloped shroud configurations with nominal tip gap and compares the resulting F with the corresponding L_{cav}/R in each case. As this analysis is focused on the interface between the main flow and cavity inlet toroidal vortex, fluid properties are evaluated at 99% span. Since the scalloped shroud case has a circumferentially varying cavity inlet axial length, the average inlet axial length is used for L_{cav}. For both cases, Equation 3.10a is satisfied, but the generic shroud has a significantly greater margin between F and L_{cav}/R compared to the scalloped shroud configuration. Specifically, F is nearly an order of magnitude greater than L_{cav}/R for the generic shroud configuration (but, critically, not quite, so that formation of a single core is still favored over a radial jet) while $F/(L_{cav}/R)$ is only ~ 2.3 for the scalloped shroud configuration. To confirm the coexistence of the swirling main flow and cavity inlet toroidal vortex, Figure 3-21 plots contours of normalized circumferential vorticity for the steady computations on generic and scalloped shrouds with nominal tip gap. In both contours, there is a single, circumferentially uniform inlet toroidal vortex core as represented by the negative circumferential vorticity in the cavity inlet region as expected based on Equation 3.10a.

While the steady scalloped shroud computation satisfies the limit posed in Equation 3.10a, its low $F/(L_{cav}/R)$ suggests that variations in swirl or L_{cav} may alter

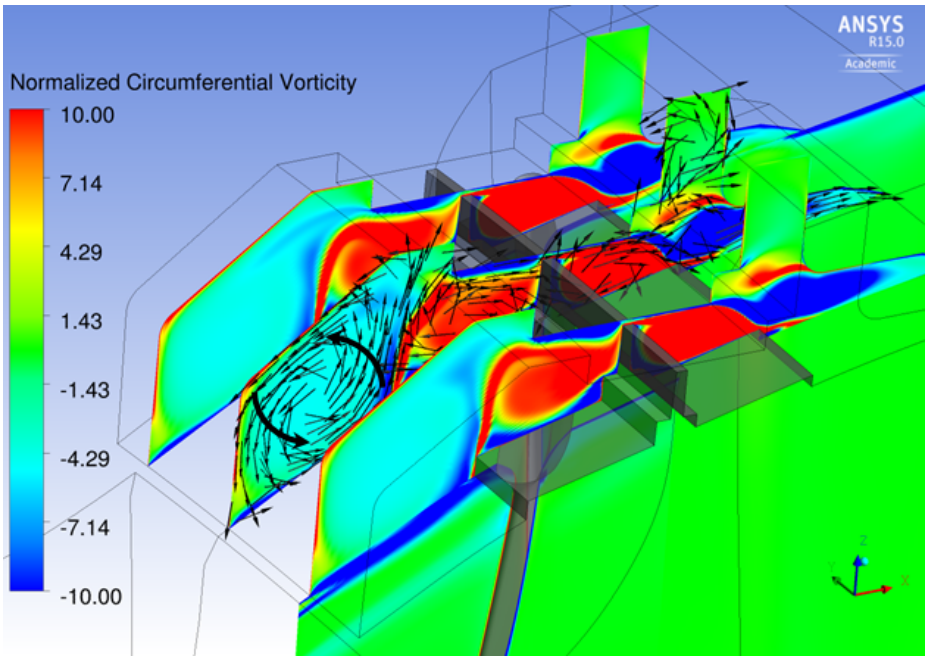

(a) Generic Shroud

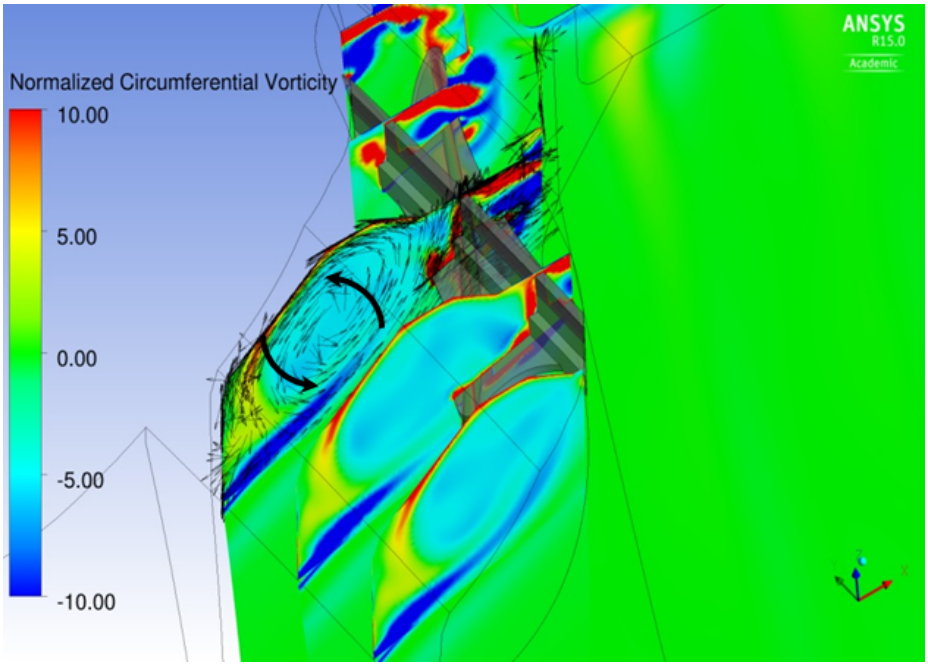

(b) Scalloped Shroud

Figure 3-21: Contours of normalized circumferential vorticity, $\omega_\theta/(v/c_x)$, in the tip shroud cavity inlet. Large region of negative vorticity (blue) represents the cavity inlet toroidal vortex.

the regime of operation of the inlet toroidal vortex. For example, higher swirl or a greater L_{cav} would tend to lower F, and in the case of greater L_{cav}, increase L_{cav}/R. By definition, the scalloped shroud cavity inlet axial length will increase above the average length used in Table 3.1. In addition, the presence of wakes induces pitchwise variation in the flow field [32] from the averaged value used in the steady computation comparison. Therefore, the unsteady scalloped shroud case would be the most likely to violate the limit described by Equation 3.10b.

The sensitivity of F to variations in the contributing values is found by taking the differential change in F:

$$\frac{dF}{F} = -2\left(\frac{du_\Theta}{u_\Theta} - \frac{du_X}{u_X} + \frac{dL_{cav}}{L_{cav}}\right), \tag{3.11}$$

The differential changes in velocities arise due to circumferential variation in flow properties and presence of wakes previously washed out by the mixing plane approximation in the steady case. Figure 3-22 shows several cross-sections of the tip shroud cavity flow at different circumferential locations with overlaid velocity vectors showing the circulating flow in the cavity inlet (not time-averaged). Upstream of the cavity, the contour in the stator domain highlights the regions of large variation in $\frac{du_\Theta}{u_\Theta} - \frac{du_X}{u_X}$ at 99% span. Table 3.2 lists the normalized change in F and local ratio of $F/(L_{cav}/R)$ for each of the three planes. The plane with the large single core, Plane 3, has the greatest $F/(L_{cav}/R)$ at ~ 2. Plane 1, which at this time has just past one of the stator wakes and is entering the stator passage freestream, has a distorted single core as well as a 10% lower $F/(L_{cav}/R)$ compared to Plane 3. However, the most interesting plane, Plane 2, displays a highly distorted core with redistributed vorticity. The local $F/(L_{cav}/R)$ for this plane has dropped below 1 due to the momentum deficit of the upstream stator wake and a larger local cavity inlet axial length. Thus, it does not satisfy the limit in Equation 3.10a and instead falls within the regime described by Equation 3.10b.

The other operational limit of the cavity inlet toroidal vortex, namely the radial

Plane	dF/F	$F/(L_{cav}/R)$
Plane 1	-0.12	1.79
Plane 2	-0.70	0.57
Plane 3	0.082	1.99

Table 3.2: Variation of sensitivity in F and $F/(L_{cav}/R)$ for cavity inlet vortex at several circumferential cuts.

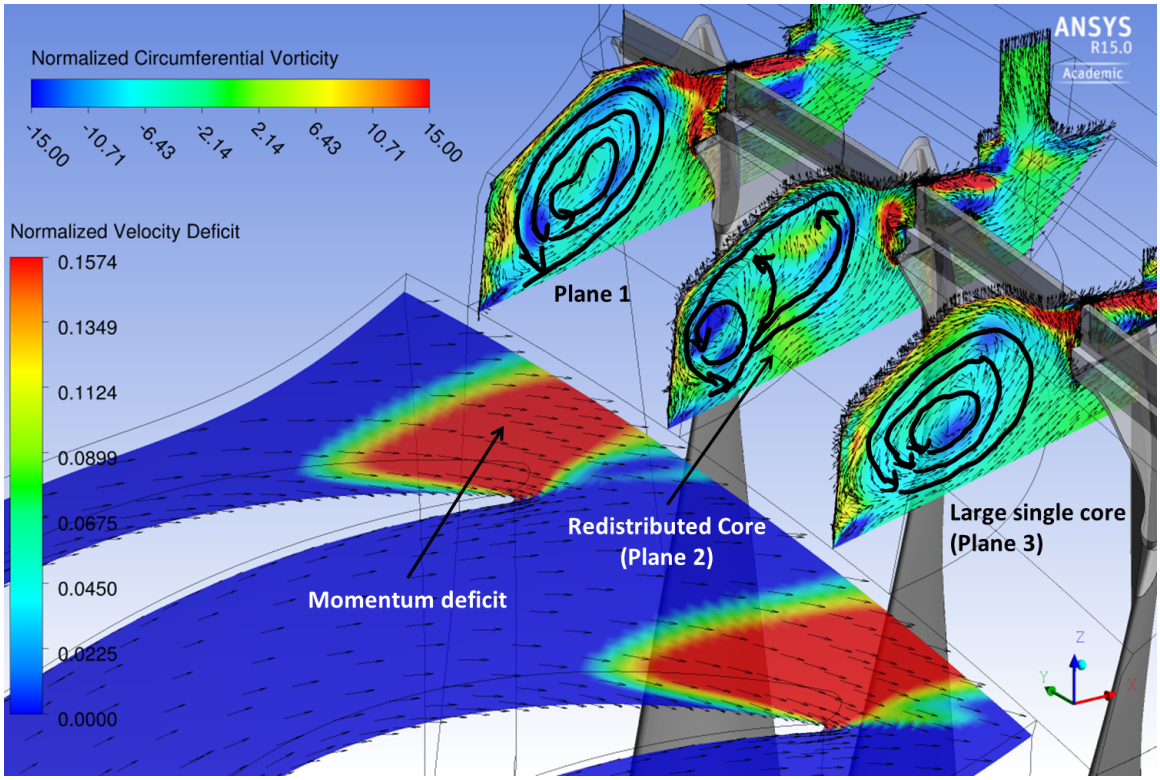

Figure 3-22: Instantaneous circumferential variation of cavity inlet vortex core cross-section and stator wake momentum deficit (99% span) for unsteady scalloped shroud configuration.

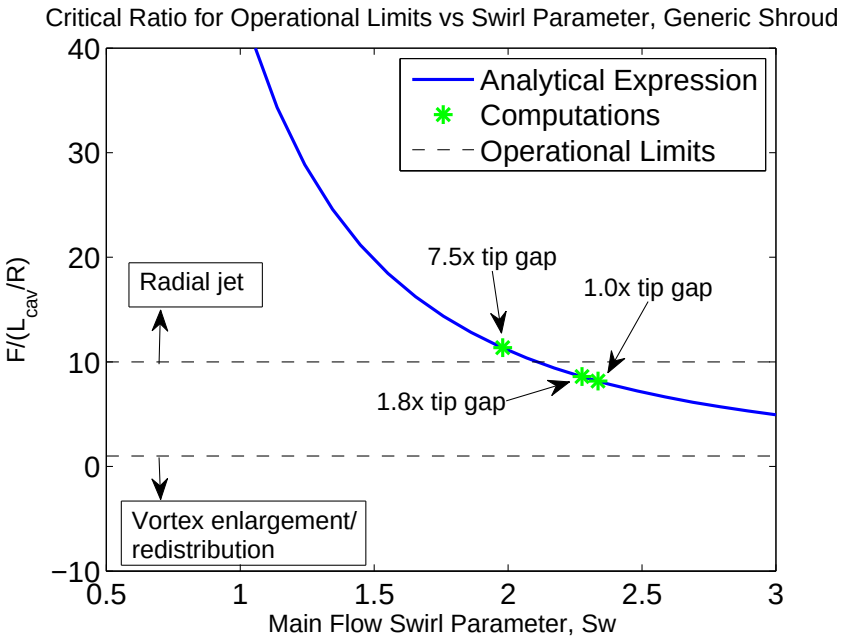

Figure 3-23: Comparison of hypothesized cavity inlet vortex radial jet limit with computational results.

jet limit, will be exceeded if the cavity inlet length and/or the swirl of the main flow are made too small. The latter case is demonstrated in the set of variable seal gap calculations described in Chapter 2. As the tip gap is increased, it affects the expansion of the flow through the stator in the tip region, thus changing the main flow swirl parameter and shed circulation from the stator casing boundary layer. For these configurations, the cavity inlet axial length is held constant, so the only variation is in the main flow swirl parameter. The variation in $F/(L_{cav}/R)$ based on the developed analytical expression is plotted against main flow swirl parameter in Figure 3-23. The horizontal dashed lines represent the limits expressed in Equation 3.10, where the radial jet limit is defined as $F/(L_{cav}/R) = 10$ and the vortex redistribution previously demonstrated for the unsteady scalloped shroud is defined as $F/(L_{cav}/R) = 1$. In between these limits, the cavity inlet vortex and swirling main flow are expected to coexist. The computational results of several variable tip gap cases are plotted on the line by green markers. As the tip gap increases, it induces a more favorable pressure gradient such that the flow in the tip region of the interblade space expands to greater axial velocities, decreasing the main flow swirl parameter. As a result, the markers

move along the line representing $F/(L_{cav}/R)$ from Equation 3.10c. For the largest tip gap (i.e. 7.5x the nominal design value), the swirl parameter in the main flow tip region has decreased enough to increase $F/(L_{cav}/R)$ above 10 which should result in a radial jet into the cavity.

Figure 3-24 plots contours of volumetric viscous entropy generation rate within the cavity inlet region for the variable tip gap cases shown in Figure 3-23 with overlaid velocity vectors. As the tip gap is increased, the cavity inlet toroidal vortex core size decreases, and the core moves into the upstream corner of the cavity inlet region. As the core is displaced, the streamtube of fluid entering the cavity widens to occupy more of the cavity inlet axial length until, in the 7.5x case, it occupies all of the cavity inlet. For this large tip gap, the streamtube entering the cavity becomes a radial-axial jet impinging on the stationary outer casing before turning downstream to pass through the large tip gap. Thus, the evolution of the flow field matches the expected flow field configuration based on Figure 3-23. Another important implication of Figure 3-24 is the significant increase in loss in the cavity inlet region as a single inlet toroidal vortex core gives way to a radial jet. This drastic increase in loss is consistent with the findings in [14, 17] for the configuration in which a radial jet was observed. For the cavity configurations shown in [14, 17], the cavity inlet axial length is decreased significantly, driving down L_{cav}/R and increasing F. Plugging in the values for R, L_{cav}, L_{stator}, and Sw[7] given in [17], $F/(L_{cav}/R)$ is estimated to be 10.1 for the case exhibiting a radial jet in the cavity inlet. For the maximum efficiency case which decreases L_{cav} but still maintains a single inlet toroidal vortex core, $F/(L_{cav}/R)$ is estimated as 5.1. Thus the trend observed in [14, 17] quantitatively agrees with the cavity inlet toroidal vortex operational limit described in Equation 3.10c and Figure 3-23.

[7]The paper states the casing boundary layer extends to 90% stator span. Using Figure 6b in [17], the angle at 90% span is used to estimate the main flow swirl parameter by the expression $Sw = \tan\alpha$.

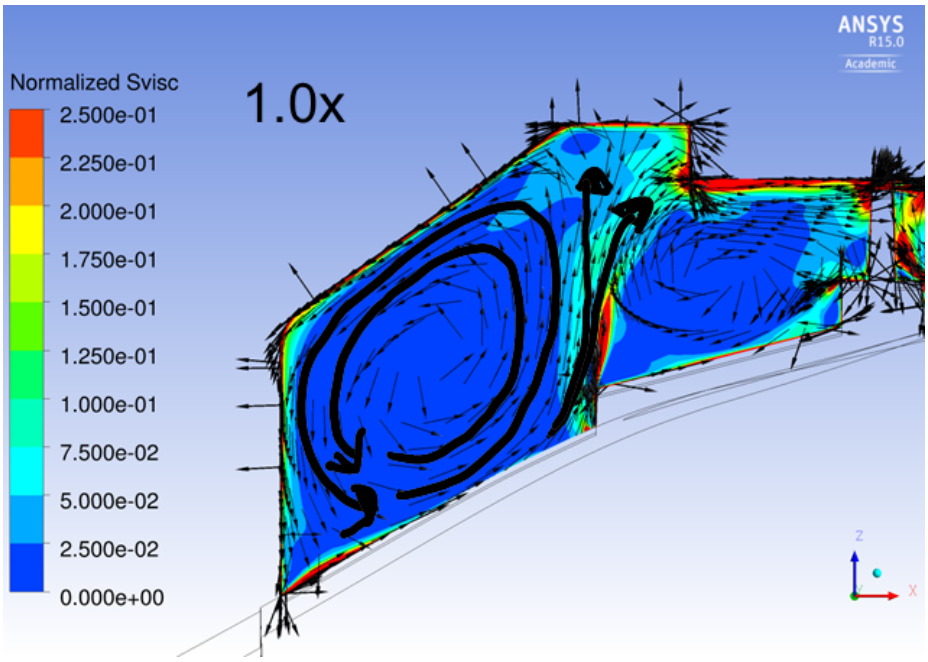

(a) Nominal gap

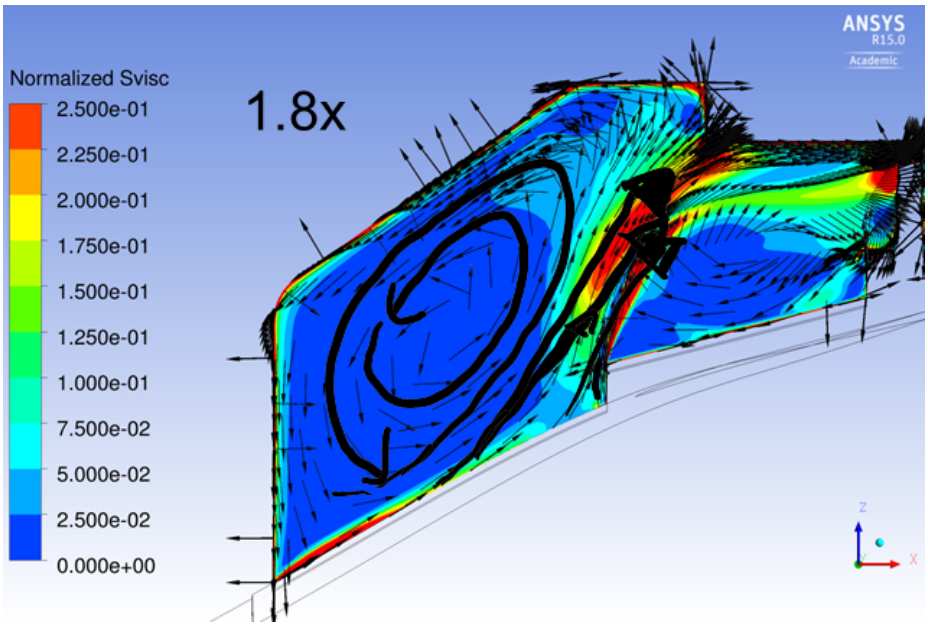

(b) 1.8x gap

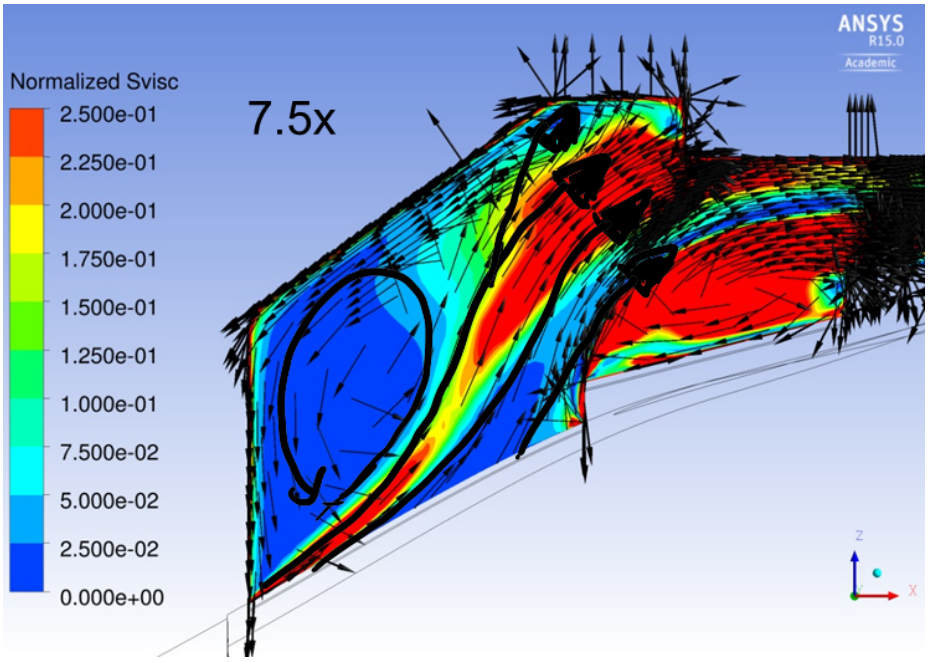

(c) 7.5x tip gap

Figure 3-24: Contours of volumetric viscous entropy generation rate with overlaid velocity vectors in the cavity inlet region for several tip gaps.

In some cases, a radial jet may be beneficial to overall efficiency despite its higher local loss in the cavity inlet region compared to a large, single core. Rosic et al. [13] report changes in computed efficiency of a computational 1.5 stage model of a low aspect ratio turbine rig when varying several cavity geometric parameters. By decreasing the cavity inlet axial length to 20% of its value in the datum case, the computed efficiency increased by 0.2% despite the formation of a radial jet in the cavity inlet. The increase in efficiency results from two factors: decreased tip leakage fraction and interaction effects associated with the low aspect ratio of the blade and downstream components.

The presence of a radial jet decreases the tip leakage mass flow fraction from 1.8% to 1.7% of the total mass flow through the machine. This decrease in tip leakage is a result of the increased stagnation pressure loss of the radial jet which lowers the effective corrected mass flow rate per unit area through the labyrinth seal. Since the labyrinth seal is fixed as cavity inlet axial length is varied, the reduction in corrected

mass flow rate per unit area corresponds to a decrease in absolute mass flow rate through the labyrinth seal. Based on the loss levels reported in this thesis and those in [8], a 0.1% reduction in tip leakage mass flow fraction should be accompanied by a 0.1% gain in efficiency.

The remaining 0.1% gain in efficiency originates in the reduction of the aforementioned interaction effects. Specifically, the stage under investigation in [13] has an aspect ratio less than unity (~ 0.71 for the rotor, to be exact). More importantly, the ratio of cavity inlet axial length to blade span is 20% in the datum configuration but just 4% in the minimum cavity inlet axial length case. The cavity inlet axial length sets the length scale of the cavity's spanwise influence (see Sections 4.2.1 and 4.3.4.2). Therefore, a greater portion of the main flow span remains unaffected by the presence of the cavity in the shorter cavity inlet case, leading to increased main flow path efficiency. In addition, for the larger cavity inlet configurations, a significant portion of main flow mass is influenced by the cavity and entrained in the cavity inlet vortex. However, the fraction of main flow which leaks through the labyrinth seal changes only slightly. This implies a significant reduction in cavity inlet mass recirculation as cavity inlet axial length decreases. As demonstrated in this thesis (see Section 3.2.2), recirculated mass upstream of the blade trailing edge can lead to formation of secondary flow structures which may have adverse effects on flow through the blade passage and downstream components [14,17]. While the recirculated mass in this thesis affects only a negligible fraction of the total span and occurs in the absence of any downstream blading, the test turbine in [13] has a much lower aspect ratio and additional downstream stages. Thus, the secondary flows from recirculated cavity inlet mass flow have a significantly greater impact on overall efficiency. Therefore, in this particular low aspect ratio turbine, decreasing the cavity inlet axial length until the formation of a radial jet is beneficial. However, in more realistic turbine geometries where cavity inlet lengths are already small fractions of main flow span, increasing $F/(L_{cav}/R)$ by decreasing L_{cav} or decreasing Sw is only expected to increase loss.

The contrast between the results of References [14, 17] and [13] underscore an important implication of machine size and the proposed cavity inlet vortex opera-

tional limits. The machine size is not by itself important to the operational limits as they depend on an interplay between machine size, cavity inlet axial length, upstream vane casing length, and main flow swirl. However, the engineering trade-off in terms of tip shroud cavity loss inherent in the violation of the operational limits may depend on machine size. For smaller machines with low aspect ratio blades, it may be advantageous to exceed the radial jet limit of $F/(L_{cav}/R)$ by trading increased cavity inlet losses for lower cavity mass flow fraction, thereby decreasing lost work in the main flow path, tip jet free expansion losses, and cavity exit mixing losses. For larger machines, however, where the cavity mass flow fraction is already small and its influence on the main flow path minimal, the cavity inlet design should seek to obey the hypothesized operational limits.

3.2.4.4 Importance of Radial versus Axial Elongation

The second caveat to the qualitative design guideline in Section 3.2.4.2 is that the orientation of the major axis with respect to the main flow may indeed play a significant role in determining the loss level of the cavity inlet toroidal vortex. In References [14,17], the elongation was purely radial while the present configuration includes both radial and axial elongation. Previous literature [2] divides flows over cavities (such as the cavity inlet region) into three categories: high loss, mid loss, and low loss, depending on the aspect ratio of the cavity cross-section (see Figure 3-25). The qualitative design guideline of maximum permissible radial elongation would typically lie within the low loss category (i.e. $d/t \geq 1$) as seen in [14, 17]. Even vortex cores with some axial elongation (as in the present configuration) could reduce losses attributable to the cavity inlet vortex, provided the major axis is at a sufficiently high angle that the cavity boundary is not more representative of the high loss case in Figure 3-25.

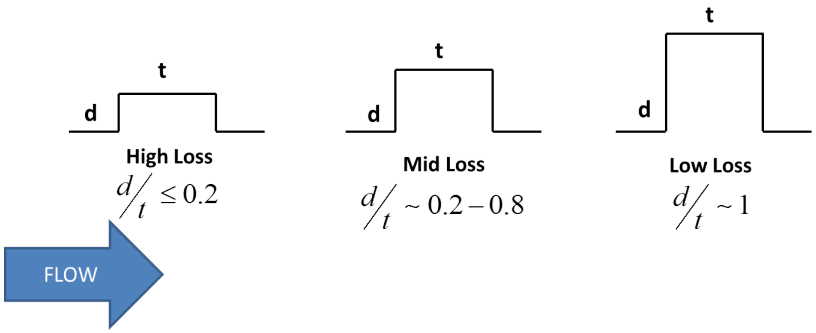

Figure 3-25: Schematic of high, mid, and low loss cavities, according to [2].

3.3 Summary of NGV-Rotor Interaction Effects in Generic Cavity

Chapter 3 assessed the role of NGV-rotor induced flow unsteadiness on loss generation and flow response in a generic tip-shroud cavity system. The key findings are summarized here.

1. Vane-rotor interaction incurs an additional 0.25% debit in efficiency in the cavity inlet per 1% of main flow through the cavity.

2. Flow unsteadiness introduced by the vane-rotor interaction enhances the strength of the cavity inlet toroidal vortex.

3. The cavity inlet toroidal vortex strength is the key controlling parameter for loss (viscous losses along the stationary outer casing and shear layer losses at the cavity inlet-main flow interface) and cavity inlet recirculating mass.

4. Cavity inlet mass recirculation creates a passage vortex in the rotor tip region, which can be of increased significance in the performance of turbine stages with lower aspect ratios or subsequent blade rows.

5. Control of loss generation and mass recirculation may be achieved by controlling the local swirl velocity of the inlet toroidal vortex via its size (cross-sectional area or perimeter) and contained circulation. Available results appear to suggest

an elliptical cross-section with radial major axis is optimal, with an elongation (ratio of major to minor axis) as high as possible while still sustaining a vortex core. Operational limits for the vortex core based on flow swirl and turbine characteristic lengths were developed.

Chapter 4

The Hybrid Blade Design for Mitigating Cavity Mixing Losses

The systematic investigation of the generic and scalloped shroud configurations revealed two primary loss mechanisms of equal importance: the free expansion of the tip seal leakage jet and mixing out of the circumferential momentum disparity at the cavity exit. Chapter 2 also showed that any attempt at aerodynamically controlling the cavity exit mixing losses would only increase overall loss in efficiency, necessitating a hardware solution instead. To that end, this chapter presents a proposed tip seal geometry, known as the Hybrid Blade, designed to reduce the cavity mixing losses. First, the underlying concept which inspired the Hybrid Blade design is described and a brief overview of the computational model provided. A model of the cavity influence on the main flow path is then developed to help design the Hybrid Blade and extrapolate its anticipated performance. This model is also generally applicable to any cavity configuration so long as a suitable baseline main flow path may be defined and an expression for the cavity mass flow rate formulated. Next, the performance of the Hybrid Blade from computations is compared with the other cavity configurations and the analytical extrapolation using the cavity influence model. Finally, some design modifications are suggested to improve the efficiency of the Hybrid Blade which address unanticipated factors not taken into account during the design formulation.

4.1 The Hybrid Blade Underlying Concept and Configuration Details

Throughout the analyses presented in Chapters 2 and 3, the cavity accounts for roughly 0.4% debit in stage efficiency. Of that, half comes from the leakage jet over the tip seal, and the other half from the downstream mixing due to the circumferential momentum disparity when the cavity flow rejoins the main flow. In fact, the scalloped shroud configuration was shown to have an additional 0.1% debit in efficiency due to increased mixing losses, creating even greater opportunity to improve device efficiency by mitigating mixing losses. One potential solution would be to introduce a new tip seal geometry which turns the cavity flow the same amount as if it had passed through the rotor (near zero swirl at the cavity exit).

4.1.1 Physical Reasoning Motivating the Hybrid Blade Design

The simplest way to incorporate turning elements into the tip shroud design would be to cut grooved channels into the tip seal, thereby extracting the swirl (and consequently, additional work) from a portion of the cavity flow (see Figure 4-1). In addition, design constraints imposed by radial and axial movement of the tip and structural limits within the blade restrict the available modification options involving addition of turning elements (station or rotating) while retaining a radial sealing fin. Unless the spacing between the outer casing and the outer most edge of the tip seal is reduced, however, cutting channels in the tip seal will only increase the area over the tip seal and thus the cavity mass flow fraction. Typically in labyrinth seal design, clearances between rotating and stationary components are reduced to the absolute smallest possible mechanical tolerances, implying that maintaining the same total flow area over the tip seal is impossible.

A simple thought experiment based on Figure 4-2 and guided by Equation 2.8 which describes the scaling of mixing losses seems to indicate that using turning ele-

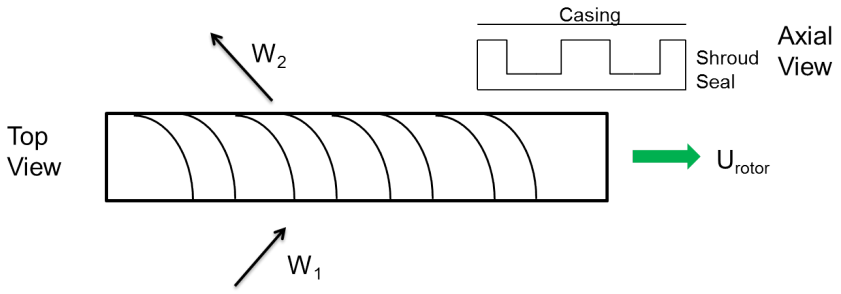

Figure 4-1: Schematic of tip seal flow area incorporating turning channels for reducing circumferential momentum disparity between cavity flow and main flow.

ments while increasing the tip seal area will only increase loss. To begin this thought experiment, consider Figure 4-2. The blue area in Figure 4-2 marks the original, unmodified flow area over the tip seal while the green regions represent the additional flow area created by milling the turning channels in the tip seal. As observed in the variable seal gap calculations, the flow over the tip seal remains choked, even when nearly doubling the tip seal area. While the flow is choked (assuming the mass flux is uniform over the total flow area), the same amount of mass must pass through the original flow area as in the unmodified tip seal, with additional cavity mass flow passing through the additional flow area. The circumferential momentum disparity between the turned and unturned portions of the cavity flow would be the same as the disparity between the cavity exit flow and rotor exit flow in the unmodified case. However, since the mixing would then occur at significantly higher velocities because the mixing location is near the minimum flow area, the overall expected loss would be higher. This result was observed in the scalloped shroud case in Section 2.2.3 when the point of mixing occurred closer to the tip seal compared to the generic shroud configuration. This logic suggests that the only possibility of decreasing loss would be to increase the tip flow area enough to change the cavity inlet properties and unchoke the tip seal. The ability to change cavity inlet flow properties by changing the tip gap follows from the non-uniform flow properties of the main flow path and increased capture area as the tip gap is increased. The physics of choking in swirling flow and how changes in cavity inlet flow properties affect choking are reviewed in detail in Appendix F. When increasing the flow area so drastically, the turning elements

essentially become miniature blades, still turning the cavity flow to reduce mixing losses and extracting work, but also fundamentally changing the loss mechanisms.

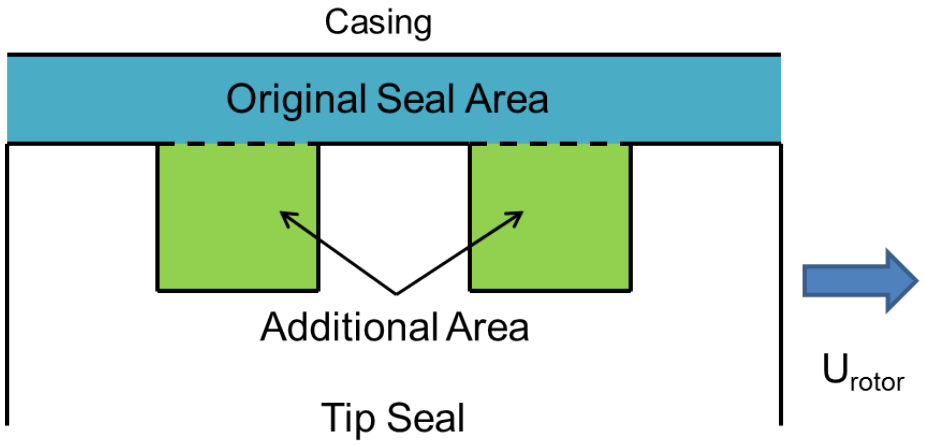

Figure 4-2: Schematic of tip seal flow area incorporating turning channels highlighting flow area regions.

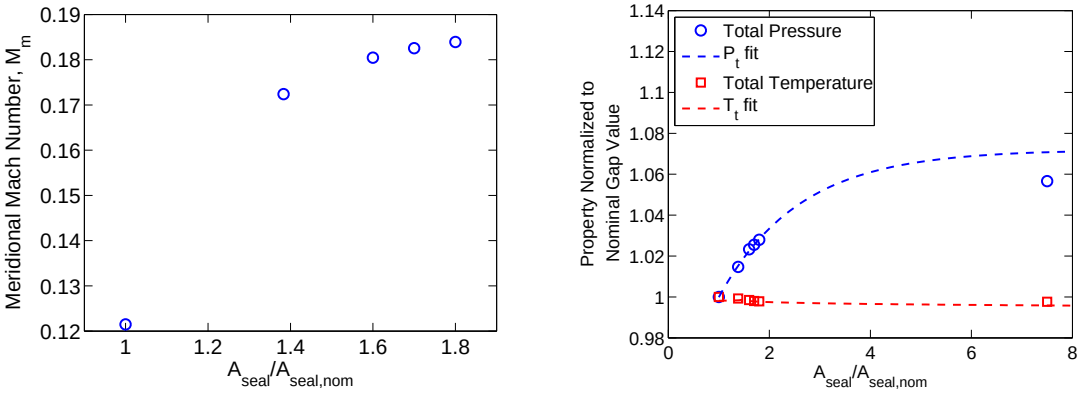

(a) Meridional Mach number

(b) Stagnation properties.

Figure 4-3: Variation of critical flow properties in cavity inlet versus tip seal flow area.

The question remains of how great an area increase over the tip seal is required to sufficiently modify the cavity inlet properties and unchoke the flow. Once again, the shroud region is assumed to be a simple area contraction with isentropic flow from the inlet to the minimum area over the tip seal. Using the set of computations in which the tip seal gap was varied, trends in stagnation properties and inlet meridional Mach number at the cavity inlet were developed (see Figure 4-3). Both cavity inlet stagnation pressure and stagnation temperature asymptotically approach a constant

value, as does the inlet meridional Mach number. Using the isentropic flow equation for the critical area (given a Mach number at a known area):

$$\frac{A}{A^*} = \left(\frac{\gamma+1}{2}\right)^{-\frac{\gamma+1}{2(\gamma-1)}} \frac{\left(1+\frac{\gamma-1}{2}M^2\right)^{\frac{\gamma+1}{2(\gamma-1)}}}{M}, \tag{4.1}$$

the maximum tip gap which would remain choked was found to be 7 times the nominal tip gap. Knowing that replacing a simple gap with turning elements designed to extract work would lead to an increase in flow relative Mach number (due to decrease in fluid static temperature as work is extracted), an area larger than this minimum choke area was chosen. Specifically, the modified tip geometry was designed to have a minimum flow area 7.5 times the nominal tip gap, which would correspond to a meridional Mach number of 0.8 for a simple tip gap. Figure 4-4 plots the contours of meridional Mach number for a tip gap with 7.5 times the nominal tip gap, demonstrating that this extrapolation does indeed result in a meridional Mach number over the tip seal of ~ 0.8.

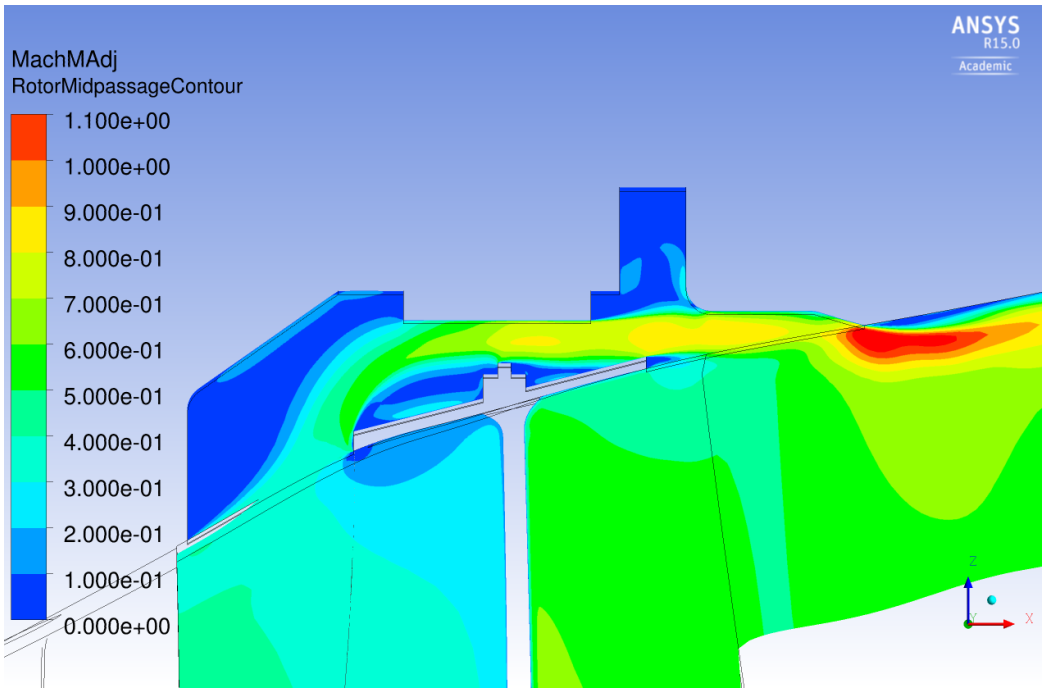

Figure 4-4: Contours of meridional Mach number for generic shroud case with a tip gap of 7.5 times the nominal gap height.

The Hybrid Blade concept is a direct result of the above analysis. It is so named because the main blade is still a high aspect ratio, shrouded blade, but it is coupled with a row of small unshrouded blades above the main blade shroud. The total flow area over the tip seal is designed to be 7.5 times the nominal gap flow area. The computational geometry used to assess the effectiveness of this design in mitigating mixing loss is shown in Figure 4-5. As evident in the figure, the turning elements (referred to as "bladelets" for the remainder of this thesis) are mated with the scalloped shroud configuration. This was done in part to evaluate their performance in a more realistic turbine geometry, but also to take advantage of the unstructured mesh in the cavity domain. The structured main flow domains had a similar mesh density as in the scalloped shroud with simple seal configuration shown in Chapter 1. The total number of nodes and elements in the main flow path are 2.2 million and 2.09 million, respectively, with 1.56 million and 1.48 million in the rotor domain. In the structured domain, all elements are hexahedral with expansion ratios, volume ratios, and edge length ratios all within the "best practices" ranges given in the CFX manual[1]. The cavity domain which includes the Hybrid Blade tip configuration has a much higher mesh density in order to capture the detailed flow structures. In this unstructured domain, the total number of nodes is 5.74 million with approximately 16.8 million elements split nearly evenly between tetrahedral and wedge elements. The mesh density in the Hybrid Blade cavity domain is more than 3 times the density of the scalloped shroud with simple seal due to the requirements imposed by resolution of the bladelet passages. Consequently the majority of the increased mesh density in the Hybrid Blade configuration versus the scalloped shroud with simple seal shown in Chapter 1 clusters around and within the bladelets. Before computationally evaluating the Hybrid Blade design's effectiveness, however, the next section details a model of the cavity coupling between the main flow path which contributed to the design in Figure 4-5. This model also demonstrates the usefulness of the scaling rules developed

[1]There are a few elements with characteristics outside these suggested range, but they are a decidedly negligible fraction of the total number of elements. In addition, they are localized to the rotor blade trailing edge at the root, well away from the cavity flow field which is the focus of this thesis.

in Chapter 2, even for configurations as drastically different from the generic shroud (upon which they were based) as the Hybrid Blade case.

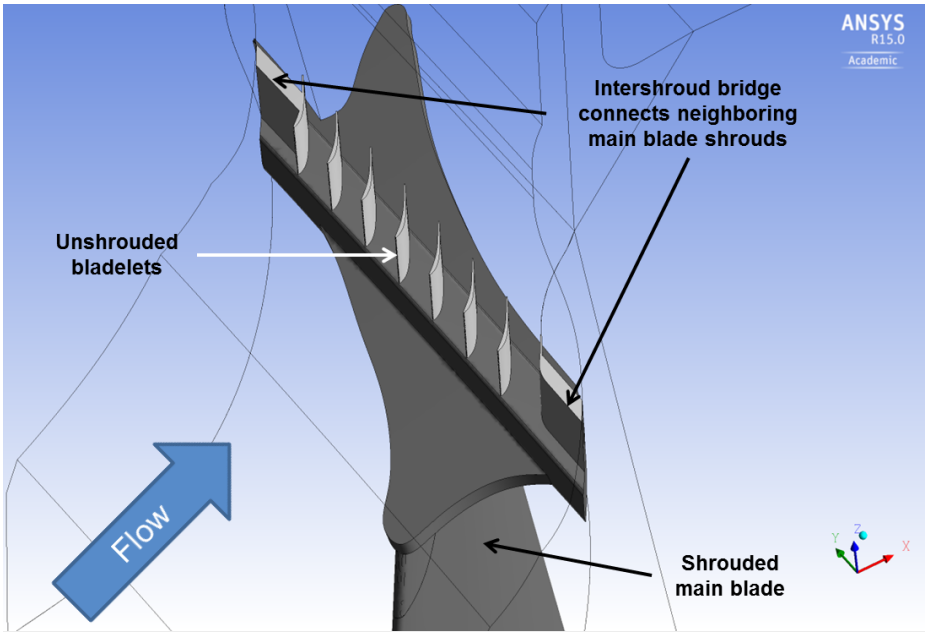

Figure 4-5: Computational geometry for the Hybrid Blade configuration.

4.2 Cavity Coupling with the Main Flow Path

While the scaling rules presented in Chapter 2 reasonably estimate the losses in tip shroud cavity flows, they depend on previous knowledge of some of the flow properties. Typically these properties are extracted from mean line or throughflow code solutions prior to running full computational fluid dynamics calculations. However, standard mean line and throughflow tools may not account for the presence of the cavity and the effect it has on fluid distribution in the main flow path. This shortcoming has the potential to adversely affect the accuracy of the scaling rule estimates of losses associated with the cavity. Thus, it would be beneficial to have a model of the cavity's influence on the main flow path to improve the accuracy of the preliminary design tools. In addition, such a model may reduce development time and cost by considering the cavity earlier in the design process. Such a practice could potentially reduce the number of iterations required to refine the design or allow comparison of

different cavity geometries without using more costly computational fluid dynamics calculations. One example of cavity comparison (and in fact the motivating comparison behind this model's development) will be demonstrated in this chapter by assessing the Hybrid Blade performance against that of the generic shroud. First, the details of the cavity coupling model are presented.

4.2.1 Cavity as a Potential Flow Sink-Source Pair with Finite Separation

Consider the practical functions of each cavity region. The cavity inlet ingests some amount of fluid from the main flow path at the rotor leading edge while the cavity exit returns that fluid to the main flow path at the rotor trailing edge. In essence, the cavity inlet serves as a circumferential line sink as seen by the main flow path, and the exit appears as a line source. Figure 4-6 depicts a schematic of this sink-source concept (overlaid on the axisymmetric generic shroud configuration) where the black circle represents the sink and the white circle, the source. The sink and source are separated by a finite distance, L, given by the length of the cavity. Radii r_1 and r_2 are the distances from the sink and source, respectively, to a point of interest in the main flow path.

The tip seal regulates the passage of fluid between the two "plenums" of the cavity inlet and exit regions. By continuity, the mass flow which enters the cavity inlet and leaves the cavity exit is the same and is also equal to the mass flow rate over the tip seal. Thus the strengths of the sink and the source are equal and determined by the tip seal. Together, the sink and source reduce the mass flux (mass flow per unit area, G) through the main flow. This can be expressed by the general formula:

$$\Delta G = -\frac{m}{2\pi r_1} + \frac{m}{2\pi r_2}, \tag{4.2}$$

where m is the sink/source strength in units of kg m^{-1} s^{-1}. Equation 4.2 retains the factor of 2π in the denominator from the standard point sink/source equations.

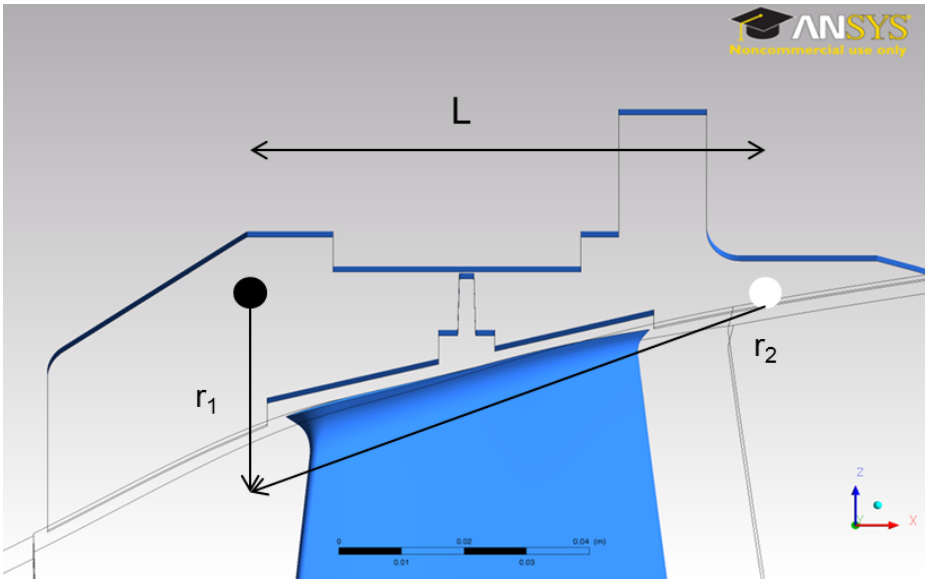

Figure 4-6: Schematic of sink-source pair with finite separation representing cavity inlet and exit.

Keeping in mind this model is only an approximation tool for preliminary design purposes, this factor was found to be necessary in order to remain consistent with the CFD (as will be shown later).

Since this strength, m, is set by the tip seal, it can be estimated with the equation for corrected mass flow, given by:

$$m = \frac{\Delta \dot{m}_{seal}}{R_{seal}\theta_0} = \Delta\delta P_t \sqrt{\frac{\gamma}{RT_t}} D\left(M_{seal}\right), \tag{4.3}$$

where $\Delta\delta$ represents a change in tip gap versus a baseline and θ_0 is the angular extent of the cavity domain of interest (in this case, the computational domain). The term, $D(M_{seal})$, is the standard corrected mass flow per unit area expression:

$$D(M) = \frac{M}{\left(1 + \frac{1+\gamma}{2}M^2\right)^{\frac{\gamma+1}{2(\gamma-1)}}}, \tag{4.4}$$

Choosing the baseline geometry shown in Figure 1-3 (which has no cavity domain), the change in tip gap becomes the tip gap of the current case, by definition. The

change in mass flux in the main flow path due to the presence of the cavity as a function of normalized spanwise coordinate is then given by:

$$\Delta G(\xi) = \frac{\delta P_t \sqrt{\frac{\gamma}{RT_t}} D(M_{seal})}{2\pi b} \left(-\frac{1}{1-\xi} + \frac{1}{\sqrt{(1-\xi)^2 + (L/b)^2}} \right), \tag{4.5}$$

where b is the blade span and ξ is then the normalized spanwise coordinate (equal to 0 at the root and 1 at the tip). As previously mentioned, application of Equation 4.5 must be referenced to a baseline. This caveat is not just to estimate the change in mass flow rate through the tip seal, but also to account for change in mass flux of the main flow due to expansion of the main flow area through the turbine. The difference in mass flux profiles between the rotor leading edge and the rotor inlet for the baseline case accounts for the effect of the flow area change on the mass flux profile when it is subtracted from the same difference for a given tip gap case.

4.2.2 Assessment of Cavity Coupling Model with Computations

Having derived an expression for the change in mass flux in the main flow path due to ingestion by the cavity, the model must be assessed against some of the computational cases already presented before it may be used to extrapolate the performance of the Hybrid Blade. Figures 4-7 and 4-8 compare the CFD-derived change in spanwise mass flux with the computed change based on Equation 4.5 for the nominal and 1.8x tip gap cases, respectively. The computed change in mass flux at the outer-most spanwise coordinate ($\xi = 0.995$) is pinned to the value of the second outer-most point to account for the trend reversal observed in the CFD (i.e. the two outer-most points on the blue curves in Figures 4-7 and 4-8). Allowing for the pinning of the tip value and the inclusion of the 2π factor to match magnitudes of the computations, the simple model described by Equation 4.5 closely agrees with the computational results.

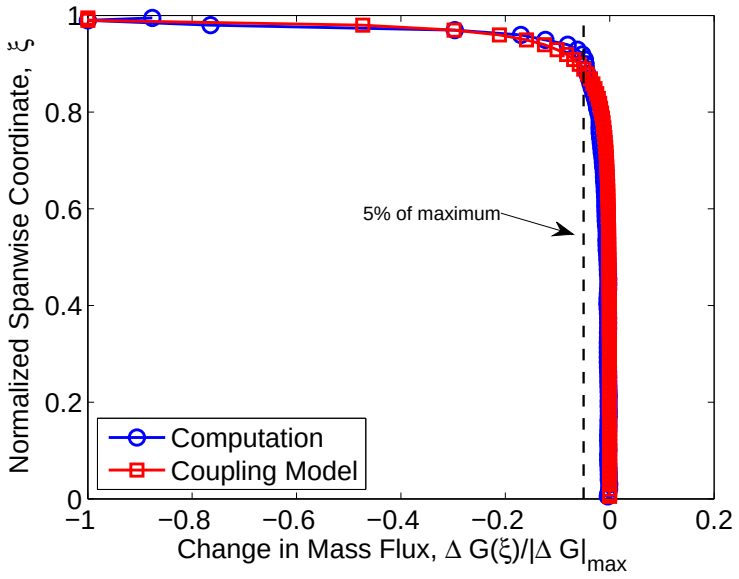

Figure 4-7: Assessing cavity coupling model estimated reduction of main flow mass flux against CFD results for steady nominal tip gap case.

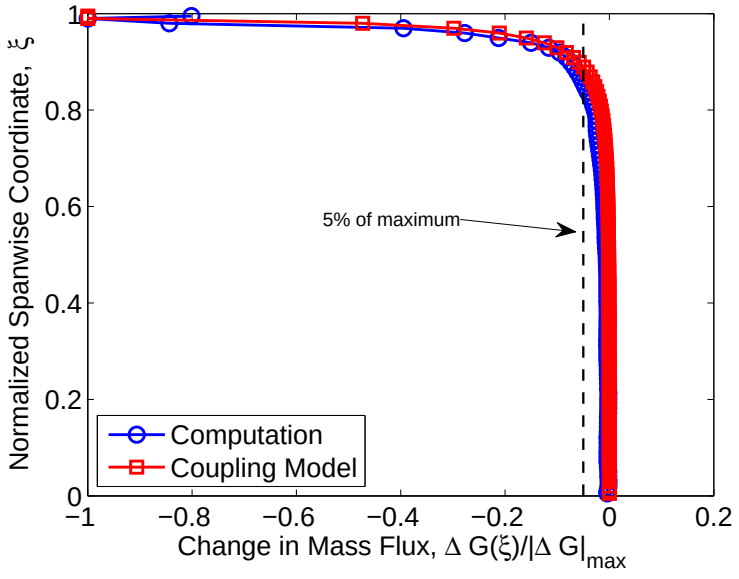

Figure 4-8: Assessing cavity coupling model estimated reduction of main flow mass flux against CFD results for steady 1.8x tip gap case.

The above assessment focused on steady cases utilizing the mixing plane approximation. In theory, though, the cavity coupling model should also apply for time-averaged unsteady cases. Figure 4-9 plots the predicted mass flux deficit using the model against the time-averaged unsteady profile from the computations. While the two profiles are in qualitative agreement, they do not agree as well quantitatively as in Figures 4-7 and 4-8. Specifically, the computational profile displays an oscillatory nature absent in the profile estimated by the model. Most notable is the local maximum and *positive* change in mass flux near 95% span observed in the computational profile.

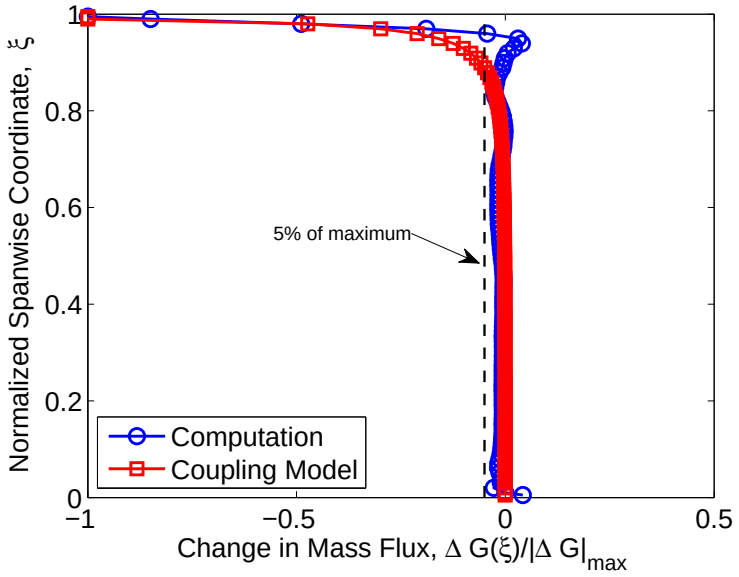

Figure 4-9: Comparison of coupling model estimated reduction in main flow mass flux with computational results for the time-averaged unsteady nominal tip gap case.

Both the oscillatory nature and local maximum in the time-average unsteady computational profile may be attributed to the cavity inlet recirculation phenomenon described in Section 3.2.2. The cavity inlet is not a simple sink as originally assumed, but rather an unbalanced sink-source pair of its own with a sink near the shroud leading edge and a source near the upstream edge of the cavity inlet. Similarly, the cavity exit has another unbalanced sink-source pair with a source near the downstream edge of the cavity exit, and a sink representing main flow ingress at the trailing

edge of the shroud. The cavity coupling model previously presented captures the general features of the combination of these separate pairs with an effective sink and source, respectively. For a steady flow with mixing plane approximation, the original effective sink-source pair is sufficient. However, the finer features in the spanwise mass flux profiles of Figure 4-9 (especially the local maximum near 95% span) may only be replicable using two sink-source pairs to model the cavity effects on the main gas path. The large difference in mass flux profiles in steady versus time-average unsteady calculations is consistent with the large difference in recirculating mass fraction discussed in Section 3.2.2. That is, while the recirculating fraction is finite under the mixing plane approximation, it appears small enough to not significantly affect the spanwise variation in mass flux. Accounting for unsteadiness, however, nearly doubles the recirculating mass fraction which significantly affects the spanwise mass flux profile, motivating the potential quad sink/source refinement. Figure 4-10 depicts an example schematic of this potential quad sink/source refinement. For the intent here, the effective sink-source pair is sufficient to capture the trends of interest for the Hybrid Blade design.

4.2.3 Extrapolation of Hybrid Blade Performance

Combining Equation 4.5 with the extrapolated tip gap size necessary to prevent choking, an estimation of the performance changes may be calculated for the case when using the proposed bladelets. It is assumed that the bladelets have been designed to remove all the swirl so that the cavity flow exits the bladelet row with no swirl, as the main flow does. Thus the loss mechanisms are different. The loss mechanisms are expected to be those typically associated with unshrouded turbine blades, namely blade profile losses and mixing of the tip leakage vortex. The mass flux profile generated using the cavity coupling model can be used to estimate the mass flow rate through the cavity as well as the expected work reduction in the main gas path due to the increase of the cavity mass flow rate. Based on the angular momentum of the cavity flow and Euler's turbine equation, an estimate of the change in specific stagnation enthalpy across the bladelets is obtained. To estimate both the bladelet

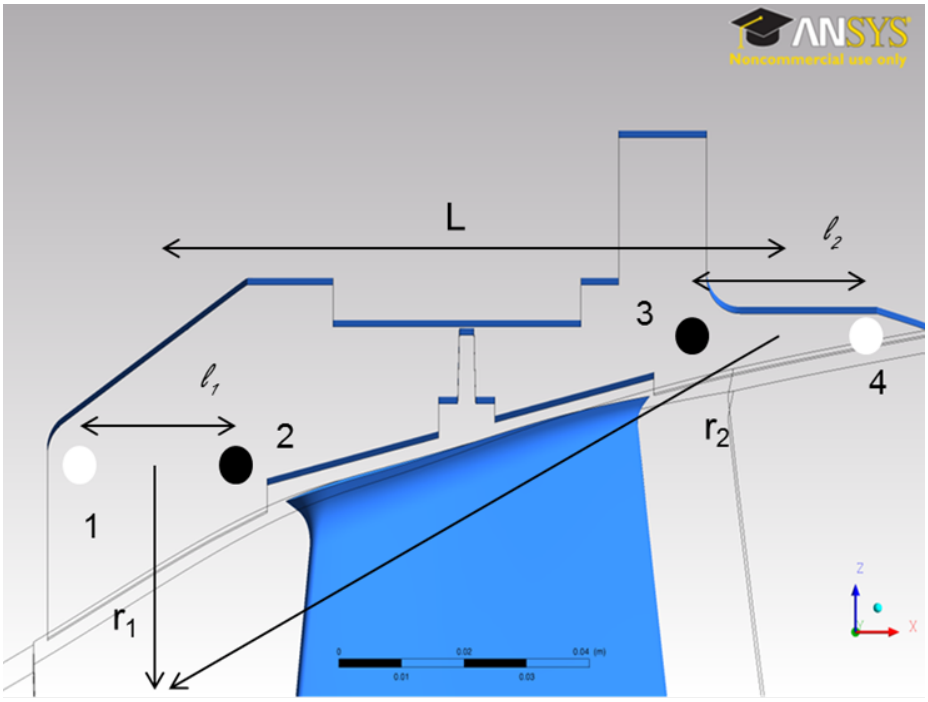

Figure 4-10: Sample schematic of arrangement of sinks (black) and sources (white) to refine cavity model to account for cavity inlet mass recirculation.

work output and viscous loss requires delineating what proportion of the cavity flow will pass through the bladelet passages versus that which will pass over the bladelet tips.

Based on scalings for unshrouded turbine blades in [22], the percentage of mass flow over the bladelet tip and the loss associated with the blade may be estimated, depending on the bladelet tip gap as a percentage of bladelet span. Specifically, the leakage fraction is $2 - 2.5\%$ per 1% tip gap, and the estimated loss is 3% per 1% tip gap (which includes an estimate for profile loss). However determining the tip gap size produces a range of possible values depending on whether the geometric gap is used or the presence of a vena contracta is taken into account. In the conservative estimate, the tip gap is taken as the geometric value of 10% of the span of the unshrouded bladelets. Typically, however, leakage over unshrouded blades separates, creating a vena contracta subject to a contraction coefficient. Based on trends published by Ward-Smith [24], this contraction coefficient may be estimated as 0.6, resulting in an effective tip gap of 6%. An optimistic estimate leverages results published by

Sakulkaew [33] which found that losses in blades with large tip gaps reached a plateau for gaps above 3.4% (thus this is taken as the effective tip gap in the optimistic estimation). Table 4.1 compares several of the key quantities extrapolated from the analytical model with results of computations on the geometry in Figure 4-5. The first row, $\dot{m}_{f_{cav}}$, represents the fraction of the main flow which passes through the cavity. The second row estimates the fraction of the main flow which does not pass through either the main rotor blade or the bladelet passages.

Comparison of the columns in Table 4.1 demonstrates the utility of the simple analytical model in that the estimations of key flow features using a realistic assumption for bladelet tip gap agrees very well with the computations. Specifically, the estimated mass flow fractions (both through the cavity and the fraction which does not pass through either the rotor blade or bladelets) for the 6% tip gap case are in accord with those calculated in the CFD. While the prediction of change in work output for the 6% tip gap is pessimistic compared to that computed by the CFD, a difference of only 0.3% demonstrates good agreement between the coupling model and more accurate computations. The two reported differences in efficiency for the computations (i.e. last column) in Table 4.1 represent the change in overall stage efficiency and change considering cavity losses only, respectively. The following sections explain in detail how these differences in loss generation arise.

Key Quantity	10% **tip gap**	6% **tip gap**	3.4% **tip gap**	**CFD**
$\dot{m}_{f_{cav}}$	2.6%	2.6%	2.6%	2.2%
$\dot{m}_f$ through no blading	0.65%	0.39%	0.22%	0.39%
$\Delta\dot{W}_{stage}$	-0.4%	-0.3%	-0.2%	$+0.02\%$
$\Delta\eta$	-0.1%	0%	0.2%	$-0.2\%(0\%)$

Table 4.1: Comparison of computed key quantities with previously extrapolated values using cavity coupling model and scaling rules.

4.3 Computational Results for the Hybrid Blade Design

In order to assess with greater fidelity the performance of the Hybrid Blade design, computations were performed on the geometry in Figure 4-5. This section will examine the differences in loss mechanisms common to the scalloped shroud configurations with single tip seal and with bladelets (e.g. cavity exit mixing losses, blade profile losses). The loss levels of these disparate mechanisms (e.g. free expansion losses of the tip seal leakage jet versus bladelet profile and tip leakage losses in the Hybrid Blade configuration) are then compared to determine the effects on overall efficiency.

4.3.1 Overview of Hybrid Blade Loss Levels

Before categorizing the Hybrid Blade losses by mechanism, the overall loss of the stage will be presented and briefly discussed. Figure 4-11 compares the accumulation of loss in the Hybrid Blade and scalloped shroud configurations by plotting the difference in loss (Hybrid Blade minus scalloped shroud) as a function of axial coordinate. As before, the black vertical lines mark axial locations corresponding to vane/blade leading and trailing edges, mixing plane, and the diffuser inlet. The magenta dashed lines added to Figure 4-11 define the axial extent of the bladelets. Overall, the Hybrid Blade actually increases the stage debit in efficiency by 0.2%. However, closer inspection reveals that half of this loss increase arises in the stator domain while the other half is spread throughout the rotor and cavity domains. These losses were unanticipated by the simple model in Section 4.2.3 which instead assumed that the losses associated with the main blades would remain approximately constant. Focusing exclusively on the axial range between rotor leading edge and diffuser inlet (where the majority of cavity loss generation occurs), the net difference in loss accumulation between the Hybrid Blade and simple tip seal configurations is approximately 0, which agrees with the estimate based on a 6% bladelet tip gap in Section 4.2.3.

To further support this interpretation of Figure 4-11, the cavity and main flow

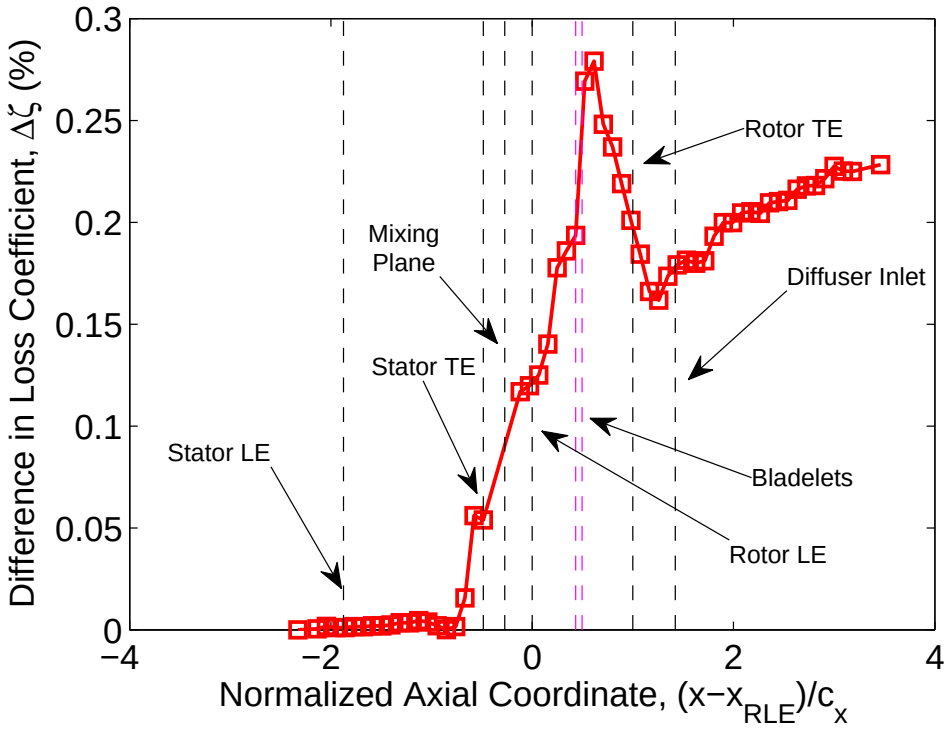

Figure 4-11: Difference in axial accumulation of loss, Hybrid Blade configuration minus scalloped shroud with simple tip seal configuration.

path may be separated using a series of control volumes. The viscous loss may then be integrated and summed through these control volumes to generate separate loss profiles for each flow path. Figure 4-12 demonstrates how these volumes are defined and separated. The product of temperature and volumetric viscous entropy generation rate are then integrated in each control volume to estimate the dissipated power due to viscous effects. It should be noted this method is only an approximate and qualitative analysis due to overlapping control volumes resulting from finite mesh cell volumes and details of control volume definition in the post-processor (note the jagged appearance of the control volumes in Figure 4-12 due to the individual cell volumes). Nevertheless, Figures 4-13 and 4-14, which plot the integrated difference in loss coefficient (Hybrid Blade minus simple seal with scalloped shroud) for the cavity only and main flow only, respectively, agree reasonably well quantitatively with the results shown in Figure 4-11. Namely, the loss in the Hybrid Blade case increases slightly upstream and through the bladelets (marked by magenta dashed lines) to a total of approximately $\sim 0.2\%$ greater loss than the simple seal[2]. However, downstream the loss decreases in both flow paths to near-zero difference. As this decreased difference in loss occurs in the mixing region downstream of the bladelets/tip seal, it is attributed to a reduction in mixing losses relative to the simple seal when using the Hybrid Blade configuration. Figure 4-15 confirms that the integrated viscous dissipation from the main flow is localized to the interface between cavity and main flow rather than distributed throughout the main rotor span.

Therefore the preliminary analysis would seem to indicate the Hybrid Blade was successful in reducing, at least partially, the mixing losses at the cavity exit. However, the expected gain in efficiency is offset by greater loss upstream of and through the bladelets compared to the free expansion loss of the tip seal leakage jet. The following sections explain in detail how these differences in loss generation arise.

[2]Figure 4-11 shows a maximum difference of 0.28%, but includes an offset of 0.1% from stator loss, implying 0.18% arises in the rotor and cavity. As Figures 4-13 and 4-14 omit the stator loss contribution, the observed 0.18% total increase is in accord with Figure 4-11.

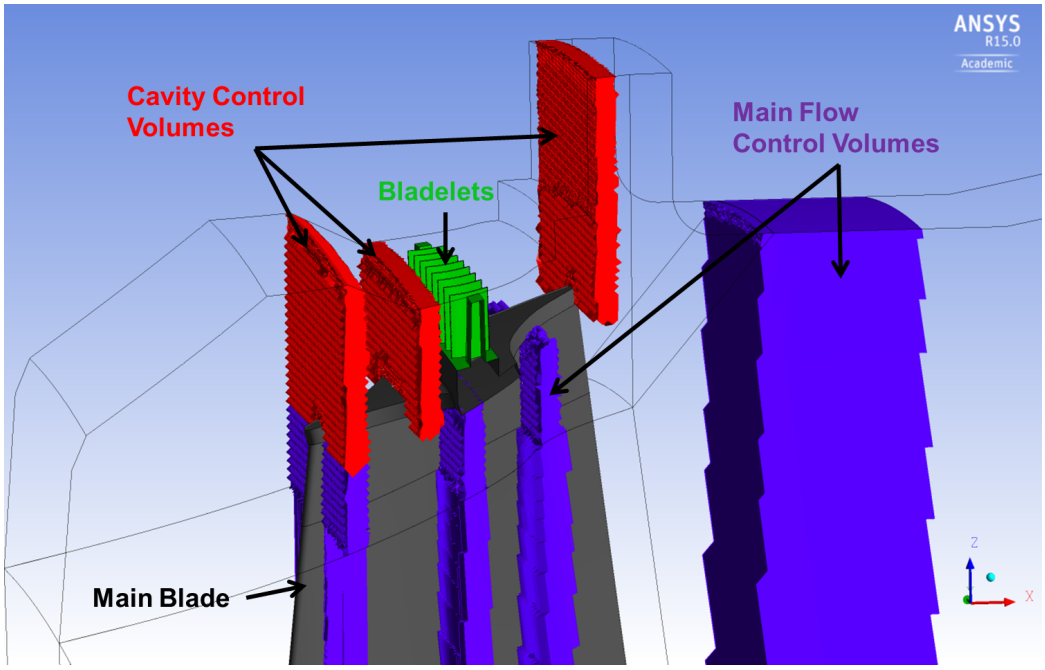

Figure 4-12: Sample control volumes used to isolate viscous loss generation in cavity flow and main flow for the scalloped shroud-based configurations.

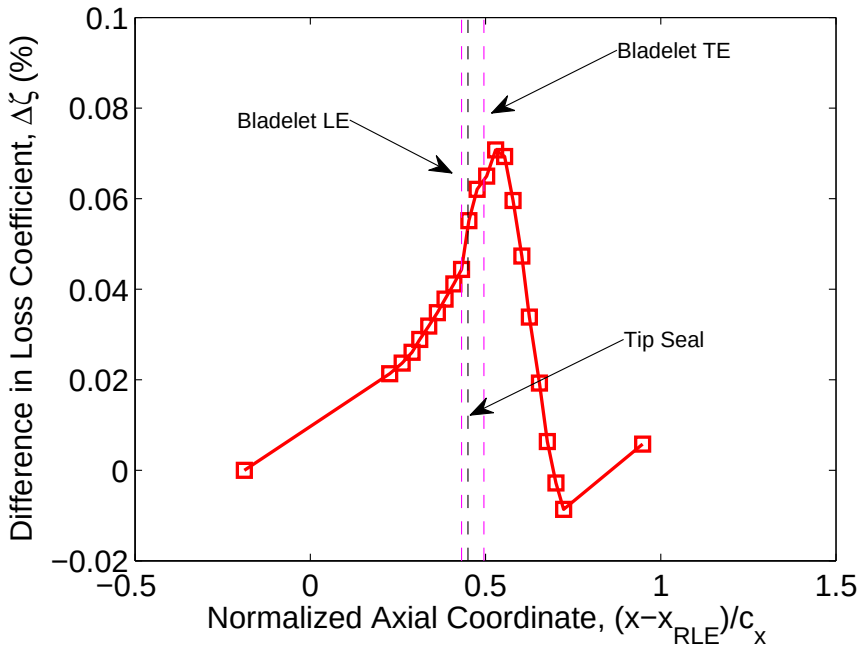

Figure 4-13: Difference in integrated viscous loss generation for cavity flow only, Hybrid Blade minus simple seal.

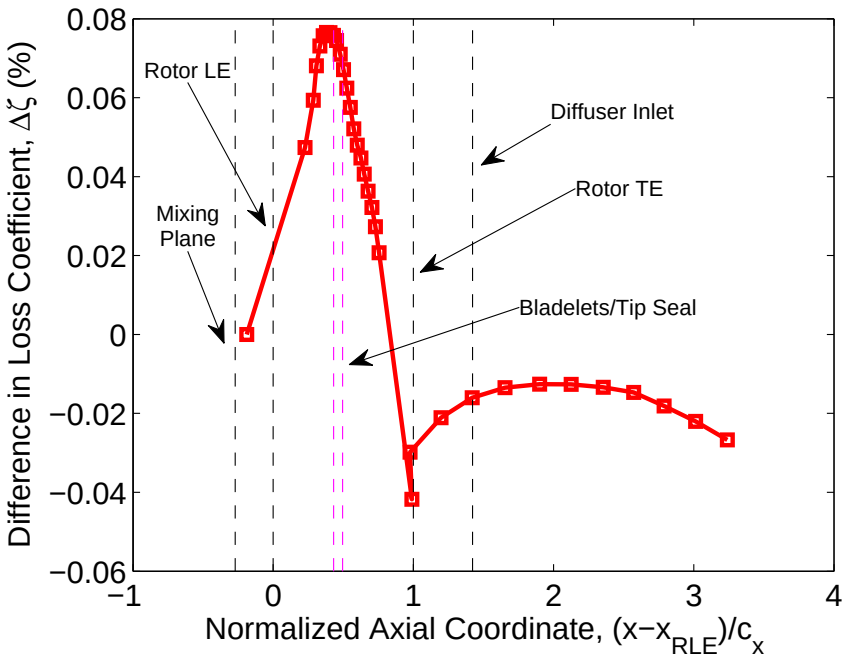

Figure 4-14: Difference in integrated viscous loss generation for main flow only, Hybrid Blade minus simple seal.

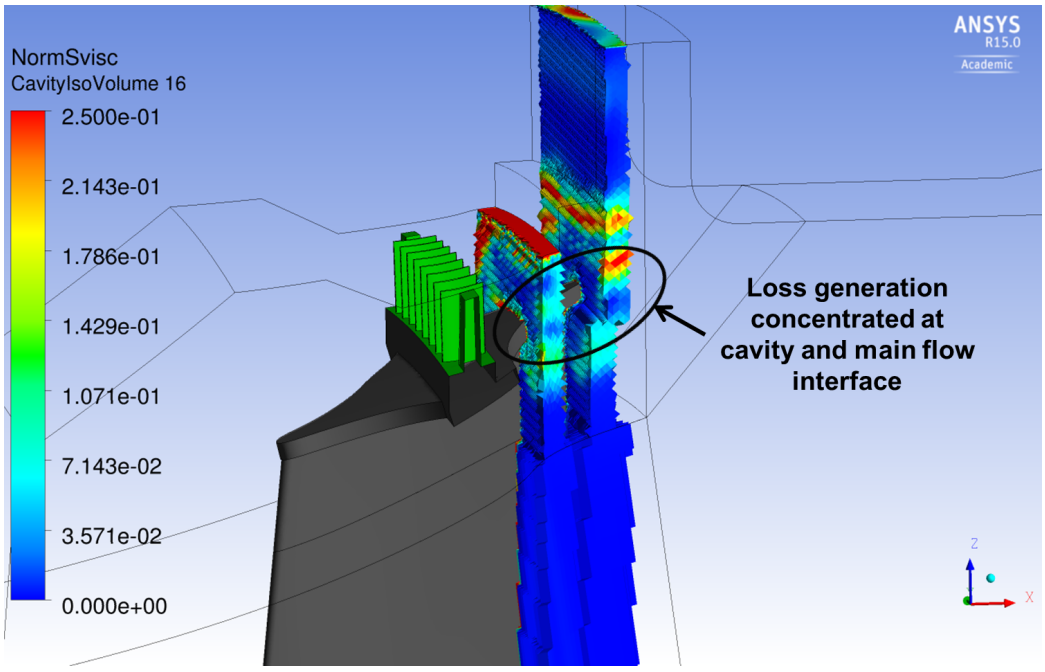

Figure 4-15: Local volumetric viscous entropy generation rate is significant in cavity control volumes and in rotor control volumes immediately at the interface between cavity flow and main flow.

4.3.2 Reduction in Mixing Losses using the Hybrid Blade

The stated goal of the Hybrid Blade design was to mitigate the mixing losses between the cavity exit flow and rotor exit flow, so it is only logical the breakdown by individual loss mechanism should begin with this loss mechanism. Returning to Figure 4-11, the decrease in the difference in accumulated loss downstream of the bladelets coincides with the mixing region for the scalloped shroud. Since the rotor domain is the same in both the Hybrid Blade and standard tip seal cases, this decrease in loss difference implies that the mixing losses in the Hybrid Blade case are between 0.1% and 0.2% less than those in the simple tip seal configuration. A significant reduction in loss in the mixing region of the cavity domain is visually confirmed in Figure 4-16 which plots contours of volumetric entropy generation rate for the scalloped shroud with simple seal and the Hybrid Blade configurations. The contour is a constant radius plane plotted at 5% bladelet span. The large red region at the shroud trailing edge in Figure 4-16a indicates high volumetric viscous entropy generation rate due to mixing between the cavity flow and main flow. This large region of high loss is absent in the Hybrid Blade configuration, as shown in Figure 4-16b.

The scale of this mixing loss reduction can also be estimated using Equation 2.8 and the same comparison technique as performed in Section 2.2.3. Although, the more complete form of Equation 2.8 from Appendix E is required to account for the significant difference in mass flow through the cavity in the Hybrid Blade case versus the simple tip seal. The ratio of expected mixing loss of the Hybrid Blade to the simple tip seal ("scallop") is then given by:

$$\frac{\zeta_{hybrid}}{\zeta_{scallop}} = \frac{\dot{W}_{ideal_{scallop}}}{\dot{W}_{ideal_{hybrid}}} \frac{(\dot{m}_1 + \dot{m}_2)_{hybrid}}{(\dot{m}_1 + \dot{m}_2)_{scallop}} \frac{(\dot{m}_{f1}\dot{m}_{f2})_{hybrid}}{(\dot{m}_{f1}\dot{m}_{f2})_{scallop}} \frac{\left(\Delta v^2 + 4v_1 v_2 \sin^2(\theta/2)\right)_{hybrid}}{\left(\Delta v^2 + 4v_1 v_2 \sin^2(\theta/2)\right)_{scallop}}, \tag{4.6}$$

The ratio of ideal stage work output (first fraction on right hand side of Equation 4.6) is nearly 1 as noted in Table 4.1. The other important factors for the Hybrid

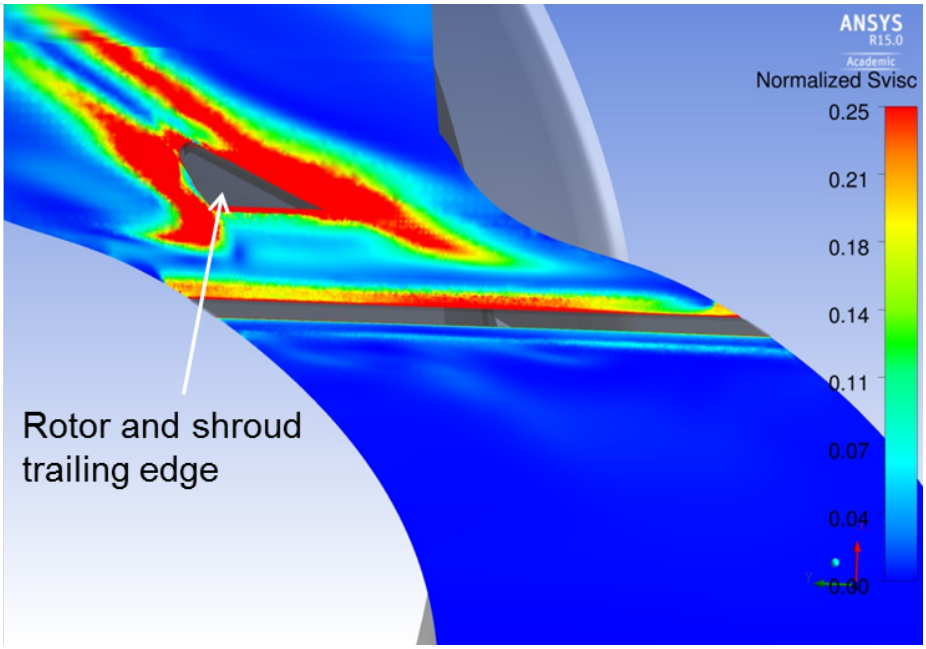

(a) Scalloped shroud with simple tip seal.

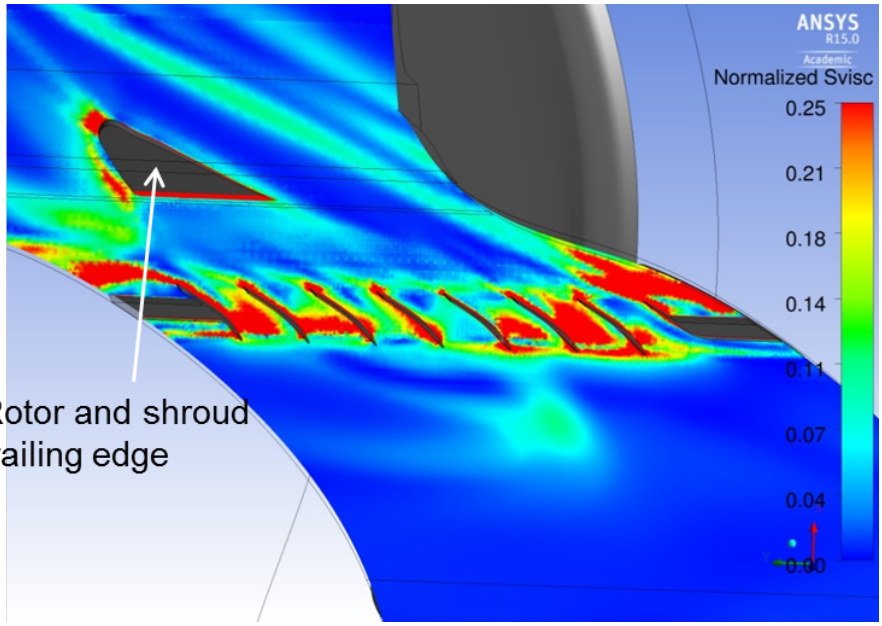

(b) Hybrid Blade configuration.

Figure 4-16: Contours of volumetric viscous entropy generation rate at bladelet 5% span to compare mixing losses between cavity flow and main flow.

Blade case are listed in Table 4.2, normalized to their respective values for the simple tip seal with scalloped shroud. Use of these tabulated values in Equation 4.6 yields an expected mixing loss for the Hybrid Blade of approximately 54% the loss in the simple tip seal, scalloped shroud configuration. As presented in Section 2.2.3, the mixing losses associated with the simple tip seal with scalloped shroud are 0.3%, which translates to $\sim 0.16\%$ mixing loss in the Hybrid Blade case. This is consistent with the 0.14% decrease observed in Figure 4-11 between the bladelet row exit and inlet to the diffuser.

$\dot{m}_1 + \dot{m}_2$	$\dot{m}_{f1}\dot{m}_{f2}$	Δv	$v_1 v_2$	θ
1.46	2.11	0.16	0.53	0.97

Table 4.2: Key mixing loss flow properties in the Hybrid Blade case, normalized to values for the simple seal with scalloped shroud.

As evident in the values of Table 4.2, the largest change in flow properties which contribute to changes in mixing losses are the reductions in difference in velocity magnitudes and the product of velocities at which mixing occurs. Separating the changes in velocity by component, it is found that while the Hybrid Blade indeed removes swirl and reduces the circumferential momentum disparity, the axial component also plays a significant role. Quantitatively, the difference in circumferential velocity between streams in the Hybrid Blade case is 10% of the difference between streams in the simple seal case. Similarly, the difference in axial velocity between streams in the Hybrid Blade configuration is 15% that of the simple seal. In the simple seal scalloped shroud case, the tip leakage jet is still near sonic velocities due to the mixing process's proximity to the choked tip seal. Mixing begins at the same axial location in the Hybrid Blade configuration but the axial velocity is significantly lower for two reasons: (i) the bladelets are unchoked due to the large flow area increase outlined in Section 4.1.1, and (ii) the turning elements have extracted some of the mechanical energy of the flow, thereby limiting the axial velocity to similar magnitudes as in the main flow path (as opposed to the sonic velocities of the simple seal). Thus both the computations and simple scaling rules indicate that the Hybrid Blade design is successful at mitigating a large portion of the cavity mixing losses.

4.3.3 Comparison of Tip Seal Jet Free Expansion and Bladelet Loss Mechanisms

Despite reducing the mixing losses as designed, there is no net change in cavity loss when using the Hybrid Blade in place of the scalloped shroud configuration. This was first noted when examining Figure 4-11 in detail which shows an equally steep rise in loss accumulation upstream of the bladelets as the steep decline in loss downstream of the bladelets. Figure 4-16 shows the high loss regions associated with flow separation off sharp corners upstream of the bladelets and within the bladelets themselves. Since the Hybrid Blade configuration is a completely different design than the simple seal, the two cases have completely different loss mechanisms (free expansion loss of the tip seal jet for the simple seal, profile and tip leakage vortex losses for the bladelets). Using the loss accumulation technique, Figure 4-17 quantifies the loss levels of each loss mechanism, demonstrating that the bladelet losses exceed those of the tip seal leakage jet by $\sim 0.1\%$. This result is consistent with the jump observed in Figure 4-11 across the bladelet row.

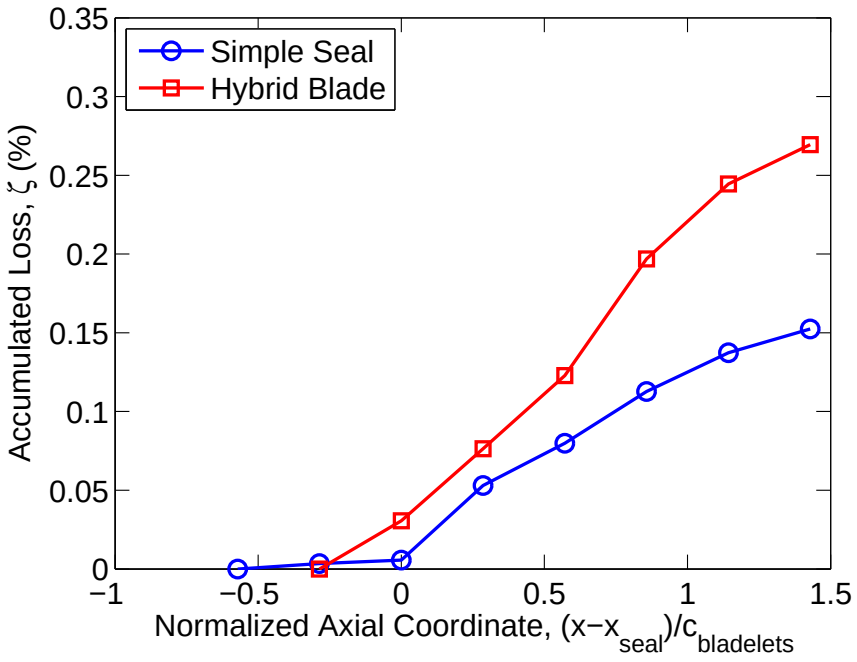

Figure 4-17: Comparison of loss accumulation through simple seal/bladelets only.

The higher observed loss through the bladelets compared to the free expansion of the tip jet is also an unexpected result. Free expansion through a rapid area expansion should generate the most loss of any process between two pressures, and certainly more than expansion through turning elements designed to reduce pressure by extracting work. Figure 4-17 appears contradictory to this reasoning, but in fact it is somewhat misleading since the two configurations pass distinctly different mass flow rates. If the loss is instead plotted on a per unit mass flow basis, as done in Figure 4-18, it is apparent that the simple seal generates much more loss per unit mass flow than the bladelets (nearly 3 times as much, in fact).

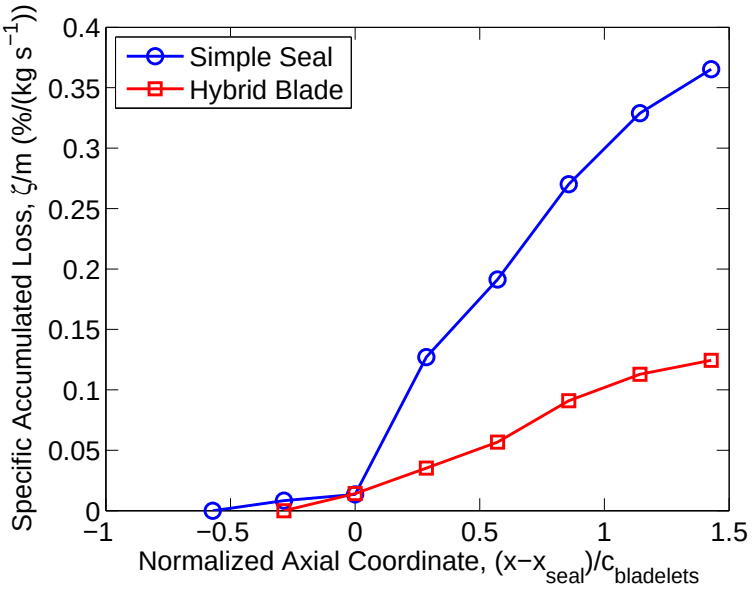

Figure 4-18: Comparison of loss accumulation *per unit mass* through simple seal/bladelets only.

Nevertheless, the loss generated by the bladelets is still larger than desired to improve overall efficiency. Rather than quantifying the bladelet losses on the basis of the ideal work output for the entire stage, Figure 4-19 plots the loss accumulation normalized to the ideal work output of the bladelets alone. In essence, it is the isolated efficiency of the unshrouded bladelets. Modern turbine blades have greater than 90% isentropic efficiency, but these bladelets are operating at only about 80%. One contributing factor to this loss in efficiency is low Reynolds number (bladelet $Re \sim 50,000$ based on axial chord) effects such as boundary layer thickness increase.

Yet, a bladelet efficiency of approximately 90% should still be achievable based on the research work of Austin DiOrio [21]. The results in [21] are for small-core compressors, but some of the findings still apply, including the low Re boundary layer thickening effect. However, the separation of laminar boundary layers noted in Figure 3-3 of [21] (based on research in [34]) which cause a more substantial drop in efficiency is less of a concern in turbine blades due to the favorable pressure gradient. Regardless, DiOrio notes a drop in efficiency of 5% compared to the high-efficiency large scale design. Since the bladelets are based on the main blade design which has an efficiency of $\sim 93\%$ (see Chapter 2), a similar drop in efficiency due to low Re number effects would still beget an expected efficiency of 88% if properly designed. In fact, DiOrio demonstrated a recovery of up to 3% in stage efficiency when optimizing his small core compressor for low Reynolds numbers of $\sim 100,000$. However, the current bladelets are essentially scaled airfoil cross-sections from 90% span of the main blade ($Re \sim 700,000$), taken for convenience as a simple model for the proposed turning elements. Thus the bladelets are not optimized for the low Reynolds number flows in the cavity and less efficient than they could be.

The size of the stage and corresponding Reynolds number is not the only reason typical modern turbine blades are so efficient. The high levels of efficiency in modern blades were achieved by also controlling and mitigating main path secondary flows. The loss scalings for the bladelet profile and tip leakage vortex losses used in Section 4.2.3 assumed a flow field relatively free of such non-ideal flow features. However, Figure 4-20 demonstrates this is not the case by plotting contours of normalized viscous entropy generation rate near the bladelet midchord.

Several bladelet passages in Figure 4-20 feature large regions of relatively high viscous entropy generation rate, especially near the bladelet hub and upper span, due to the increased circumferential asymmetry of the scalloped shroud. For example, the outer blade passages (i.e. nearest the remainder of the radial sealing fin) show large regions of high loss near the bladelet hub due to separation from the shroud rail (see also Figure 4-16b for pitchwise near-endwall loss distribution through the bladelets). The middle bladelet passages, directly downstream of the main blade leading edge,

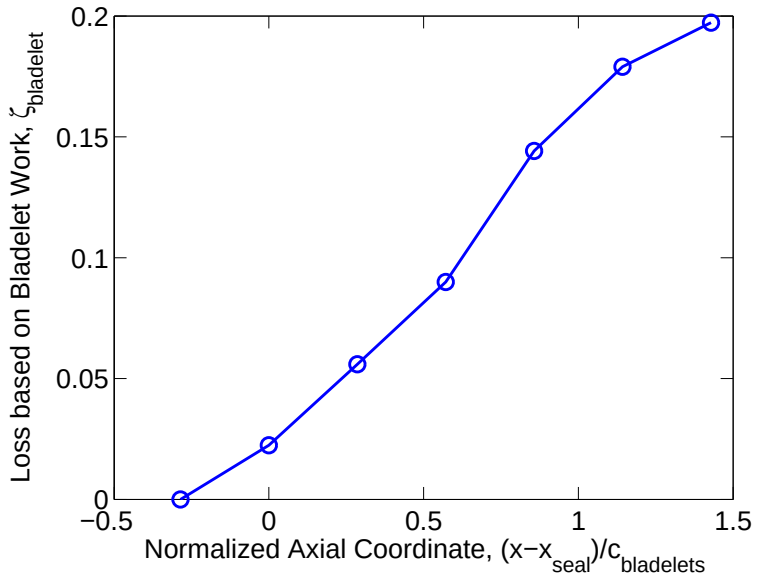

Figure 4-19: Loss accumulation through Hybrid Blade bladelets, normalized to the ideal bladelet work output.

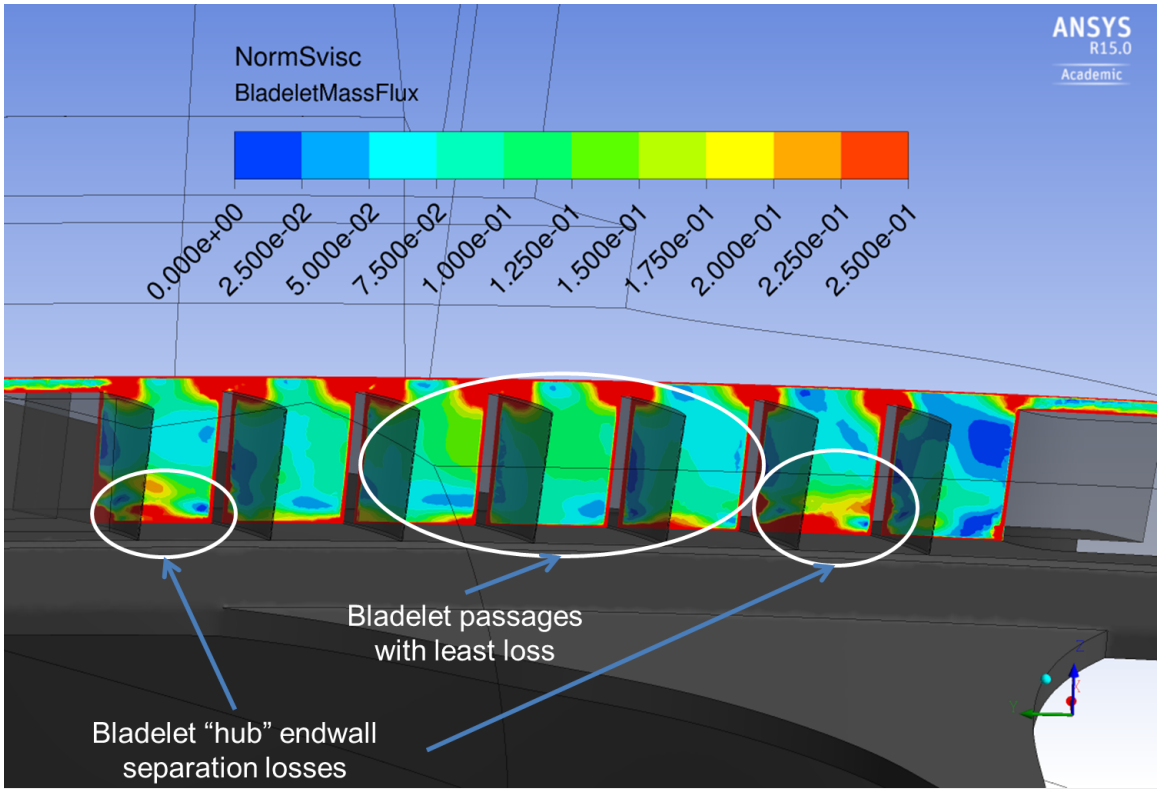

Figure 4-20: Contour of volumetric viscous entropy generation rate at bladelet mid-chord.

have moderate loss in the upper 50% span due to locally higher mass flux, as shown in Figure 4-21. In the generic shroud case, there is some minor fluctuation in the mass flow ingress distribution (recall Figure 3-10), but the cavity inlet is far enough upstream of the blade pressure side to keep the circumferential variation low. In addition, there is sufficient axial separation between the axisymmetric shroud leading edge and tip seal for the flow to begin a transition to uniform flow, re-attach, and form another toroidal vortex. Both the uniform cavity mass flow ingress and longer effective inlet length contributed to more uniform expected inlet conditions for the bladelet row if mounted on a generic shroud rather than the scalloped shroud configuration. In fact, the large 7.5x tip gap case demonstrates this expected uniform inlet streamtube with the generic shroud, as shown in Figure 4-4. The greatest sources of asymmetry leading to non-ideal bladelet inlet conditions are significant radial velocities in the outer bladelet passages and separation off the sharp corners of the shroud rail (see Figures 4-21 and 4-22). In fact, the three middle bladelet passages, downstream of the blade leading edge and longest portion of the blade shroud, most nearly exhibit the assumed flow uniformity. The contour in Figure 4-20 shows these are also the bladelet passages with the lowest volumetric viscous entropy generation rate. If the bladelet inlet flow field can be made more uniform and the bladelets optimized for low Reynolds numbers, it is conceivable that the bladelet loss can be reduced to the same level as the free expansion of the tip seal leakage jet, representing a bladelet efficiency of 90%. At this performance level, the reduction in mixing losses described in Section 4.3.2 would be reflected at the stage level.

4.3.4 Loss Increases in Hybrid Blade Main Flow Path: Stator Domain

Even if the bladelet losses can be reduced to the same loss level as the tip seal jet free expansion losses from the simple seal case, the cavity efficiency would only increase enough (an anticipated gain of 0.2%) so that the net change in overall stage efficiency would be negligible. The cavity efficiency gain would offset the efficiency penalties

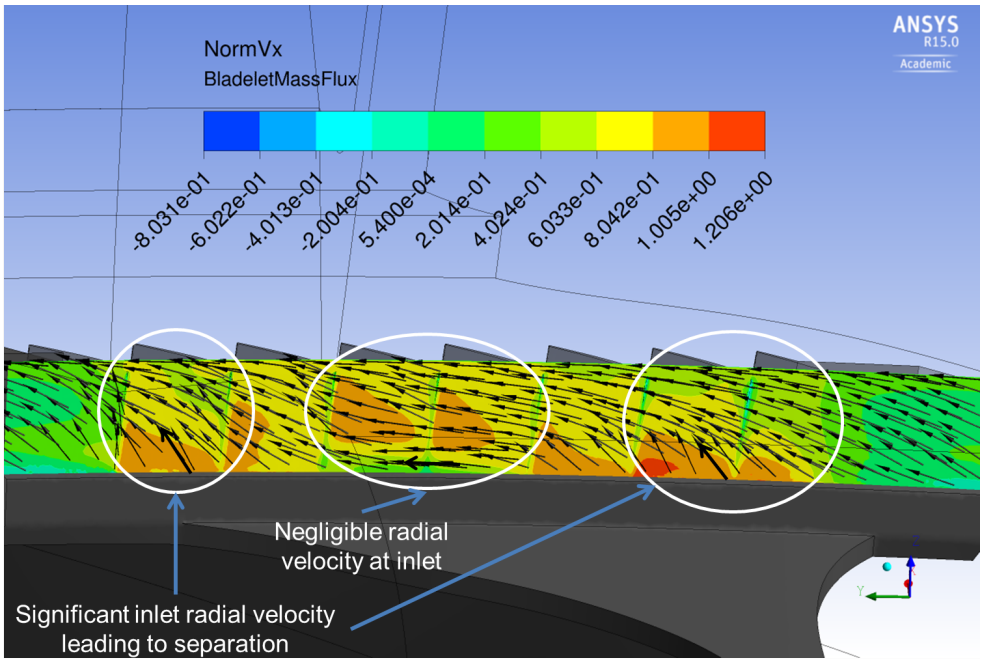

Figure 4-21: Contour on axial plane of normalized axial velocity at bladelet row inlet with overlaid tangential flow vectors (black arrows).

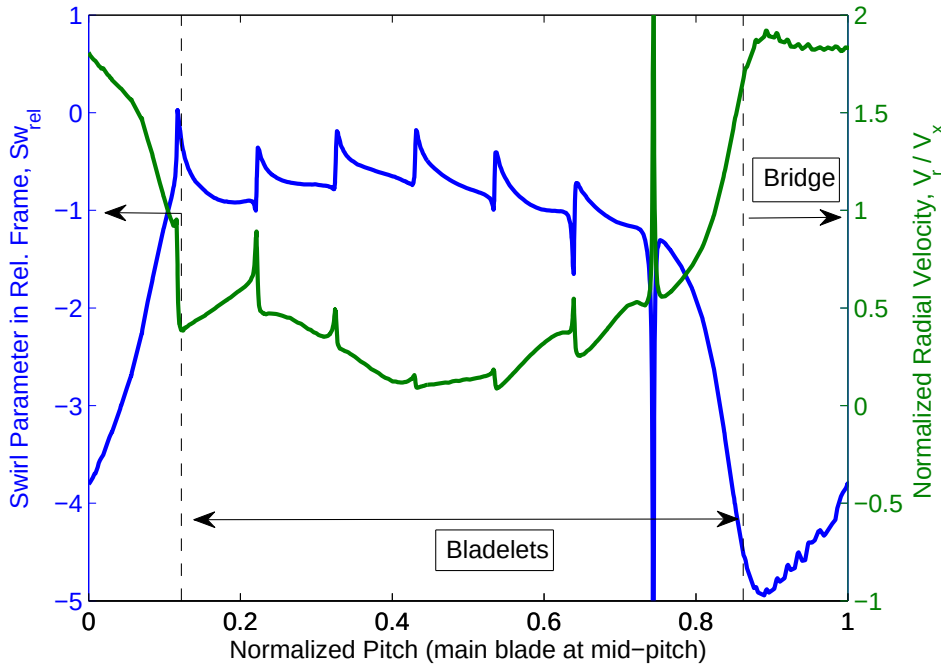

Figure 4-22: Circumferential variation at bladelet inlet, midspan, of relative swirl and radial velocity.

observed in the main flow path in Figure 4-11. The origin of these additional main flow inefficiencies is the topic of the next two sections, and it will be argued that they may be eliminated by proper design.

4.3.4.1 Origin of Increased Loss in Hybrid Blade Stator

The discussion will first focus on the stator domain which, according to Figure 4-11, includes an additional 0.1% debit in efficiency in the Hybrid Blade case compared to the simple seal configuration. Based on the axial distribution of loss accumulation, the reductions in efficiency accumulate to significant levels in the last $\sim 10\%$ of the stator chord. To localize these losses in the spanwise direction, a local loss coefficient can be defined reminiscent of Equation 1.7:

$$\zeta_{local} = \frac{\dot{W}_{loss}/\dot{m}_{stream}}{\dot{W}_{ideal}/\dot{m}_{stream}} = \frac{c_p \left(T_{t,TE} - T_{t,LE} \left(P_{t,TE}/P_{t,LE} \right)^{\frac{\gamma-1}{\gamma}} \right)}{c_p T_{t,LE} \left(1 - \left(P_{t,TE}/P_{t,LE} \right)^{\frac{\gamma-1}{\gamma}} \right)}, \tag{4.7}$$

where the local ideal work, $\dot{W}_{ideal}$, is always evaluated across the rotor (the ideal work output of the stator is 0 by definition). Equation 4.7 implicitly assumes no flow across streamlines so that each streamtube undergoes an isolated expansion process. Each isolated expansion process generates a small amount of loss, which then sums to the total loss over the entire span of the vane/blade. While not necessarily quantitatively rigorous near the endwalls, this approach does allow for qualitative comparison between configurations and provides insight into the spanwise range over which loss generation changes. Away from the endwalls where the inviscid flow assumption is valid and secondary flows minimal, Equation 4.7 can give a reasonable order of magnitude estimate for loss per unit mass flow of a given spanwise streamtube. Figure 4-23 plots the difference in local loss coefficient through the stator (Hybrid Blade case minus simple seal case). While there is a slight reduction in loss below midspan, there is a more significant increase in loss for the top half of the blade with local maximums above 80% span.

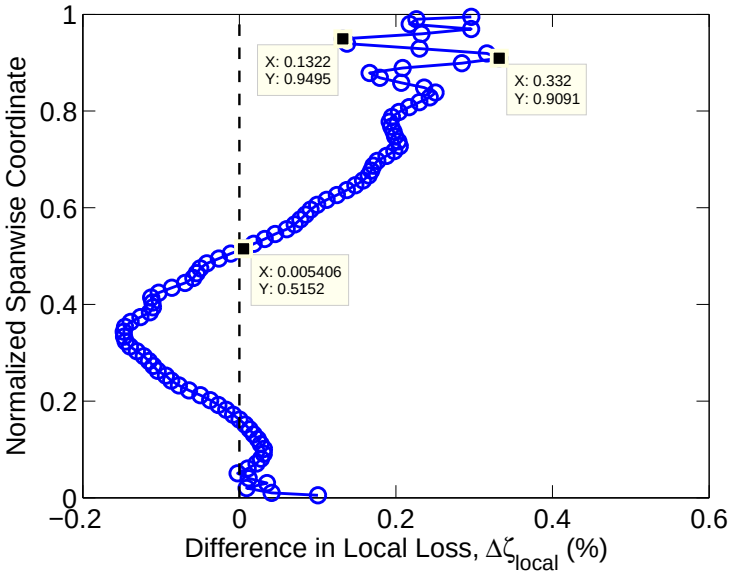

Figure 4-23: Spanwise variation of difference in local loss generation through stator (Hybrid Blade minus simple seal with scalloped shroud).

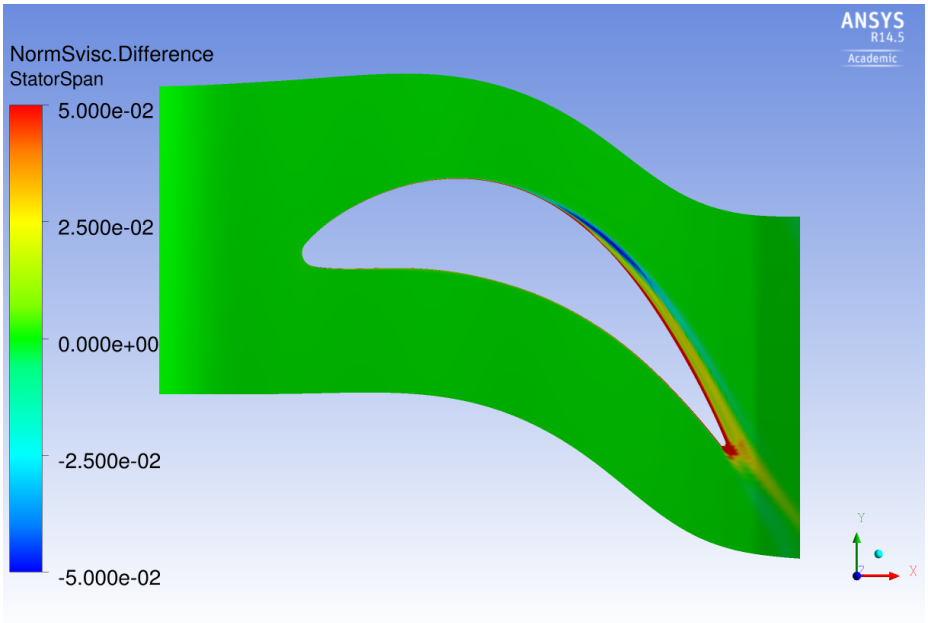

Figure 4-24: Contour of difference in volumetric viscous entropy generation rate in the stator at 95% span (Hybrid Blade minus simple seal with scalloped shroud).

Guided by the profile in Figure 4-23, contour plots of volumetric viscous entropy generation rate are created to isolate flow structures responsible for the increased loss. Figure 4-24, for example, shows the difference in volumetric viscous entropy generation rate (Hybrid Blade minus simple seal) at 95% span in the stator. The only difference appears in the boundary layer on the trailing edge portion of the airfoil suction side, extending downstream into the stator wake. The positive difference indicates an increase in loss generation, explaining the increased loss at the stator trailing edge and through the mixing plane (which would generate more loss when mixing out the stronger wake) observed in Figure 4-11.

Over-expansion of the main flow through the stator passage causes the increased boundary layer and wake loss observed in Figure 4-24. Figure 4-25 supports this finding by plotting the contours of difference in absolute Mach number between the two cases (again Hybrid Blade minus simple seal). The contour clearly demonstrates an increased flow Mach number through the downstream portion of the stator passage, and the beginning of this increased Mach number region coincides with the axial location of increased loss in Figure 4-24. In order to have this effect, however, the Hybrid Blade cavity must have a greater upstream influence than the generic shroud cavity since there was no significant variation in the stator flow field observed in the variable seal gap computations.

4.3.4.2 Quantification of Cavity Upstream Influence

The order of magnitude of the upstream influence of the cavity may be estimated using the Laplacian of a pressure perturbation, as done in [20] to estimate the length scale of upstream influence associated with a blade row:

$$\nabla^2 p' = \frac{\partial^2 p'}{\partial x^2} + \frac{\partial^2 p'}{\partial y^2} = 0, \tag{4.8}$$

One of the key properties of Laplace's equation is that it lacks an intrinsic length scale. Therefore, if the length scale in one direction is specified, it also sets the

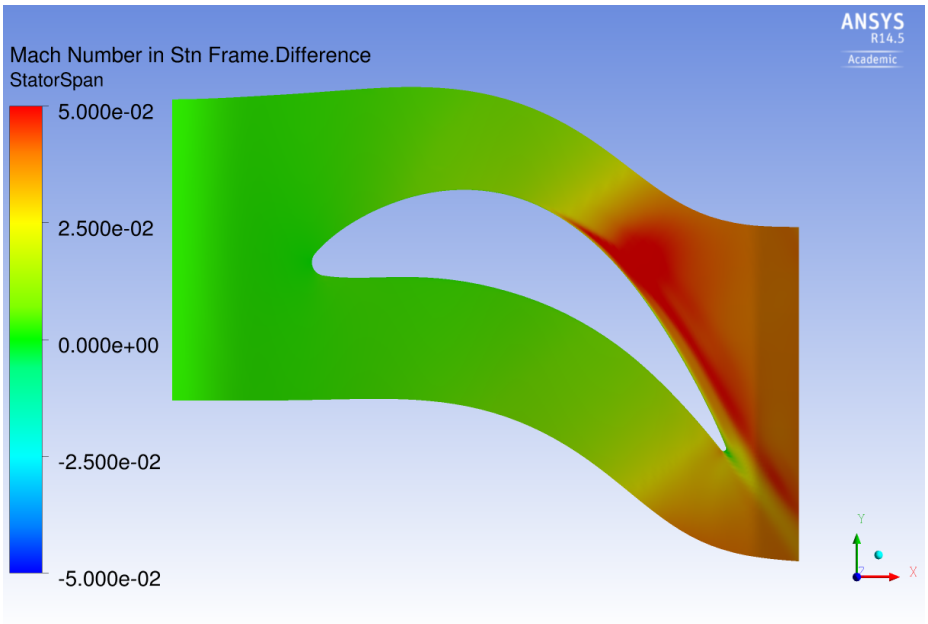

Figure 4-25: Contour of difference in flow Mach number in the stator at 95% span (Hybrid Blade minus simple seal with scalloped shroud).

length scale in the transverse direction. For example, if the length scale is specified in y, then the x direction must have the same characteristic length scale. While the generic shroud configuration is the only axisymmetric cavity geometry (i.e. only two characteristic length scales in axial and radial directions), Chapter 3 established that the controlling flow feature of the cavity inlet region is the inlet toroidal vortex. Even in the scalloped shroud with simple seal configuration, the circumferential variation of the cavity inlet toroidal vortex was minimal. Thus, for the purposes of analyzing the steady computations with a mixing plane approximation, the scalloped shroud geometries also have only two characteristic length scales (axial and radial) which must be considered.

These axial and radial length scales are set by the axial extent of the cavity inlet toroidal vortex and the radial height of the cavity inlet region, respectively. Their values were originally listed as part of Table 1.2 but are given here for convenience: The normalizations used in Table 4.3 were chosen for easy comparison of cavity and main flow characteristic length scales. For instance, according to Equation 4.8, the cavity radial length scale will set its length scale of upstream influence. Table 4.3 clearly demonstrates how the larger radial length scale in the scalloped shroud con-

Case	Cavity Inlet Axial Length, L_x (%span)	Cavity Inlet Radial Length, L_R (%blade spacing)
Generic Shroud	7	67
Scalloped Shroud	10.4	152

Table 4.3: Characteristic length scales of cavity inlet regions for each shroud configuration.

figurations can affect the stator flow field while changes in the cavity region in the generic shroud configuration do not. Specifically, the scalloped shroud radial length scale is 50% greater than the spacing between stator trailing edge and rotor leading edge while in the generic case the radial length scale is less than this spacing. The upstream influence is visualized in Figure 4-26 which plots the coefficient of pressure over the vane and blade for the generic shroud and scalloped shroud configurations (including the Hybrid Blade) with annotations marking the different length scales. The increased upstream influence of the Hybrid Blade's scalloped shroud cavity corresponds to the beginning of significant departure of the Hybrid Blade stator loading from that of the generic shroud configuration.

The simple seal with scalloped shroud has the same enhanced upstream influence. The effect, however, is more pronounced in the Hybrid Blade configuration due to the larger flow area over the tip and hence significantly greater proportion of main flow entrained by the Hybrid Blade cavity. In addition, the difference in cavity flow field between the Hybrid Blade and simple seal scalloped shroud configurations may explain why the former increases stator loss. The simple seal is designed to create a strong adverse pressure gradient to limit cavity ingress. The Hybrid Blade, on the other hand, not only has the larger flow area which enhances ingress, but also by definition sustains a favorable pressure gradient to allow the gas to expand and work to be extracted. Thus, the upper portion of the stator span sees a more favorable pressure gradient in the Hybrid Blade case, leading to the over-expansion and higher Mach numbers observed in Figure 4-25. This effect was not anticipated in the Hybrid

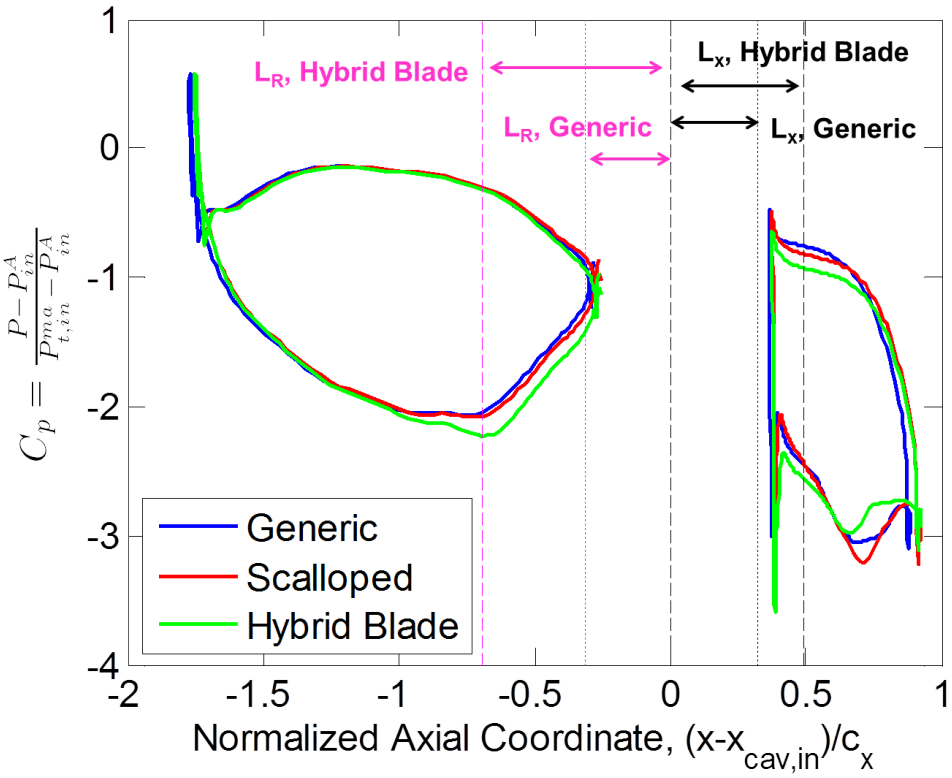

Figure 4-26: Distribution of coefficient of pressure, C_p, for main configurations overlaid with important cavity characteristic length scales.

Blade conceptual design, but it is reasonable that the nozzle guide vane, optimized for a drastically different cavity geometry, would not perform as efficiently with the Hybrid Blade configuration. As a result, it should be possible to recover the 0.1% of lost efficiency through the stator if the Hybrid Blade is taken to detailed design, as the vane could then be optimized for that cavity configuration.

4.3.5 Loss Increases in Hybrid Blade Main Flow Path: Diffuser

The remainder of the additional 0.2% increase in overall stage loss observed in Figure 4-11 is generated through the downstream diffuser. While the trend in Figure 4-11 implies that more loss is generated throughout the Hybrid Blade diffuser length compared to the simple seal case (technically true due to slightly greater dissipation in the diffuser shroud boundary layer), Figure 4-27 shows significant amounts of loss are generated in discrete regions. These finite regions of loss generation appear in several of the other tip shroud configurations as well but are only measurable in larger tip seal gaps such as the 1.8x and 7.5x tip gap cases (see Figure 4-28).

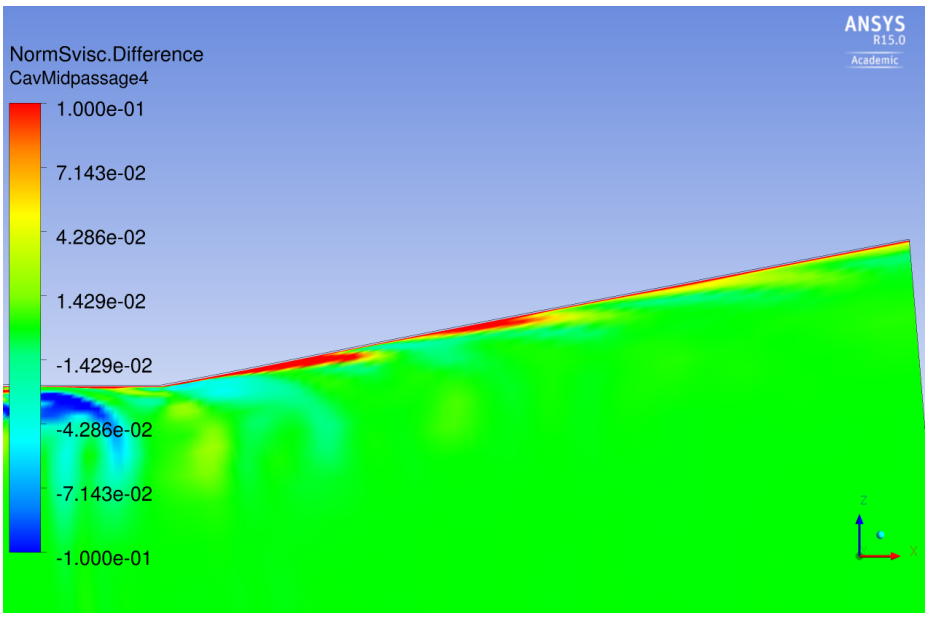

Figure 4-27: Contour of difference in volumetric viscous entropy generation rate near downstream diffuser endwall (Hybrid Blade minus simple seal with scalloped shroud).

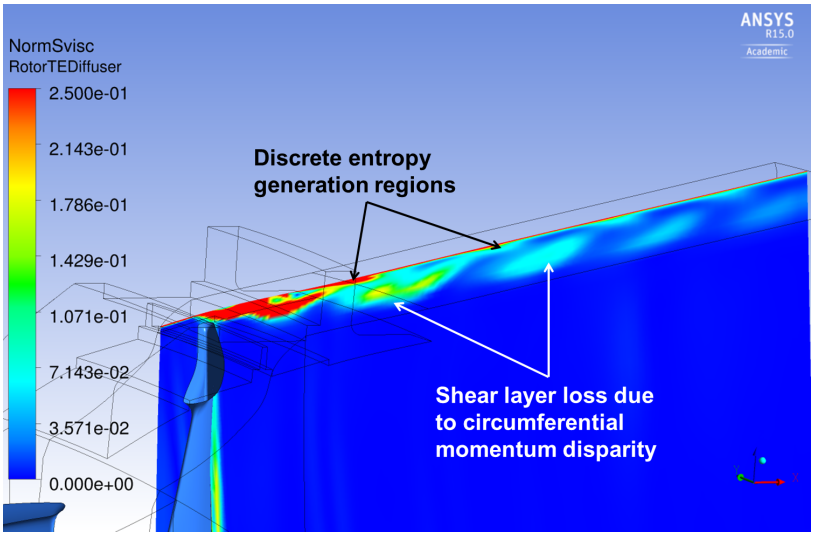

(a) 1.8x tip gap.

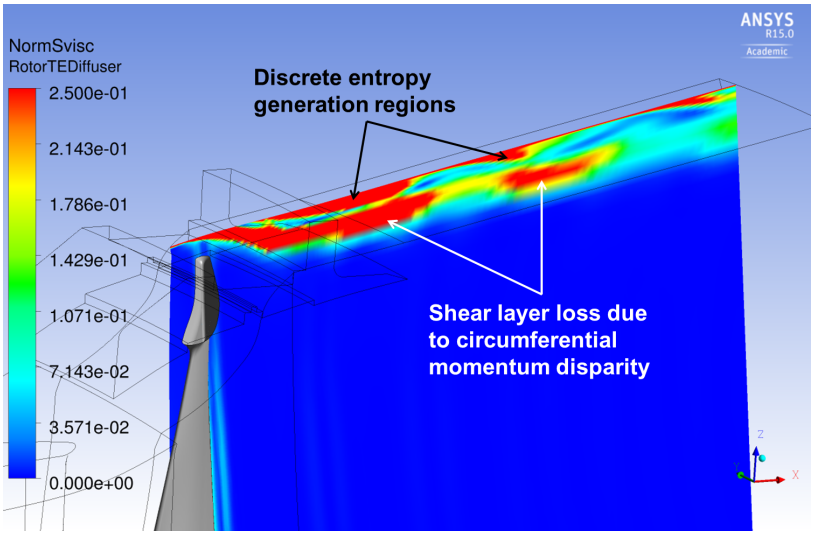

(b) 7.5x tip gap.

Figure 4-28: Viscous entropy generation rate near diffuser shroud endwall for large tip gap cases demonstrating existence of discrete loss regions.

These localized regions of loss generation near the diffuser endwall correlate spatially with an interaction between the rotor trailing vortex and the diffuser shroud endwall boundary layer. Specifically, the positive (clockwise swirling) blade trailing vortex causes convection of the negative (counter-clockwise swirling) vorticity boundary layer away from the endwall, as depicted in the circumferential vorticity contour in Figure 4-29 for the Hybrid Blade configuration. In this figure, the blade trailing

vortex is marked by the pink surface which bounds the vortex core at a constant magnitude of vorticity (i.e. isosurface of vorticity). This trailing vortex has both axial and circumferential components due to the high stagger of the rotor blade tip. As the swirl of the blade trailing vortex induces redistribution of the boundary layer, it draws low momentum fluid away from the wall into the higher momentum main flow. The mixing of these two fluids with differing momentum then generates entropy. For completeness, Figure 4-30 links the same vortex interaction to the discrete entropy generating regions observed in Figure 4-28. Again, the blade trailing vortex with positive circulation is marked by a pink surface of constant vorticity while the boundary layer is represented by the regions of negative vorticity (blue regions) in the contours.

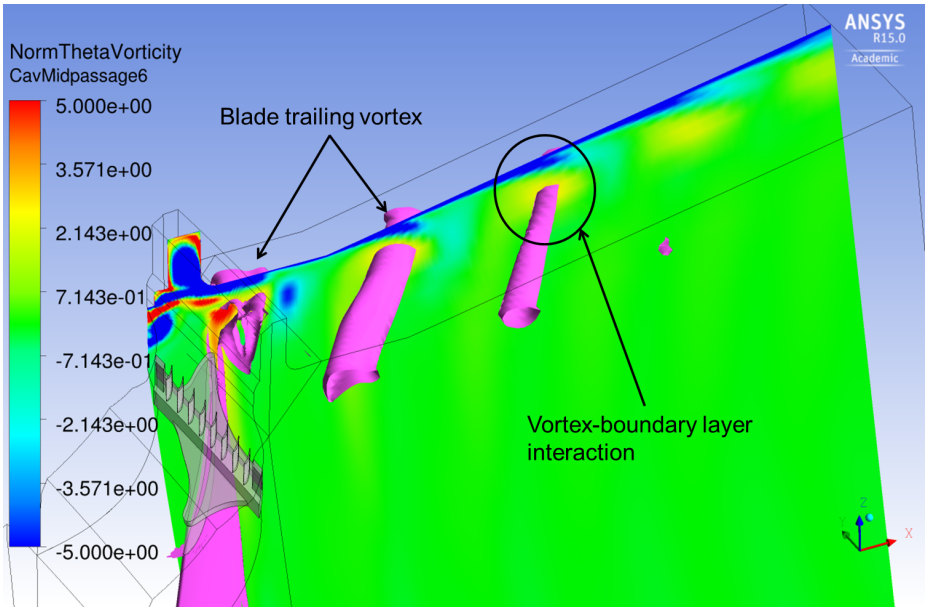

Figure 4-29: Contour of circumferential vorticity near downstream diffuser shroud endwall with isosurface bounding blade trailing vortex core, Hybrid Blade case.

While this interaction does generate entropy, it also benefits diffuser performance, especially in the Hybrid Blade configuration. The diffuser mated with this last stage has an aggressive opening angle, making boundary layer separation a significant concern. In the Hybrid Blade configuration, the flow near the endwall contains less momentum than in the simple seal case. Yet, it does not separate, and Figures 4-29

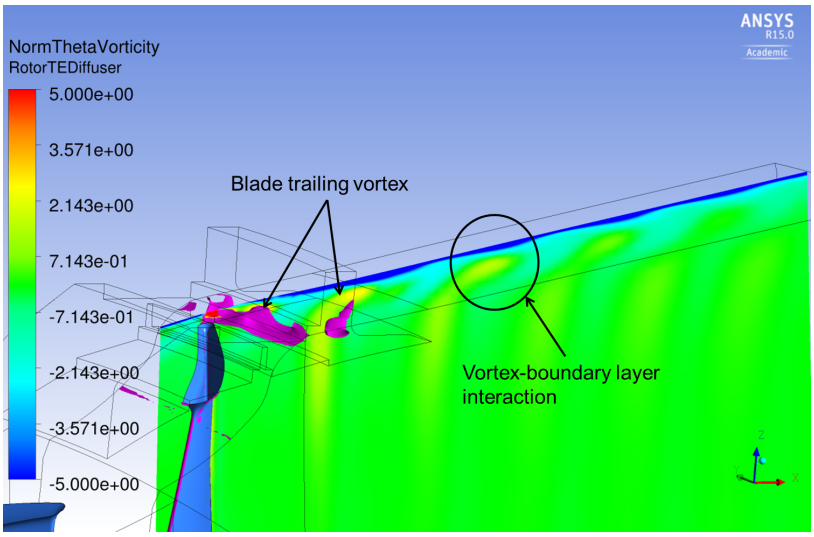

(a) 1.8x tip gap.

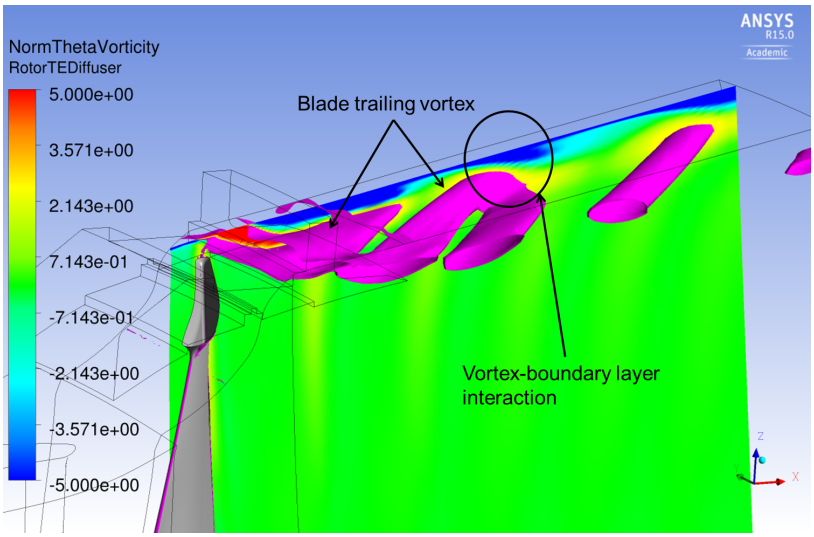

(b) 7.5x tip gap.

Figure 4-30: Contours of circumferential vorticity near downstream diffuser shroud endwall with isosurface bounding blade trailing vortex core, large tip gap cases.

and 4-30 imply that the vortex interaction increases the boundary layer resilience to separation. This increased resistance to separation is related to the intended function of leading edge extensions on aircraft. The entire purpose of leading edge extensions such as chines and strakes on fighter aircraft is to expand the range of achievable angle of attack before separation from the wing. The vortices they generate entrain high momentum fluid from the freestream flow and transport it to the wing surface, thereby energizing the boundary layer and delaying separation at high angles of attack [35, 36] (see Figure 4-31). Similarly, vortices near the endwall would transport higher momentum fluid from the inviscid main flow towards the endwall, energizing the boundary layer and allowing the use of a more aggressive diffuser. In Figures 4-29 and 4-30, the upstream side of the blade trailing vortex convects high momentum fluid toward the endwall while the evident convection of negative vorticity away from the wall represents removal of low momentum fluid from the boundary layer. Also apparent is the reduction in boundary layer thickness immediately downstream of each redistribution of negative vorticity from the endwall (the blue bulges diverging from the outer casings in Figures 4-29 and 4-30).

Like the stator loss associated with the Hybrid Blade, the increased debit in efficiency through the diffuser may be recoverable with proper design. While vortices to increase momentum transport in the endwall boundary layer are effective, it is not clear that the blade trailing vortex strength observed in the Hybrid Blade case is required to prevent boundary layer separation. If the strength of the blade trailing vortex could be reduced without causing boundary layer separation, it would also reduce the amount of low momentum fluid entrained into the mainstream, thus reducing the mixing with the main flow and associated viscous entropy generation. The next section will describe other proposed design modifications for a second iteration of the Hybrid Blade based on the computational results presented thus far. These recommendations are intended to eliminate/mitigate unintended loss sources induced by introduction of the Hybrid Blade design to further improve the efficiency.

Figure 4-31: Operational example of leading edge extension (i.e. strake) on a F-18 Super Hornet used to generate a vortex along wing upper surface to delay separation. *Source: Wikipedia,* ***http://en.wikipedia.org/wiki/Strake_(aeronautics)***

4.3.6 Synthesis of Loss Mechanisms and Definition of Performance Limits

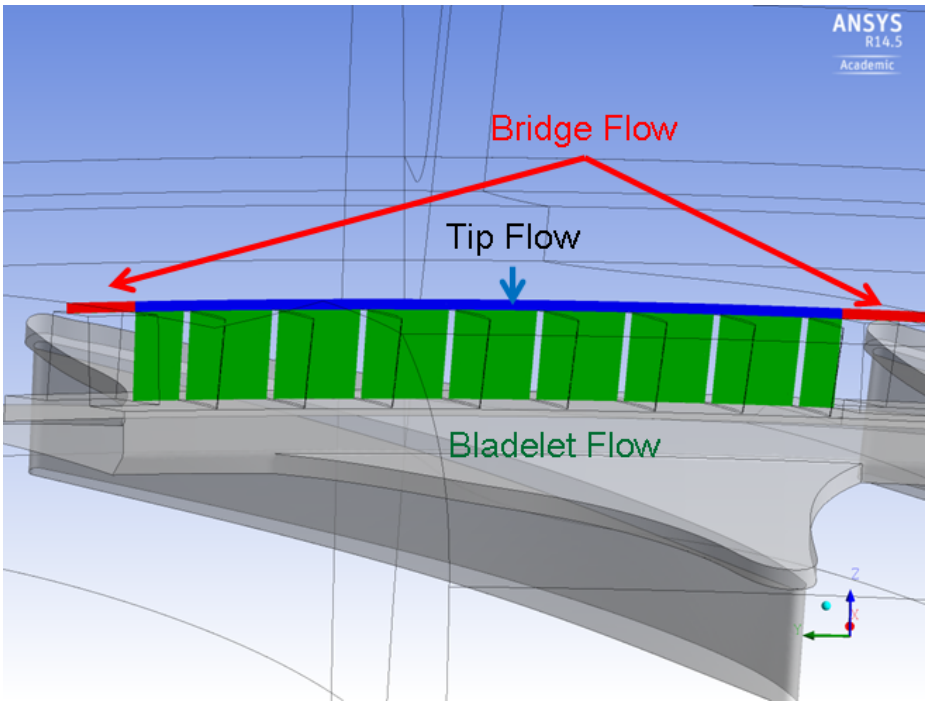

Figure 4-32: Classification of Hybrid Blade cavity flow components for extrapolation of performance with extension of intershroud bridge.

The loss scalings developed in Chapter 2 allow a more detailed extrapolation of the performance of the Hybrid Blade design. In doing so, requirements of bladelet efficiency for net stage performance gain can be quantified for the turbine stage under investigation in this thesis. The Hybrid Blade flow area can be split into several flow regimes to which the free expansion or mixing control volume analyses are then applied (see Figure 4-32). The portion of the cavity flow which passes through the bladelets ("Bladelet Flow" in Figure 4-32) is estimated to yield a viscous lost work proportional to the anticipated work output of the bladelets with the proportionality factor depending on the bladelet efficiency. After summing up the extrapolated viscous lost work, it can be divided by the ideal stage work output from the first iteration to get an estimate for the loss coefficient associated with the cavity. The primary assumptions in this analysis are:

1. The portion of flow over intershroud bridge (jet) mixes with main flow only (i.e. neglect mixing at intershroud bridge edges)

2. The flow through the bladelets mixes first with the bladelet tip flow. The resulting mixed flow then mixes with the main flow.

3. The mass flux through the bladelet passages is uniform, consistent with choked flow. Uniform mass flux also implies clean flow through the bladelet passages (i.e. no separation or high radial velocities as observed in Figure 4-21).

Assumption 3 uses choked flow because only a small decrease in flow area is required to reduce the Hybrid Blade flow area from 7.5 to 7 times the nominal gap flow area, the maximum flow area at which the gap is estimated to remain choked. The same assumption then allows the specification of a single independent variable, the percentage of pitch occupied by the intershroud bridge, which will set the mass flow rates of the various components of Hybrid Blade cavity flow. Then, applying the various control volume loss scalings, a parametric variation in expected cavity loss is created for a specified bladelet efficiency as shown in Figure 4-33.

The first feature of note in Figure 4-33 is the instantaneous increase in loss incurred when reducing the flow area from the value in the first iteration of the Hybrid Blade, as high as 0.5% for less efficient bladelets. This increase in loss manifests from two contributing factors: (i) increase in mass flow rate per unit area at choke means the reduction in flow area does not change cavity mass flow rate as significantly, and (ii) all loss processes occur at higher velocities due to the sonic condition. The second feature to note is that the simple scalings show that for bladelets which are approximately 82% efficient, there will be no net change in loss between a configuration with bladelets and a configuration with a simple seal. This is consistent with the findings from the computations on both Hybrid Blade configurations and the 6% effective tip gap analytical approximation in Table 4.1. The estimated value of 0.5% for the simple seal configuration produced by the application of these simple scalings is the same loss level calculated in the simple seal computations on the scalloped shroud, supporting the validity of this extrapolation approach. Based on the more detailed extrapolation

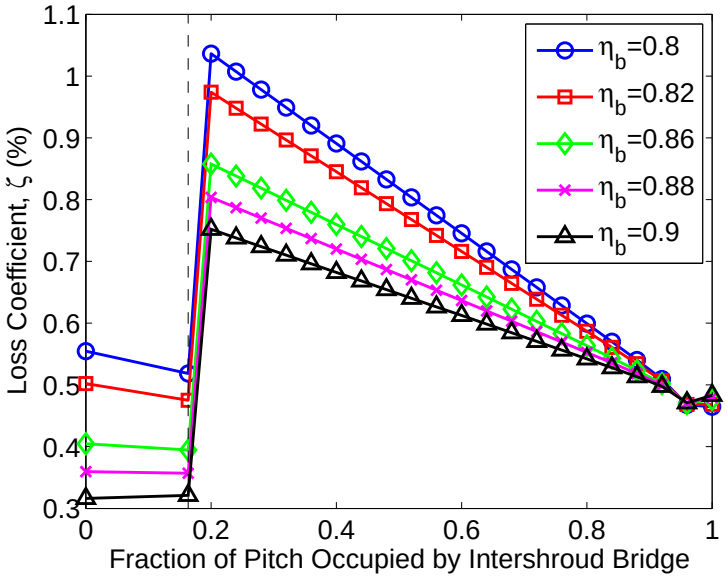

Figure 4-33: Extrapolation of overall cavity loss in the Hybrid Blade configuration versus proportion of cavity occupied by intershroud bridge. The black dashed line indicates the fraction of the pitch occupied by the intershroud bridge in the Hybrid Blade computations.

embodied by Figure 4-33, a bladelet efficiency of 90% (argued achievable in Section 4.3.3 based on results in [21]) will result in an improvement in stage efficiency of $\sim 0.15\%$. This is also consistent with the analysis of Figures 4-18 and 4-19. Thus it is recommended that the next design iteration on the Hybrid Blade concept focus on optimizing the bladelet design for low Reynolds number effects and reduction of bladelet inlet flow asymmetry to increase their efficiency to as close to 90% as possible.

The analysis which underlies the results presented in Figure 4-33 assumes that the Mach number trends of the variable seal gap cases hold despite the inclusion of the bladelets. However, the CFD results of the Hybrid Blade designs suggest the flow Mach number through the bladelets may be lower than anticipated based on the simple seal gap variation. Specifically, the flow areas in the Hybrid Blade design and the 7.5x tip gap case are the same, yet the Mach number near minimum area in the Hybrid Blade design is ~ 0.6 compared to 0.8 over the 7.5x tip seal. This, in turn, suggests that the Mach number through the bladelets may in fact be less than sonic even when increasing the proportion of the pitch occupied by the intershroud bridge. To estimate how the Mach number affects the simple scaling extrapolations, a linear

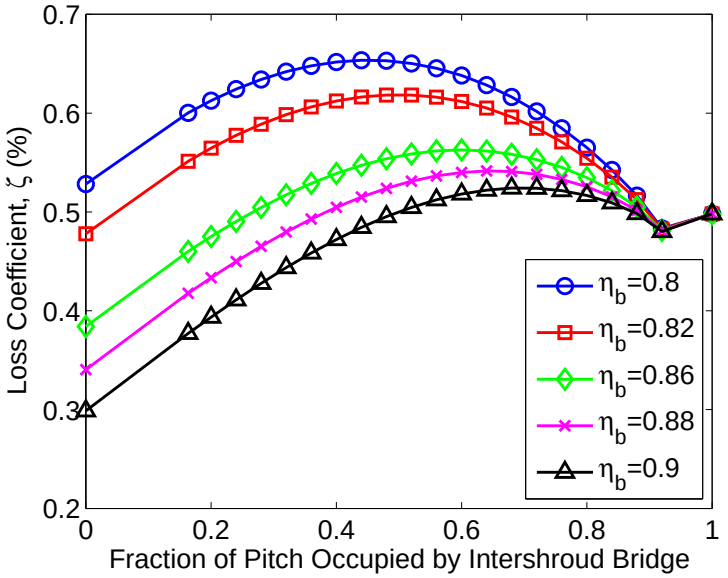

Figure 4-34: Extrapolation of overall cavity loss in the Hybrid Blade configuration versus proportion of cavity occupied by intershroud brdige with linearly varying bladelet Mach number.

increase in Mach number with intershroud bridge pitch fraction is incorporated into the analysis of Figure 4-33. The Mach number is assumed to linearly increase from 0.55 at the Hybrid Blade design point (20% pitch occupied by the intershroud bridge) to 1 at 90% pitch occupied by the intershroud bridge. The results of the simple cavity loss estimations using this assumed flow characteristic are presented in Figure 4-34. The magnitudes at the Hybrid Blade design point remained unchanged compared to Figure 4-33. While the sharp increase due to choking has been eliminated, the loss still increases to a maximum somewhere between the Hybrid Blade design point and the simple seal configuration. This is consistent with the thought experiment which requires that the flow area over the blade tip must drastically increase when using turning elements in order to improve overall efficiency. In addition, the bladelet efficiency threshold required to yield the same stage efficiency improvement of 0.15% is still 90%. The upper bound of stage efficiency improvement using the Hybrid Blades (assuming a bladelet efficiency of 96% to represent the limit of zero tip leakage flow) is estimated to be 0.28%.

4.4 Summary of Hybrid Blade Effectiveness at Mitigation of Cavity Loss Mechanisms

This chapter has examined in detail the performance of a modified cavity geometry proposed to mitigate the mixing losses at the cavity exit while simultaneously replacing the free expansion losses of the tip seal jet with different, potentially controllable loss mechanisms. Known as the Hybrid Blade, the design incorporates turning elements into the shroud geometry to reduce the circumferential momentum disparity at the cavity exit and extract work from the cavity flow. To help facilitate the design of the Hybrid Blade and extrapolate its performance, a novel approach to modeling the cavity influence on the main flow path was also developed. The major findings of these analyses are listed below.

1. The cavity influence on the main flow path can be modeled using a sink-source pair with finite separation. The line sink is located at the cavity inlet with source at the cavity exit, and their strengths are equal and opposite and set by the tip seal.

2. The Hybrid Blade design successfully reduces the cavity exit mixing losses (gain in efficiency of $\sim 0.15\%$). However this gain in efficiency is offset by greater bladelet profile loss compared to the free expansion loss of the tip seal jet in the simple seal configuration.

3. Regions of high separation and non-ideal incidence in the outer bladelet passages (near the intershroud bridge) generate some of the losses associated with bladelet profile loss. The remainder of the responsible bladelet profile loss is inherent in the bladelets' small size (due to low Reynolds number effects). It is argued that the bladelet profile loss may be reduced through detailed design and optimization of the bladelets for low Reynolds number and the asymmetric cavity inlet flow field.

4. The favorable pressure gradient and increased upstream influence of the Hybrid

Blade configuration leads to significant over-expansion at the stator trailing edge, increasing loss in the stator domain by 0.1% debit in efficiency. This loss in efficiency may be recovered by optimizing the stator design to the Hybrid Blade configuration instead of the simple seal. It also serves to emphasize the interaction effects between the cavity flow and main flow path, and the importance of accounting for these effects early in a holistic design approach for the stage.

5. Blade trailing vortices near the diffuser outer casing likely increase the endwall boundary layer's resilience to separation despite the reduction in flow momentum induced by bladelet work extraction. This vortex-boundary layer interaction also creates finite regions of higher loss near the diffuser shroud endwall relative to the simple seal configuration, accounting for a 0.1% debit in efficiency compared to the simple seal. The loss through the diffuser may be reduced by decreasing the strength of the blade trailing vortices while still avoiding separation in the diffuser.

6. The best achievable improvement is estimated to be $\sim 0.2\%$ through the reduction of the mixing losses at the cavity exit. The limiting flow processes are the profile and tip vortex losses associated with the bladelets. Synthesis of the loss mechanisms in the cavity estimates a required bladelet efficiency of 90% to realize this performance gain. If the bladelets could be manufactured with an ideal zero tip clearance, the upper bound of efficiency improvement is estimated to be 0.28%.

Chapter 5

Summary and Conclusions

This thesis assessed the aerothermodynamics of turbine tip shroud cavity flow with the overall goal of improving efficiency and component durability. Specific technical objectives were formulated which built upon each other in pursuit of this goal. First, the important aerodynamic loss and thermal loading mechanisms had to be identified and quantified. Next, their variation with important parameters also required quantification in the form of scaling rules to aid in the design process. Finally, using the developed scaling rules as a design tool, design strategies and geometric modifications were sought which would mitigate the losses or reduce lifetime-limiting thermal loads.

To interrogate the tip shroud flow physics, several sets of computations were performed, both steady Reynolds-averaged Navier-Stokes (RANS) computations with a mixing plane approximation as well as unsteady RANS (URANS) computations. These different sets of computations varied the tip shroud geometry (three different tip shroud configurations plus variation of tip gap height), the operating pressure ratio (by adjusting the static pressure outlet condition), and the mass flow rate of an injected sealing flow within the domain. All of these variations served to perturb the tip shroud cavity flow field in pursuit of the second technical objective. Namely, they were used to elucidate the scalings of the identified loss levels with relevant geometric and operating parameters. The important parameters characterizing tip shroud cavity flow include:

1. Tip gap-to-span ratio

2. Ratio of cavity inlet radial length scale to axial length scale

3. Ratio of cavity inlet radial length scale to main blade axial spacing

4. Fraction of total mass flow which passes through the cavity

5. Blade pressure ratio

6. Difference in cavity exit and rotor exit swirl parameters

In addition to calculations, simple control volume analyses contributed to the formulation of these loss scalings. One of the three tip shroud configurations modeled, the Hybrid Blade, was designed by the application of these loss scalings to estimate the possible efficiency gains of eliminating the cavity exit mixing losses.

The primary metric for performance is lost opportunity to do work via viscous entropy generation, quantified in terms of debits to component isentropic efficiency. Reported changes are small given the small tip gap-to-span ratio and cavity mass flow fraction in this configuration, but an effort to estimate the uncertainty in debit in efficiency yielded an expected uncertainty of $\sim 0.02\%$ (see Appendix B). To be conservative, only those changes amounting to at least 3 times this uncertainty are reported as significant (analogous to a 95% confidence interval). Since these changes are at least 0.06%, they are rounded to 0.1% according to common reporting practice in the literature.

In addition to the semi-random uncertainties inherent in the comparison of computations using debit in efficiency, the choice of turbulence model introduces additional systematic uncertainty to the reported findings. While the trends in overall loss remain unaffected, the details of each loss mechanism (i.e. free expansion of the tip jet, mixing between cavity flow and main flow, and inlet toroidal vortex losses) depend on the choice of turbulence model. Thus, the choice of turbulence model may affect the proportion of total loss attributable to each mechanism when attempting to divide loss generation into discrete processes. The chosen turbulence model, shear stress

transport (SST), conforms to industry-standard CFD best practices and is the suggested model for separated flows according to the solver's (ANSYS CFX) operational manuals. Nevertheless, there exists a need to assess the impact of the turbulence model on tip shroud cavity flow modeling.

While these uncertainties may modify the loss levels of each mechanism, the trends in loss generation within each mechanism (i.e. free expansion of the tip jet, mixing between cavity flow and main flow, and inlet toroidal vortex losses) are in accord with reported findings [7, 8, 11–14, 17] and analysis [10] in the literature. Specifically, the linear relationship between leakage fraction and stage efficiency penalty cited in References [8, 13] agrees well with the dependence found in this study. The present investigation divided this loss into two primary mechanisms of equal importance, in accord with the results presented in Reference [12] which also noted a near-equal split between cavity exit mixing and leakage losses within the cavity itself (see Chapter 2). The importance of the circumferential momentum disparity in the mixing loss level previously cited by References [7, 8, 11, 12] is confirmed, but the importance of other mixing factors such as leakage fraction and mixing stream velocities is also highlighted in the scalloped shroud and Hybrid Blade results (see Sections 2.2.3 and 4.3.6). Meanwhile, experiments and computational models in References [14, 16, 17] support the finding that unsteadiness can affect and enhance the cavity inlet toroidal vortex. The test rigs investigated in References [13,14,17] also serve as useful external test cases for the cavity inlet vortex operational limit model. Using the published data and rig specifications, this model quantitatively explains the different flow structures observed in the published flow fields (see Section 3.2.4.3).

In addition to agreement with published literature, the computational results herein agree with complementary control volume analyses presented in this thesis. The sensitivities in the control volume models may be estimated using a similar procedure as described in Appendix B. The control volumes are generic, so the derived scalings will also be generally applicable to different geometries provided the underlying assumptions are reasonable (see Appendices C and E). One exception is the choice of a single radial sealing fin for the free expansion of the tip seal jet model as

some tip shroud configurations use multiple sealing fins. Section 5.2.3 revisits this discussion of the model limitations in the context of recommendations for future work.

5.1 Main Conclusions

The main conclusions from this thesis which contribute to the current knowledge base, within the constraints of the aforementioned uncertainties and sensitivities, are as follows:

1. The tip shroud cavity flow incurs approximately 1% debit in efficiency per 1% main flow through the cavity, consistent with loss levels published in References [8,13]. The primary loss mechanisms with their corresponding loss level scalings have been synthesized for these and previously studied configurations in the literature, and they are:

   (a) Free expansion of the tip seal jet. The loss is proportional to fraction of main flow mass which passes through the cavity and scales with the stagnation pressure ratio across the tip seal.

   (b) Mixing at the cavity exit between cavity flow and main flow. The generated loss is a function of the mass flow rate through the cavity, the square of the velocity difference between streams, the product of the velocities at mixing, and the relative angle between the streams.

   (c) Frictional losses and shear layer mixing in the cavity inlet associated with vane-rotor interaction. The loss increases with increasing cavity inlet toroidal vortex average local swirl velocity (characterized by average vorticity and related to contained circulation and core size) and the fraction of ingested fluid which is recirculated into the main flow path.

   (d) The tip seal jet, mixing at cavity exit, and the vane-rotor induced flow unsteadiness each account for approximately one-third of the total loss (0.38%, 0.38%, and 0.25% debits in efficiency per 1% main flow through

the cavity, respectively). The proportion of total cavity loss attributable to the exit mixing process increases with increasing tip gap.

2. The main flow perceives the cavity as a sink-source pair. This provides a simple, direct way to estimate the main flow redistribution due to the tip shroud cavity.

3. The attributes of an effective tip shroud cavity include:

   (a) Minimal tip shroud cavity mass flow fraction and blade tip pressure ratio.

   (b) Zero difference in swirl parameter and velocity magnitude between the cavity flow and main flow.

   (c) Minimal cavity inlet volume with maximum allowable cavity inlet radial to axial length ratio while retaining a cavity inlet toroidal vortex.

   The Hybrid Blade design concept (shown in Figure 1-7) satisfies the second attribute while replacing the loss mechanisms which motivate the first and third attributes with different loss mechanisms. The Hybrid Blade as designed herein successfully recovers 1/2 of the loss associated with mixing in the Scalloped Shroud with knife-edge seal configuration, with a best achievable recovery of 2/3 of the mixing loss. However, this gain in efficiency is offset by the efficiency limits of the bladelets themselves. Examination of results in literature [21, 22] suggest that these losses can be minimized, and the improvement in overall stage efficiency recovered, by proper optimization of the bladelets for low Reynolds number flows and asymmetric inlet conditions.

5.2 Future Work

One of the stated goals of this thesis was the synthesis of knowledge regarding tip shroud cavity flow to delineate the major factors which influence turbine performance. While substantial progress toward achieving this stated goal was made, the results from this thesis suggest several avenues for potential future work to be elaborated in the following. These avenues fall into two basic categories: (i) configurations with

potential to improve flow characteristics and hence performance (see Section 5.2.1 and 5.2.2), and (ii) generalized scalings and understanding of flow physics (see Sections 5.2.3 and 5.2.4).

5.2.1 Optimization of the Hybrid Blade Configuration

The most immediate task for future work is the optimization of the Hybrid Blade configuration to realize the $\sim 0.2\%$ improvement in efficiency achievable by nearly eliminating the cavity exit mixing losses. In order to attain this improvement in efficiency, the bladelets should be optimized for low Reynolds number flow in an effort to reduce the profile and tip vortex losses which cancel out the efficiency gains in the current configuration. In addition, the stage must be redesigned to improve the matching of the upstream vane and downstream diffuser to account for the different effects of the Hybrid Blade influence as compared to the simple seal. Specifically, the favorable pressure gradient and significantly increased mass flow rate through the Hybrid Blade configuration causes an over-expansion in the stator tip region. Downstream, the large blade trailing vortex interacts with the boundary layer in the diffuser, generating shear loss. Matching of components should focus on preventing this upstream over-expansion and reducing the strength of the blade trailing vortex.

5.2.2 Free Expansion of the Tip Seal Leakage Jet

The Hybrid Blade concept proposed in this thesis endeavors to mitigate mixing losses at the cavity exit, replacing the free expansion loss of the tip seal leakage jet with equally inefficient bladelet profile losses in the process. However, this design only explicitly addresses one of the two primary loss mechanisms of the tip shroud cavity. The other, the free expansion loss, is generally accepted as a necessary penalty to minimize the cavity mass flow rate. Yet, there may be potential to address this loss as well.

Minimizing the cavity mass flow rate and generation of the free expansion loss are not necessarily linked inextricably. Small cavity mass flow rates are achieved simply

by minimizing the flow area over the tip seal for a given pressure ratio and relying on choking of the seal to limit the mass flow rate. The free expansion losses are a result of the conventional design choice to use sealing fins with their accompanying rapid area changes. More gradual area variation is generally prohibited due to stress concerns on the blade as the additional mass would significantly increase the centrifugal force the blade must counter. However, what if the sealing fin were attached to the outer casing rather than the shroud as proposed by Mahle et al. [37]? Mahle et al. proposed this reversed sealing fin design (radial fin on the outer casing, ablative honeycomb on the tip shroud) in order to increase the cavity flow velocity at mixing to improve efficiency for their particular geometry. Yet their design still used the conventional wisdom of rapid area changes.

Instead, this proposal of future work advocates a honeycomb insert on the tip shroud with radial sealing element on the outer casing, but including contouring of the sealing element to provide gradual flow area change (see Figure 5-1). Such a configuration should reduce the recirculation zones throughout the cavity and make the flow more uniform, significantly reducing the loss generated by the jet expansion process. The pressure ratio across the blade must be considered as well in this design. It was demonstrated in the design of the Hybrid Blade concept that the current pressure ratio, $P_{TE}/P_{t,LE}$, is well below the critical pressure necessary to choke the nominal tip seal gap. For a geometry like the one depicted in Figure 5-1, this would lead to further expansion of the flow downstream of the minimum flow area into a supersonic flow regime. In addition, this proposed geometry, as currently configured, makes no attempt at turning the cavity flow (the gradual area decrease precludes inclusion of turning elements either upstream or downstream on the shroud due to axial drift of the blade). As a result, the expected mixing loss at the cavity exit will be greater than that in the nominal tip gap case due to the increased velocity and circumferential momentum of the cavity flow at mixing (similar to the discussion in Section 2.2.3). Yet, there may be a way to avoid this increased mixing loss.

While the modified sealing geometry may prohibit the use of large physical turning elements, it may be possible to use aerodynamic features to accomplish a similar effect.

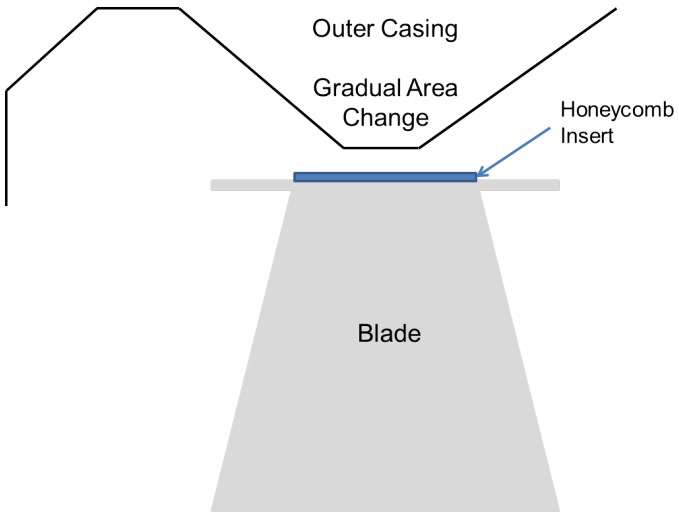

Figure 5-1: Schematic of gradual area change seal to limit mass flow rate while limiting free expansion losses.

Specifically, weak oblique shocks are often used in supersonic aircraft inlets to turn an incoming flow into the inlet duct while compressing it nearly isentropically. If cleverly-designed geometric additions could be added to the trailing edge of the tip shroud prior to interaction with the main flow, a system of weak oblique shocks may be able to turn and compress the flow in such a way as to minimize the mixing losses at the exit as well. This solution would lack the advantage of extracting work from the cavity flow, but it could reduce the losses generated by *both* tip jet expansion and cavity-main flow mixing. The kinetic energy deficits usually irreversibly converted to internal energy would instead be reversibly converted to mechanical potential energy in the form of higher static pressure.

The above proposal is acknowledged as conjecture requiring further analysis prior to computations (to inform both feasibility and design should it prove possible). Nevertheless, it is worth exploring as the options are few for mitigating free expansion losses while limiting cavity mass flow rate.

5.2.3 Further Generalization of Findings

Significant effort was expended to derive the loss scalings presented in Chapter 2 in terms of general flow properties or turbine design parameters. Subsequent chapters assessed their application to two distinctly different cavity configurations, demon-

strating their consistency with the more rigorous computational models. Nevertheless, they, and the main flow-cavity flow coupling model, were derived for a single sealing fin arrangement. As such, one potential area for future study would be the generalization (and perhaps modification) of these scalings to different seal configurations.

For example, both the tip seal free expansion and cavity exit mixing loss control volume analyses, as well as the sink-source pair model of the cavity, require some knowledge of the mass flow through the cavity. For a single sealing fin, this mass flow rate is quantified easily by the corrected mass flow relation. However, this expression will change if multiple sealing fins are used. The cavity coupling model only requires quantification of the mass flow rate. The loss scalings, on the other hand, also depend on specific flow properties with the additional complication that the free expansion process necessarily influences the downstream mixing process. One possible approach would be to develop a method for serial application of the free expansion loss equations to each sealing fin. The incorporation of the geometric scaling factor to account for incomplete mixing motivated in Section 2.2.1 may prove useful in this approach, though a linear dependence on this scaling factor is unlikely.

In addition to more complex sealing arrangements, further generalization of the findings contained in this thesis could include the investigation of the effects of choice of turbulence model on the loss levels and scalings. It was mentioned that the incomplete nature of the mixing processes in the cavity implies turbulence could have a significant effect on the computed loss levels. While the presented control volume analysis for each loss mechanism agreed with the loss levels calculated by the SST model used here, it may be of interest to verify other turbulence models have negligible impact.

5.2.4 Cavity Inlet Toroidal Vortex

In addition to the two identified primary loss mechanisms for simple tip seals (namely the free expansion of the tip seal jet and mixing losses at the cavity exit), several interesting flow phenomena with foreseeable or previously demonstrated impacts on

overall turbine performance were linked to the cavity inlet toroidal vortex. This flow structure dominates the cavity inlet region and controls loss levels and flow properties upstream of the tip seal, the fraction of cavity flow which recirculates and re-enters the main flow upstream of the blade, and, by extension, the secondary flows through the turbine tip region. Since the changes in loss levels and turbine performance were so small as to not be easily measurable, scaling rules were not derived for these mechanisms as was done for the free expansion or mixing processes. However, qualitative design guidelines were suggested based on a simple model of a vortex core with circular cross-section. This model was developed to explain the different operational regimes of the cavity inlet vortex observed in the present computations and in the literature. It was also used as a basis to describe how the unsteady flow phenomenon of vorticity redistribution in the cavity inlet may arise.

It is important to note that the cavity inlet toroidal vortex core in the present case is not circular, but rather elliptical, in cross-section. This distinction requires a modification of the simple radial equilibrium equations used in the model with a circular core if a more precise physical model is desired. Without this more precise physical model, Section 3.2.4 could only attempt a qualitative description of vortex equilibrium conditions. The rest of this section provides a suggestion on where to begin this analysis for any future work which may seek a quantitative scaling of inlet vortex effects on efficiency.

5.2.4.1 Quantification of Inlet Vortex Limits,

The expression for operational limits of the cavity inlet toroidal vortex derived in Section 3.2.4 explains the current computational results reasonably well and qualitatively explains the computational results of References [14, 17]. However, additional cases varying important parameters (e.g. machine radius, main flow swirl, cavity inlet axial length) in a systematic manner would be of value for assessing the utility of the derived limits. Such a systematic study would determine the limiting conditions within which the proposed analysis is applicable.

Furthermore, the stated limit for vorticity redistribution (i.e. Equation 3.6b) is

less rigorously defined compared to the other limits and may benefit from additional analysis. An alternate approach to determine the operational limit expressed in Equation 3.6b would be the vortex kinematics discussed in Sections 8.6 through 8.8 of [20] which references the work published in [29–31, 38, 39]. Hall [38] focuses on the effect of pressure gradients along a vortex core centerline on the core axial velocity and the relationship with core swirl. Cho [39] and Darmofal et al. [29] approach the core from the outside, examining vortex core response to external conditions (i.e. pressure perturbations) for unconfined and confined vortex cores, respectively. Pagan [30] and Delery [31] each published experimental data showing that vortex breakdown (i.e. core expansion and vorticity redistribution) occurs at a threshold of approximately 75% of the value calculated by the vortex models of Cho and Darmofal et al. The cavity inlet toroidal vortex is in reality a combination of all three of the situations studied by Hall, Cho, and Darmofal et al. It is partially confined by the turbine outer casing and tip shroud while also subject to a steady, oscillatory variation in shed circulation induced by the upstream vanes. However, it also is subjected to external pressure waves from the rotor potential field. In addition, since the shroud is rotating with the blade, the cavity inlet length may be changing in time (e.g. scalloped shroud) at a frequency equivalent to the rotor blade passing frequency. All of these researchers point to the vortex circulation as a stabilizing parameter against vortex breakdown (i.e. rapid core area expansion) due to these pressure gradients. This would suggest that the time-dependent vorticity distribution observed in [17] and Figure 3-22 is a balance between vortex circulation, blade loadings, core inlet characteristic lengths, and main flow swirl velocity (which sets the reference velocity on the toroidal vortex core axis). These important parameters (with the exception of blade loading) appear in Equation 3.10, but basing the derivation on the experimental work in [30, 31] and analytical work in [29, 39] may permit a more rigorous definition of the limit.

5.2.4.2 Quantification of Elliptical Vortex Cores

This thesis recommended designing cavity inlets to create toroidal vortices with elliptical rather than circular cross-sections. However, these guidelines were only qual-

itative based on trends in the presented computations and in the literature [14, 17]. Future work should focus on quantifying the optimum aspect ratio to minimize viscous losses on the cavity wall and the recirculating mass. To do this, a mathematical model of the vortex filament must be developed which quantifies the fluid properties and vortex kinematics. Such a model would also permit a quantitative description of the dividing streamline trajectory as qualitatively discussed in Section 3.2.4.

The suggested starting point for this analysis is the extensive and mathematically rigorous examination of curved vortices presented by Marshall [40]. This paper formed the mathematical basis for Darmofal et al. While the analysis is performed for vortices of circular cross-section, the methods used (namely, what Marshall calls a "directed curve model") are extensible to elliptical cross-sections as well. Essentially the directed curve model is a local coordinate system with a set of "balance" laws and constitutive equations that apply to the local coordinates themselves. The coordinates are described by a set of three orthogonal vectors called directors. It is these directors which must be modified to transition from a circular cross-section core to a core with elliptical cross-section as two of the directors describe what would be the major and minor axes of the ellipse. Completion of this suggested future work could then potentially identify the optimum aspect ratio of the cavity inlet toroidal vortex core to minimize frictional losses and mass recirculation.

Appendix A

Sensitivity of Results to Changes in Operational Back Pressure

This appendix presents the results for those computations which varied the operating back pressure of the stage. These results seek to answer the question of how cavity loss levels and scalings change, if at all, during off-design operation. While industrial power turbines will likely run at design conditions for the majority of their operational lifetime, off-design operation may occur, which in turn may affect how losses are generated. Operating conditions were changed by either lowering or raising the imposed back pressure as this is the more likely off-design operation condition for industrial power turbines. Varying the back pressure was also chosen as it directly relates to the free expansion losses of the tip seal jet as discussed in Section 2.2.1, and will influence the velocities in the mixing processes discussed in Section 2.2.2. The low back pressure case reduced the back pressure by approximately 14% of design (or -0.6 times the design diffuser inlet dynamic head), while the high back pressure case increased it by 10% (or $+0.4$ times the design diffuser dynamic head).

A.1 Variation of Generic Shroud Losses with Off-Design Operation

The presented results focus on the generic shroud configuration, first examining the effects under the steady mixing plane approximation and then in time-accurate computations. The effects on the scalloped shroud configuration are also briefly discussed.

A.1.1 Steady Off-Design Operation

The losses associated with the cavity for each back pressure case are plotted in Figure A-1. The off-design operating points result in slight reductions in efficiency, totaling no more than 0.1%. For the low back pressure, a portion of that change arises in the free expansion of the tip seal jet as expected from the discussion in Section 2.2.1, but the majority of the change appears in the mixing process. For high back pressure, there is a slight reduction in tip free expansion losses and mixing losses in CV1, but there is a significant increase in loss through the diffuser, presumably due to the stronger adverse pressure gradient. As these cases have no injected sealing flow, all the mixing is between tip seal leakage flow and main flow.

Since the flow velocities will increase, both in the cavity and the main flow, and since the blades are likely to over-turn the flow with the lower back pressure (see Figure A-2), the increase in mixing losses is to be expected (similar logic applies to the opposite trends in the high back pressure case). The higher velocities will increase the product of velocities term in Equation 2.8 while the over-turning will increase the circumferential velocity difference, thus raising the magnitude of the squared velocity difference as well.

The free expansion losses of the tip seal leakage jet can be directly quantified as follows. In Section 2.2.1, this loss was shown to depend strongly on the cavity mass flow fraction. Equation 2.4 and the findings of Cunningham [3] both indicate that the pressure ratio across the tip affects both cavity mass flow fraction and the total loss. Specifically, Equation 2.4 states that the loss should be proportional to $\dot{m}_{f_{cav}} \ln \pi_t$.

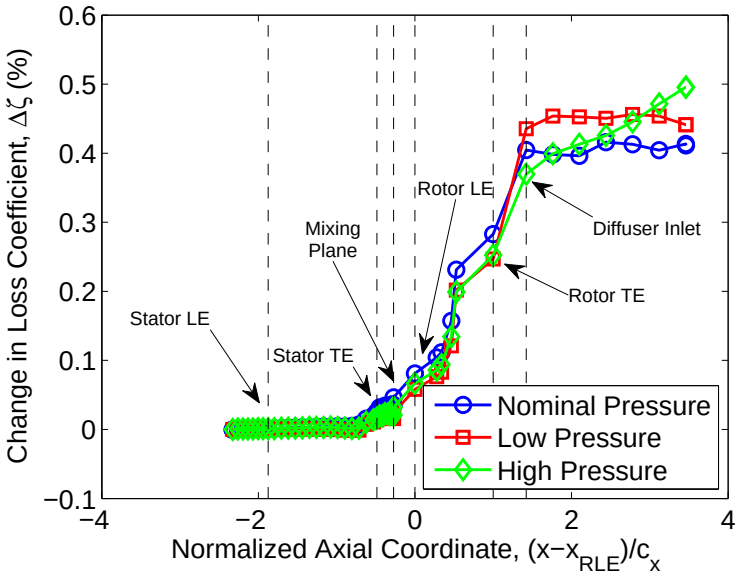

Figure A-1: Variation of axial accumulation of loss at different operating conditions.

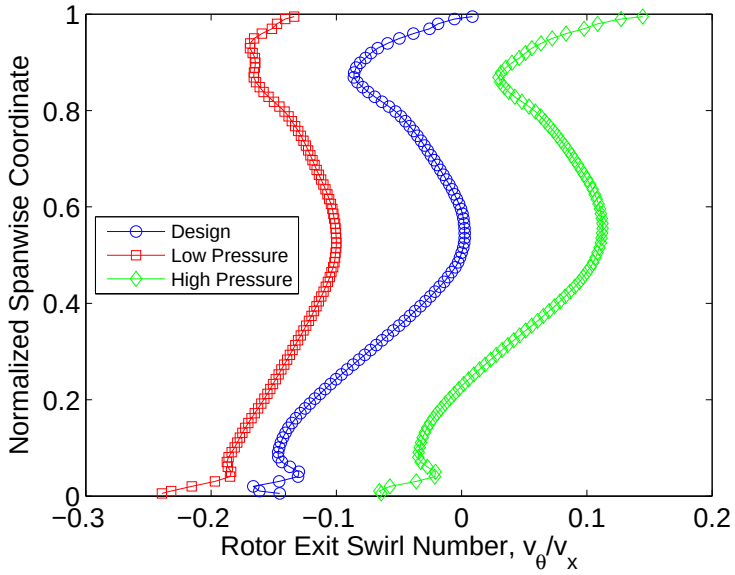

Figure A-2: Spanwise profiles of swirl at the rotor exit. Negative swirl indicates over-turning of exit flow. Positive swirl indicates under-turning of exit flow.

Indeed, Figure A-3 shows that the loss associated with the free expansion of the tip seal jet is linearly proportional to this product. This same figure also plots a data series with independent variable as simply $\ln \pi_t$, and this data series displays an even closer 1-to-1 correspondence between change in design value and change in resultant loss. This is because while the mass flow fraction over the tip seal does change slightly with operating condition, the magnitude of the change is much less than that in the pressure ratio across the blade row. This suggests that when applying Equation 2.4, the variation in mass flow fraction will dominate for changes in tip geometry or inlet stagnation properties while variation in the pressure ratio term dominates for changes in operating condition.

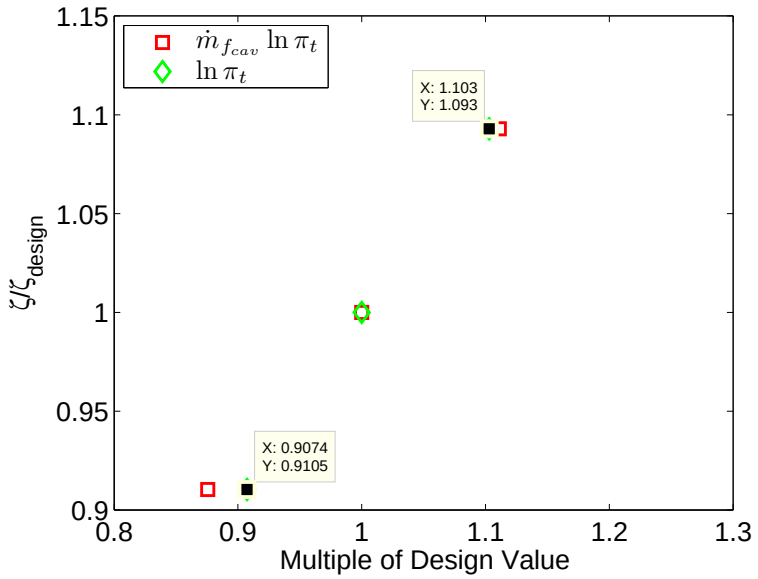

Figure A-3: Variation of free expansion losses at different operating conditions.

The off-design cases demonstrate that no additional cavity loss mechanisms arise when operating away from the design back pressure with the exception of slight increase in loss in the diffuser for higher pressures. In addition, the scalings proposed in Section 2.1 may be used to estimate the change in loss at these off-design points.

A.1.2 Sensitivity of Vane-Rotor Interaction Effects to Off-Design Operation

Having explored in Chapter 3 how the tip shroud cavity flow field changes when allowing for NGV-rotor interaction, the response of this interaction subject to off-design conditions merits a brief discussion. In short, losses due to the NGV-rotor interaction remain essentially unchanged during operation at off-design back pressures. Figure A-4 shows that the loss profiles for the two off-design conditions trace well the loss profile at design. While there is some variation in the axial accumulation of loss and in overall stage debit in efficiency, the differences are negligibly small (i.e. $\leq 0.05\%$ difference in debit in efficiency). In addition, it is worth noting that these differences (which arise in the diffuser) are small despite large changes in back pressure compared to the diffuser inlet dynamic head. Specifically the low back pressure case lowers the pressure compared to the nominal case by 60% of the nominal diffuser inlet dynamic head while the high back pressure case increases the pressure by 40% nominal diffuser inlet dynamic head. Therefore the effects of NGV-rotor interaction remain the same as those analyzed throughout the rest of this chapter.

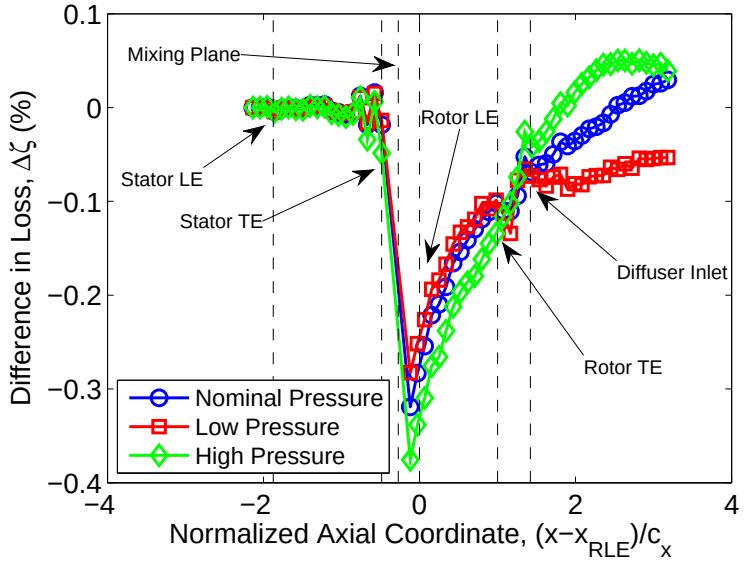

Figure A-4: Axial profiles of difference in loss accumulation between time-averaged unsteady and steady cases at different back pressures.

The explanation likely lies in comparison of the reduced frequencies in these cases, defined as:

$$\beta = \frac{\omega L}{U}, \tag{A.1}$$

where ω is the radian frequency of the unsteadiness; L is a characteristic length scale; and U is a characteristic flow velocity. Since the geometry and rotor speed (which sets ω) remained unchanged between cases, U is the only variable in Equation A.1 which changes. Even in the diffuser where the influence of the back pressure is greatest, the average flow velocities vary by only $\sim 1\%$. This implies that altering the radian frequency which characterizes the system unsteadiness (i.e. the blade passing frequency) would be more important in affecting contributions to loss of unsteady interactions and operation at off-design conditions. However, industrial power turbines like the one under investigation here spend the vast majority of their operational lifetimes at design conditions to maximize electrical power output. In addition, as demonstrated in Section 6.3.1 of [20], favorable pressure gradients such as those found in nozzles and turbine stages tend to dampen the effects of unsteadiness. Based on this reasoning, focusing on the analysis of unsteady effects in turbine tip shroud cavity flows at design conditions is sufficient for identifying and quantifying the primary flow features involved.

A.1.3 Off-Design Operation and Shroud Asymmetry

When operating the scalloped shroud configuration at the off-design back pressures with a mixing plane approximation, the trends in the primary loss mechanisms remain unchanged compared to nominal back pressure operation. Figure A-5 plots the difference in axial accumulation of loss between the scalloped shroud and generic shroud at the various operating back pressures. The trends for both low and high back pressure (relative to design) operating points follow the same pattern as the nominal design pressure case: negligible overall difference in loss across the stage but

with slight reduction through the stator offset by slight increase through the rotor and cavity. The axial variation is of similar magnitude and trend at all three operating points, suggesting that the free expansion losses and mixing losses behave similarly as described in Chapter 2 for the nominal back pressure operating point. As such, there is no evidence of coupling between the shroud asymmetry and changes in operating back pressure.

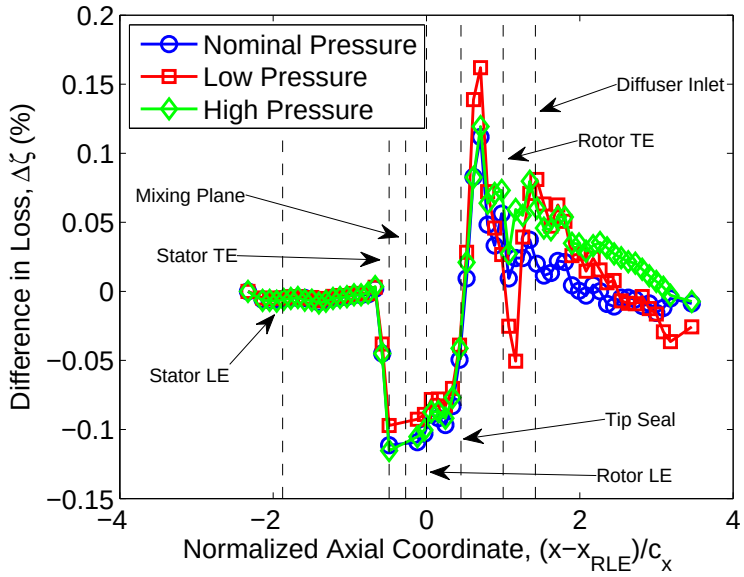

Figure A-5: Difference in accumulated loss as a function of axial coordinate, scalloped case minus generic case, at various operating back pressures.

A.2 Summary of Off-Design Operation Results

The findings from the computations simulating off-design operation are:

1. Operation of the stage at roughly ±10% of the design back pressure only results in a 0.1% increase in lost efficiency. This change in loss agrees well with the simple scalings posited in Chapter 2.

2. The NGV-rotor interaction is negligibly affected by variation of operating back pressure, suggesting variation of rotor speed is the primary way of affecting the unsteady interaction for a fixed geometry.

3. No evidence was observed to support a coupling between shroud asymmetry and changes in operating back pressure to generate additional loss or new loss mechanisms.

Appendix B

Estimation of Uncertainty in Loss

This appendix endeavors to estimate the error associated with the viscous lost work loss quantification approach described in Section 1.4. Typically, residuals are used to quantify error, but since CFX non-dimensionalizes its residuals by some obscure and indeterminate factor, other methods must be used. The method used here is based upon traditional error estimation for experimental research. Since this thesis is built around comparison of one case to another to determine loss level scalings to improve component design, systematic errors will be canceled out. Thus, all error is associated with "random error".

In computations, random error refers to variations in solution properties once the solution is considered converged[1] as these errors give the uncertainty in the important flow properties like pressure, temperature, etc. To demonstrate this uncertainty, Figure B-1 plots the variation in two sample monitor point properties as a function of timestep for a steady calculation which has reached a converged solution. Variation of all properties follow similar trends as either Figure B-1a or Figure B-1b, depending on location. There were a total of 8 monitoring points defined, each measuring all the important flow variables. These points were located at the stator trailing edge at both midspan and tip, rotor leading and trailing edges at both midspan and tip,

[1]Computation is considered converged when all RMS residuals are less than 1×10^{-4} and all monitor points have constant or periodic properties.

and 2 points within the cavity inlet. Monitor points at the cavity inlet plane and rotor trailing edge tip have similar time histories to Figure B-1a. On the other hand, monitor points at the stator trailing edge (midspan and tip), rotor leading edge tip, and rotor trailing edge at midspan follow the trend depicted in Figure B-1b.

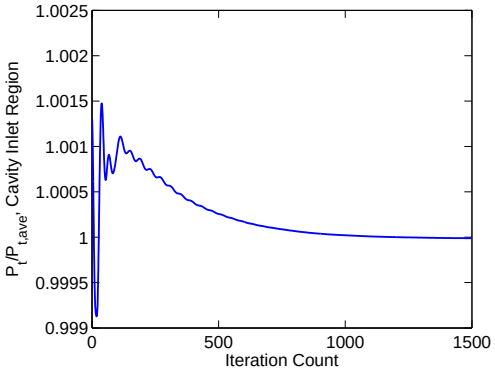

(a) Variation of P_t in the center of the cavity inlet region.

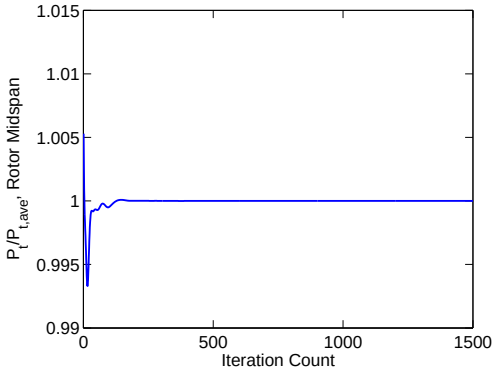

(b) Variation of P_t at the rotor leading edge, midspan.

Figure B-1: Varition of sample flow property at two example monitor points for a well-converged steady, generic shroud configuration computation.

The uncertainty for a particular property is taken as 3 times the averaged standard deviation of all the monitor points throughout the domain (the factor of 3 is used to define a better than 95% confidence interval). Using this estimated uncertainty, traditional error propagation techniques are applied according to Taylor [41] to estimate the uncertainty in the loss coefficient, ζ. Since ζ depends on averaged stagnation properties, and the uncertainties cannot be propagated through these averages, it is assumed that the uncertainties of the averaged values are the same as those in the local properties from the monitor points. The error propagation formula is given by:

$$\delta f = \sqrt{\sum_i \left(\frac{\partial f}{\partial x_i} \delta x_i \right)^2}, \tag{B.1}$$

Recalling the definition of loss coefficient, ζ:

$$\zeta = \frac{\dot{W}_{visc,loss}}{\dot{W}_{ideal}}, \tag{B.2}$$

it is evident that estimating the uncertainty in Equation B.2 first requires quantification of the uncertainties in $\dot{W}_{visc,loss}$ and $\dot{W}_{ideal}$. The expressions for viscous lost work and ideal work output are given by:

$$\dot{W}_{visc,loss} = \dot{m} c_p \left(T_{t,2}^{ma} - T_{t,1}^{ma} \left(\frac{P_{t,2}^{wa}}{P_{t,1}^{wa}} \right)^{\frac{\gamma-1}{\gamma}} \right), \tag{B.3}$$

and

$$\dot{W}_{ideal} = \sum \dot{m}_i c_p (T_{t,i}^{ma})(1 - (\frac{P_{t,out}^{wa}}{P_{t,i}^{wa}})^{\frac{\gamma-1}{\gamma}}), \tag{B.4}$$

Equations B.3 and B.4 show that the uncertainties in $\dot{W}_{visc,loss}$ and $\dot{W}_{ideal}$ will depend on stagnation pressure and temperature and the mass flow rate. For example, the uncertainty in $\dot{W}_{ideal}$ is given by:

$$\delta\dot{W}_{ideal} = \sqrt{\left(\frac{\partial \dot{W}_{ideal}}{\partial \dot{m}} \delta\dot{m} \right)^2 + \left(\frac{\partial \dot{W}_{ideal}}{\partial T_{t_1}} \delta T_t \right)^2 + \left(\frac{\partial \dot{W}_{ideal}}{\partial P_{t_1}} \delta P_t \right)^2 + \left(\frac{\partial \dot{W}_{ideal}}{\partial P_{t_2}} \delta P_t \right)^2}, \tag{B.5}$$

The expression for the uncertainty in ζ can then be written as:

$$\delta\zeta = \sqrt{\left(\frac{\partial \zeta}{\partial \dot{W}_{visc,loss}} \delta\dot{W}_{visc,loss} \right)^2 + \left(\frac{\partial \zeta}{\partial \dot{W}_{ideal}} \delta\dot{W}_{ideal} \right)^2}, \tag{B.6}$$

Substituting in the relevant partial derivatives and uncertainties into Equation B.6,

the cumulative error in loss, $\delta\zeta$, over the stage is estimated to be 0.02% for the steady, generic shroud configuration with no injected leakage flow. Traditionally in experimental research, random errors are taken as normally distributed so that 95% of measured values will fall within $\sim$ 2.78 standard deviations of the true value. Assuming a similar level of desired confidence (as was done in the uncertainties of individual flow properties), a minimum threshold to report a difference in stage loss is taken as 3 times the calculated uncertainty in loss, or 0.06%. For the purposes of reporting results, this difference will be rounded up to 0.1% as convention holds that efficiencies should be reported only to the precision of 0.1%.

Appendix C

Control Volume Estimation of Free Expansion Losses

This appendix details the derivation of the tip seal jet free expansion loss scaling presented in Section 2.2.1. The approach is based on a simple control volume analysis which estimates the entropy change due to stagnation pressure loss during the free expansion process.

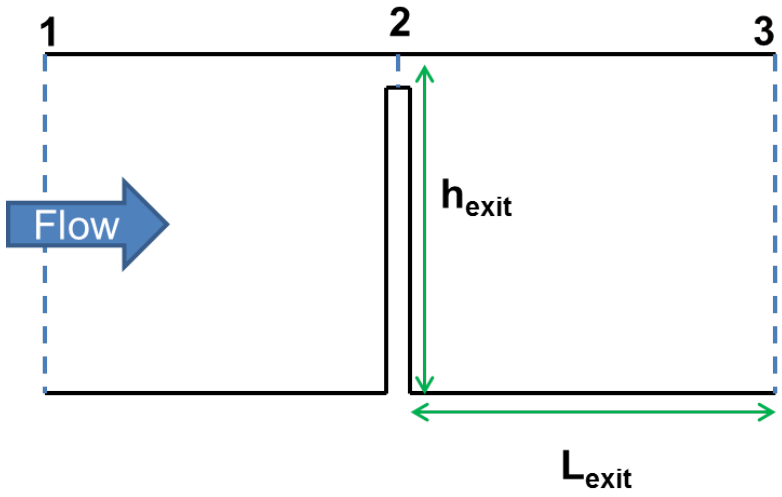

Figure C-1: Schematic of simple contraction at the tip seal with an incoming swirling flow.

To begin, consider the simple area contraction shown in Figure C-1 with a control

volume defined by the control surfaces at stations 1 and 3 and the solid walls at top and bottom. Within this control volume, the following assumptions are applied to guide and simplify the analysis:

1. The flow is isentropic between stations 1 and 2.
2. Contraction coefficient at the orifice is approximately 1 (i.e. $A_{throat}/A_2 = 1$).
3. Inlet and exit areas are the same (i.e. $A_1 = A_3$).
4. The meridional velocity is sonic at station 2 (consistent with choked flow).
5. The change in radius of the streamlines from station 1 to 2 and station 2 to 3 is small compared to the radius (i.e. $\Delta r/r \ll 1$).
6. No external torque applied by the boundaries, nor energy exchange (heat transfer or work input/output) with the environment.
7. Streamlines of flow leaving station 2 are initially parallel just downstream of the area contraction.

It follows from assumption 6 that the angular momentum of the fluid is constant from inlet to exit. Since the change in radius is negligible as stated in assumption 5, the circumferential velocity of the flow is also constant, $v_\theta = v_{\theta_1} = const.$ There are 4 other unknowns of the final state which are required to calculate the loss due to free expansion: P_3, T_3, u_{m_3}, and ρ_3. Thus, 4 equations are required, and those 4 equations will be the conservation of mass, conservation of linear momentum, and conservation of energy equations plus the ideal gas equation of state.

Applying continuity, the first equation for the control volume is found:

$$\rho_3 u_{m_3} = \frac{A_2}{A_3}\rho_2 u_{m_2} = \frac{A_2}{A_3} P_2 \sqrt{\frac{\gamma}{RT_2}}, \tag{C.1}$$

where assumption 4 has been used to replace u_{m_2} with the speed of sound as defined as $a^2 = \gamma P/\rho$. Next, conservation of momentum in the axial direction is applied for steady flow:

$$\int_{CS} \rho \vec{v} \vec{v} \cdot d\vec{A} = \int_{CS} P d\vec{A} + \vec{F}_{body}, \tag{C.2}$$

Substituting in the values at each station, the conservation of momentum expression between stations 2 and 3 becomes:

$$P_3 A_3 + \rho_3 A_3 u_{m_3}^2 = P_2 A_3 + \rho_2 A_2 u_{m_2}^2, \tag{C.3}$$

The appearance of A_3 on the left-hand side of Equation C.3 is a result of assumption 7 which requires a uniform static pressure over the entire cross-sectional area immediately downstream of station 2. Equation C.3 can be re-arranged to yield:

$$P_3 + \rho_3 u_{m_3}^2 = P_2 \left(1 + \gamma \frac{A_2}{A_3}\right), \tag{C.4}$$

which is the form given in Section 2.2.1.

Moving on to the conservation of energy equation, assumption 6 implies the energy of the flow is constant throughout the domain. For an ideal gas with constant specific heats, this is equivalent to a constant stagnation temperature at all stations:

$$T_{t_1} = T_{t_2} = T_{t_3} = T_3 + \frac{1}{2c_p}\left(u_{\theta_1}^2 + u_{m_3}^2\right), \tag{C.5}$$

With all three conservation equations defined, the final equation necessary to find the final uniform state after the free expansion is the ideal gas equation of state, $P = \rho RT$, giving the final system:

$$\frac{A_3}{A_2}\frac{P_3}{RT_3} u_{x_3} = C_c P_{t_2} \sqrt{\frac{\gamma}{RT_{t_2}}} \frac{\rho_2}{\rho_{t_2}} \sqrt{\frac{T_2}{T_{t_2}}} \tag{C.6a}$$

$$P_3 + \rho_3 u_{x_3}^2 = P_2 \left(1 + \gamma \frac{A_2}{A_3}\right) \tag{C.6b}$$

$$T_3 + \frac{u_{x_3}^2}{2c_p} = T_{t_2} - \frac{u_\theta^2}{2c_p} \tag{C.6c}$$

$$P_3 = \rho_3 R T_3 \tag{C.6d}$$

The system of equations in Equation C.6 are coupled and require an iterative solution technique. In this thesis, MATLAB was employed to carry out this solution with inlet stagnation properties and geometric feautres specified as inputs. The static properties at station 2 were calculated from the inlet stagnation properties by taking advantage of assumption 1 which implies that not only T_t, but also P_t, is constant from station 1 to 2. The expressions for finding the static properties at the throat are:

$$T_2 = \frac{T_{t_1} - \frac{u_{\theta_1}^2}{2c_p}}{1 + \frac{\gamma - 1}{2}}, \tag{C.7a}$$

$$P_2 = P_{t_1} \left(1 + \frac{\gamma - 1}{2} \left(1 + \frac{u_{\theta_1}^2}{\gamma R T_2}\right)\right)^{\frac{-\gamma}{\gamma - 1}}, \tag{C.7b}$$

Upon solution of Equation C.6, the Mach number at station 3 must be calculated so that the stagnation pressure, P_{t_3} may be found. Then, a maximum loss coefficient associated with the free expansion of the tip seal jet may be defined by:

$$\zeta_{max} = \frac{-\dot{m} R T_3}{\dot{W}_{ideal}} \ln \frac{P_{t_3}}{P_{t_1}}, \tag{C.8}$$

Equation C.8 estimates the maximum loss for two reasons. First, the control volume analysis inherently assumes a uniform state which is the end result after the full expansion and mixing out of the jet. Second, in order to get the viscous lost work, the entropy generated should be multiplied by the temperature at which it was generated and this product integrated over the entire process. However, this integration is impossible to define for a simple control volume analysis. Since the static temperature must monotonically rise from the minimum at station 2 until station 3, scaling by T_3 yields the maximum possible dissipated power, as if all the entropy were generated at the maximum temperature in the expansion process. Nevertheless, the simple control volume analysis agrees exceptionally well with loss computed with CFD as shown in Section 2.2.1.

The expression in Equation C.8 may be re-written in terms of design parameters (though with less accuracy and physical rigor than the control volume analysis). The ideal work output, $\dot{W}_{ideal}$, can be approximated by the work output of the stage, $\dot{W}_{out} = \dot{m}_{tot}\Delta\bar{h}_t = \dot{m}_{tot}U^2\bar{\psi}$, where ψ is the stage loading. The Mach number at the tip can be used to estimate the mixed out static temperature, T_3, at the cavity exit. To do so, RT_3 is replaced with:

$$\frac{a_{tip}^2}{\gamma} = \frac{1}{\gamma}\frac{V_{tip}^2}{M_{tip}^2}, \tag{C.9}$$

where V_{tip} is the flow velocity at the rotor exit and at the rotor tip. Using the Mach number in the relative frame, the circumferential flow velocity is designed to be equal and opposite to the rotor tip speed. Thus, Equation C.9 becomes:

$$\frac{1}{\gamma}\frac{V_{tip}^2}{M_{tip}^2} = \frac{1}{\gamma}\frac{U_{tip}^2}{M_{tip}^2}\left(1+\phi_{tip}^2\right), \tag{C.10}$$

where ϕ_{tip} is the flow coefficient at the blade tip, $\phi_{tip} \equiv V_{x_{tip}}/U_{tip}$. Substituting the approximate expression for $\dot{W}_{ideal}$ and Equation C.10 into Equation C.8 yields:

$$\zeta_{max} = -\frac{\dot{m}_{f_{cav}}}{\gamma \psi_{tip} M_{tip}^2} \left(1 + \phi_{tip}^2\right) \ln \pi_t, \tag{C.11}$$

Equation C.11 has several more approximations than Equation C.8 which results from the control volume analysis. Therefore, it is suggested that Equation C.11 be used only as a qualitative design guideline and comparison method between tip shroud flow field designs. For quantitative comparison, the more rigorous control volume analysis and its result expression should be used.

Appendix D

Mass Flow Rate Variation with Pressure Ratio through Sharp-Edged Orifice

This appendix will compare in greater detail the findings published by Cunningham in [3] regarding the mass flow rate through sharp-edged orifices. To assess the utility of Cunnigham's findings applied to the simple seal configurations, two sample geometries were made (see Figures D-1 and D-2), one to replicate Cunningham's results, and one to approximate simply the tip seal geometry in Figure 1-2.

Figures D-3 and D-4 compare the ratio of static to total pressure as a function of axial location from Cunningham's published experiments and from the computational results, respectively. Qualitatively, the trends are the same, most notably that the sonic line (i.e. the point where the pressure ratio drops below the critical ratio) moves closer to the leading edge of the orifice plate as the downstream static pressure is lowered. These results increase the confidence that the CFD can accurately model sonic flow through orifice-like contractions.

To confirm that the tip seal behaves like a simple 2D orifice, and that the mass flow phenomenon is directly related to this geometrical feature, Figure D-5 compares the mass flow rate through the seal as a function of the ratio of downstream static to

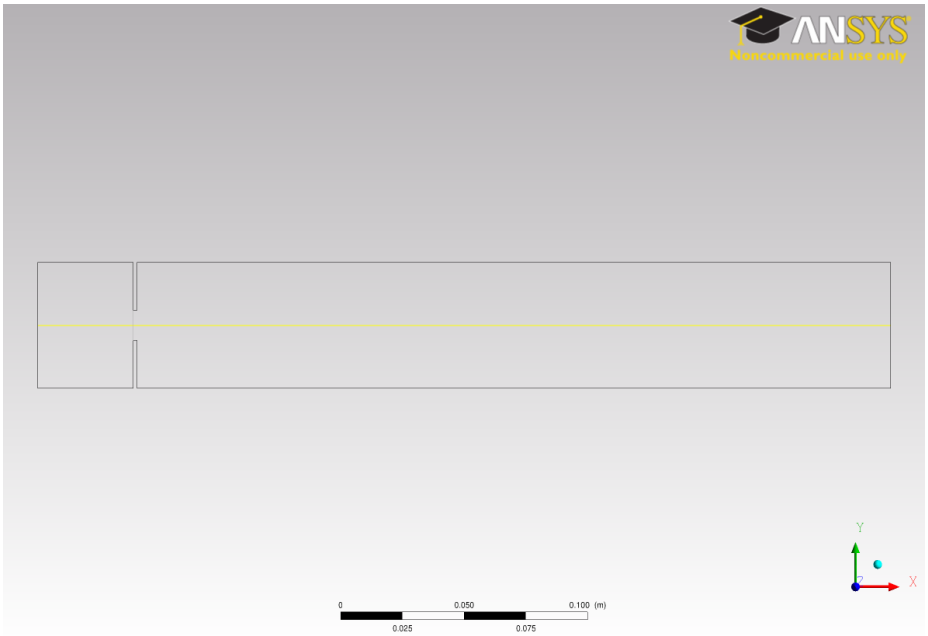

Figure D-1: Computational geometry to model results from Cunningham [3].

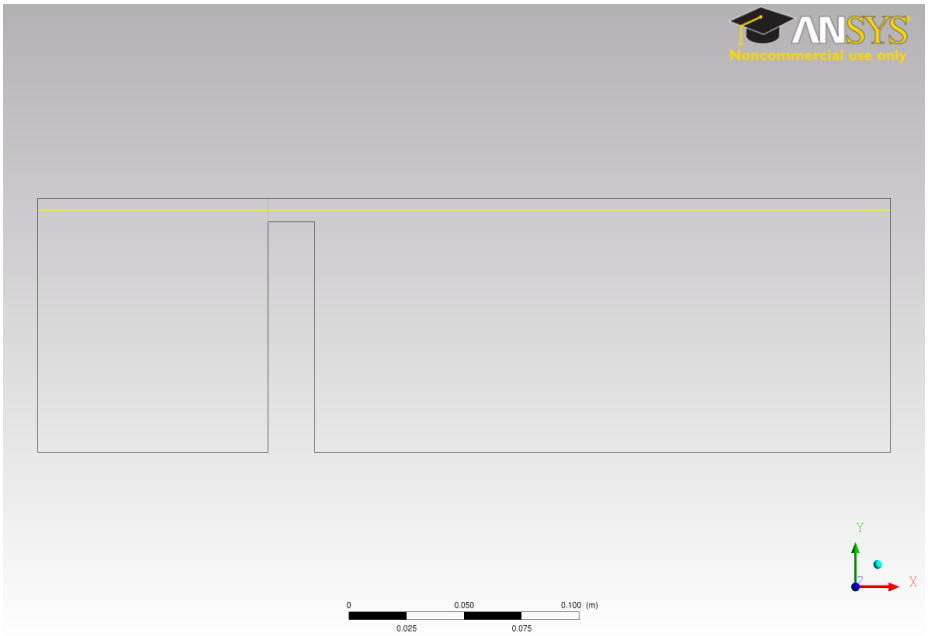

Figure D-2: Computational geometry to approximate the tip seal geometry of the turbine blade.

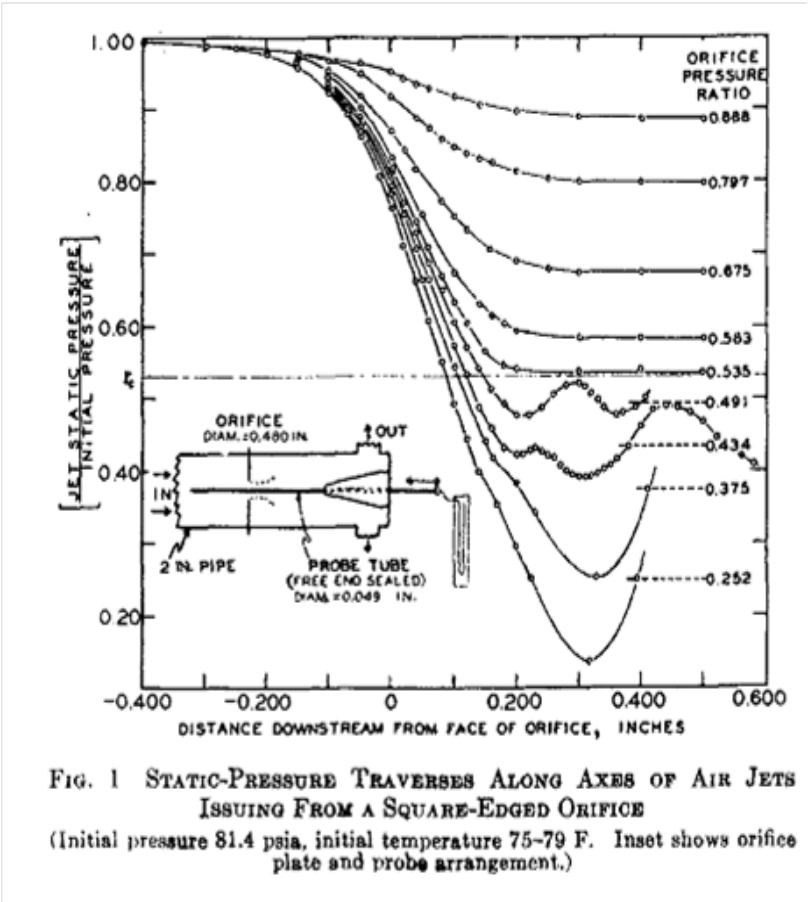

FIG. 1 STATIC-PRESSURE TRAVERSES ALONG AXES OF AIR JETS ISSUING FROM A SQUARE-EDGED ORIFICE

(Initial pressure 81.4 psia, initial temperature 75–79 F. Inset shows orifice plate and probe arrangement.)

Figure D-3: Experimental measurements of pressure ratio as a function of axial location from Cunningham's work [3].

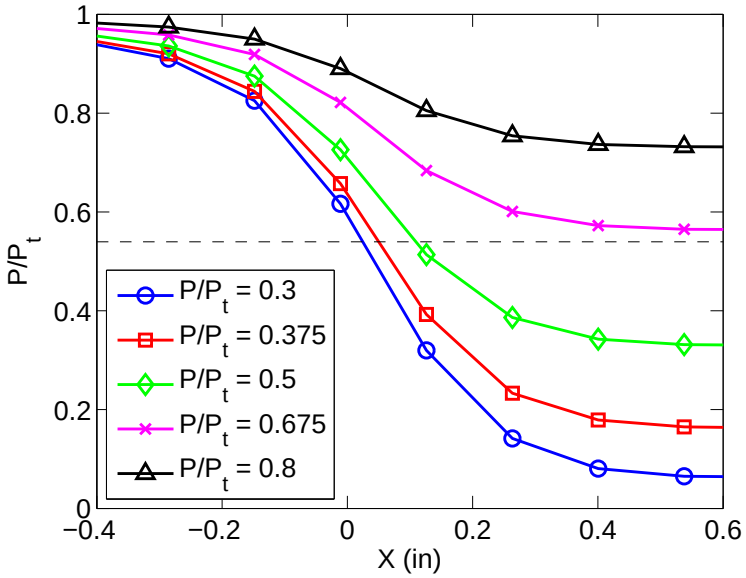

Figure D-4: Computed pressure ratio as a function of axial location for the model of Cunningham's experimental apparatus.

upstream stagnation pressures for the basic seal geometry in Figure D-2 and the actual generic shroud geometry. The figure demonstrates a strong agreement between the two, diverging only slightly at higher pressure ratios. Figure D-6 compares contours of meridional Mach number (the relevant Mach number for determining the sonic condition in swirling flows) to demonstrate how the vena contracta gets smaller as the injected diffuser leakage mass flow rate is increased. The black horizontal line is a line of constant radius to aid in comparison of the size of the supersonic region (colored as red-orange). Based on the results in these figures, it is clear that the flow over the tip seal behaves like sonic flow through a 2D orifice and is consistent with the experimental findings of Cunningham.

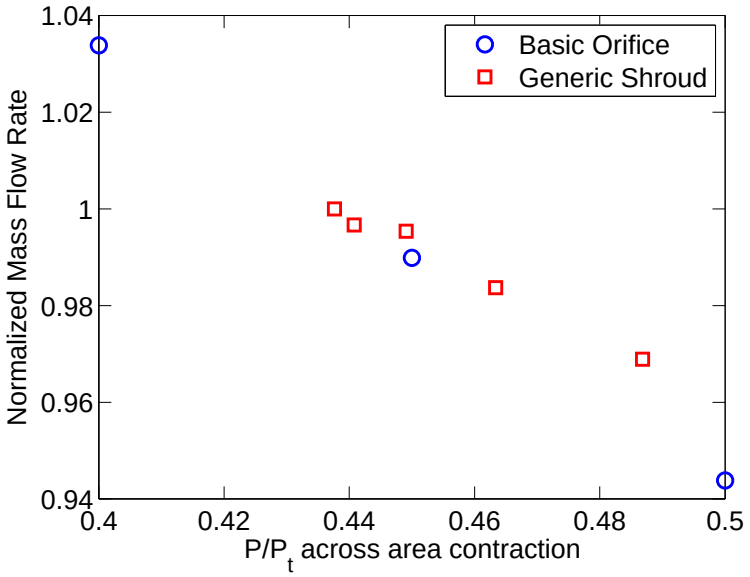

Figure D-5: Variation of mass flow rate through the sealing orifice as a function of orifice pressure ratio for the basic 2D orifice and the generic shroud computations. Mass flow rate in each data series is normalized to the mass flow rate for the pressure ratio corresponding to the no injected sealing flow case.

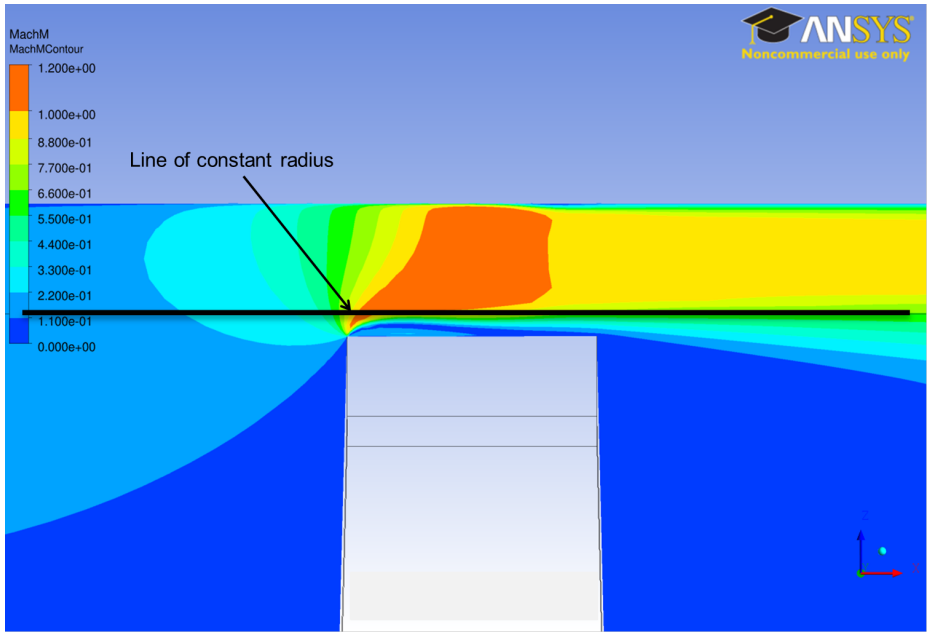

(a) Nominal sealing mass flow rate.

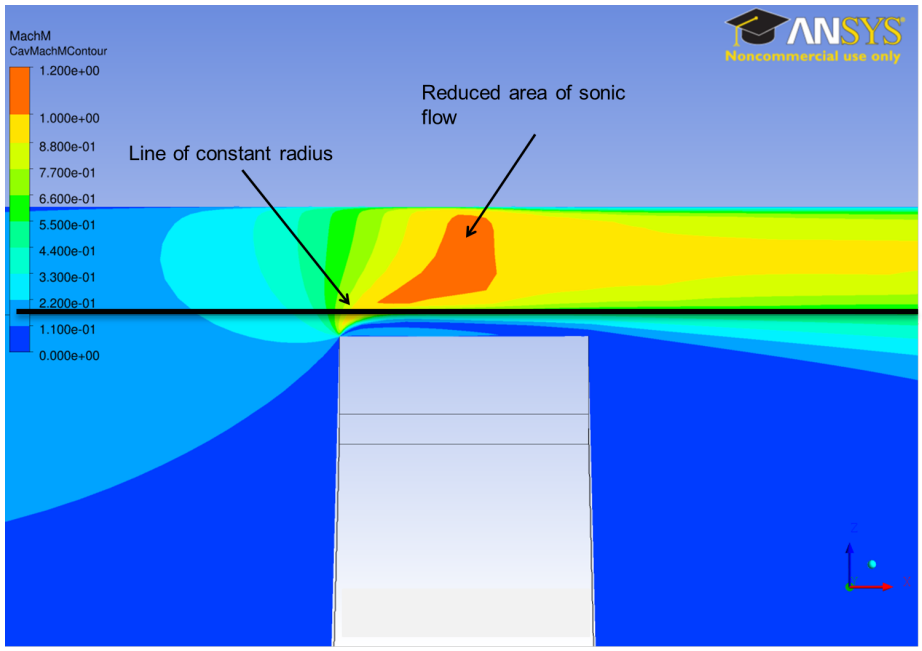

(b) Sealing mass flow rate 4x nominal.

Figure D-6: Contours of meridional Mach number above the tip seal for different injected sealing mass flow rates.

Appendix E

Mixing Loss between Two Streams

This appendix presents a simple control volume analysis for calculating the lost opportunity to do work due to viscous mixing of two streams. Imagine two uniform streams interacting in an arbitrary control volume as shown in Figure E-1. The vector $\sum \vec{F}$ represents the net direction and magnitude of all forces acting on the control volume, including pressure and body forces.

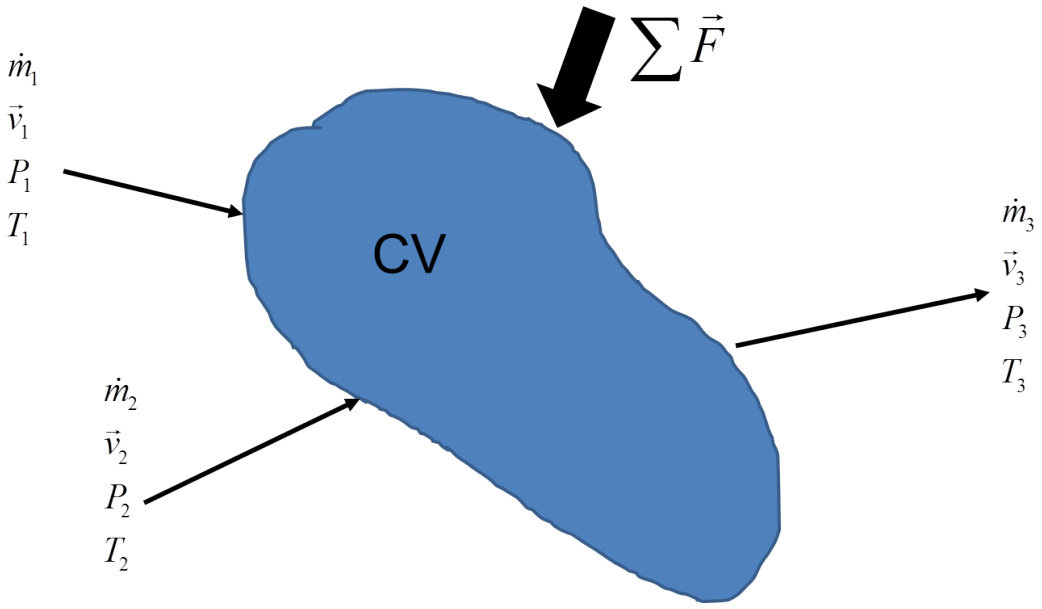

Figure E-1: Arbitrary control volume for the mixing of two uniform streams.

Applying continuity is straightforward, yielding:

$$\dot{m}_1 + \dot{m}_2 = \dot{m}_3 \tag{E.1}$$

The steady conservation of momentum equation applied to this control volume is given by:

$$\dot{m}_1\vec{v}_1 + \dot{m}_2\vec{v}_2 + \sum \vec{F} = \dot{m}_3\vec{v}_3 \tag{E.2}$$

Substituting in the continuity equation, the momentum equation can be re-arranged to yield an expression for the mixed-out velocity, $\vec{v}_3$:

$$\vec{v}_3 = \frac{\sum \vec{F}}{\dot{m}_1 + \dot{m}_2} + \dot{m}_{f_1}\vec{v}_1 + \dot{m}_{f_2}\vec{v}_2, \tag{E.3}$$

The main equation for calculating viscous lost work is the conservation of energy equation. The energy equation is expressed as:

$$\frac{\partial E_{CV}}{\partial t} = 0 = \dot{m}_1 h_{t_1} + \dot{m}_2 h_{t_2} - \dot{m}_3 h_{t_3}, \tag{E.4}$$

To find an expression for the lost opportunity to do work due to viscous effects, it is assumed that the lost kinetic energy after mixing is transferred irreversibly to internal energy by viscous effects. Thus, the difference in static enthalpy from before and after mixing gives an upper bound on the viscous lost work. Mathematically, this is expressed as (after substituting in the continuity equation and Equation E.3):

$$\frac{2\dot{W_{loss}}}{\dot{m}_1+\dot{m}_2} = \dot{m}_{f_1}v_1^2 + \dot{m}_{f_2}v_2^2 - \left(\frac{\sum \vec{F}}{\dot{m}_1+\dot{m}_2} + \dot{m}_{f_1}\vec{v}_1 + \dot{m}_{f_2}\vec{v}_2\right)\cdot\left(\frac{\sum \vec{F}}{\dot{m}_1+\dot{m}_2} + \dot{m}_{f_1}\vec{v}_1 + \dot{m}_{f_2}\vec{v}_2\right), \quad \text{(E.5)}$$

Defining θ as the relative angle between inlet streams 1 and 2 according to the definition of the dot product:

$$\vec{v}_1 \cdot \vec{v}_2 = v_1 v_2 \cos\theta \quad \text{(E.6)}$$

the dot product term on the right-hand side of Equation E.5 can be expanded and like terms gathered to express the viscous lost work as depending on three parameters: the difference in inlet stream velocity magnitudes, the angle between the streams, and the sum of all forces on the control volume. This relationship is given by:

$$\frac{2\dot{W_{loss}}}{\dot{m}_1+\dot{m}_2} = \dot{m}_{f_1}\dot{m}_{f_2}\left[(v_1-v_2)^2 + 4v_1v_2\sin^2\frac{\theta}{2}\right] - F', \quad \text{(E.7)}$$

where the relationship, $\dot{m}_{f_1} = 1 - \dot{m}_{f_2}$ has been used to group the mass flow fractions on the right-hand side of Equation E.7. The term F' represents the group of terms dependent on the sum of forces acting on the control volume, and its value is given by:

$$F' = \left(\frac{\left|\sum \vec{F}\right|}{\dot{m}_1+\dot{m}_2}\right)^2 + \frac{2\left|\sum \vec{F}\right|}{\dot{m}_1+\dot{m}_2}\left(\dot{m}_{f_1}v_1\cos\alpha + \dot{m}_{f_2}v_2\cos\beta\right), \quad \text{(E.8)}$$

where α and β are the relative angles between the net force vector and the velocity vectors of streams 1 and 2, respectively.

By keeping the F' term, reversible transfers of kinetic energy to pressure increases

(which are incorporated in static enthalpy) may be accounted for and will not contribute to viscous lost work. In practice, this force term may be difficult to define as pressure levels before and after mixing are not necessarily known *a priori*. Dropping the term, then, will give an upper bound on the viscous losses due to mixing. However, for mixing processes which occur in regions small compared to the overall domain (for example, due to purge flow injection or cavity exit flow mixing in turbomachines), this assumption is reasonable. It is under similar assumptions that Zlatinov expanded the mixing loss model developed by Young and Wilcock [27] to include swirling flow [1], and it can be shown that Equation E.7 reduces to their expression under the same assumptions.

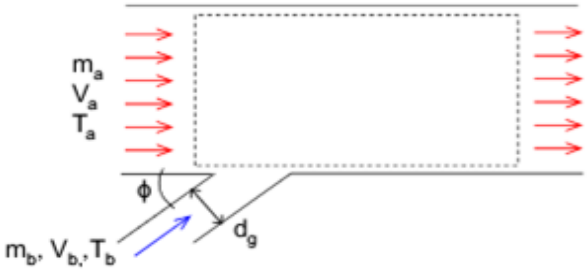

Figure E-2: Simple axisymmetric model of mixing between an injected flow and main flow [1].

Specifically, Zlatinov examined the case of an injected flow (shown in Figure E-2) under the following assumptions:

1. Axisymmetric, constant radius, swirling flow

2. Constant flow area

3. $\dot{m}_b \ll \dot{m}_a$ such that outlet properties are very nearly the same as the inlet properties.

Under these assumptions (and taking streams a and b as streams 1 and 2, respectively), Equation E.7 reduces to:

$$\frac{2\dot{W}_{loss}}{\dot{m}_a} = \frac{\dot{m}_a}{\dot{m}_b}\left((v_a - v_b)^2 + 4v_a v_b \sin^2\frac{\phi}{2}\right), \tag{E.9}$$

as F' goes to zero, $\dot{m}_a + \dot{m}_b \approx \dot{m}_a$, and $\dot{m}_{f_a} \approx 1$, all by assumption 3. Expanding Equation E.9 yields:

$$\dot{W}_{loss} = \frac{\dot{m}_b}{2}\left(v_a^2 - 2v_a v_b + v_b^2 + 2v_a v_b - 2v_a v_b \cos\phi\right), \tag{E.10}$$

By once again applying the definition of the dot product and the implication of assumption 3 that the static temperature is approximately constant throughout the mixing process, Zlatinov's mixing equation is recovered:

$$\Delta\dot{S}_{visc} = \frac{\dot{m}_b}{2T_a}\left((v_{a_1} - v_{b_1})^2 + (v_{a_2} - v_{b_2})^2 + (v_{a_3} - v_{b_3})^2\right), \tag{E.11}$$

where the numeric subscripts indicate coordinate directions. Thus, the more general Equation E.7 is consistent with the simpler analysis performed by Zlatinov.

Appendix F

Influence of Area Ratio on Choking Condition in Swirling Flow

This appendix explains how increasing the tip gap height can unchoke the tip seal without changing the pressure ratio across the blade (which also sets the pressure ratio across the seal) by changing the cavity inlet flow properties. Typical compressible flow analysis (i.e. 1D, isentropic flow) maintains that once the pressure ratio across the throat is fixed at or below the critical pressure ratio, the flow will always be sonic at the throat. In the more complicated flow conditions present in tip shroud cavity flow, both of the key assumptions of this approach are violated. Namely, the flow is non-isentropic (viscous losses on walls within the cavity) and three-dimensional instead of one-dimensional. The former violation is not significant enough to explain the unchoking due to a change in minimum area. In fact, frictional effects tend to increase the likelihood of choking of compressible flows. The multi-dimensional nature of the tip shroud cavity flow, however, does explain the area dependence of choking. Specifically, the presence of swirl in the flow introduces another degree of freedom in the traditional isentropic flow equations.

To illustrate this, consider an annular area contraction with constant radius, swirling flow as a simple model of the tip seal in the turbine geometry (see Figure F-1). Station 1 represents the shroud leading edge; station 2 is the tip seal with

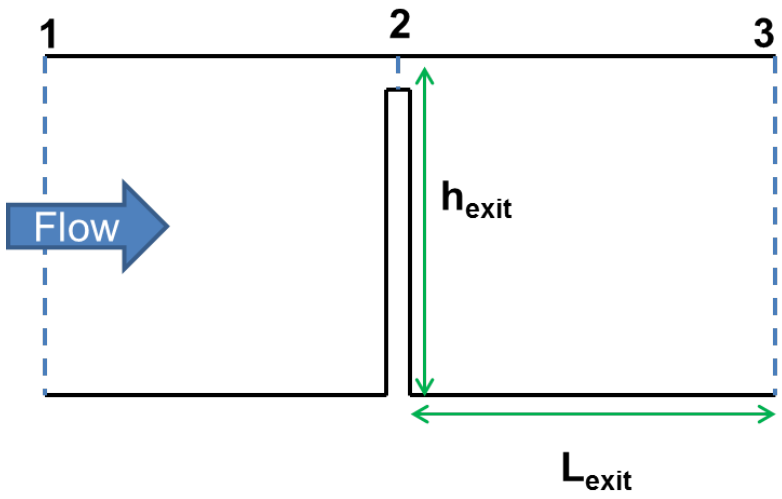

Figure F-1: Schematic of simple contraction at the tip seal with an incoming swirling flow.

tip gap, δ; station 3 represents the shroud trailing edge. In swirling compressible flow, the meridional Mach number, rather than the total Mach number, determines whether or not a flow is choked. A swirling flow is considered choked if the meridional Mach number at the minimum area is unity. Meridional Mach number is related to total Mach number by:

$$M_m = M_{tot} \cos \alpha, \tag{F.1}$$

where M_{tot} is the total Mach number, M_m is the meridional Mach number, and α is the local swirl angle (in either stationary or rotor-relative frame so long as the total Mach number is consistent with the frame choice). Substituting Equation F.1 into the compressible flow relation for static-to-stagnation pressure yields:

$$\frac{P_{out}}{P_{t,in}} = f(M_m, \gamma, \alpha) = \left(1 + \frac{\gamma - 1}{2} M_m^2 \sec^2 \alpha\right)^{\frac{-\gamma}{\gamma - 1}}, \tag{F.2}$$

where P_t is the stagnation pressure, P is the static pressure, and γ is the ratio of specific heats for the fluid.

For choked flow at a throat ($M_m = 1$), Equation F.2 states that the critical pressure ratio across the throat is a function of both fluid properties (i.e. γ) and local swirl angle, α. In constant radius flows with no torque input, as the flow area decreases, the axial velocity must increase to satisfy continuity. However, the circumferential velocity remains constant in order to satisfy conservation of angular momentum. Therefore, the local swirl angle is in fact a function of area, and the swirl angle will decrease as the flow area decreases. Mathematically this is expressed with an influence coefficient for isentropic, constant radius flow with negligible torque or energy transfer:

$$d\alpha = \frac{\sin 2\alpha}{2(1 - M_m^2)} \frac{dA}{A}, \tag{F.3}$$

Thus Equation F.2 is also implicitly dependent on local flow area. Figure F-2 demonstrates how the critical pressure ratio for choked flow varies with local swirl angle for a fixed ratio of specific heats. The blue line is a plot of Equation F.2. The black dashed lines indicate the CFD-calculated static-to-stagnation pressure ratio across the cavity for various tip gaps (static pressure is evaluated at the shroud trailing edge/station 3; stagnation pressure is evaluated at the shroud leading edge/station 1). The red points represent the critical pressure ratios required for choking given the CFD-calculated local swirl angle at the tip seal (station 2) for each tip gap. The green points mark the inlet swirl angles at the shroud leading edge (station 1) for each tip gap as calculated in the CFD.

The interpretation of Figure F-2 shows that in order for a given tip gap to be choked, its corresponding red point must lie above the black dashed line. In other words, the applied pressure ratio across a tip gap for a given local swirl angle must be below the blue line to choke the flow. Physically, this indicates that the applied pressure ratio across the cavity is lower than the critical pressure ratio to generate sonic flow at the throat. Only the nominal and 1.8x tip gaps exhibit this behavior while the larger 7.5x tip gap does not. This would suggest that the meridional Mach

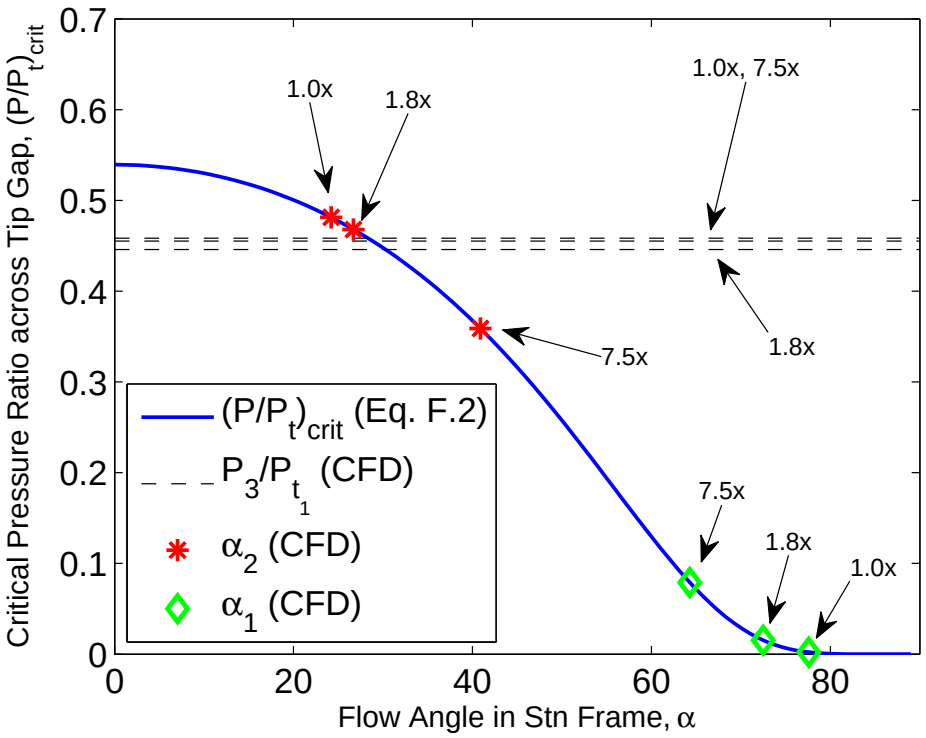

Figure F-2: Variation of the critical pressure ratio for choked flow as a function of local swirl angle. The blue line is a plot of Equation F.2. The black dashed lines indicate the static-to-stagnation pressure ratio across the cavity for various tip gaps (static pressure is evaluated at the shroud trailing edge; stagnation pressure is evaluated at the shroud leading edge). The red points represent the critical pressure ratios required for choking given the measured local swirl angle at the tip seal for each tip gap. The green points mark the inlet swirl angles at the shroud leading edge for each tip gap.

number at the tip seal for the 7.5x tip gap should be subsonic and thus unchoked, which is consistent with the unchoked flow over the tip observed in Figure 4-4. The other important implication evident in Figure F-2 is the change in local swirl angle from the cavity inlet (green points) to the area contraction at the tip seal (red points). The nominal tip gap has the greatest decrease in angle with the 1.8x tip gap exhibiting only a slightly smaller decrease. The 7.5x tip gap, however, shows a significantly lower change in local swirl angle from inlet to throat. These changes are consistent with Equation F.3 as the inlet-to-throat area ratio is significantly less for the 7.5x tip gap case as opposed to the nominal and 1.8x tip gap cases. The 7.5x tip gap case has a significantly lower average inlet flow angle as a result of the larger gap capturing more of the non-uniform main flow. Therefore the unchoking of the tip seal in large tip gap cases (e.g. the 7.5x tip gap) is a combination of the presence of swirl and flow non-uniformity in the main flow spanwise direction at a fixed blade tip pressure ratio.

Bibliography

[1] M. B. Zlatinov, C. S. Tan, M. Montgomery, T. Islam, and M. Harris. Turbine hub and shroud sealing flow loss mechanisms. *Journal of Turbomachinery*, 134:061027, 2012.

[2] D. S. Miller. *Internal Flow Systems*. British Hydraulic Research Association (BHRA) Information Services, Cranfield, Bedfordshire, England, 1990.

[3] R. G. Cunningham. Orifice meters with supercritical compressible flow. *Transactions of the ASME*, pages 625–638, 1951.

[4] Turbines: Shrouded vs unshrouded turbines. `http://www.rolls-royce.com/about/technology/gas_turbine_tech/turbines.jsp`. Accessed: 2014-6-29.

[5] G. M. Laskowski, R. S. Bunker, J. C. Bailey, G. Ledezma, S. Kapetanovic, G. M. Itzel, M. A. Sullivan, and T. R. Farrell. An investigation of turbine wheelspace cooling flow interactions with a transonic hot gas path-part ii: Cfd simulations. *Journal of Turbomachinery*, 133:041020, 2011.

[6] C. Cao, J. W. Chew, P. R. Millington, and S. I. Hogg. Interaction of rim seal and annulus flows in an axial flow turbine. *Journal of Engineering for Gas Turbines and Power*, 126:786–793, 2004.

[7] A. M. Wallis, J. D. Denton, and A. A. J. Demargne. The control of shroud leakage flows to reduce aerodynamic losses in low aspect ratio, shrouded axial flow turbine. *Journal of Turbomachinery*, 123:334–341, 2001.

[8] B. Rosic and J. D. Denton. Control of shroud leakage loss by reducing circumferential mixing. *Journal of Turbomachinery*, 130(2):021010, 2008.

[9] J. Gao, Q. Zheng, G. Yue, and L. Sun. Control of shroud leakage flows to reduce mixing losses in a shrouded axial turbine. In *Proc. IMechE Vol. 226 Part C: J. Mechanical Engineering Science*, pages 1263–1277, 2012.

[10] J. D. Denton. Loss mechanisms in turbomachines. *Journal of Turbomachinery*, 115(4):621–656, 1993.

[11] S. D. Hunter and S. R. Manwaring. Endwall cavity flow effects on gaspath aerodynamics in an axial flow turbine. In *Proceedings of ASME TurboExpo 2000*, May 8-11 2000.

[12] J. Gier, B. Stubert, B. Brouillet, and L. de Vito. Interaction of shroud leakage flow and main flow in a three-stage lp turbine. In *Proceedings of ASME TurboExpo 2003*, June 16-19 2003.

[13] B. Rosic, J. D. Denton, and E. M. Curtis. The influence of shroud and cavity geometry on turbine performance-an experimental and computational study. In *Proceedings of ASME TurboExpo 2007*, May 14-17 2007.

[14] R. S. Abhari, K. G. Barmpalias, A. I. Kalfas, N. Shibukawa, and T. Sasaki. The impact of rotor inlet cavity volume and length scale on efficiency. In *Proceedings of ASME TurboExpo 2012*, June 11-15 2012.

[15] M. Pau, F. Cambuli, and N. Mandas. Shroud leakage modeling of the flow in a two stage axial test turbine. In *Proceedings of ASME TurboExpo 2008*, June 9-13 2008.

[16] A. Pfau, J. Schlienger, D. Rusch, A. I. Kalfas, and R. S. Abhari. Unsteady flow interactions within the inlet cavity of a turbine rotor tip labyrinth seal. *Journal of Turbomachinery*, 127:679–688, 2005.

[17] K. G. Barmpalias, R. S. Abhari, A. I. Kalfas, T. Hirano, N. Shibukawa, and T. Sasaki. Design considerations for axial steam turbine rotor inlet cavity volume and length scale. *Journal of Turbomachinery*, 134:051031–1, 2012.

[18] A. Pfau, A. I. Kalfas, and R. S. Abhari. Making use of labyrinth interaction flow. In *Proceedings of ASME TurboExpo 2004*, June 14-17 2004.

[19] N. A. Cumpsty and J. H. Horlock. Averaging non-uniform flow for a purpose. In *Proceedings of ASME TurboExpo 2005*, June 6-9 2005.

[20] E. M. Greitzer, C. S. Tan, and M. B. Graf. *Internal Flow: Concepts and Applications*. Cambridge University Press, New York, 2006.

[21] A. G. DiOrio. Small core axial compressors for high efficiency jet aircraft. Master's thesis, MIT, Cambridge, MA, 2010. Dept. of Aeronautics and Astronautics.

[22] S. Mazur. Turbine tip clearance loss mechanisms. Master's thesis, MIT, Cambridge, MA, 2013. Dept. of Aeronautics and Astronautics.

[23] F. M. White. *Fluid Mechanics*. McGraw-Hill, New York, 2008.

[24] A. J. Ward-Smith. *Internal Fluid Flow*. Clarendon Press, Oxford, England, 1980.

[25] E. Fried and I. E. Idelchik. *Flow Resistance: A Design Guide for Engineers*. Hemisphere Publishing Co., New York, 1989.

[26] E. M. Curtis, J. D. Denton, J. P. Longley, and B. Rosic. Controlling tip leakage flow over a shrouded turbine rotor using an air-curtain. In *Proceedings of ASME TurboExpo 2009*, June 8-12 2009.

[27] J. B. Young and R. C. Wilcock. Modeling the air-cooled gas turbine: Part 2-coolant flows and losses. *Journal of Turbomachinery*, 124:214–221, 2002.

[28] J. D. Coull, N. R. Atkins, and H. P. Hodson. Winglets for improved aerothermal performance of high pressure turbines. *Journal of Turbomachinery*, 136:091007, 2014.

[29] D. L. Darmofal, R. Khan, E. M. Greitzer, and C. S. Tan. Vortex core behaviour in confined and unconfined geometries: A quasi-one-dimensional model. *Journal of Fluid Mechanics*, 449:61–84, 2001.

[30] D. Pagan. *Contribution a L'Etude Experimental et Theoretique de L'Eclatement Tourbillonnaire en Air Incompressible*. PhD thesis, L'Universite Paris VI, Paris, France, 1989.

[31] J. M. Delery. Aspects of vortex breakdown. *Progress in Aerospace Sciences*, 30:1–59, 1994.

[32] A. Pfau, A. I. Kalfas, and R. S. Abhari. Making use of labyrinth interaction flow. In *Proceedings of ASME TurboExpo 2004*, June 14-17 2004.

[33] S. Sakulkaew, C. S. Tan, E. Donahoo, C. Cornelius, and M. Montgomery. Compressor efficiency variation with rotor tip gap from vanishing to large clearance. *Journal of Turbomachinery*, 135:031030, 2013.

[34] A. Schäffler. Experimental and analytical investigation of the effects of reynolds number and blade surface roughness on multistage axial flow compressors. *Journal of Engineering for Power*, 102:5–12, 1980.

[35] J. D. Anderson, Jr. *Fundamentals of Aerodynamics*. McGraw-Hill, New York, fifth edition, 2011.

[36] P. K. Kundu and I. M. Cohen. *Fluid Mechanics*. Academic Press, San Diego, 2008.

[37] I. Mahle and R. Schmierer. Inverse fin arrangement in a low pressure turbine to improve the interaction between shroud leakage flows. In *Proceedings of ASME TurboExpo 2011*, June 6-10 2011.

[38] M. G. Hall. Vortex breakdown. *Annual Review of Fluid Mechanics*, 4:195–218, 1972.

[39] D. Cho. Effect of vortex core stagnation pressure on tip clearance flow blockage in turbomachines. Master's thesis, MIT, Cambridge, MA, 1995. Dept. of Aeronautics and Astronautics.

[40] J. S. Marshall. A general theory of curved vortices with circular cross-section and variable core area. *Journal of Fluid Mechanics*, 229:311–338, 1991.

[41] J. R. Taylor. *An Introduction to Error Analysis*. University Science Books, Sausalito, CA, 1997.